Johannes A. Kramer

An Aluminum Optical Clock Setup and Its Evaluation Using Ca$^+$

An Aluminum Optical Clock Setup and Its Evaluation Using Ca^+

Von der QUEST-Leibniz-Forschungsschule der

Gottfried Wilhelm Leibniz Universität Hannover

zur Erlangung des akademischen Grades

Doktor der Naturwissenschaften
Dr. rer. nat

genehmigte Dissertation von

Johannes Albrecht Kramer, Dipl.-Phys.

2023

An Aluminum Optical Clock Setup and Its Evaluation Using Ca$^+$

Johannes A. Kramer

Referent: Prof. Dr. Piet O. Schmidt
Gottfried Wilhelm Leibniz Universität Hannover und
Physikalisch-Technische Bundesanstalt, Braunschweig
Korreferent: PD Dr. Ekkehard Peik
Physikalisch-Technische Bundesanstalt, Braunschweig
Korreferent: Dr. Christian Roos
Universität Innsbruck, Innsbruck
Tag der Disputation: 15.07.2022

Johannes A. Kramer: *An Aluminum Optical Clock Setup and Its Evaluation Using Ca*$^{+}$, © March 10, 2023

With a little bit of imagination, anything is possible.

— Richard Dean Anderson

Someone once told me that time was a predator that stalked us all our lives.
But I rather believe that time is a companion who goes with us on the journey
and reminds us to cherish every moment because they'll never come again.

— Jean Luc Picard

Abstract

With the ongoing improvement in the accuracy of optical atomic clocks, new tools for timekeeping and for answering open questions of fundamental physics become available. At this time, no other physical quantity can be measured more precisely than the frequency ratio between the best performing optical clocks. Beating already now the accuracy of the SI definition of the second by more than two orders of magnitude, they will be the foundation of its re-definition in the future (Riehle, 2015). The best clocks nowadays can resolve cm-scale height differences in the gravitational potential and thus are valuable tools in the field of geodesy and global navigation systems (Mehlstäubler et al., 2018). The ticking rates of optical clocks of dissimilar atomic species depend differently on the value of fundamental physical constants. Hence, comparing their clock frequencies with high accuracy helps to unravel the inconsistencies in our understanding of the Universe and its evolution (Stadnik, 2017; Calmet and Keller, 2015).

At the time of writing this thesis the most accurate clock is the optical aluminum ion clock at the National Institute of Standards and Technology (NIST) with an inaccuracy below 1×10^{-18} (Brewer et al., 2019b). This remarkably low inaccuracy results from the low sensitivity of this ion to external perturbations and careful analysis of the remaining systematic frequency shifts.

This thesis reports about the progress of the aluminum ion clock that is set up at the German National Metrological Institute, Physikalisch-Technische Bundesanstalt (PTB) in Braunschweig. All known relevant systematic frequency shifts are discussed. The systematic shifts were measured on the co-trapped logic ion $^{40}\mathrm{Ca}^{+}$, which is advantageous due to its higher sensitivity to external fields compared to $^{27}\mathrm{Al}^{+}$. The shift analysis includes the systematic shift due to the rapidly oscillating magnetic field of the ion trap, called trap-induced ac Zeeman shift. Using the method described in Ref. (Gan et al., 2018), we measured a magnetic field of 21.27(17) µT, which is higher compared to other reported values (Gan et al., 2018; Brewer et al., 2019b). Due to the high accuracy of this method we could measure the shift with an uncertainty of 2.3×10^{-19}. Improvements on the uncertainty of the shift due to background gas collisions have been achieved by a refurbishment of the vacuum chamber, which lead to a reduction of background pressure by one order of magnitude to 11(6) nPa, and the application of refined mathematical models (Hankin et al., 2019; Davis, Dubé, and Vutha, 2019), yielding an uncertainty of the collisional shift of 3.9×10^{-19}. The lower chamber pressure also improved the overall performance of the experiment, because the probability of ion-loss due to heavy collisions and chemical reactions of the aluminum ion with hydrogen was significantly reduced. The uncertainty in the 2nd-order Doppler shift due to excess micromotion has been reduced by one order of magnitude since the last report (Scharnhorst, 2018) to 1.2×10^{-19}. The described setup aims at building an optical clock that is capable to reach a total inaccuracy of 1×10^{-18} and below. The reported first coherent excitation of the aluminum clock transition in this experiment marks a milestone in the planned start of actual clock operation in the near future. A minimum linewidth of 10 Hz was achieved, currently limited by uncompensated fiber noise. Errors in the clock state detection using a quantum logic protocol are discussed and resulted in an estimated error probability of 0.1 %.

The presented aluminum ion clock will be an important part of the time-keeping infrastructure at PTB and in the international network of optical clocks, because its characteristics with regard to the sensitivities to external perturbations and constancy of fundamental constants is complementary to other atomic species. Utilizing its high accuracy for frequency comparisons across PTB campus and by fiber links to other places in Europe (Predehl et al., 2012; Droste et al., 2013; Raupach, Koczwara, and Grosche, 2014), it will contribute to the points stated in the beginning, and may help to resolve the deviations of frequency ratios between optical clocks of different species that were reported in Ref. (Beloy et al., 2021).

Keywords: single-ion clock, frequency metrology, optical atomic clock, high accuracy, systematic frequency shifts, quantum-logic spectroscopy, ac Zeeman shift, micromotion, 2$^{\text{nd}}$-order Doppler shift, collisional shift

Zusammenfassung

Durch die fortschreitende Verbesserung der Genauigkeit von optischen Atomuhren stehen neue Werkzeuge zur Zeitmessung und für die Beantwortung offener Fragen in der grundlegenden Physik zur Verfügung. Keine andere physikalische Größe kann derzeit präziser gemessen werden als das Frequenzverhältnis der besten optischen Uhren. Schon heute die Genauigkeit der SI Definition der Sekunde um mehr als zwei Größenordnungen übertreffend, werden sie die Grundlage für die zukünftige Neudefinition dieser Größe darstellen (Riehle, 2015). Die aktuell besten Uhren lösen Höhenunterschiede im Graviationspotential von wenigen cm auf und sind deshalb wertvolle Werkzeuge im Arbeitsfeld der Geodesie und des globalen Navigationssystems (Mehlstäubler u. a., 2018). Die Tickraten von optischen Uhren unterschiedlicher atomarer Spezies hängen unterschiedlich stark vom Zahlenwert von Fundamentalkonstanten ab. Daher helfen Vergleiche von Uhrenfrequenzen mit hoher Genauigkeit Inkonsistenzen in unserem Verständnis des Universums und seiner Entwicklung zu enträtseln (Stadnik, 2017; Calmet und Keller, 2015).

Die derzeit genaueste Uhr ist die optische Aluminiumionenuhr am National Institute of Standards and Technology (NIST) mit einer Ungenauigkeit unter 1×10^{-18} (Brewer u. a., 2019b). Diese bemerkenswert hohe Genauigkeit resultiert aus der geringen Empfindlichkeit dieses Ions gegenüber äußeren Störungen und der sorgfältigen Analyse der übrigen systematischen Frequenzverschiebungen.

Diese Thesis berichtet vom Fortschritt der Aluminiumionenuhr, die am deutschen nationalen Metrologieinstitut, Physikalisch-Technische Bundesanstalt (PTB), in Braunschweig gebaut wird. Alle relevanten systematischen Frequenzverschiebungen werden diskutiert. Die systematischen Verschiebungen wurden auf dem Logikion $^{40}\text{Ca}^+$ gemessen, was einen Vorteil darstellt, da dieses sensitiver auf äußere Felder ist als $^{27}\text{Al}^+$. Die Analyse der systematischen Verschiebungen beinhaltet jene Verschiebung, die durch das schnell oszillierende Magnetfeld der Ionenfalle hervorgerufen wird, welche falleninduzierte ac Zeeman Verschiebung genannt wird. Durch die Anwendung der in Ref. (Gan u. a., 2018) beschriebenen Messmethode wurde ein Magnetfeld von $21.27(17)\,\mu\text{T}$ gemessen, was ein größerer Wert ist, verglichen mit anderen berichteten Werten (Gan u. a., 2018; Brewer u. a., 2019b). Aufgrund der hohen Genauigkeit der Methode, konnten wir die resultierende Frequenzverschiebung mit einer Unsicherheit von 2.3×10^{-19} messen. Eine Verbesserung bezüglich der Unsicherheit aufgrund von Hintergrundgaskollisionen konnte mittels einer Überarbeitung der Vakuumkammer, was zu einer Reduzierung des Hintergrundgrunddruckes um eine Größenordnung auf $11(6)$ nPa führte, und der Anwendung verbesserter mathematischer Modelle (Hankin u. a., 2019; Davis, Dubé und Vutha, 2019) erreicht werden, was in einer Unsicherheit von 3.9×10^{-19} resultierte. Der niedrigere Druck in der Kammer verbesserte außerdem die Betriebsfähigkeit des Experimentes, da die Häufigkeit von Ionenverlusten durch starke Kollisionen und chemischen Reaktionen vom Aluminiumion mit Wasserstoff signifikant reduziert wurde. Die Unsicherheit in der Dopplerverschiebung zweiter Ordnung, hervorgerufen durch Überschussmikrobewegung, konnte seit dem letzten Bericht darüber (Scharnhorst, 2018) um eine Größenordnung auf 1.2×10^{-19} reduziert werden. Der beschriebene Aufbau zielt darauf ab eine optische Uhr aufzubauen, die in der Lage ist eine Gesamtungenauigkeit von 1×10^{-18} und weniger zu erreichen. Die vorgestellte erstmalige kohärente Anregung des Aluminiumuhrenübergangs in diesem Experiment markiert einen Meilenstein für den in der nahen Zukunft geplanten Start des Uhrenbetriebs. Eine minimale Linienbreite von 10 Hz wurde erreicht, welche zu dieser Zeit durch unkompensiertes Faserrauschen limitiert war. Fehler in der Uhrenzustandsdetektion mit einem Quantenlogikprotokoll werden diskutiert, mit dem Resultat einer abgeschätzten Fehlerwahrscheinlichkeit von 0.1 %.

Die vorgestellte Aluminiumionenuhr wird ein wichtiger Teil der Zeitmessungsinfrastruktur an der PTB und im internationalen Netzwerk optischer Uhren sein, da ihre Eigenschaften hinsichtlich äußerer Störungen und der Konstanz von Fundamentalkonstanten komplementär zu anderen Atomsorten sind. Von ihrer hohen Genauigkeit Gebrauch machend, wird diese bei Frequenzvergleichen auf dem PTB Gelände und über Faserverbindungen zu anderen Orten in Europa (Predehl u. a., 2012; Droste u. a., 2013; Raupach, Koczwara und Grosche, 2014) zu den eingangs erwähnten Punkten beitragen, und möglicherweise dabei helfen, die in Ref. (Beloy u. a., 2021) berichteten Ungereimtheiten von Frequenzverhältnissen von optischen Uhren verschiedener Spezies aufzulösen.

Schlagworte: Einzelionenuhr, Frequenzmetrologie, optische Atomuhr, hohe Genauigkeit, systematische Frequenzverschiebungen, Quantenlogikspektroskopie, ac Zeemanverschiebung, Mikrobewegung, Dopplerverschiebung zweiter Ordnung, Kollisionsverschiebung

Contents

III Measurements & Characterization

IV Summary & Outlook

V Appendix

List of Figures

List of Tables

Acronyms

ADEV	Allan deviation
AOM	acousto-optical modulator
AR	anti reflective
BBO	barium borate ($\beta - BaB_2O_4$)
BBR	blackbody radiation
BGC	background gas collisions
BSB	blue sideband
CCD	charged coupled device
CEO	carrier-envelope offset
CFS	collisional frequency shift
CTE	coefficient of thermal expansion
DDS	direct digital synthesis
DP	double-pass
ECDL	external cavity diode laser
EIT	electronically-induced transparency
EMM	excess micromotion
EOM	electro opitcal modulator
FNC	fibre noise cancellation
FPGA	field programmable gate array
FSR	free spectral range
GSC	ground state cooling
GUM	Guide to the Expression of Uncertainty in Measurement
HC	Hänsch-Couillaud
HFSS	Ansys high-frequency structure simulator
HRR	helical resonator
CIPM	International Committee for Weights and Measures
IP	in-phase

IMM	intrinsic micromotion
KTP	potassium titanyl phosphate
LO	local oscillator
MNPQ	Messen, Normen, Prüfen und Qualitätssicherung - Transfer program
OP	out-of-phase
PCF	photonic-crystal fiber
PDH	Pound-Drever-Hall
PLL	phase-locked loop
PM	polarization maintaining
PMT	photomultiplier tube
PPKTP	periodically poled potassium titanyl phosphate
PPLN	periodically poled lithium niobate
PTB	Physikalisch-Technische Bundesanstalt
QL	quantum logic
QND	quantum non-demolition
QPN	quantum projection noise
RF	radio frequency
ROI	region of interest
RSB	red sideband
rms	root mean square
SBC	sideband cooling
SHG	second harmonic generation
SNR	signal-to-noise ratio
SP	single-pass
TA	tapered ampflifier
TAI	Temps Atomique International
ULE	ultra-low expansion
UHV	ultra-high vacuum
UV	ultra violet
VCO	voltage controlled oscillator
WGD	waveguide doubler

Part I

Introduction & Theory

This part introduces the topic of optical atomic clocks. By describing their applications and comparing different optical atomic clock types, the experiment is put into context with the research on new time-keeping standards and their imprortance for answering questions in fundamendal science. It furthermore contains the basic theoretical treatment of trapped ions and their interaction with lasers.

1 Clock Concepts

The following chapter gradually unfolds the topic of time, time-keeping and optical atomic clocks. It introduces the key features *accuracy* and *stability* of clocks, describes how optical frequencies are measured and how optical clocks due to their superior performance in these features improve the established and enable new applications of clocks. The chapter closes with an overview of the different optical clock types.

1.1 A Few Brief Thoughts on the Nature of Time

Time is a useful concept to divide the perceivable world into three distinct parts: the past, the present and the future. It is therefore helpful to organize future activities, under present conditions and past experiences. Clocks are tools which count time by the observation of a particular steady uniform oscillation with defined frequency, which means we have previous knowledge about the number $2n$ of oscillatory peaks in one second. Hence, after counting n oscillations, i.e., a frequency of $n\,\mathrm{s}^{-1} := n\,\mathrm{Hz}$, one second has passed and the clock ticks one tick further. Increasing the frequency, the resolution in which we can divide events grows. This is one of the reasons why the oscillations used for time-keeping increased from the rotation of earth around the sun ($1.9 \times 10^{-6}\,\mathrm{Hz}$) and its own axis ($6.9 \times 10^{-4}\,\mathrm{Hz}$), over the swinging from pendulums (0.1 to 100 Hz), to the current definition of the second by billions of oscillations of electromagnetic microwaves ($9 \times 10^{9}\,\mathrm{Hz}$), to the state of the art, where quadrillion oscillations of light waves (0.3 to $3 \times 10^{15}\,\mathrm{Hz}$) are measured. It is favorable to go to even higher frequencies. A possible physical limit could be the period of about $5.39 \times 10^{-44}\,\mathrm{s}$, as it is the time needed for light to travel the so-called Planck length. A quantum-gravity theory will someday give an understanding on what happens exactly at these scales, but up to now the merging of these independently very successful theories was not possible.

Time is progressing only forwards. We can envision this by the pure existence of non-time-reversible physical processes of our everyday life. It is therefore the direction the universe evolves. Time is one of the four space-time coordinates we assign to events, with the spatial coordinates being the other three. But it is a relative physical quantity. Special relativity states, that two clocks moving with respect to each other will measure the same event at different *local* times. The resting observer will measure its *proper* time $\Delta\tau$ on a resting clock and on a moving clock the *dilated* time

$$\Delta \mathrm{t} = \gamma \Delta\tau \tag{1.1}$$

with

$$\gamma = \frac{1}{\sqrt{1-(\frac{v}{c})^2}}\,, \tag{1.2}$$

where c is the speed of light. It is a relative effect, because no inertial frame is preferential. In consequence the situation is invertible.

General relativistic theory (GRT) connects gravity with curvature in space-time. Massive objects curve space-time and all free-falling particles, including light, move along those space-time gradients. An emerging consequence is that clocks will therefore not only disagree on the time between two events due to their different velocities but also due to different gravity potentials. Therefore, because of gravity, clocks at larger gravitational potential W tick at lower rates compared to the same clock in a smaller gravitational potential

$$\frac{\mathrm{d}\tau}{\mathrm{d}t} = 1 - \frac{1}{c^2}W(t)\,, \tag{1.3}$$

which can be restated to a frequency shift of a clock at position P and frequency ν_P in relation to a point with gravity potential W_0 and proper frequency ν_0

$$\frac{\Delta\nu}{\nu_P} = \frac{\nu_P - \nu_0}{\nu_P} = \frac{W_P - W_0}{c^2} \approx \frac{-gH}{c^2}\,, \tag{1.4}$$

where H is the vertical distance between two equipotential surfaces of W_P and W_0, and g is the gravitational acceleration. This effect is called gravitational red-shift (Einstein, 1911; Pound and Rebka Jr, 1959; Mehlstäubler et al., 2018). If the accuracy of two clocks is better than the magnitude of gravitational red-shift, they can be used to quantify their height-difference in a gravity field. One application of high-accuracy clocks is therefore probing of the gravitational potential and the measurement of height differences of clocks in it (Delva and Lodewyck, 2013; Mai, 2013; Lisdat et al., 2016; Mehlstäubler et al., 2018).

1.2 Components of a clock

The history of time-keeping is thousands of years old and so the devices and techniques improved the accuracy over this time by more than 16 orders of magnitude. The building blocks of a clock are universal for most clocks, e.g. pendulum and water clocks do not have a reference, but the particular components can span a variety of devices and physical effects which have to work together in a meaningful way.

Atomic frequency standards consist of a local oscillator (LO), a reference and a frequency counter. Atomic clocks additionally incorporate a human readable display of the time, which is generated by counting all oscillations of the frequency standard's LO starting from a defined time-point (Riehle, 2004). The frequency of the LO, locked to its reference, must be calibrated against the

SI definition of the second[1]. The additional steps which are needed to build a *clock* out of *frequency standard* are of technical nature and thus these terms are often used interchangeably, also in this thesis.

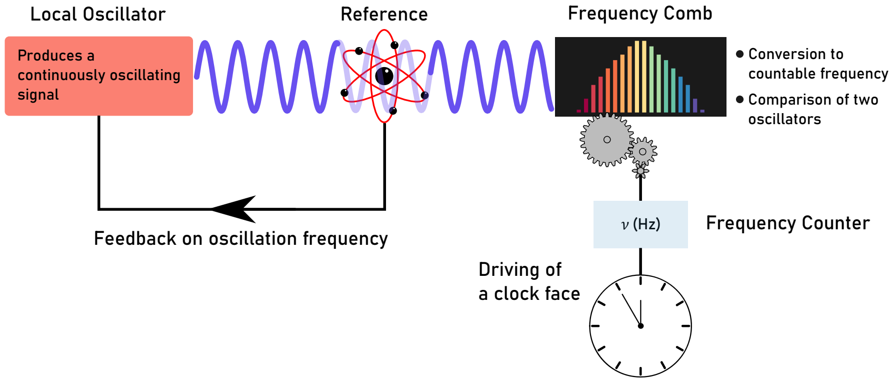

Figure 1.1: Schematic of an optical atomic clock apparatus. A LO sends out laser light which interrogates the reference atom by exciting it near its resonance. Feedback is given onto the laser when the laser frequency drifts away from atomic resonance to stabilize the laser to the atomic resonance. A frequency comb is used to divide the optical laser frequency to electronically processable frequency ranges, which can then be counted and measure a time interval. Two lasers can be compared via the same optical frequency comb, such that clock comparisons over a wide range of atomic species and frequencies is possible.

In Fig. 1.1 a schematic drawing of an optical atomic clock is shown. There, a laser acts as LO which sends out electromagnetic waves at a certain frequency. Usually, the laser's frequency is pre-stabilized to a reference cavity (Riehle, 2004; Amairi, 2014; Matei et al., 2017) in order to mitigate the frequency fluctuations of the free-running laser.

Frequency standards must be universal, i.e., running under all environmental conditions at the same frequency in all places in the universe. But LOs, even those of the same kind, run at different frequencies and will drift in frequency. Even locking them on cavities will imprint the drift of the reference cavity on the oscillator. Therefore, an absolute reference is needed. Since this is naturally fulfilled by atoms of the same atomic species, they are ideal reference systems. The interaction between the laser radiation and the atom changes the energetic state of the atom, when the laser's frequency and the atom's internal frequency are matched to some degree. This can be measured by detecting the atom's state and a feedback signal can be derived, which is used to steer the laser back to the atomic resonance.

Since the oscillations of laser light are too fast to be directly measured by electronic devices, an apparatus that converts them to countable frequencies is needed. Such a tool is the optical frequency comb (Hänsch, 2006; Hall, 2006). The signal derived from laser and frequency comb is down-converted from the laser frequency to electronically processable frequencies in the radio frequency (RF) domain and counted by electronic frequency counters. Frequency comb and frequency counter are introduced in the following section.

---

[1] Strictly speaking, only if the LO's frequency is at some point in the chain compared to the frequency of a primary standard, i.e., controlled by a realization of the SI second, it is called a frequency standard.

1.3 Measuring Optical Frequencies

As mentioned above, it is not possible to count optical frequencies directly, because electronic devices are not fast enough. Though indirect measurements are possible. Overlapping two laser beams with equal polarization and geometric beam parameters will create a beat note between the two electromagnetic fields. Impinging this superimposed beam onto a photo-diode detector reveals the difference frequency ν_{beat} between them

$$\nu_{\mathrm{beat}} = \left|\nu_{\mathrm{laser}} - \nu_{\mathrm{ref}}\right| \ . \tag{1.5}$$

The frequency of the oscillator under test (ν_{laser}) can be measured precisely if the other oscillator's frequency (ν_{ref}) is well-known. The main issue here is that the reference frequency must be near the frequency under test, such that ν_{beat} lies within the bandwidth of the detection photo-diode. While a comparison between two optical frequency standards of the same kind, for example two $^{27}\mathrm{Al}^+$ clocks, can be readily performed, the possible high frequency gap between two oscillators of different atomic clock species has to be bridged.

Bridging of large frequency gaps is possible by putting in chains of oscillators and setting up beat notes between subsequent pairs. There, it is utilized that integer harmonics of optical frequencies (Franken et al., 1961; Savage and Miller, 1962; Ashkin, Boyd, and Dziedzic, 1966) can be generated by non-linear processes, such that bridged frequency difference between adjacent oscillators is maximized but still measurable. By using these beat-notes to phase-stabilize each member of the oscillator chain to its predecessor a step-wise reduction (or increase) of frequency from the starting frequency of the oscillator under test and the reference oscillator at the other end of the frequency gap can be accomplished. For example in Ref. (Schnatz et al., 1996) a frequency chain was used to bridge the gap between the $^3\mathrm{P}_1$ - $^1\mathrm{S}_0$ intercombination line of $^{40}\mathrm{Ca}$ (455986.240494 GHz) to a Cs atomic clock (9.2 GHz). However, frequency chains are susceptible to errors and occupy lots of space, often spanning several rooms because of the high number of lasers needed.

With the invention of the frequency comb, which was rewarded with the Noble price in physics to Theodor W. Hänsch and J. Hall in 2005 (Hänsch, 2006; Hall, 2006), counting optical frequencies became feasible. Frequency combs are compact devices and are able to offer output ports, that cover the LO frequencies of many optical clocks simultaneously.

1.3.1 Frequency Combs

Even though optical frequency combs may be complicated devices, the main idea of the working principle is based on fundamental mathematics (Hänsch, 2006; Hall, 2006; Cundiff and Ye, 2003).

Supposing a continuous series of laser pulses. The laser field of a single pulse can be written as oscillating electric field $\tilde{E}(t, \nu_{\mathrm{c}}) = E_0 \cos\left(2\pi\nu_{\mathrm{c}}t\right)$. The laser field at a distance L will be a series of consecutive pulses each separated by a time $T = L/v_{\mathrm{g}}$, with v_g the group velocity of the pulse. The carrier wave travels with the phase velocity and hence accumulates a phase $\Delta\phi$ in each pulse, which is depicted in the top part of Fig. 1.2. If the pulse envelope is repeated periodically $A(t-T) = A(t)$, the resulting electric field amplitude can be written as

$$E(t) = \mathrm{Re}\left(A(t)\tilde{E}(t,\nu_\mathrm{c})\right) = \mathrm{Re}\left(A(t)E_0 e^{-i(2\pi\nu_\mathrm{c}t)}\right) , \tag{1.6}$$

where Re(.) indicates the real part. Because of the periodicity of $A(t)$, it can be expanded into its Fourier components

$$E(t) = \mathrm{Re}\left(E_0 \sum_n A_n e^{-i(n2\pi\nu_\mathrm{rep}t)} e^{-i(2\pi\nu_\mathrm{c}t)}\right) \tag{1.7}$$

$$= \mathrm{Re}\left(E_0 \sum_n A_n e^{-i2\pi(n\nu_\mathrm{rep}+\nu_\mathrm{c})t}\right) \tag{1.8}$$

$$= \mathrm{Re}\left(E_0 \sum_{n'} A_{n'} e^{-i2\pi(n'\nu_\mathrm{rep}+\nu_\mathrm{CEO})t}\right) , \tag{1.9}$$

with coefficients A_n. In the last step the sum was renumbered to get $\nu_\mathrm{CEO} < \nu_\mathrm{rep}$, with ν_CEO the carrier-envelope offset (CEO) frequency. The inequality $\nu_\mathrm{c} \neq k \cdot \nu_\mathrm{rep}$ prevents the output spectrum to be an integer harmonic of the repetition rate. Nevertheless, the Fourier-transform of the pulse sequence reveals a comb-like frequency spectrum centered around ν_c with comb teeth separated by ν_rep. The large bandwidth of the comb is achieved by using short (fs) pulses and broadening the spectrum by self-phase modulation via intensity-dependent index of refraction. The position of the n^th comb tooth can be written in frequency space as

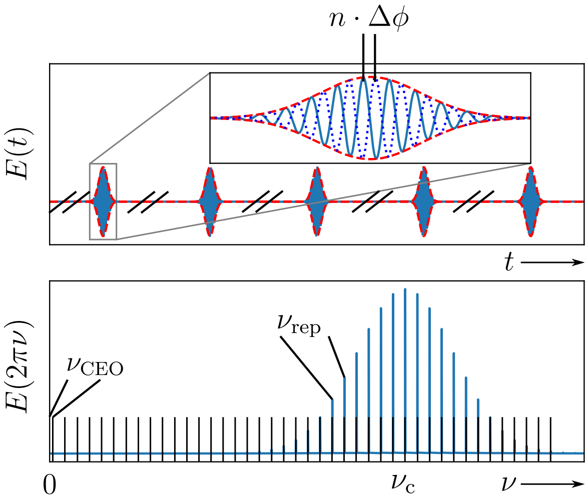

Figure 1.2: Top: A series of short laser pulses (fs) with envelopes $A(t)$. The carrier inside the n^th pulse accumulates a phase shift of $n\Delta\phi$. Bottom: The resulting spectrum in frequency space comprises of distinct comb teeth, which are separated by the repetition rate frequency ν_rep. The spectrum has an offset which is called CEO frequency ν_CEO. (Hänsch, 2006; Hall, 2006; Cundiff and Ye, 2003)

$$\nu_n = \nu_\mathrm{CEO} + n \cdot \nu_\mathrm{rep} , \tag{1.10}$$

with ν_{CEO} the carrier envelope offset frequency and ν_{rep} the repetition rate (few 10 MHz to a few GHz.). This constitutes a mapping of an optical frequency to two RF frequencies. Both frequencies can be made accessible to electronic measurements and to frequency stabilization devices. Moreover, by generating a beat-note between the laser under test and the light from the frequency comb on a photo-diode, the laser's frequency can be measured precisely by

$$\nu_{\mathrm{laser}} = \nu_{\mathrm{CEO}} + n\nu_{\mathrm{rep}} \pm \nu_{\mathrm{beat}} \; . \tag{1.11}$$

The integer number n of the comb tooth nearest to the laser frequency must be known. This can be achieved by measuring the laser frequency coarsely with a wavemeter with sufficient resolution and by observing the sign of the beat-note. Every comb tooth will create a beat-note, but these are either outside the photo-diode's bandwidth or can be electronically filtered out. The comb teeth also create beat-notes among each other at the repetition rate, which can then be used to stabilize the repetition rate frequency to a microwave frequency reference.

In Ch. 4.3 the existing frequency comb in the laboratory will be described.

1.3.2 Frequency Counters

In the last section it was described how optical frequencies can be transformed to an electronically measurable quantity by generating a beat-note between laser and a frequency comb tooth. For the clock it also necessary to count this beat-note frequency with fixed acquisition rate and without gaps between the measurements, which means the counting must be dead-time free.

This can be accomplished by the usage of frequency counters. These count the number of zero-crossings of an input RF-signal (Benkler, Lisdat, and Sterr, 2015)

$$V(t) := V_0 \sin(\Phi(t)) = V_0 \sin(2\pi\nu_0 t + \phi(t)) \; , \tag{1.12}$$

with instantaneous phase $\Phi(t)$, amplitude V_0, frequency ν_0 and residual phase $\phi(t)$ due to noise. ν_0 is the time-independent and true, but unknown frequency of the device under test. The observed instantaneous frequency is given by

$$\nu(t) = \frac{1}{2\pi}\frac{\mathrm{d}\Phi}{\mathrm{d}t} = \nu_0 + \frac{1}{2\pi}\frac{\mathrm{d}\phi}{\mathrm{d}t} \; . \tag{1.13}$$

As will be described in the next chapter, for better comparability between clocks that run at different frequencies, the absolute frequency is converted into fractional frequency data, i.e.,

$$y(t) := \frac{\nu(t)}{\nu_0} - 1 = \frac{1}{2\pi\nu_0}\frac{\mathrm{d}\phi}{\mathrm{d}t} \; . \tag{1.14}$$

The goal of a counter measurement is to find an estimator $\overline{y}$ for the expectation value $\langle y \rangle$ together with a reasonable estimate on its uncertainty $u(\overline{y})$ (Benkler, Lisdat, and Sterr, 2015). The former is calculated by averaging the ensemble of time averaged counter results $\overline{y_i}$. A reasonable estimate of this statistical uncertainty however requires an analysis of the dominating noise type during averaging. The dominant noise type can change over the course of increasing averaging time. For example, white phase noise is more correlated compared to white frequency noise, resulting in faster averaging to smaller uncertainties.

1.4 Accuracy and Stability of Clocks

As indicated above, the acquisition of frequency data includes a statistical distribution around the estimator of the mean frequency. This measured mean frequency could however be shifted by a systematic offset. Therefore, the performance of a clock is quantified by two values: Its accuracy and its stability, which are referring to the *systematic* and the *statistical uncertainty* of the clock (Riehle, 2004). Whereas the latter is evaluated entirely by statistical methods and is therefore a type A uncertainty u_A, the former is a type B uncertainty, u_B, which includes all other information about possible deviations from the unperturbed frequency value (Metrology (JCGM/WG 1), 2008).

1.4.1 Accuracy

Environmental effects, such as the finite temperature of the environment, background gas pressure, electric and magnetic fields, and the atom's residual velocity, influence the clock transition frequency. In consequence, a measured clock transition frequency ν will be shifted from its unperturbed frequency ν_0 by a systematic frequency offset. The accuracy of a clock is then defined as the *systematic uncertainty* u_B with which this frequency offset is known and is typically given in an systematic uncertainty budget, listing the magnitude and sign of the individual frequency shifts and their uncertainties u_{B_i}. Since different atomic species have differently pronounced sensitivities to these contributions, those species with small or easily characterizable shifts are preferred. $^{27}\mathrm{Al}^+$ is for example a clock ion, which has a small sensitivity to external electric field gradients (quadrupole shift) and which has one of the smallest known shifts due to it's environmental temperature, called black body radiation (BBR) shift. The systematic uncertainty budget of this clock is discussed in Ch. 7 .

1.4.2 Stability

The stability of a clock is its *statistical uncertainty*, u_A, when repeatedly measuring the LO's frequency by probing the reference for a finite interaction time T_{int}. The result of such measurements is a series of frequencies ν_i which are scattered around some center frequency ν_0. Because of this scattering, the series of frequency values are averaged over the measurement time τ

$$\overline{\nu}_i = \frac{1}{\tau}\int_{t_i}^{t_i+\tau} \nu(t)\mathrm{d}t \; , \qquad (1.15)$$

to get an estimate of the mean frequency. For convenience the absolute frequency values are transformed to dimensionless fractional frequency data $\overline{y}_i = \overline{\nu}_i/\nu_0$. The frequency fluctuations can be caused by many noise processes whose time-dependence shows different correlations. In consequence, different types of noise will dominate the averaging process over the course of growing averaging times. A tool for quantifying the averaging behavior is the standard Allan deviation (ADEV) $\sigma_y(\tau)$ (Allan, 1966; Barnes et al., 1971; Rutman, 1978)

$$\sigma_y(\tau) = \sqrt{\left\langle \sum_{i=1}^{2} \left(\overline{y}_i - \frac{1}{2} \sum_{j=1}^{2} \overline{y}_j \right)^2 \right\rangle}\,, \tag{1.16}$$

where here $\langle\,.\,\rangle$ denotes the average over all adjacent frequency value pairs.

For atomic clocks one inherent noise contribution comes from the probabilistic measurement process. After the interaction of the LO with one atom, the state of the latter is a superposition of the ground and excited state and is measured by a projective measurement. Its outcome contains exactly one bit of information, say "yes" or "no", and the probability to get one of these values from the superposition state can approach 100 %, yet under no circumstance be precisely 100 %. In consequence, a superposition of states cannot be determined in a single experiment, but must be repeated to give a probability distribution. The statistical spread is called quantum projection noise (QPN) and will be discussed in Ch. 6.3.1. Ultimately, for N uncorrelated atoms the ADEV of QPN is given by (Riehle, 2004)

$$\sigma_y(\tau) = \kappa \frac{\Delta\nu}{\nu_0} \sqrt{\frac{T_{\text{cyc}}}{N T_{\text{int}} \tau}}\,, \tag{1.17}$$

where T_{cyc} is the total clock cycle time, $\Delta\nu$ the probed linewidth of the resonance and $\kappa \sim 1$ is a factor that depends on the used atom-laser interrogation method and the signal-to-noise ratio (SNR). Two typical interrogation methods are Rabi[2] and Ramsey interrogation[3], which are described in Ch. 2.3.1 and 2.3.2. Eq. (1.17) is often referred to as *quantum projection noise* or *standard quantum limit*, since it is based on the interrogation of uncorrelated atoms.

Another noise contribution is connected to the dead-time $T_{\text{cyc}} - T_{\text{int}}$ between clock interrogations, i.e., the periods in which the clock laser is without feedback from the atom. This can be found in the literature as the *Dick-effect* (Dick, 1987; Dick et al., 1990; Santarelli et al., 1998). Dead-times are a necessity in atomic clocks, because after the projective measurement and due to heating processes, or loss of the atom, the atom has to be prepared again for the next interrogation. The stroboscopic clock interrogation leads to a down-sampling of high-frequency laser noise to low-frequency noise, which the feedback onto the clock laser fails to compensate.

---

[2] $\sigma_y(\tau) = \frac{0.264}{\nu_0}\sqrt{\frac{T_{\text{cyc}}}{N T_{\text{int}}^2 \tau}}$ (Oelker et al., 2019).

[3] $\sigma_y(\tau) = \frac{1}{2\pi\nu_0}\sqrt{\frac{T_{\text{cyc}}}{N T_{\text{int}}^2 \tau}}$ (Riehle, 2004).

From these two fundamental noise processes it can be deduced, how to improve the stability of a clock. This includes applying long interrogation times for better frequency averaging, a high atomic clock frequency ν_0, reduction of dead-time, interrogating multiple atoms, and a laser with low frequency noise. The scaling $\propto 1/\sqrt{N}$ in Eq. 1.17 could in principle be improved by using correlated atoms, giving at best a scaling of $\propto 1/N$ (Wineland et al., 1992; Bollinger et al., 1996). However, the actual gain through entangled states depends on many parameters, including the type of entanglement, the atom number, the number of used clock ensembles, probe time and laser coherence time (Wineland et al., 1992; Huelga et al., 1997; Leroux et al., 2017; Schulte et al., 2020; Pedrozo-Peñafiel et al., 2020). The detrimental effect of dead-time can be mitigated by using ensembles of clocks which operate together in forms of compound clocks (Schioppo et al., 2017; Dörscher et al., 2020).

1.5 SI Definition of the Second

The increasing improvement of optical atomic clocks over the last 20 year call for a revision of the SI second by the International Committee for Weights and Measures (CIPM). In November 2019 the CIPM has agreed under the supervision of the 26th General Conference on Weights and Measures (CGPM) on a re-definition of SI units, which marks a milestone, tracing back all SI units to physical constants. However, the definition of the SI second remained the same (BIPM, 2019):

> The second, symbol s, is the SI unit of time. It is defined by taking the fixed numerical value of the cesium frequency, Δ_{Cs}, the unperturbed ground-state hyperfine transition frequency of the cesium 133 atom, to be 9 192 631 770 when expressed in the unit Hz, which is equal to 1/s.

The reason for sticking to the old definition does not lie in a lack of candidates, nor their individual performance. As will be shown in Ch. 1.7, there is a huge zoo of potential candidates. The field of optical clocks is expanding and progressing rapidly in many directions (Riehle, 2015), for example in a growing field of new atomic candidates (Ch. 1.7), or the compactification of physical components of the clock apparatus such as miniaturized laser and vacuum systems (Delehaye and Lacroûte, 2018; Hannig et al., 2019; Schwarz et al., 2019; Stuhler et al., 2021), chip-based traps and integrated optics (Pelucchi et al., 2021; Hoang et al., 2021; Ivory et al., 2021). This would reduce clock setups from experiments, that span several laboratory rooms to compact devices with potentially lower costs. Low costs are not a direct requirement for the new SI second definition, but they will influence the availability of the second-defining standard in the metrology institutes around the globe.

So far, no candidate has proven a unique selling point in the combination of accuracy, stability, reliability and costs. Therefore, committing now onto one candidate would be a mere choice of flavor and disobey the quick dynamics of this field at this time, potentially diminish scientific progress (Riehle, 2015). A first milestone to a new definition of the SI second is the validation of at least three clocks with systematic uncertainties that are two orders of magnitude better than that of the current Cs standard, i.e., they must prove systematic uncertainties in the low 10^{-18} region (CCTF, 2016). Several realizations of neutral atom and ion-based optical clocks, e.g. in Refs. (Huntemann et al., 2016; McGrew et al., 2018; Brewer et al., 2019b), report sufficient low systematic uncertainties. Their validation by frequency comparisons to the 10^{-18} level is the next step. Current best comparisons reach uncertainties in the low 10^{-17} up to high 10^{-18} range (Doerscher et al., 2021; Beloy et al., 2021). Subsequent milestones are the realization and validation of at least three optical clocks of the same species in different institutes, the measurement of their absolute frequencies with accuracies limited by Cs in order to guarantee continuity, a regular contribution to Temps Atomique International (TAI) and the frequency comparison between at least five other optical frequency standards in order to allow closures and links between different optical standards (CCTF, 2016).

Following the proposed road-map of the CIPM (Riehle, 2015; CCTF, 2016; Riehle et al., 2018; Lodewyck, 2019), there will be a re-definition; and the $^{27}\mathrm{Al}^{+}$ as clock ion is a promising candidate.

1.6 Applications for Highly Accuracy and Stable Clocks

Apart from the perspective of playing part in a future realization of the SI definition of the second, there are more reasons for the scientific research on ultra accurate clocks. Clock comparisons are excellent tools for shining a light on unsolved questions in fundamental physics as for example in the field of the Standard Model of particle physics, the search for dark matter, and testing of Einstein's theories of special and general relativity. They Fig. 1.3 gives an overview of applications in which atomic clocks can contribute.

Comparing two clocks based on the same species in a frequency ratio measurement enables the measurement of systematic shifts as for example performed in Ref. (Chou et al., 2010), where a clock frequency shift caused by the clock laser was measured by increasing the clock laser intensity in one of the clocks. Therefore, these measurements are an important tool for the validation of clocks and are part of the requirement for a redefinition of the SI second.

Furthermore, accuracies and stabilities in clock comparisons are already nowadays exceeding those of the SI second (Network et al., 2021). Reaching inaccuracies in the 10^{-18} regime, they can be used as probes for measuring the gravitational potential, revealing height differences on the cm scale (Chou et al., 2010; McGrew et al., 2018; Mehlstäubler et al., 2018; Beloy et al., 2021).

While for the latter application in principle one species would be sufficient, comparison between clocks of different species provide another application. This is for example to test, if fundamental constants were not constant in time or space. These effects become visible by small changes in the transition frequencies, which depend on the atomic properties and which are unique for every atomic system. For example, whereas the $^{27}\mathrm{Al}^{+}$ clock transition

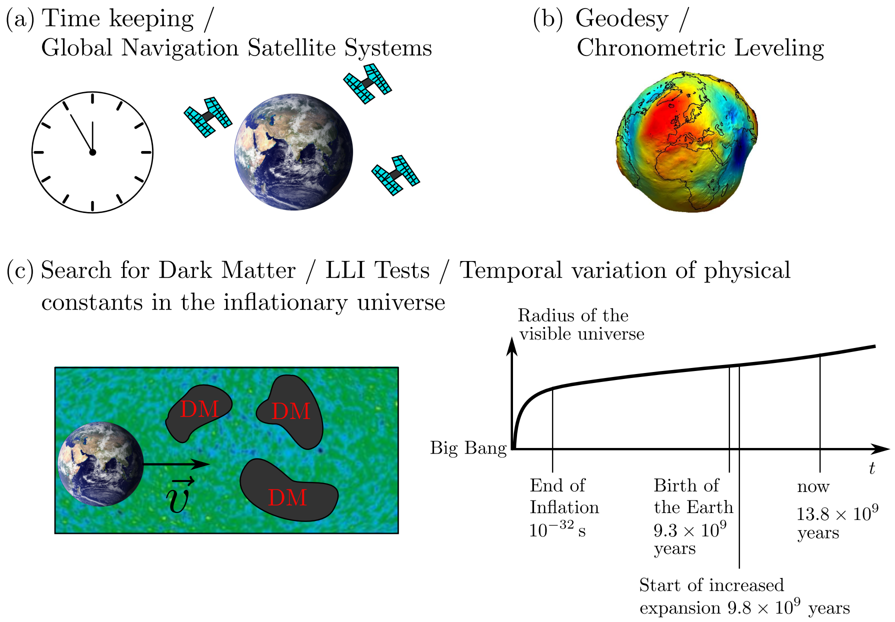

Figure 1.3: Research areas where highly accurate and stable clocks can contribute. (a) Traditional time-keeping by contributing to the Atomic Time Scale UTC (Bauch et al., 2012). Clocks are a necessity for the Global Navigation Satellite Systems (GNSS), which provide information about the location on earth (Batori et al., 2020). (b) The gravitational red-shift allows for measurements of cm-scale height differences in the gravitational potential by clock comparisons (Mehlstäubler et al., 2018). (c) As the earth travels through the universe, some theories beyond the Standard Model of particle physics suggest, that it may pass regions of dark matter (DM) which may shift the clock transition (Arvanitaki, Huang, and Van Tilburg, 2015; Wcisło et al., 2018; Beloy et al., 2021). Other candidates for DM, so-called ultra light DM, are assumed to have a homogeneous distribution in the universe and lead to oscillations of the clock frequency at their mass-dependent Compton frequency. It is also known that the earth is traveling with a few hundred km/s with respect to the isotropic microwave background (colored background), which defines a specific reference frame. Clock comparisons can shed light on the question if physical constants stay the same in every reference frame, which is a feature called Local Lorentz Invariance (LLI) (Sanner et al., 2019; Lange et al., 2021). In the Inflationary universe theory, temporal variations of physical constants, including the fine-structure constant α and the electron to proton mass ratio μ, enter naturally (Calmet and Keller, 2015). The $^{27}\mathrm{Al}^{+}$ clock transition is slightly sensitive to changes of α but not sensitive to changes of μ. By frequency comparisons of ultra-accurate clocks with different sensitivities, those variations could be measured (Karshenboim, 2006; Rosenband et al., 2008; Godun et al., 2014; Stadnik, 2017; Calmet and Keller, 2015). All mentioned effects could manifest in clock frequency changes in dependence of time and/or space. These modulations of the clock frequency, which is given by the difference between the ground and excited state energy, divided by the Planck constant h, must be distinguished from the influences of environmental fields such as electric and magnetic fields E and B, temperature T, acceleration a, velocity v and gravitational potential W.

frequency is relatively insensitive to relative changes in the fine-structure constant α, given by

$$\frac{\Delta\nu}{\nu} = K\frac{\Delta\alpha}{\alpha} \, , \tag{1.18}$$

with a sensitivity coefficient $K_{\mathrm{Al}^+} = 0.008$, and thus could serve as an anchor point in comparisons, other standards are more sensitive, as for example the octupole transition in $^{171}\mathrm{Yb}^+$ $K_{\mathrm{Yb}^+} = -5.95$ (Flambaum and Dzuba, 2009; Ludlow et al., 2015). The reason why we suspect that α could change over time, is that some theories predict it must have changed very rapidly during the inflationary time of the universe, i.e., the short period of exponential expansion after the Big Bang (Karshenboim, 2006; Calmet and Keller, 2015). With the much slower expansion of universe now, the temporal variation of α must be very small though. A recently evaluated comparison of the electric quadrupole (E2) and octupole (E3) clock transitions in $^{171}\mathrm{Yb}^+$ constrains a temporal variation of α to $\frac{1}{\alpha}\frac{\mathrm{d}\alpha}{\mathrm{d}t} = 1.0(1.1) \times 10^{-18}/\mathrm{yr}$ (Lange, 2021). Also, in theories beyond the Standard Model of particle physics dark matter candidates can be introduced which couple to the electromagnetic tensor, and thus potentially influence fundamental constants as for example α, clock frequency ratio measurements can put constraints on coupling constants and masses of these particles (Safronova et al., 2018; Beloy et al., 2021).

The iQLOC 1 aluminum clock will therefore be a valuable contributor in these comparisons, taking advantage of the excellent infrastructure of available high accuracy clocks at Physikalisch-Technische Bundesanstalt (PTB) and at other European metrology institutes via the *European optical fibre link network* (Schioppo et al., 2022).

1.7 The Growing Field of Optical Clocks

There is a large variety of existing optical atomic clocks, the remainder of this chapter briefly reports about these, before advancing in the next chapter to the theoretical treatment of the $^{27}\mathrm{Al}^+$-$^{40}\mathrm{Ca}^+$ clock. This overview is by no means complete, further information can be found e.g. in Ref. (Ludlow et al., 2015).

Single Ion Clocks Single ion clocks, based for example on the $^2\mathrm{S}_{1/2}$-$^2\mathrm{F}_{7/2}$ electric octupole transition (E3) in $^{171}\mathrm{Yb}^+$ (Huntemann et al., 2012b; Godun et al., 2014; Huntemann et al., 2016; Doerscher et al., 2021) or the hyperfine-induced $^1\mathrm{S}_0$-$^3\mathrm{P}_0$ transition in $^{27}\mathrm{Al}^+$ (Cui et al., 2022) clocks offer superior experimental control over the trapped ion, leading to exceptionally low inaccuracies in the 10^{-18} regime. The current world record for the clock with the lowest evaluated fractional systematic uncertainty is an $^{27}\mathrm{Al}^+$ system with an inaccuracy of 9.4×10^{-19} (Brewer et al., 2019b). In Ch. 7.10 the limiting effects of the $^{27}\mathrm{Al}^+$ clock described in this thesis are discussed. Other single ion clock candidates include $^{115}\mathrm{In}^+$ (Keller et al., 2019; Ohtsubo et al., 2020) and $^{176}\mathrm{Lu}^+$ (Arnold et al., 2018; Arnold et al., 2019), $^{40}\mathrm{Ca}^+$ (Huang et al., 2021), $^{88}\mathrm{Sr}^+$ (Dubé, Bernard, and Gertsvolf, 2017), $^{199}\mathrm{Hg}^+$ (Rosenband et al., 2008), $^{40}\mathrm{Ba}^+$ (Arnold et al., 2020), $^{171}\mathrm{Yb}^+$ (E2 transition) (Doerscher et al., 2021; Lange, 2021; Chepurov et al., 2021). The feasibility of a $^{223}\mathrm{Ra}^+$ single ion optical clock is studied in Ref. (Versolato et al., 2011) recent progress is described in Ref. (Holliman et al., 2022). Due to the fact that only a single ion is interrogated, QPN limits the short term stability such that longer averaging times are required compared to multi-ion or lattice clocks. For example, in Ref. (Beloy et al., 2021) frequency ratio measurements between a single ion $^{27}\mathrm{Al}^+$

clock and two neutral atomic lattice clocks, based on ^{171}Yb and ^{87}Sr, reached a stability of $3.1(2) \times 10^{-16}$ for the Yb/Sr, and a stability of $1.3(1) \times 10^{-15}$ for the Al^{+}/Yb and Al^{+}/Sr ratio.

Neutral Atomic Clocks Hundreds to tens of thousands of neutral atoms, as for example ^{87}Sr (Lodewyck et al., 2016; Koller et al., 2017; Bothwell et al., 2019; Ohmae et al., 2021), ^{199}Hg (Yamanaka et al., 2015), ^{171}Yb (Nemitz et al., 2016; McGrew et al., 2018; Kobayashi et al., 2018) , ^{174}Yb (Barber et al., 2008) are pre-cooled in so called magneto-optic traps (MOT) and then kept in optical lattices formed by strong counter propagating laser beams (Oates and Ludlow, 2015). Profiting from the increased SNR due to the large number of simultaneously interrogated atoms, these clocks reach lower instabilities than single ion clocks. Their systematic uncertainty budgets often contain a substantial contribution from blackbody radiation (BBR) and the field shifts induced by the light shifts of the lattice laser. These field-induced shifts can be mitigated by operating the trapping laser field at the *magic wavelength* (Katori et al., 2003; Takamoto and Katori, 2003). Recently achieved accuracies are competitive to single ion clocks (Doerscher et al., 2021), with a best reported accuracy of 1.4×10^{-18} (McGrew et al., 2018) and instability of $< 1 \times 10^{-20}$ (Bothwell et al., 2022) at an averaging time of 1×10^{5} s. Neutral atomic lattice clocks proved transportability (Poli et al., 2014) and the requirement for steady reloading after the destructive detection has been relaxed, enabling a few interrogations per cycle.

Highly Charged Ions In addition to the aforementioned clock candidates a literally new dimension in the periodic table of elements has been made accessible by the progress in experimental control and mathematical calculations of atomic structures of highly charged ions (HCI) as for example Ba^{4+} with its clock state having a lifetime of several seconds (Beloy, Dzuba, and Brewer, 2020). HCIs are especially interesting for tests of fundamental physics, because the outer electrons are tightly bound to the core and therefore sensitive to effects related to the nucleus, special relativity and quantum electrodynamics. Because of the tightly bound electrons, HCI experiments are also insensitive to external fields making them interesting atomic clock candidates. Recent progress includes coherent laser spectroscopy (Micke et al., 2020) and algorithmic ground state cooling (GSC) (King et al., 2021) on $^{40}\mathrm{Ar}^{13+}$.

Nuclear Clocks Especially interesting for an application as optical clock (Peik and Tamm, 2003) and the search for changes in the fundamental constants (Peik et al., 2021) are nuclear clocks. Among them, the laser-accessible transition between two isomeric states of the nucleus of ^{229}Th is one of the most promising, with an expected systematic uncertainty of 1.5×10^{-19} (Campbell et al., 2012; Seiferle et al., 2019). The nuclear transition is largely immune to external fields due to the small size of the nucleus and being shielded by the outer electrons. In contrast to electronic transitions, nuclear transitions are dependent on the strong force and are therefore excellent tools for the search for new physics. An interesting implication of nuclear clocks is the possibility to dope the atoms into a host crystal, enabling a solid-state optical clock (Rellergert et al., 2010) and thus increasing the number of simultaneously interrogated nuclei dramatically. It is known that the transition energy of ^{229}Th is about 8 eV with an expected linewidth in the mHz range. The optical clock community is waiting with excitement for the precise value of the transition frequency to be found (Porsev et al., 2010).

Multi-Ion Clocks The simultaneous interrogation of multiple ions kept in the same trap increases the SNR and thus reduces the averaging time needed to reach at certain accuracies (Mehlstäubler et al., 2018). Ions with total angular momentum $J \leq 1/2$ are favorable, for example ^{27}Al^{+} or ^{115}In^{+}, since ions with non-vanishing quadrupole moment suffer from inhomogeneous frequency shifts on the order of $\approx$10 Hz. Those shifts arise from the electric-field gradient experienced by one ion caused by neighboring ions (Herschbach et al., 2012; Keller et al., 2019). Multi-ion clocks offer also the perspective of beating the standard quantum limit by the generation of spin-squeezed states (Wineland et al., 1992; Ludlow et al., 2015; Leroux et al., 2017; Schulte et al., 2020; Pedrozo-Peñafiel et al., 2020).

Designed Clocks There is also an approach that is aiming at creating noise-free quantum subspaces which would make ion clocks as for example ^{40}Ca^{+} competitive. External fields are applied to create robust dressed states, which are insensitive to magnetic field fluctuations and canceling the quadrupole shift of a multi-ion crystal (Roos et al., 2006; Shaniv, Akerman, and Ozeri, 2016; Aharon et al., 2019; Pelzer et al., 2021).

Compound Clocks Most optical atomic clocks are limited in their probe time and thus statistical uncertainty of the reference oscillator, as the usable probe time. Whereas for shorter probe times the phase error decreases, the statistical uncertainty grows. Several concepts of compound clocks exist, for example interleaved, and hence dead-time-free (Biedermann et al., 2013; Schioppo et al., 2017; Oelker et al., 2019) or synchronous interrogation (Takamoto, Takano, and Katori, 2011; Hume and Leibrandt, 2016) of two clocks; or two atomic references which are interrogated nearly synchronously by a shared clock laser (Dörscher et al., 2020). In Ref. (Clements et al., 2020) a lifetime-limited interrogation of two independent ^{27}Al^{+} clocks was demonstrated.

Active Optical Clocks It is also envisioned to build active optical clocks, e.g. the optical counterparts to the active hydrogen maser (Goldenberg, Kleppner, and Ramsey, 1960). Using the laser radiation of such active optical clocks as clock light would improve the stability of lattice clocks by one to two orders of magnitude, since the laser linewidths used for interrogation are nowadays limited to $\sim$10 mHz by thermal noise on the dielectric coatings of the cavity mirrors (Ludlow et al., 2007; Matei et al., 2017). Using the narrow clock transitions of optical standards opens the possibility of lasers with linewidths $\ll$1 mHz (Meiser et al., 2009). However, the long lifetime of the clock transition and comparable low number of radiating atoms and therefore low emission rates require the lasing mechanism to be more involved. Such superradiant sources incorporate collective couplings of the atoms with the electromagnetic field modes of a cavity in order to produce coherent light with sufficient output power. So far only pulsed superradiance light has been observed (Norcia et al., 2016; Laske, Winter, and Hemmerich, 2019; Schäffer et al., 2020), but research is on-going to build a continuous superradiant light source.

2 The Atomic Reference

The heart of any atomic clock is the atom itself. A single free-falling atom in empty space, isolated from the rest of the universe, even from the oscillator, which is then magically ticking at the atom's internal frequency, would be the perfect reference for a clock. But it is clear, that in any conceivable experiment on a fixed space on earth, the environment interacts with the ion in order to keep it in place and the oscillator has to interact with the ion in order to infer information about its internal energy state.

In this chapter the experimental apparatus approximating this situation is studied. It starts with introducing the used clock and logic ion and continues with a theoretical description of the trap, that enables to keep the ion at the same spot in space for long times, while still enabling optical access for the lasers. The remainder of this chapter then attends to the interaction between laser radiation and ion.

2.1 Clock and Logic Ion

The iQLOC 1 experiment is based on a $^{27}\mathrm{Al}^{+}$-$^{40}\mathrm{Ca}^{+}$ crystal held by a linear Paul trap inside an ultra-high vacuum chamber.

2.1.1 Clock Ion – $^{27}\mathrm{Al}^{+}$

As pointed out in the introduction, aluminum is a suitable clock ion because it exhibits a transition which has a couple of remarkable properties. The transition energy between ground and excited clock state corresponds to short wavelength photons. Additionally, the long natural lifetime of the excited states corresponds to a narrow linewidth for the emitted and absorbed photons. $^{27}\mathrm{Al}$ has the atomic number 13, a weight of $m = 26.98154\,\mathrm{u}$ (atomic mass unit) and is the only stable isotope of Al. It belongs to the Mg isoelectronic sequence.

The transition wavelengths and lifetimes in $^{27}\mathrm{Al}^{+}$ can be found in Fig. 2.1 and Tab. 2.1. Besides the clock transition described in the next section, the $\left|{}^{1}\mathrm{S}_{0}\,, m_F = +5/2\right\rangle \leftrightarrow \left|{}^{3}\mathrm{P}_{1}\,, m_F = +7/2\right\rangle$ ($^{27}\mathrm{Al}^{+}$-logic) transition at 267 nm is used for state preparation and quantum logic (QL), which will be described in Ch. 6.1. In Ref. (Guggemos et al., 2019) the frequency of this transition and the Landé g-factor of the $^{2}\mathrm{P}_{1}$ state have been determined to 1 122 842 857 334 736(85) Hz and $g_{^{3}\mathrm{P}_{1},F=7/2} = 0.428\,133(2)$.

2.1.1.1 The Clock Transition

An atom or ion that is continuously radiating light at the clock frequency would be optimal. Due to the challenges in building an active optical clock (Ch. 1.7)

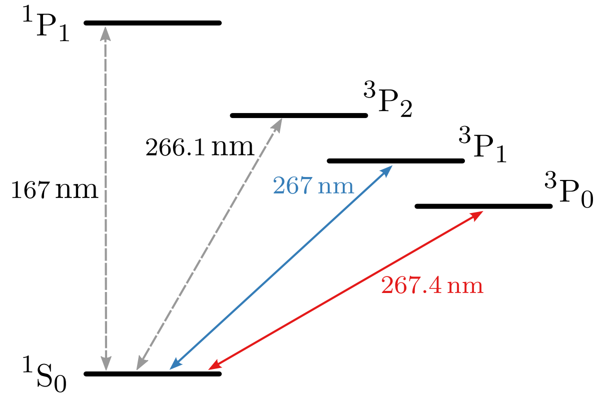

Figure 2.1: Level scheme (not to scale) of ^{27}Al$^+$. Red: clock transition between $(3s^2)$ ^{1}S$_0$ ↔ $(3s3p)$ ^{3}P$_0$, blue: logic transition. Wavelengths and lifetimes of the excited states are shown in Tab. 2.1.

Table 2.1: ^{27}Al$^+$ transition wavelengths and lifetimes. References: If not otherwise marked by symbol the data is from Ref. (Martin and Zalubas, 1979), *(Rosenband et al., 2007), †(Kumar et al., 2021), §(Guggemos et al., 2019), $^\diamond$(Träbert et al., 1999), ‡(Brage et al., 1998).

Transition	λ (nm)	τ (s)	Type
$(3s^2)$ ^{1}S$_0$ – $(3s3p)$ ^{3}P$_0$	267.4	$20.6^{*,\dagger}$	HFI
$(3s^2)$ ^{1}S$_0$ – $(3s3p)$ ^{3}P$_1$	$267^\S$	$305 \times 10^{-6\diamond}$	Intercombination
$(3s^2)$ ^{1}S$_0$ – $(3s3p)$ ^{3}P$_2$	266.1	$284^\ddagger$	M2
$(3s^2)$ ^{1}S$_0$ – $(3s3p)$ ^{1}P$_1$	167.1	7×10^{-10}	E1

most of the research is focused on passive optical clocks. If one would reduce the concept of a passive optical clock to a single core idea, then one would arrive at the clock transition, which is in an aluminum ion clock the change of the Alion's internal energy state between the ground state ^{1}S$_0$ and the excited state ^{3}P$_0$.

A single photon transition with no change in the total angular momentum quantum number J of the electronic configuration is forbidden by selection rules in any electric or magnetic multipole order. However, ^{27}Al$^+$ has non-zero nuclear spin ($I = 5/2$) and thus the interaction between the core and the electronic system results in energy shifts and energy splittings known as hyperfine splitting. As another consequence of the hyperfine interaction, the total electronic angular momentum J in combination with all electronic numbers is not longer sufficient to completely specify a state. The eigenstates of the combined Hamiltonian of electronic system and hyperfine interaction are described by the "good" quantum number $F = I + J$ and M_F and read like $|\Gamma F M_F\rangle$, where I is the nuclear spin, F the total angular momentum quantum number and Γ is denoting all other quantum numbers here. The net result is that the "new" states can be written as mixtures of states with different J, giving rise to for example ^{1}S$_0$ ↔ ^{3}P$_0$ transitions (Brage et al., 1998).

In consequence, a single photon can introduce transitions between the ground and clock states of $^{27}\mathrm{Al}^{+}$. This enables direct laser excitation of the clock transition, which has a narrow natural linewidth of $\approx 8\,\mathrm{mHz}$ (Rosenband et al., 2007) and the latest absolute frequency measurement yields a value of 1 121 015 393 207 859.50(36) Hz (Leopardi et al., 2021). The Landé g-factors are $g_{^1\mathrm{S}_0,F=5/2} = -0.000\,792\,48(14)$ and $g_{^3\mathrm{P}_0,F=5/2} = -0.001\,976\,86(21)$ (Rosenband et al., 2007). Because $J = 0$ for both states, which implies spherical symmetry, the clock transition's quadrupole shift is negligible and remaining hyperfine Zeeman shifts are 11.1 kHz/mT and 27.7 kHz/mT for the ground and the excited clock state, respectively. Due to its tiny differential polarizability, the BBR in $^{27}\mathrm{Al}^{+}$ is one of the smallest known, which is a large contribution in many optical clock systematic uncertainty budgets (Safronova, Kozlov, and Clark, 2011). This and other systematic frequency shifts will be discussed in Ch. 7.

2.1.1.2 Cooling of $^{27}\mathrm{Al}^{+}$

The ability to cool the clock ion near the motional ground state and excited state detection is essential for clock operation. The E1 transition at 167 nm could in principle be used for laser cooling but up to now it is hard to find reliable lasers operating at such short wavelengths, even though there are efforts for building lasers in the deep ultra violet (Scholz et al., 2012; Li et al., 2018). Aside from the experimental issues such laser would introduce to the laboratory, the minimum Doppler temperature using this transition would be too high for subsequent ground-state cooling techniques, due to the large natural linewidth of 230 MHz of this transition.

2.1.2 Logic Ion – $^{40}\mathrm{Ca}^{+}$

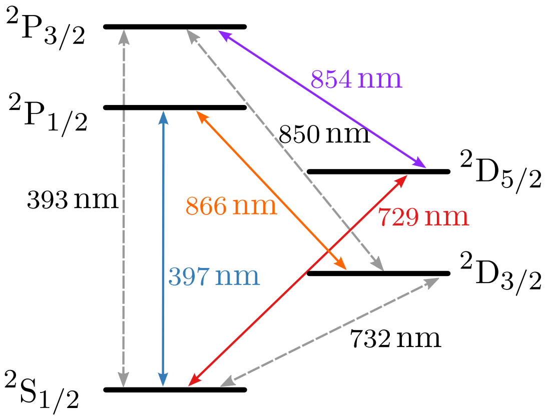

Figure 2.2: Level scheme (not to scale) of $^{40}\mathrm{Ca}^{+}$. Available lasers in this experiment are colored.

In order to overcome the lack of a suitable cooling and detection transition, $^{27}\mathrm{Al}^{+}$ is trapped together with a single $^{40}\mathrm{Ca}^{+}$ ion. Due to their coupled motion, it is possible to laser cool $^{40}\mathrm{Ca}^{+}$ and sympathetically cool the $^{27}\mathrm{Al}^{+}$ ion and to infer information from the latter's internal state conducting quantum logic spectroscopy (QLS). ^{40}Ca^{+} was chosen over ^{9}Be^{+}, which was the first quantum logic optical clock (Schmidt et al., 2005; Rosenband et al., 2007) or ^{25}Mg^{+}, which has an almost perfect mass ratio (Brewer et al., 2019b), because lower Doppler temperatures and thus smaller systematic shifts and uncertainties are possible (Wübbena et al., 2012).

Table 2.2: ^{40}Ca^{+} transition wavelengths and their respective lifetimes (reciprocal Einstein *A* coefficients, see Ref. (James, 1998)) (James, 1998). The measured transition frequencies are from Refs. $^{\diamond}$(Shi et al., 2017), *(Wan et al., 2014), †(Chwalla et al., 2009), §(Gebert et al., 2015) and the measured lifetimes of the D-levels are from ‡(Kreuter et al., 2005).

Transition	λ (nm)	τ (s)	measured ν
$^2S_{1/2} - {}^2P_{3/2}$	393.4	7.4×10^{-9}	761 905 012.599(82) MHz$^{\diamond}$
$^2S_{1/2} - {}^2P_{1/2}$	396.8	7.7×10^{-9}	755 222 765.896(88) MHz*
$^2S_{1/2} - {}^2D_{5/2}$	729.1	1.168(9)‡	411 042 129 776 393.2(1.0) Hz†
$^2S_{1/2} - {}^2D_{3/2}$	732.4	1.176(11)‡	
$^2D_{3/2} - {}^2P_{3/2}$	849.8	9.01×10^{-7}	
$^2D_{5/2} - {}^2P_{3/2}$	854.2	1.01×10^{-7}	
$^2D_{3/2} - {}^2P_{1/2}$	866.2	9.43×10^{-8}	346 000 234.867(96) MHz§

Also, ^{40}Ca^{+} is a well-understood atomic system, the level energies are shown in Fig. 2.2 and Tab. 2.2. Its atomic mass is $m = 40\,\mathrm{u}$ and the net nuclear spin is $I = 0$, therefore ^{40}Ca^{+} has no hyperfine splitting. The Landé g-factors for the ground and excited logic state are $g_{^2S_{1/2}} = 2.002\,256\,64(9)$ (Tommaseo et al., 2003) and $g_{^2D_{5/2}} = 1.200\,334\,0(3)$ (Chwalla et al., 2009), respectively. All needed lasers are commercially available as diode lasers. A frequency-doubled 794 nm diode laser enables Doppler cooling at 397 nm, ground-state cooling by means of electronically-induced transparency (EIT) cooling, and state detection for the ^{40}Ca^{+} ion on the $^2S_{1/2} \leftrightarrow {}^2P_{1/2}$ electric dipole transition with a natural linewidth of $\approx 20.7\,\mathrm{MHz}$. A laser at 866 nm clears out the $^2D_{3/2}$ state, which is populated during Doppler cooling and detection. The 854 nm connects the $^2D_{5/2}$ and $^2P_{3/2}$ states and thus clears out state population from ^{40}Ca^{+}'s qubit $^2D_{5/2}$ state. From the short lived $^2P_{3/2}$ state the ion decays to its ground state $^2S_{1/2}$ and to $^2D_{3/2}$ and $^2D_{5/2}$. A laser at 729 nm drives carrier and sideband transitions between the ^{40}Ca^{+} qubit electric quadrupole transition $^2S_{1/2} \leftrightarrow {}^2D_{5/2}$, which has a natural linewidth of $\approx 150\,\mathrm{mHz}$ (James, 1998).

2.2 Linear Paul Trap

Ions are susceptible to electromagnetic fields and thus can be trapped by arrangements of static magnetic and electric fields, called Penning traps (Dehmelt, 1968), and by combinations of static and dynamic electric fields, called Paul traps (Paul and Steinwedel, 1953). Hans Dehmelt and Wolfgang Paul were both awarded with the Nobel prize in physics in 1989, together with

Norman F. Ramsey, for their pioneering work on these devices (Dehmelt, 1990; Paul, 1990).

In this section, the concepts of linear Paul traps are introduced, following the thoughts in Ref. (Leibfried et al., 2003).

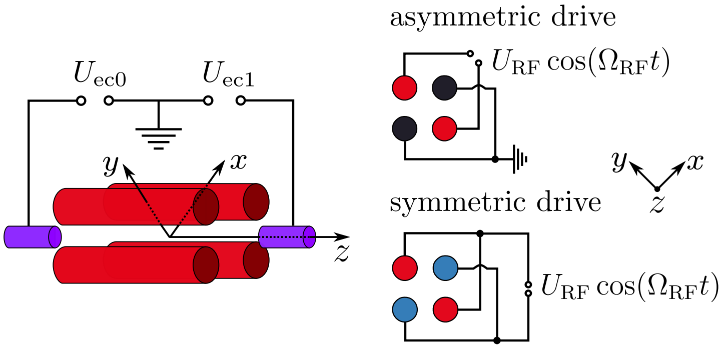

Figure 2.3: Sketch for the electrode configuration of a linear Paul trap. Left: A static voltage U_{ec} is applied to the endcaps (violet), for the sake of flexibility they can be applied independently of one other. Red: RF electrodes. Top right: In the asymmetric drive two opposing electrodes are kept at RF ground while the remaining two are at RF voltage with same polarity. Bottom right: In the symmetric drive all RF electrodes are at RF potential with opposing one being at the same phase.

Starting from an electric potential with quadrupolar spatial form and adding up a static and a time-dependent potential, one can write the potential as

$$\Phi = \frac{U}{2}\left(\alpha x^2 + \beta y^2 + \gamma z^2\right) + \frac{\tilde{U}}{2} \cos\left(\Omega_{\mathrm{RF}} t\right) \left(\tilde{\alpha} x^2 + \tilde{\beta} y^2 + \tilde{\gamma} z^2\right) \tag{2.1}$$

Electric potentials without charge densities must fulfill the Laplace equation

$$\Delta\Phi = 0 \tag{2.2}$$

at all times. Equation (2.1) can only hold this condition if

$$\alpha + \beta + \gamma = 0 \tag{2.3}$$

$$\tilde{\alpha} + \tilde{\beta} + \tilde{\gamma} = 0 \tag{2.4}$$

are fulfilled. This implies that there is no purely static quadrupolar potential that is repelling or attracting in all three coordinates at the same time. In fact the *Earnshaw theorem* states that there is no static electric or magnetic potential able to stably trap objects alone. For trapping a charged particle it is therefore necessary to use a combination of static electric and magnetic fields, called Penning traps, or to have a dynamic part, as in Paul traps. The relation between the constants (2.4) are defined by the symmetries and geometries of the specific realization of the electrodes used to create the dynamic and static potentials. A dynamic potential would be sufficient to trap single ions ($\alpha = \beta = \gamma = 0$ and $\tilde{\alpha} + \tilde{\beta} = -\tilde{\gamma}$) in a 3D oscillating trap, while in a linear Paul Trap ($-(\alpha + \beta) = \gamma$ and $\tilde{\alpha} = -\tilde{\beta}$, $\tilde{\gamma} = 0$) a static part is needed, because there the time varying potential is applied only radially.

In this experiment the trap configuration is a linear Paul trap, which comprises four opposing blades driven by a RF circuit, described in Ch. 3.3, with an ion-to-blade distance of $r \approx 800\,\mu\text{m}$ and two opposing endcap electrodes at positive voltages with an ion-to-endcap distance of $2500\,\mu\text{m}$. Assuming that the endcap potential at the trap center is perfectly radially symmetric $\alpha = \beta = -\gamma/2 < 0$, and that the long extension of the RF blades along z together with its symmetry gives no RF field along z, results in the following total potential for an electrode configuration as shown in Fig. 2.3.

$$\phi(x, y, z, t) = \underbrace{\frac{U_{\text{ec}}}{d^2}\left(z^2 - \frac{x^2 + y^2}{2}\right)}_{\text{endcap}} + \underbrace{\frac{U_r}{2r^2}(x^2 - y^2)\cos(\Omega_{\text{RF}} t)}_{\text{blades}} \tag{2.5}$$

with d, r as the effective distances, from trap center to endcap electrode and RF blade, respectively. These can differ substantially from the real distances if the electrodes have no hyperbolic shape. A beneficial property of linear Paul traps is that they allow multiple trapped ions to be placed on a linear ion string on the z-axis at the zero node of the RF electric field, and in 3D structures. The former is in particular useful for multi-ion clocks, because of the good optical accessibility with laser beams up to single addressable ions and low and homogeneous frequency shifts that can arise from imperfections in the quadrupole potential (Pyka et al., 2014).

The motion of quantum particles is ultimately given by quantum mechanics. Nevertheless, a study of the classical equations of motion gives insight into the resulting motional frequencies and stability.

Solving for the classical motion of a single particle of mass m and charge $Z|e| = Q$ underlying a potential of the form (2.1) the motion decouples spatially. The calculations can be performed separately for the coordinates u_j with $j \in \{x, y, z\}$. The standard equation of motion is

$$\ddot{u}_j = -\frac{Q}{m}\frac{\partial \Phi}{\partial u_j}\,, \tag{2.6}$$

which can be rewritten to a Mathieu equation

$$\ddot{u}_j + \frac{\Omega_{\text{RF}}}{4} u_j \left[a_j + 2q_j \cos\left(\Omega t\right)\right] = 0 \tag{2.7}$$

using the substitutions

$$a_x = -\frac{4QU_{\text{ec}}}{md^2\Omega_{\text{RF}}^2}\,, \qquad q_x = \frac{2QU_r}{mr^2\Omega_{\text{RF}}^2} \tag{2.8}$$

$$a_y = -\frac{4QU_{\text{ec}}}{md^2\Omega_{\text{RF}}^2}\,, \qquad q_y = -\frac{2QU_r}{mr^2\Omega_{\text{RF}}^2} \tag{2.9}$$

$$a_z = \frac{8QU_{\text{ec}}}{md^2\Omega_{\text{RF}}^2}\,, \qquad q_z = 0 \tag{2.10}$$

Equation (2.7) is a well-known type of differential equation with periodic coefficients $\propto \exp\left(i\beta_j\right)$, which can be solved in the framework of *Floquet*'s theorem. The β_j are not to be confused with the trap parameter β from above. The parameters are usually $|a_j|$, $q_j^2 \ll 1$ and in the iQLOC 1 trap for typical axial and radial secular frequencies of $\omega_z = 2\pi \times 1.1\,\mathrm{MHz}$ and $\omega_x = 2\pi \times 1.92\,\mathrm{MHz}$ these values are given by $a_x = -0.0031,\ q_x = 0.2095 \ll 1$.

2.2.1 Classical Motion in Linear Paul Traps

To lowest order in a_x and q_x the characteristic factor β_j becomes

$$\beta_j \approx \sqrt{a_j + \frac{q_j^2}{2}} \tag{2.11}$$

and the amplitude of motion along the j-axis is

$$u_j(t) \approx A_j \cos\left(\omega_j t\right) \left[1 + \frac{q_j}{2} \cos\left(\Omega_{\mathrm{RF}} t\right)\right] \tag{2.12}$$

with

$$\omega_j = \frac{\beta_j \Omega_{\mathrm{RF}}}{2} \tag{2.13}$$

as the secular frequency of the motion. The left hand side gives rise to a motion at a fraction of the trap drive frequency which is called secular motion. In addition to that, the ion will undergo intrinsic micromotion at the trap drive frequency Ω_{RF}, which has under typical operating trap conditions only a small amplitude compared to the secular motion, since $q_J \ll 1$. This intrinsic micromotion is an inherent feature of RF driven traps, and cannot be compensated for. Additional terms of micromotion, called excess micromotion (EMM), caused by phase-lag ϕ_{RF} between RF electrodes of same polarity and by a displacement of the ion's center position from the RF null due to an additional dc electric field at the center of the ion trap.

The kinetic energy carried by uncompensated micromotion leads to a 2^{nd} order Doppler shift of the clock transition. Best efforts must be undertaken to compensate the displacement from RF null by pushing the ion back, using dc voltage compensation electrodes and to avoid phase-lag micromotion by careful adjustment of wire lengths to the RF electrodes. The EMM shift in the presented experiment is studied in Ch. 7.2.

2.2.2 Stability

Up to certain values of the a_x and q_x parameters, β_x is purely real and the solutions are bound oscillations. If β_x becomes complex the ion's motion gets unbound and the particle leaves the trap. For fixed a_z the allowed sets (q_x, a_x) and (q_y, a_y) lie in-between an inner line with $\beta_i = 0$ and an outer line with $\beta_i = 1$. In the region where both bands overlap, a stable trap operation is apparent. Fig. 2.4 shows a stability diagram for a linear Paul trap with $a_z = 0.0062$. There are additional instabilities arising from deviations from the quadratic potential, described by higher orders of the trapping potential, which appear at points in the stability diagram, where integer multiples of the

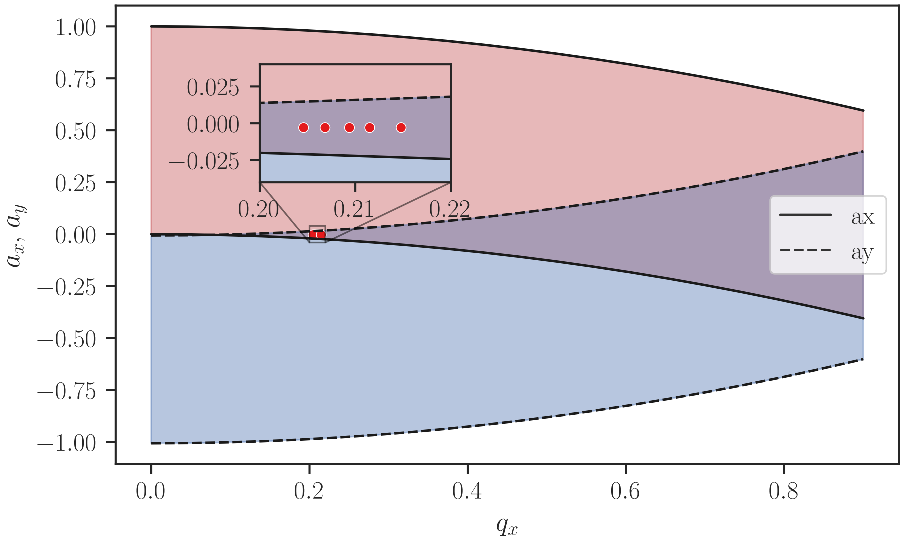

Figure 2.4: Stability diagram for the linear Paul trap configuration with $a_z = 0.0062$. The region where the a_x and a_y-stable regions overlap is stable. The inset shows measured parameters with varying input powers to the helical in the range from 30.3 to 30.7 dBm, which equals $U = 290$ to $304\,\mathrm{V}$ on the RF blades with symmetric drive (Ch. E.4).

secular frequencies, and combinations thereof, are equivalent to the trap drive frequency (Drakoudis, Söllner, and Werth, 2006)

$$n_x\omega_x + n_y\omega_y + k_z\omega_z = \Omega_{\mathrm{RF}}\ , \quad k_z = 0, 1, 2, \dots\ . \tag{2.14}$$

A plot of the instabilities for $N = n_x + n_y = 3 \dots 10$ with $k_z = 0, 1, 2, 3$ is shown in Fig. 2.5. These instabilities are related to higher-order contributions

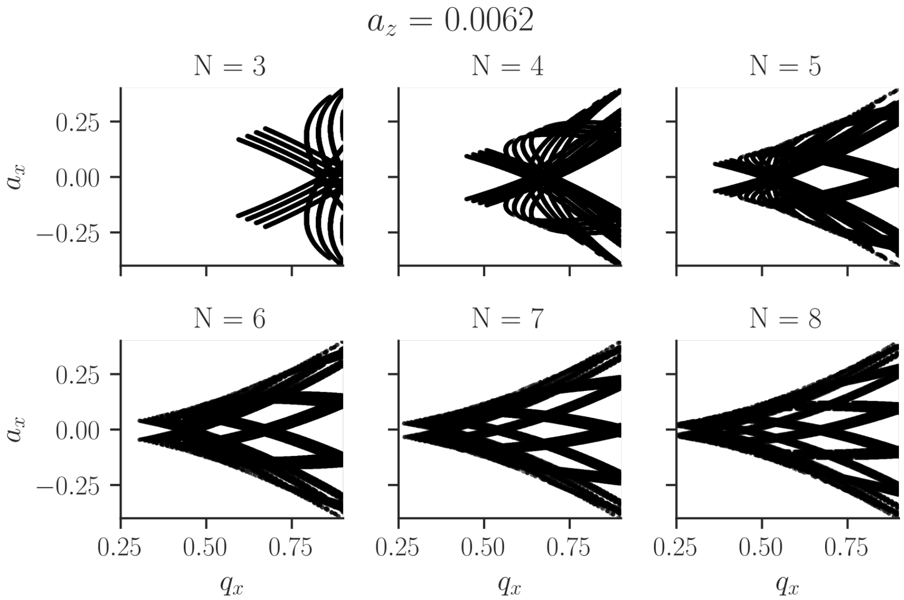

Figure 2.5: Instabilities for a linear Paul trap.

to the quadrupolar trapping field and hence have less impact with increasing

N, due to the high symmetry of the trap. Therefore, these instabilities are not observed under typical experimental conditions.

2.3 Atom Light Interaction

In the described optical atomic clock experiment, both, the clock and the logic ion, are manipulated by laser radiation. The interaction between laser field and atomic system is simplified to a single laser light field at frequency ω_L, driving a single transition between two atomic states, named ground state $|g\rangle$ and excited state $|e\rangle$. The two states form a simple two-level system, sketched in Fig. 2.6. This is given for situations where the internal states are non-degenerate and small-linewidth laser sources are used in order to resonantly couple only the two states. A semi-classical description is used, where the atom and the motion is described by quantum mechanics and the laser field classically by an electric field vector $\vec{E}$.

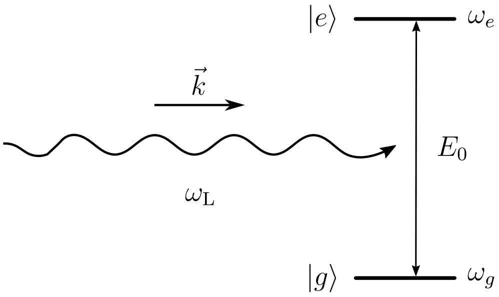

Figure 2.6: The electric field of a laser beam with wavevector $\vec{k}$ and frequency ω_L couples ground and excited state with energies $\hbar\omega_g$ and $\hbar\omega_e$, separated by an energy $\hbar\omega_0$.

Ground and exited state are separated by an energy difference of $E_0 = \hbar(\omega_e - \omega_g) = \hbar\omega_0$, with angular frequencies $\omega = 2\pi\nu$ and reduced Planck constant $\hbar = h/(2\pi)$. The corresponding atomic two-level Hamiltonian can be written in terms of Pauli spin operators $\vec{\sigma}$, utilizing the equivalence to a spin 1/2-system in a static magnetic field and rescaling the energy of the two-level system (Wineland et al., 1998; Leibfried et al., 2003)

$$\hat{H}^{(\mathrm{e})} = \frac{\hbar}{2}\omega_0\hat{\sigma}_z\ , \tag{2.15}$$

with $\hat{\sigma}_z = |e\rangle\langle e| - |g\rangle\langle g|$. A general pure state of the two-level system is a superposition of ground and excited state.

$$\psi^{(\mathrm{e})} = c_g(t)e^{-i\frac{\omega_0 t}{2}}\,|g\rangle + c_e(t)e^{i\frac{\omega_0 t}{2}}\,|e\rangle\ . \tag{2.16}$$

The complex coefficients are normalized to $|c_g(t)|^2 + |c_e(t)|^2 = 1$.

The light-field propagating along the z-direction impinging onto the trapped particle can be represented by a running-wave electric field vector

$$\vec{E}(t) = \frac{\vec{E}_0}{2}\left(e^{i(k_z z - \omega_\mathrm{L} t + \phi)} + e^{-i(k_z z - \omega_\mathrm{L} t + \phi)}\right)\ , \tag{2.17}$$

with wavevector $k_z = k = 2\pi/\lambda_\mathrm{L}$, where λ_L is the laser wavelength. The Hamiltonian for the coupling of this plane wave of laser light to the dipole moment $\vec{\mu}_d$ of the ion's electronic systemlevels is given by

$$\hat{H}^{(\mathrm{i})}(t) = -\vec{\mu}_d \cdot \vec{E}(z,t) \ , \tag{2.18}$$

In general $\hat{H}^{(\mathrm{i})}$ can also describe a coupling to other aspects of the driving electro-magnetic field as for example the coupling between the quadrupole moment and the field gradient of the light field in the quadrupole interaction (Ludlow et al., 2015).

In the following two subsections two general types of laser-atom interrogation are presented. Both are valid tools for the clock interrogation of $^{27}\mathrm{Al}^+$. The Rabi interrogation is additionally a tool for ground state cooling (GSC) and quantum logic (QL) spectroscopy.

2.3.1 Rabi Excitation

The first technique is named Rabi interrogation. In its simplest description, effects emerging from ion's motion, their finite size, and decoherence processes are neglected. Considerations of these properties follow in subsequent chapters.

The spatial extent of the ion's wavefunction at rest is small compared to the wavelength of the electric field and therefore the spatial dependence of the electric field can be dropped in a dipole approximation. The interaction can then be written as $\hat{H}^{(\mathrm{i})} = -\vec{\mu}_d \cdot \vec{E}(t)$. Here, the electric field vector is simply $\vec{E} = \vec{E}_0 \cos(\omega t)$ and $\vec{\mu}_d$ may be associated by the electric dipole operator in this case.

The dynamics of the internal states of the ion can be described by the Schrödinger equation

$$i\hbar\frac{\partial}{\partial t}\psi(t) = \hat{H}\psi(t) = \left(\hat{H}^{(\mathrm{e})} + \hat{H}^{(\mathrm{i})}(t)\right)\psi(t) \ , \tag{2.19}$$

with $\psi(t)$ the time-dependent part of the wavefunction.

When the ion is prepared in a pure state and neglecting decoherences, the state of the ion will stay pure and can be written in the form of Eq. 2.16. After inserting Eq. 2.16 into Eq. 2.19 and taking the scalar product, the equation of motion for the state coefficients is a coupled differential equation system

$$\dot{c}_{g,e}(t) = i\frac{\Omega_0}{2}\left(e^{\pm i(\omega_\mathrm{L}-\omega_0)t} + e^{\mp i(\omega_\mathrm{L}+\omega_0)t}\right)c_{e,g}(t) \ , \tag{2.20}$$

for the coefficients $c_g(t), c_e(t)$. The strength of coupling is determined by the Rabi frequency Ω_0, which is given in the case of dipole interaction, by $\Omega_0 = \Omega_{eg} = \Omega_{ge} = eE_0/\hbar\left\langle e\middle|\hat{\vec{r}}\middle|g\right\rangle$, where $\hat{\vec{r}}$ is the position operator and e the elementary charge. Fast oscillating parts of Eq. (2.20) will average to zero over the course of time between two observations in the experiment. They can therefore be omitted in a so-called *rotating wave approximation*. Introducing the detuning $\delta = \omega_\mathrm{L} - \omega_0$ and using the substitutions

$$\tilde{c}_{g,e}(t) = c_{g,e}(t)e^{\mp i\frac{\delta}{2}t} \ , \tag{2.21}$$

the equation system Eq. (2.20) can be written in the form of

$$\frac{\mathrm{d}}{\mathrm{d}t}\begin{pmatrix}\tilde{c}_g(t)\\ \tilde{c}_e(t)\end{pmatrix} = \frac{i}{2}\begin{pmatrix}-\delta & \Omega_0\\ \Omega_0 & \delta\end{pmatrix}\begin{pmatrix}\tilde{c}_g(t)\\ \tilde{c}_e(t)\end{pmatrix}\,, \tag{2.22}$$

and can be solved to

$$\tilde{c}_{g,e}(t) = i\frac{\Omega_0}{\Omega}\sin\left(\frac{\Omega}{2}t\right)\tilde{c}_{e,g}(0) + \left(\cos\left(\frac{\Omega}{2}t\right) \mp \frac{i\delta}{\Omega}\sin\left(\frac{\Omega}{2}t\right)\right)\tilde{c}_{g,e}(0)\ . \tag{2.23}$$

Here, the generalized Rabi frequency

$$\Omega = \sqrt{\delta^2 + \Omega_0^2} = \sqrt{(\omega_\mathrm{L} - \omega_0)^2 + \Omega_0^2} \tag{2.24}$$

was introduced. When the ion at the start of the laser-ion interaction is prepared in the electronic ground state ($\tilde{c}_g(t=0) = 1$ and $\tilde{c}_e(t=0) = 0$), it will undergo a state population transfer between ground and excited state like

$$|\tilde{c}_e(t)|^2 = \frac{\Omega_0^2}{\Omega^2}\sin^2\left(\frac{\Omega t}{2}\right) = \frac{\Omega_0^2}{2\Omega^2}\left(1 - \cos\left(\Omega t\right)\right)\ . \tag{2.25}$$

For a π-pulse time, defined by the interaction time $t = \tau_i = \pi/\Omega_0$, the population in the excited state is maximized, where full state transfer ($|\tilde{c}_e|^2 = 1$) happens only on resonance $\delta = 0$. Many of the conducted experiments in this document are Rabi frequency scans: Observation of the excitation probability $|\tilde{c}_e(\nu_\mathrm{L})|^2 = p(\nu_\mathrm{L})$ while scanning the detuning of the laser frequency at constant laser power and constant interaction time. The lineshape is depicted in Fig. 2.7. It incorporates sidelobes and a full width at half maximum of FWHM$\approx 0.8/\tau_i$. For increasing detunings the generalized Rabi frequency is growing but the maximum state population of the excited state decreases.

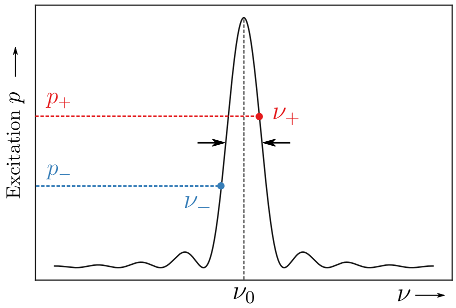

Figure 2.7: Clock error signal generation from two-sided Rabi interrogation. The transition is probed on two sides of the resonance slope separated by $2\delta_p = \nu_+ - \nu_-$. The imbalance in excitation probability is used as error signal for a feedback on the clock laser frequency.

During clock operation it suffices to probe at two points left ν_- and right ν_+ from the center frequency ν_0, with a detuning δ_p from ν_0 that gives around half of the maximum excitation, see Fig. 2.7. An error signal can then be synthesized by

$$e = \delta_p \frac{p_+ - p_-}{2} \ , \tag{2.26}$$

which used to feed back onto the laser frequency ν_L giving a frequency correction $\nu' \longrightarrow \nu_\mathrm{L} + g \cdot e$ with gain $g \leq 1$. This is a first order integrator. Generating the error signal around half the maximum excitation probability makes it the most sensitive for frequency deviations, since there the Rabi lineshape is the steepest. Under realistic conditions the laser frequency, usually pre-stabilized by a cavity, will drift. This drift causes a frequency offset if not included in the feedback. In order to accommodate for it, the drift rate is estimated over some time and a constant frequency sweep is applied to the laser frequency. This is possible because the drift rates of ultra-high stability cavities are measurable and can be predicted very well. The iQLOC 1 clock cavity drifts with 130 mHz/s (Amairi, 2014) and cryogenic silicon cavities reach slow drift rates of 60 µHz/s (Robinson et al., 2019).

2.3.2 Ramsey Interrogation

Another scheme for precise determination of transition frequencies is the Ramsey method (Ramsey, 1990). Here only the final formula is given, for further details see for example (Riehle, 2004) from where the remainder of this subsection is taken from.

The main idea behind Ramsey interrogation is to split the atom-laser interaction into two parts. In the section in-between, the laser is usually turned off and the system evolves freely. The probability to find the ion in the excited state after two interrogations of length τ_i and dead time T is (Riehle, 2004)

$$p(\tau_i + T + \tau_i) \approx \frac{1}{2} \sin^2\left(\Omega_0 \tau_i\right) \left[1 + \cos\left(\left(\omega - \omega_0\right) T\right) + \Delta\Phi\right] \ , \tag{2.27}$$

where $\Delta\Phi$ accounts for the accumulated phase deviation between atomic system and the interrogating laser. Maximum contrast of the achieved signal is given at an interaction "area" of $\Omega_0 \tau_i = \pi/2$. The phase $\Delta\Phi$ shifts the central feature away from resonance by

$$\frac{\Delta\nu_\Phi}{\nu_0} = -\frac{\Delta\Phi}{2\pi\nu_0 T} \ . \tag{2.28}$$

One main advantage of Ramsey interrogation is the gain in frequency resolution: The FWHM is given by

$$\Delta\nu = \frac{1}{2T} \ , \tag{2.29}$$

which is half of the width of a Rabi pulse of equal duration T. Thus the derived Ramsey error signal is steeper than in the Rabi case.

The applied laser pulses can introduce significant shifts on the measured resonance frequency due to the dynamical Stark effect, i.e., the light field couples non-resonantly to other energy levels. These light shifts can be suppressed by tailoring the pulse sequence in more sophisticated interrogation schemes based on the Ramsey method, e.g. *Hyper-Ramsey* (Yudin et al., 2010; Huntemann et al., 2012a; Hobson et al., 2016) or *Auto-Balanced Ramsey Spectroscopy* (Sanner et al., 2018).

2.3.3 Coupling to the Motion of the Ion

The simple two-level system does not account for the quantized motional energy of the ion inside the trap. An inclusion of these into the interaction with laser radiation is the foundation to sub-Doppler temperature laser cooling and quantum logic spectroscopy (Schmidt et al., 2005).

The quantum mechanical treatment of motion assumes that the potential has quadratic dependence in each coordinate, which is a good assumption for the region around the trap center (Wineland et al., 1998; Leibfried et al., 2003). Then the motion in the three coordinates decouples and can be treated independently and it resembles the Hamiltonian of a harmonic oscillator with frequency ω_i , with $i \in \{x, y, z\}$ (Wineland et al., 1998). The motion of a single ion in direction i is then given by

$$H_i^{(\mathrm{m})} = \hbar\omega_i \left(\hat{n}_i + \frac{1}{2}\right) , \tag{2.30}$$

where $\hat{n}_i = \hat{a}_i^\dagger \hat{a}_i$ is the number operator, the product of raising and lowering operator and $\hbar\omega_i/2$ is the vacuum energy which is omitted in the following calculations. In the Schrödinger picture, the motional part of the wavefunction can be written as

$$\left|\psi^{(\mathrm{m})}\right\rangle = \sum_{n=0}^{\infty} C_n e^{-n\omega_i t} \left|n\right\rangle , \tag{2.31}$$

with C_n being a complex number. The Hamiltonian describing the coupling between laser field and ion (Eq. 2.18) can be expanded using Pauli spin matrices

$$\hat{H}^{(\mathrm{i})} = \frac{\hbar\Omega}{2}(\hat{\sigma}_+ + \hat{\sigma}_-)(e^{i(k\hat{z}-\omega_\mathrm{L}t+\phi)} + e^{-i(k\hat{z}-\omega_\mathrm{L}t+\phi)}) \tag{2.32}$$

with the raising and lowering Pauli spin matrices $\hat{\sigma}_+ = 1/2(\hat{\sigma}_x + i\hat{\sigma}_y)$ and $\hat{\sigma}_- = 1/2(\hat{\sigma}_x - i\hat{\sigma}_y)$. The total Hamiltonian reads to be

$$\hat{H} = \hat{H}^{(\mathrm{m})} + \hat{H}^{(\mathrm{e})} + \hat{H}^{(\mathrm{i})} . \tag{2.33}$$

It is insightful to transform into the *interaction picture*, with respect to $\hat{H}_0 = \hat{H}^{(\mathrm{e})} + \hat{H}^{(\mathrm{m})}$ and $\hat{H}^{(\mathrm{i})}$ as the interaction. The transformation is performed by $\hat{H} \to \hat{H}' = \hat{U}_0^\dagger(t)\hat{H}^{(\mathrm{i})}\hat{U}_0(t)$, with $\hat{U}_0(t) = e^{-i(\hat{H}_0/\hbar)t}$ and the new states $\left|\tilde{\psi}(t)\right\rangle = \hat{U}_0^\dagger(t)\left|\psi(t)\right\rangle$. By writing the motion in terms of raising and lowering operators $\hat{z} = z_0(\hat{a} + \hat{a}^\dagger)$ with the spread of the zero-point wavefunction

$z_0 = \sqrt{\hbar/(2m\omega_z)}$ (Wineland et al., 1998), the Hamiltonian in the *interaction picture* is given by

$$\hat{H}_{\text{int}} = \frac{\hbar\Omega}{2}\hat{\sigma}_+ e^{i\left(\eta\left(\hat{a}e^{-i\omega_z t}+\hat{a}^\dagger e^{i\omega_z t}\right)-\delta\cdot t+\phi\right)} + h.c. \,, \tag{2.34}$$

with the secular motional frequency ω_z and the Lamb-Dicke parameter $\eta = kz_0$. Fast oscillating terms $\propto e^{\pm i(\omega_{\text{L}}+\omega_0)t}$ have been omitted in the *rotating wave approximation*. Transitions then occur for detunings of $\delta = (n' - n)\omega_z$.The dynamics between the pure states $|g, n\rangle$ and $|e, n'\rangle$ is given by the Schrödinger equation

$$i\hbar\frac{\partial}{\partial t}\left|\tilde{\psi}(t)\right\rangle = \hat{H}_{\text{int}}\left|\tilde{\psi}(t)\right\rangle \tag{2.35}$$

which leads to a system of differential equations for the coefficients of the state $\left|\tilde{\psi}(t)\right\rangle = C_{g,n}(t)\,|g,n\rangle + C_{e,n'}(t)\,|e,n'\rangle$ which can be solved using Laplace transformations (Wineland et al., 1998). Like in the case without coupling to motion (Ch. 2.3.1) sinusoidal Rabi oscillations between $|g, n\rangle$ and $|e, n'\rangle$ occur, if any additional detuning Δ_{res} from the resonances, i.e., $\delta = (n' - n)\omega_z + \Delta_{\text{res}}$, is small compared to the motional secular frequency $\Delta_{\text{res}} \ll \omega_z$. On resonance, i.e., $\Delta_{\text{res}} = 0$, the time evolution of an initial state

$$\left|\tilde{\psi}(t)\right\rangle = C_{g,n}(t)\,|g,n\rangle + C_{e,n'}(t)\,|e,n'\rangle \tag{2.36}$$

can be written for the complex coefficients C in matrix form as

$$\begin{pmatrix} C_{e,n'}(t) \\ C_{g,n}(t) \end{pmatrix} = T_n^{n'}(t)\begin{pmatrix} C_{e,n'}(0) \\ C_{g,n}(0) \end{pmatrix} \,, \tag{2.37}$$

with

$$T_n^{n'}(t) = \begin{pmatrix} \cos\left(\frac{\Omega_{n'n}t}{2}\right) & -ie^{i(\phi+\pi|n'-n|/2)}\sin\left(\frac{\Omega_{n'n}t}{2}\right) \\ -ie^{-i(\phi+\pi|n'-n|/2)}\sin\left(\frac{\Omega_{n'n}t}{2}\right) & \cos\left(\frac{\Omega_{n'n}t}{2}\right) \end{pmatrix} . \tag{2.38}$$

A full solution that includes detunings $\Delta_{\text{res}} \neq 0$ can be found in Ref. (Wineland et al., 1998; Leibfried et al., 2003). The coupling strengths are determined by the on-resonance Rabi frequencies

$$\Omega_{n',n} = \Omega\left|\left\langle n'\left|e^{i\eta(\hat{a}+\hat{a}^\dagger)}\right|n\right\rangle\right| = \Omega e^{-\eta^2/2}\sqrt{\frac{n_<!}{n >!}}\,\eta^{|n-n'|}\mathcal{L}_{n<}^{|n-n'|}(\eta^2) \,, \tag{2.39}$$

with $n_<$ ($n_>$)is the lesser (greater) of n and n', and the generalized Laguerre polynomials (Wineland et al., 1998; Leibfried et al., 2003)

$$\mathcal{L}_n^{(\alpha)}(X) = \sum_{j=0}^{n}(-1)^j\begin{pmatrix} n+\alpha \\ n-j \end{pmatrix}\frac{X^j}{j!} \,. \tag{2.40}$$

A special case is apparent, when the ion's motion is reduced by laser cooling below the Lamb-Dicke limit. That is the case when the amplitude of motion is small compared to the laser wavelength, which can be restated to

$$\sqrt{\left\langle \psi^{(\mathrm{m})} \,\middle|\, k^2 z^2 \,\middle|\, \psi^{(\mathrm{m})} \right\rangle} = \eta \sqrt{\left\langle \psi^{(\mathrm{m})} \,\middle|\, (\hat{a} + \hat{a}^\dagger)^2 \,\middle|\, \psi^{(\mathrm{m})} \right\rangle} \ll 1\,, \tag{2.41}$$

is fulfilled (Wineland et al., 1998). Inside this limit, transitions with a change of motional quantum number by more than one are heavily suppressed.

The Hamiltonian (2.34) inside the Lamb-Dicke regime can then be written as

$$\hat{H}^{\mathrm{LD}}_{\mathrm{int}}(t) = \frac{\hbar}{2}\Omega\hat{\sigma}_+ \left(1 + i\eta\left(\hat{a}e^{-i\omega_z t} + \hat{a}^\dagger e^{i\omega_z t}\right)\right) e^{i(\phi - \delta t)} + h.c. \tag{2.42}$$

The Rabi frequencies Eq. (2.39) can be developed to first order in the Lamb-Dicke parameter η

$$\Omega_{n',n} \approx \Omega \left| \left\langle n' \,\middle|\, (1 + i\eta(\hat{a} + \hat{a}^\dagger)) \,\middle|\, n \right\rangle \right| \tag{2.43}$$

$$= \Omega\sqrt{\delta_{n',n} + \eta^2\left(n\delta_{n',n-1} + (n+1)\delta_{n',n+1}\right)}\,, \tag{2.44}$$

where the Debye-Waller factor $\exp(-\eta^2/2)$ is ≈ 1 because of the small Lamb-Dicke factors. Transitions with no change in motional quantum number, $n = n'$,

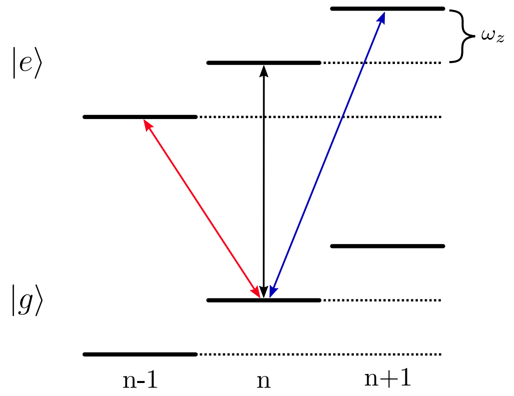

Figure 2.8: Carrier and resolved sideband transitions from ground state $|g, n\rangle$ to excited state $|e, n'\rangle$. Black: carrier, blue: blue sideband, red: red sideband. The internal energy spacing is given by ω_0, while the motional energy spacing of the quantum harmonic oscillator modes is given by ω_z.

are called carrier transitions with Rabi frequency Ω and they give rise to transitions determined by the Hamiltonian

$$\hat{H}_{\mathrm{CAR}} = \frac{\hbar}{2}\Omega(\hat{\sigma}_+ e^{i\phi}e^{-i\Delta t} + \hat{\sigma}_- e^{-i\phi}e^{i\Delta t}) \tag{2.45}$$

Tuning the laser frequency to the first red sideband (RSB) at $\delta = -\omega_z + \Delta$, driving the ion to the state $n' = n - 1$. Tuning the laser to the first blue sideband (BSB) at $\delta = +\omega_z + \Delta$ the motional quantum number increases by one upon absorption. The Rabi frequencies for red and blue sideband are given by Eq. (2.44) to be $\eta\sqrt{n}\Omega$ and $\eta\sqrt{n+1}\Omega$, respectively. Keeping again in a rotating wave approximation only the slowly varying terms, the corresponding Hamiltonians are

$$\hat{H}_{\mathrm{BSB}} = \frac{\hbar}{2}\Omega i\eta(\hat{a}^{\dagger}\hat{\sigma}_{+}e^{i\phi}e^{-i\Delta t} - \hat{a}\hat{\sigma}_{-}e^{-i\phi}e^{i\Delta t}) \tag{2.46}$$

$$\hat{H}_{\mathrm{RSB}} = \frac{\hbar}{2}\Omega i\eta(\hat{a}\hat{\sigma}_{+}e^{i\phi}e^{-i\Delta t} - \hat{a}^{\dagger}\hat{\sigma}_{-}e^{-i\phi}e^{i\Delta t}) \tag{2.47}$$

The laser field and ion are continuously exchanging energy. In general there are couplings to other states caused by higher order terms in the interaction, when the Lamb-Dicke limit is not rigorously satisfied. Coherent excitation of the the first order sidebands is the key for sideband-cooling, see Ch. 2.4.2, and quantum logic spectroscopy, see Ch. 6.

The Lamb-Dicke factors depend on the angle α between laser beam and orientation of probed secular motion

$$\eta = k\cos(\alpha)\sqrt{\frac{\hbar}{2m\omega}}\ . \tag{2.48}$$

Measuring for example the Rabi frequencies of a carrier and a ground-state cooled BSB for a known orientation of the motional mode, gives the relative orientation between laser beam and mode according to

$$\alpha = \arccos\left(\frac{1}{|k|}\frac{\Omega_{\mathrm{BSB}}}{\Omega_{\mathrm{CAR}}}\sqrt{\frac{2m\omega}{\hbar}}\right)\ . \tag{2.49}$$

2.4 Laser Cooling

Ground state cooling (gsc) is an essential prerequisite for many quantum experiments, since the finite temperature of the quantum object causes for example line broadening in optical spectroscopy, errors in quantum information processing and systematic frequency shifts in atomic clock experiments. It is also a necessity for QL (Schmidt et al., 2005). Therefore, the goal of GSC is to prepare the ion in the motional ground state, which together with the preparation of the electronic ground state, enables full control over all relevant degrees of freedom of the ion.

Short cooling times are in particular important for optical clocks, when GSC is not implemented during the clock interrogation, and hence the time for GSC introduces a substantial dead time to the clock cycle. Dead times reduce the stability of the clock due to the Dick effect, see (Quessada et al., 2003; Poli et al., 2013; Ludlow et al., 2015) and Ch. 1.4.

2.4.1 Doppler Cooling

After capturing the ion in the trap, the kinetic energy of the ion has to be reduced by Doppler cooling. Doppler cooling can be understood in a qualitative way for the case that the rate of absorption and emission, given by the natural linewidth[1] $\Gamma = 1/\tau$, is much higher than the secular motional frequencies of the particle, i.e., the motional sidebands are not resolved in Doppler cooling. It allows to make good estimates on achievable temperatures and cooling times. Here, only a brief sketch of the main idea behind Doppler cooling is given, following Ref. (Wübbena et al., 2012).

Doppler cooling is implemented by irradiating the ion with laser light on a broad transition $\Gamma > \omega_i$ red detuned by $\Delta < 0$ from resonance. The particle will get a momentum kick $\Delta p = \hbar k$ on absorption in the direction of the incoming traveling wave with wavevector $\vec{k}$. The absorption spectrum is given by a Lorentzian profile. Because the light is red detuned, the absorption probability is higher, when the ion is moving towards the laser beam, resulting in an energy loss on average. The momentum kicks from the emission process are that of a random walk around $\langle p \rangle = 0$, since the ion's emission pattern is symmetrically distributed around the position of the ion. Absorption and spontaneous emission have therefore a probability of momentum kicks that heat the ion. Scattering a large amount of photons, a cooling rate and a competing heating rate can be derived, which determine the final energy of the system when reaching their equilibrium (Wübbena et al., 2012)

$$E_{\text{limit}} = \frac{\hbar\left(4\Delta^2 + \Gamma^2\left(1 + I/I_0\right)\right)\left(1 + 3\hat{k}_x^2\right)}{48\,|\Delta|\,\hat{k}_x^2}\,, \tag{2.50}$$

where $\hat{k}_x$ is the unit wavevector component of the radiation along mode axis x, I is the laser intensity and I_0 the saturation intensity. Orienting the cooling beam equally along all motional directions ($\hat{k}_i = 1/\sqrt{3}$), the well-known Doppler limit (Leibfried et al., 2003) is achieved for low intensities $I/I_0 \rightarrow 0$ and optimum detuning $\Delta = -\Gamma/2$, which reads

$$E_{\text{Doppler-limit}} = \frac{\hbar\Gamma}{2}\,. \tag{2.51}$$

This corresponds to a Doppler cooling temperature of $T = \hbar\Gamma/(2k_B)$, with k_B the Boltzmann constant. The Doppler temperature for the $^2\mathrm{S}_{1/2} \leftrightarrow {}^2\mathrm{P}_{1/2}$ cooling transition of $^{40}\mathrm{Ca}^+$ is hence $\approx 497\,\mu\mathrm{K}$. This Doppler limit assumes equal overlap of the cooling beam with all three cooled motional mode directions. Energies below the Doppler limit in one mode can be reached by orienting the laser beam parallel to the movement direction, but this increases the temperature in the other modes (Javanainen, 1980). The Doppler limit can be described as the ion's motional state being an ensemble of Fock states $|n\rangle$, which are in thermal equilibrium with an external reservoir of temperature

$$T = \frac{\hbar\omega}{k_B \ln\left(\frac{\bar{n}+1}{\bar{n}}\right)}\,, \tag{2.52}$$

and $\bar{n}$ is the then the average population of the (ensemble) thermal distribution of Fock number states $|n\rangle$. State ensembles efficiently described by density

---

[1] The natural linewidth in the unit Hz is given by $1/(2\pi\tau)$.

matrices. The density matrix connected with Eq. (2.52) is the thermal state density matrix

$$\hat{\rho}_{\text{th}} = \frac{1}{\bar{n}+1} \sum_{n=0}^{\infty} \left(\frac{\bar{n}}{\bar{n}+1} \right)^{n} |n\rangle \langle n| \ . \tag{2.53}$$

The level $|n\rangle$ is populated with probability

$$p_{\text{th}}(n) = \frac{\bar{n}^{n}}{(\bar{n}+1)^{n+1}} \ . \tag{2.54}$$

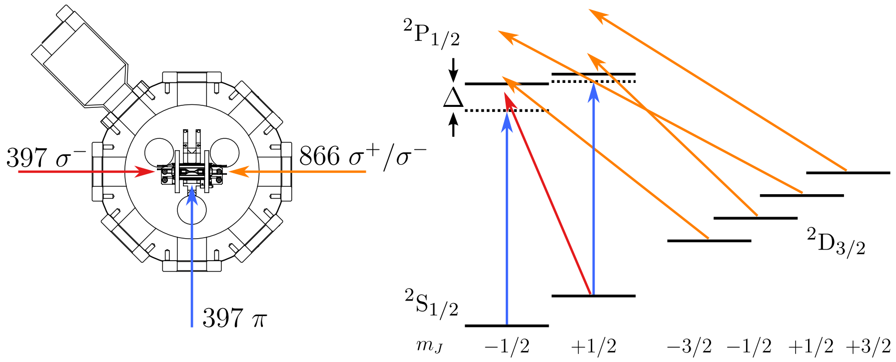

Figure 2.9: Left: Setup for Doppler cooling. Right: Used $^{40}\mathrm{Ca}^+$ transitions for Doppler cooling.

In this experiment the $^{40}\mathrm{Ca}^+$ $^2\mathrm{S}_{1/2} \leftrightarrow {}^2\mathrm{P}_{1/2}$ transition is used for Doppler cooling. The implemented Doppler cooling setup and level scheme is depicted in Fig. 2.9. Two orthogonal 397 nm beams guarantee that all motional mode directions are efficiently Doppler cooled. The π-polarized beam's wavevector has overlap with the radial modes and the σ^--polarized beam with the axial mode, respectively. In order to prevent unwanted dark resonances, both beams have a different detuning from the $^2\mathrm{P}_{1/2}$ state. A laser at 866 nm is clearing out the $^2\mathrm{D}_{3/2}$ states, which are populated by spontaneous emission from the $^2\mathrm{P}_{1/2}$ states. The laser is equally σ^+ and σ^--polarized for clearing out all $^2\mathrm{D}_{3/2}$ states. By driving these transitions the Doppler cooling resonance is broadened and the effective scattering rate is increased. In this experiment, the 866 nm laser is detuned by 1 to 3 MHz from the resonances. This detuning prevents the occurrence of dark resonances between the 866 nm and 397 nm transitions. In order to suppress the heating due to this blue detuning, the power of the 866 nm is optimized to give the lowest Doppler temperatures. With $\Gamma = 2\pi \times 20.7\,\mathrm{MHz}$ and typical axial and radial secular frequencies of $2\pi \times 1.1\,\mathrm{MHz}$ and $2\pi \times 1.92\,\mathrm{MHz}$ respectively, a Doppler limit of $\bar{n}_{\text{ax}} \approx 8.9$ and $\bar{n}_{\text{rad}} \approx 4.2$ is expected. After a typical Doppler cooling time of 1.5 to 2 ms typically mean motional occupation numbers of $\bar{n} \approx 4$ to 8 in all modes of a single $^{40}\mathrm{Ca}^+$ ion are reached as can be seen in Fig. 2.10 by the exemplary fit of a Rabi oscillation on an axial BSB to (Rasmusson et al., 2021)

$$P_{\uparrow}^{\text{BSB}}(t) = \sum_{n=0}^{\infty} p_{\text{th}}(n) \frac{1 - e^{-\gamma_{\text{dec}} t} \cos\left(\Omega_{n,n+1} t\right)}{2} \ , \tag{2.55}$$

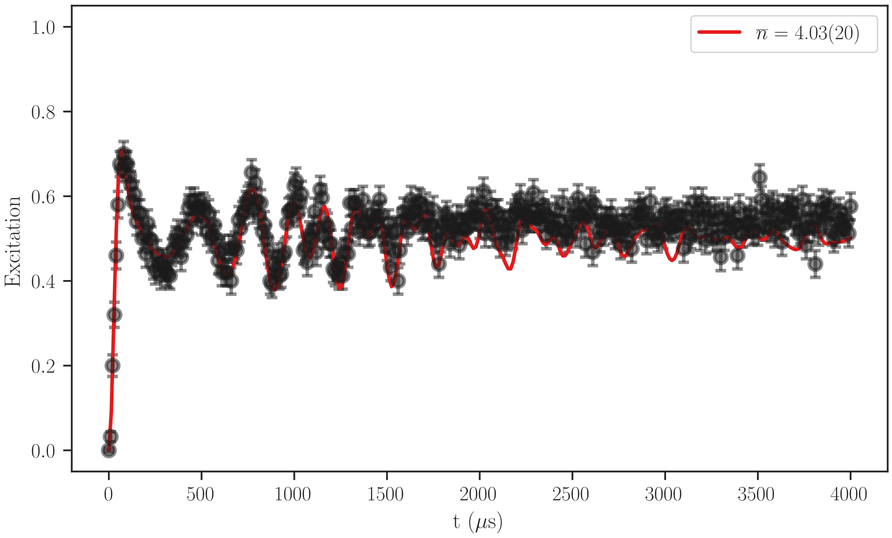

Figure 2.10: Rabi oscillation on a single $^{40}\mathrm{Ca}^{+}$ axial BSB at $\omega_z = 2\pi \times 1.1\,\mathrm{MHz}$ after Doppler cooling. The mean motional occupation number $\bar{n}$ was inferred by a fit to Eq. (2.55). The other parameters are in this case $\gamma_{\mathrm{dec}} = 562\ s^{-1}$, Lamb-Dicke parameter $\eta = 0.066$ and $\Omega = 2\pi\times\ 49.713\,\mathrm{kHz}$.

where γ_{dec} is a factor that introduces decoherence caused for example by magnetic field noise, $p_{\mathrm{th}}(n)$ is the thermal distribution Eq. (2.54) and $\Omega_{n',n}$ are the Rabi-frequencies Eq. (2.39). Lower Doppler temperatures compared to the Doppler limits stated above can be reached, when optimizing the laser cooling parameters for a single mode, because the two implemented Doppler cooling lasers at 397 nm have different orientations with respect to the motional modes. For example, in Fig. 2.10 the axial mode was cooled to $\bar{n} = 4$ while the radial modes $\omega_{x,y}$ with $\omega_x < \omega_y$ were cooled with the same cooling parameters to $\bar{n} = 6.7$ and 7.4, respectively (Rabi oscillations not shown). A compromise between good axial and radial Doppler cooling has to be found by optimizing detuning and laser powers of the axial σ^--polarized and the radial π-polarized 397 nm and of the 866 nm beam.

Quantum logic spectroscopy (Schmidt et al., 2005) in its original form requires a ground state population with $\bar{n} \approx 0$. Therefore, and for further reduction of motion-induced frequency shifts, additional cooling techniques must be implemented. The following two chapters describe two typically applied GSC methods, which are sideband cooling (SBC) and EIT cooling.

2.4.2 Sideband Cooling

The most commonly used GSC method in optical clocks is pulsed resolved-sideband cooling (SBC). After Doppler-cooling the ion is inside the Lamb-Dicke limit and motional sidebands can be individually adressed by driving a transition with $\Gamma \ll \omega_{\mathrm{secular}}$. The laser is then tuned in resonance with one of the first RSBs and in the simplest implementation turned on for interaction times given by the π-times of the respective transition. Since the Laguerre-Polynomials in Eq. (2.39) have zero-crossing at certain n', n combinations the effective Rabi frequency can become very slow and Fock state population can remain stuck in higher n states. This can be overcome by driving 2^{nd} and 3^{rd} order RSBs beforehand. Arranging the cooling pulses in an optimized way delivers smallest $\bar{n}$ and shortest cooling times (Wan et al., 2015; Rasmusson et al., 2021).

After sideband cooling a minimum occupation number of

$$\bar{n}_{\text{min}} \approx \frac{5}{16}(\Gamma/\omega_{\text{secular}})^2 \ll 1 \,, \tag{2.56}$$

can be reached (Wineland and Itano, 1979; Wineland et al., 1987). $\bar{n} \lessapprox 0.05$ are observed, particularly for $\eta \ll 1$ and $\bar{n}_{\text{init}} \lessapprox 10$ (Diedrich et al., 1989; Monroe et al., 1995).

Using this pulsed sideband cooling scheme, the cooling rate is given by the Rabi rates of the corresponding addressed sidebands. The π times for these transitions become very long when approaching $n = 0$. Typical GSC times are in the region of a few ms.

Another sideband cooling implementation is quench-cooling, where the cooling laser is continuously turned on together with a second quenching laser. In $^{40}\text{Ca}^+$ this is can be realized by coupling the narrow $\text{D}_{3/2}$ transition to the dipole allowed $\text{P}_{1/2}$ transition using the 866 nm laser. Cooling rates of 5 phonons/ms have been reported (Roos et al., 1999).

There are practical limits for the achievable $\bar{n}$, which are given motional heating, imperfect RSB π pulses, infinite RSB π times, off-resonant coupling to carrier and BSBs, as well as recoil heating upon spontaneous emission (Hemmerling et al., 2011). It is worth noting that SBC can lead to non-thermal state distributions, in particular when the starting temperature before SBC is high (Rasmusson et al., 2021).

Before advancing to the next and most used GSC method in this experiment, a simple method for measuring temperatures near the ground state is presented. The traditional thermometry model (Diedrich et al., 1989) is the ratio method: The ions are initialized in the electronic ground state $|{\downarrow}\rangle$, and then 1^{st} order RSB and BSB sidebands are driven in two consecutive experiments with equal laser powers and time. If the underlying distribution is thermal, which is assumed here and not entirely fulfilled after SBC, the ratio r of RSB to BSB can be related to the average harmonic motional level occupation $\bar{n}$ by

$$r = \frac{P^{\text{RSB}}(t)}{P^{\text{BSB}}(t)} = \frac{\bar{n}}{\bar{n}+1} \tag{2.57}$$

When the distribution is not thermal the ratio method underestimates $\bar{n}$ by an order of magnitude (Chen et al., 2017; Rasmusson et al., 2021). In (Rasmusson et al., 2021) several methods for measuring $\bar{n}$ are presented.

2.4.3 EIT Cooling

The standard GSC method in iQLOC 1 is EIT cooling. Its two implementations in this experiment have been intensively studied and presented in Ref. (Scharnhorst, 2018; Scharnhorst et al., 2018) and therefore only a brief description is given here.

The theoretical application of the so-called *dark state cooling* of atoms (Aspect et al., 1988) to trapped-ion experiments was first described in Ref. (Morigi, Eschner, and Keitel, 2000; Morigi, 2003; Eschner et al., 2003) and experimentally demonstrated in Ref. (Roos et al., 2000; Eschner et al., 2001) in a $^{40}\mathrm{Ca}^{+}$ system. One of the main advantages over other GSC methods such as SBC and its more involved implementations as for example Raman sideband cooling, is its experimental simplicity. No strong confinement is needed, hence dipole-allowed transitions can be used and only two lasers are required (Morigi, Eschner, and Keitel, 2000). Despite its simplicity, EIT cooling comes with fast cooling rates (GSC is typically achieved in 600 to 1500 µs) and low $\bar{n} < 0.1$ (Scharnhorst et al., 2018).

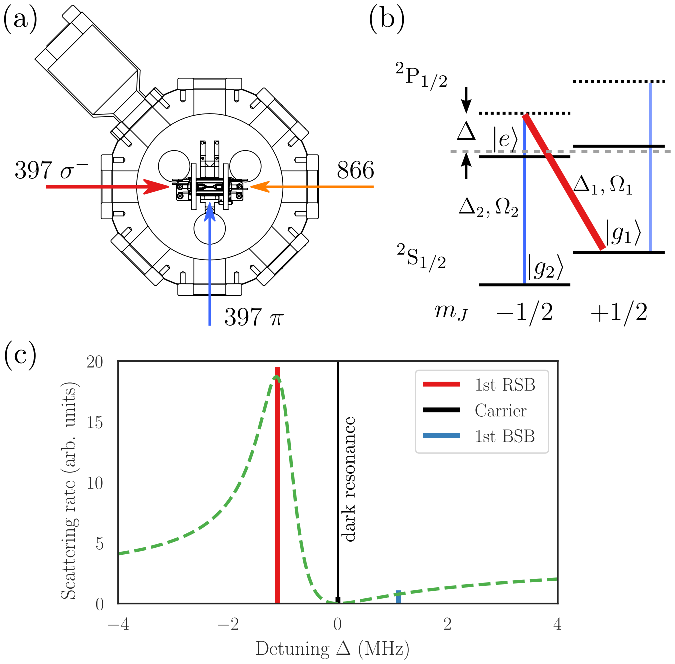

Figure 2.11: Single EIT cooling. (a) Used laser geometry. (b) Λ-shaped level scheme for single EIT cooling in $^{40}\mathrm{Ca}^{+}$. The σ^{-}-polarized 397 nm beam (red) strongly excites the $|g_1\rangle \leftrightarrow |e\rangle$ transition and has the same detuning as the lower power π-polarized 397 nm beam (blue) with respect to the $|e\rangle$ state. (c) Simulated scattering rate (dashed green line). The scattering on the carrier transition is heavily suppressed due to the occurrence of a dark resonance and scattering on the RSB is enhanced on the Fano peak, while BSB scattering is suppressed on the flat tail on the blue sideband side.

In its simplest form, called single-EIT cooling, a Λ-shaped level scheme arrangement of transitions is used, see Fig. 2.11 (a) and (b), i.e., two ground states are connected to the same upper energy level. A strong-intensity beam (397 nm σ^{-}-polarized) is blue detuned by Δ from it's bare $^{2}\mathrm{S}_{1/2} \leftrightarrow {}^{2}\mathrm{P}_{1/2}$ resonance and a second beam (397 nm π-polarized) with much less power is tuned to resonance with this virtual level.

The simultaneous driving of these transitions allows to describe the dynamics in a dressed state picture, where the atomic part of the Hamiltonian can be described by (Steck, 2022)

$$\hat{H}_{\mathrm{A}} = \hbar\Delta_{+} |g_{+}\rangle \langle g_{+}| + \hbar\Delta_{-} |g_{-}\rangle \langle g_{-}| + \hbar\Omega_{g} \left(|g_{+}\rangle |g_{-}\rangle + |g_{-}\rangle |g_{+}\rangle\right) , \quad (2.58)$$

where $|g_+\rangle$ and $|g_-\rangle$ are coherent superposition states of $|g_1\rangle$ and $|g_2\rangle$, and $\Omega_g \propto (\Delta_1 - \Delta_2)$. Δ_+, Δ_- both depend on the detunings Δ_1, Δ_2 and the ratio of Ω_1 and Ω_2. The interaction Hamiltonian is given by

$$\hat{H}_\mathrm{I} = \frac{\hbar\Omega_+}{2}\left(\hat{\sigma}_+ + \hat{\sigma}_+^\dagger\right) + \frac{\hbar\Omega_-}{2}\left(\hat{\sigma}_- + \hat{\sigma}_-^\dagger\right) \,, \tag{2.59}$$

with $\hat{\sigma}_\pm = |g_\pm\rangle\langle e|$. It turns out that $\Omega_- = 0$ (Steck, 2022), which means laser interaction only couples one of the dressed states to $|e\rangle$ (bright state) and the other is coherently trapped (dark state). Since the lasers are detuned with $\Delta_1 = \Delta_2 = \Delta$, it follows that $\Omega_g = 0$ and the atomic Hamiltonian becomes diagonal (Gray, Whitley, and Stroud, 1978).

The weak intensity beam's absorption profile takes the form of a Fano profile with two maxima at $\omega_\pm = \frac{\Delta}{2} \pm \frac{1}{2}\sqrt{\Delta^2 + \Omega_1^2 + \Omega_2^2}$ (Scharnhorst et al., 2018). Therefore, the strong laser power of the coupling beam entails an ac Stark shift, which can be tuned to match the secular frequency of the respective motional mode to be cooled ($\omega_\text{ax, rad} = -\omega_-$). The Fano profile has three distinct features, see Fig. 2.11 c):

1. Carrier transitions ($n \longrightarrow n$) are completely suppressed due to the dark resonance condition.
2. BSB transitions ($n \longrightarrow n + 1$) are partially suppressed.
3. RSB ($n \longrightarrow n - 1$) are enhanced due the narrow Fano profile maximum at ω_-.

This constitutes a cooling process with enhanced scattering on a cooling RSB transition and where the first order heating processes, e.g. carrier and BSB transitions, are heavily suppressed. Lowest temperatures are reached for higher detunings Δ, but the maximum reachable laser power puts a limit on the maximum applicable detuning. The narrow Fano profile maximum is broad enough to not be too sensitive on drifts of the motional sidebands. In fact, in our case it is possible to cool both radial $^{40}\mathrm{Ca}^+$ secular frequencies, which are ≈ 19 kHz apart, in a single cooling pulse, which can be seen by the experimentally acquired data in Fig. 2.12. There, the mean motional occupation number $\bar{n}$ of a single $^{40}\mathrm{Ca}^+$ ion, inferred from the sideband ratio of RSB and BSB (Eq. (2.57)), in dependence of the EIT cooling time is shown.

In Ref. (Scharnhorst, 2018; Scharnhorst et al., 2018) an extension of single EIT cooling to double-bright EIT cooling (Evers and Keitel, 2004) in the iQLOC 1 experiment was proven. There, the meta-stable $^2\mathrm{D}_{3/2}$ level is also coupled to the $^2\mathrm{P}_{1/2}$ state by a laser field at 866 nm, generating a second narrow Fano resonance, which can be separately tuned to a second motional sideband frequency. This can be generated, because the 397 nm and 866 nm lasers are phase stable to each other. Both lasers are phase-locked to the same ultra-stable laser, using a transfer-lock scheme (Scharnhorst et al., 2015), which is described in Ch 4.4. Double-bright EIT cooling enables simultaneous cooling of two motional modes in a single pulse and can therefore significantly reduce clock dead times.

Despite this advantage, in all GSC experiments presented in this thesis are performed with concatenated single EIT pulses.

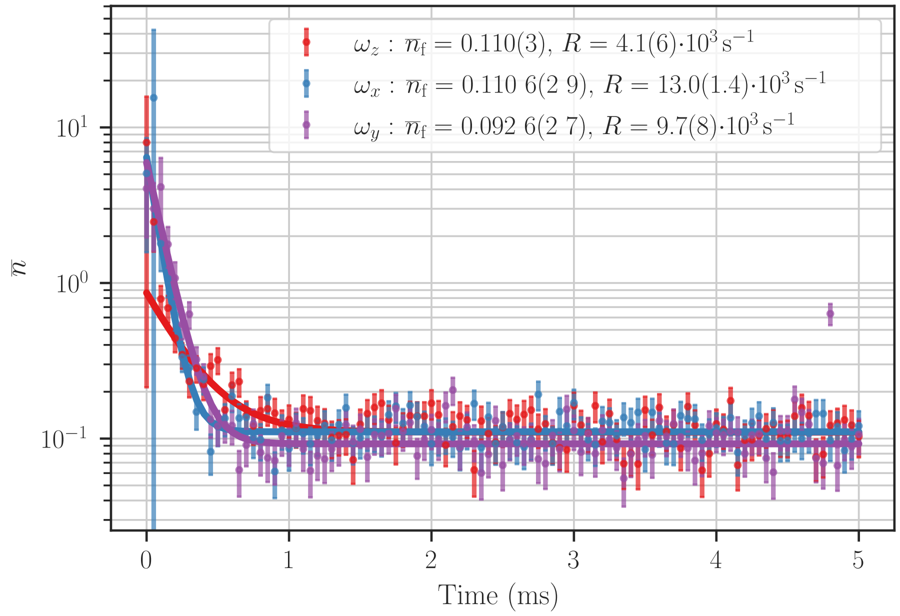

Figure 2.12: Single EIT cooling rates on $^{40}\mathrm{Ca}^+$ with secular frequencies ω_x, ω_y, ω_z = $2\pi \times 1.920,\ 1.939,\ 1.1$ MHz. The optimization of EIT coupling strengths Ω_1 and Ω_2 was performed for the axial mode and the radial modes, where in the radial case both modes are cooled with the same settings. The lines are fits to an exponential model $\bar{n}(t = 0) \cdot e^{-R \cdot t} + \bar{n}_\mathrm{f}$.

2.5 Two-Ion Crystals

As pointed out in Ch. 2.1.1.2 $^{27}\mathrm{Al}^+$ cannot be directly laser cooled and must therefore be co-trapped with a second *logic* ion, which can be laser cooled. This chapter describes the two-ion crystal motional mode structure and its impact on sympathetical cooling, which lead to the arguments why in this experiment $^{40}\mathrm{Ca}^+$ was chosen over other potential candidates as a logic ion.

2.5.1 Equilibrium Positions

A single trapped ion will have its center of motion, i.e. its equilibrium position, in the center of the trap, where the combination of dc and the RF quadrupole field potential has its minimum. Upon co-trapping a second ion, both ions will orient along the trap axis as long as the radial confinement is greater than the axial. While neutral atoms and molecules interact by short-range interaction potentials, ions with charge state Z interact mainly by the long ranging Coulomb force

$$F_\mathrm{Coulomb} = \frac{Z^2 e^2}{4\pi\epsilon_0 \left|z_1 - z_2\right|^2}\,, \tag{2.60}$$

with vacuum permittivity ϵ_0, elementary charge e and positions z_1, z_2 of the two particles along the z axis. The trapping force is given by $F_1 = Zed_0 z$, where the constants a_0 can be calculated for example by trapping the single ion 1 with mass m_1 and measuring its axial secular frequency $\omega_z = \sqrt{Zed_0/m_1}$

(Kielpinski et al., 2000). At the equilibrium position both forces are equal and both ions equilibrate around the trap center with

$$z_1 = -z_1 = \left(\frac{Z^2 e^2}{16\pi\epsilon_0 m_1 \omega_z^2}\right)^{1/3} = \left(\frac{Ze}{16\pi\epsilon_0 d_0}\right)^{1/3} , \tag{2.61}$$

which is independent of the mass. Setting $\omega_z = 2\pi \times 1.104\,\mathrm{MHz}$ the equilibrium positions are $\pm 2.6\,\mu\mathrm{m}$ for a singly charged ion pair, e.g. a $^{27}\mathrm{Al}^+$-$^{40}\mathrm{Ca}^+$ crystal. Monitoring the ion positions with a camera while moving the ion around when applying voltage offsets on the dc electrodes can be used for a calibration between ion position and dc voltage. This is in particular useful in the analysis of excess micromotion (EMM) in Ch. 7.2.

2.5.2 Two-Ion Crystal Secular Frequencies

A single ion trapped in a linear Paul trap exhibits three motional modes. They are described by their motional secular frequencies, which are the two radial modes $\omega_x \approx 2\pi \times 1.922\,\mathrm{MHz}$ and $\omega_y = 2\pi \times 1.903\,\mathrm{MHz}$, and the axial mode $\omega_z = 2\pi \times 1.104\,\mathrm{MHz}$ for typical experimental conditions in the iQLOC 1 experiment. The two radial modes are only separated by $\approx 19\,\mathrm{kHz}$ due to the high radial symmetry of the used linear Paul trap. The radial modes can be calculated from the contribution ω_p of the RF potential to the radial trap frequencies and the axial trap frequency ω_z (Wübbena et al., 2012)

$$\omega_x = \sqrt{\omega_p^2 - \alpha\omega_z^2} \tag{2.62}$$

$$\omega_y = \sqrt{\omega_p^2 - (1-\alpha)\,\omega_z^2} , \tag{2.63}$$

where α describes the symmetry of the radial modes. For the measured splitting and trap frequencies an $\alpha \approx 0.47$ is inferred, which justifies to set $\alpha = 1/2$ for the remainder of this thesis.

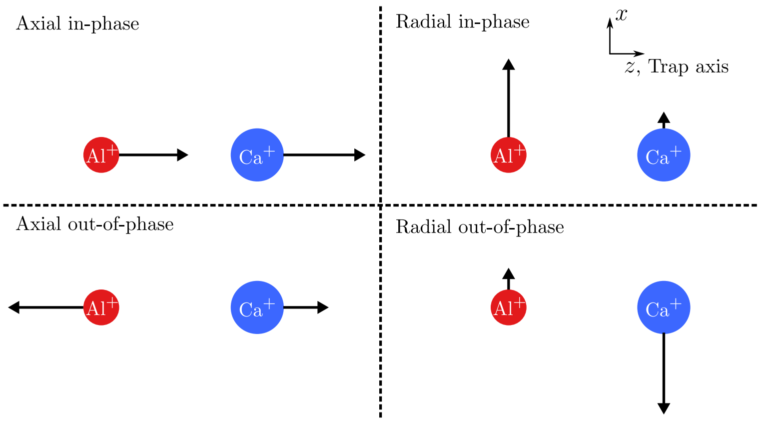

Figure 2.13: Two-ion motional modes. In the in-phase mode both ions move in the same direction, while in the out-of-phase mode they move in opposite directions. The circle diameter indicates the mass of the ions and the vector length their motional amplitude.

When a second ion is co-trapped, the motional system grows to six modes. They can be described in two classes, which are depicted in Fig. 2.13. The first being a motion where both ions move in-phase (= IP) to each other and the second where both ions move out-of phase (= OP) to each other. The frequencies of these modes can be calculated using the single ion motional frequencies of the first ion and the mass ratio, following Ref. (Wübbena et al., 2012)

$$\omega_{z,\mathrm{IP}} = \sqrt{\frac{1+\mu-\sqrt{1-\mu+\mu^2}}{\mu}\omega_z} \tag{2.64}$$

$$\omega_{z,\mathrm{OP}} = \sqrt{\frac{1+\mu+\sqrt{1-\mu+\mu^2}}{\mu}\omega_z} \tag{2.65}$$

$$\omega_{x,y,\mathrm{IP}} = \sqrt{-\frac{\mu+\mu^2-\epsilon^2(1+\mu^2)-a}{2\mu^2}} \tag{2.66}$$

$$\omega_{x,y,\mathrm{OP}} = \sqrt{-\frac{\mu+\mu^2-\epsilon^2(1+\mu^2)+a}{2\mu^2}}\ , \tag{2.67}$$

where $\mu = m_{\mathrm{Al}}/m_{\mathrm{Ca}}$ is the mass ratio of the two ions. The normalized vector components of the normal modes are given by

$$b_{x,1} = \sqrt{\frac{\mu-\mu^2+\epsilon^2\left(-1+\mu^2\right)+a}{2a}} \tag{2.68}$$

$$b_{x,2} = \sqrt{1-b_{x,1}^2} \tag{2.69}$$

$$b_{z,1} = \sqrt{\frac{1-\mu+\sqrt{1-\mu+\mu^2}}{2\sqrt{1-\mu+\mu^2}}} \tag{2.70}$$

$$b_{z,2} = \sqrt{1-b_{z,1}^2}\ . \tag{2.71}$$

They are defined such that for $^{40}\mathrm{Ca}^+$ the in-phase mode is along b_1 and the out-of-phase mode is along b_2, and reversed for $^{27}\mathrm{Al}^+$. The parameter a is defined by

$$a = \sqrt{\epsilon^4(\mu^2-1)^2-2\epsilon^2(\mu-1)^2\mu(1+\mu)+\mu^2\left[1+(\mu-1)\mu\right]}\ , \tag{2.72}$$

and $\epsilon = \sqrt{\omega_x^2/\omega_z^2+1/2}$ can be calculated by the single $^{40}\mathrm{Ca}^+$ axial and (degenerate) radial secular frequency. The equations will be used in Ch. 7.4 for calculating the individual contributions of the two ions to the energy incorporated in the secular and intrinsic micromotion (IMM).

It is important to note that the two ions have dissimilar contributions on the motion in these modes, called motional amplitudes $z_{0,i}$. In particular the radial mode amplitudes are strongly dependent on the mass ratio and decouple for mass ratios $\mu < 0.25$ and $\mu > 4$. A low motional amplitude on the cooling ion, means that this mode cannot be directly laser cooled. In Ref. (King et al., 2021) an algorithmic cooling scheme has been demonstrated, that is overcoming this issue by the usage of QL pulses. In ^{27}Al -^{40}Ca^{+} and taking typical motional frequencies from above, the resulting normal mode spectrum is listed in Tab. 2.3 together with their mode amplitudes. For example, the ^{27}Al^{+} in-phase radial mode amplitude calculates to

$$z_{0,\mathrm{Al}} = \sqrt{\langle x^2 \rangle} = |b_2| \sqrt{\frac{\hbar}{2m_1\omega_{x,y,\mathrm{IP}}}} \; . \tag{2.73}$$

Dividing these motional amplitudes by the laser wavelength and taking into account the overlap between mode and laser propagation direction gives the Lamb-Dicke factors (Eq. (2.48)).

Table 2.3: The ^{27}Al^{+}-^{40}Ca^{+} two-ion secular modes, the normalized vector components b_i and their motional ground state amplitudes $z_{0,i}$ calculated from single ^{40}Ca^{+} axial secular frequency of 1.1 MHz and 1.92 MHz radially. IP = in-phase, OP = out-of-phase. The radial modes correspond to the nearly degenerate radial mode pairs, separated by ≈ 19 kHz.

Ion	Axial IP 1.196 MHz	Axial OP 2.149 MHz	Radial IP 2.785 MHz	Radial OP 1.723 MHz
b_{Al}	0.562	0.827	0.988	0.157
b_{Ca}	0.827	0.562	0.157	0.988
$z_{0,\mathrm{Al}}$ (nm)	7.0	7.7	8.1	1.6
$z_{0,\mathrm{Ca}}$ (nm)	8.5	4.3	1.1	8.5

2.5.3 Sympathetic Cooling

As mentioned in Ch. 2.1.1.2 the aluminum ion cannot be directly laser cooled in this experiment. Doppler and EIT cooling of aluminum is therefore performed indirectly using a calcium ion, which is called sympathetic cooling. This is especially useful in quantum computing experiments, where the coherence of the qubit ion is not distorted by the cooling ion (Home et al., 2009) and in atomic (Imajo et al., 1996; Rosenband et al., 2007) and molecular (Mølhave and Drewsen, 2000; Blythe et al., 2005; Rugango et al., 2015; Wan et al., 2015) ions with rich internal level structure but no usable cooling transition.

As pointed out in the previous chapter, the two trapped ions have a shared motional system due to the repulsive Coulomb force Eq. (2.60). Therefore, by cooling one ion the other is cooled sympathetically at the same time, provided the motional amplitude of the cooling ion in this mode is not too small. When the two ions have different masses, the cooling time is strongly dependent on the initial energy of the hot sympathetically cooled ion (Guggemos et al., 2015). This is in particular an obstacle for ablation loading of ^{27}Al^{+}, where the high kinetic energy can lead to long times until the ^{27}Al^{+} ion crystallizes into the trap.

Without external heating the Doppler limit is reached independently of the mass ratio of the ions (Wübbena et al., 2012). This changes when external heating is taken into account, as then the cooling limit becomes sensitive to the mass ratio. Modes with small motional amplitude of the cooling ion are in this case cooled less efficiently, leading to smaller cooling rates and elevated final temperatures (Wübbena et al., 2012). Mass ratios close to 1 are favored, because they offer fast cooling and low equilibrium temperatures in the presence of additional motional heating (Wübbena et al., 2012). However, $^{40}\mathrm{Ca}^{+}$ with a mass ratio of 0.68 with $^{27}\mathrm{Al}^{+}$ was chosen in this experiment, because it incorporates lower Doppler temperatures than $^{25}\mathrm{Mg}^{+}$, which has an almost perfect mass ratio of 1.1 with $^{27}\mathrm{Al}^{+}$, due to the smaller linewidth of the Doppler transition ($\gamma_{\mathrm{Ca}} \approx 21\,\mathrm{MHz}$, $\gamma_{\mathrm{Mg}} \approx 41\,\mathrm{MHz}$). This reduces the 2^{nd}-order Doppler shift of the aluminum clock, when interrogated at Doppler temperature. Additionally, the laser system for detection, Doppler cooling and EIT cooling of $^{40}\mathrm{Ca}^{+}$ does not involve deep ultra violet (UV) lasers and all lasers are available as commercial diode lasers. Ground-state cooling and QL in $^{25}\mathrm{Mg}^{+}$ require a Raman laser system at 280 nm due to the hyperfine structure in this ion (Hume, Rosenband, and Wineland, 2007; Chou et al., 2010; Hemmerling et al., 2011).

Part II

Setup

The following part describes the technical realization in the presented experiment. This comprises the linear Paul trap, the vacuum chamber, the magnetic field and the used laser systems.

3 Experimental Setup

The chapter starts with a description of the used linear Paul trap and the vacuum setup and finishes with a brief summary about the experimental control system. The linear Paul trap, the old vacuum chamber and the helical resonator have already been presented in Ref. (Wübbena, 2014).

3.1 Linear Paul Trap

The electrical quadrupole field is generated by applying an RF signal with powers ranging from 1 to 8 W to a helical resonator (HRR) that is connected to the RF blades of the Paul trap inside the vacuum chamber. The linear Paul trap used in this experiment, see Fig. 3.1, is based on a design by Innsbruck university (Gulde, 2003). Its blades and endcap electrodes are made from titanium. Opposing blades have a distance of ≈800 µm and the endcap-to-endcap distance is 2500 µm. For electrical isolation the electrodes are mounted in two sapphire discs. Holes in the endcap electrodes and sapphire discs provide optical access to the trap center along the trap axis as well as at 45° to the trap axis. The Ca and Al ablation target holder, the ablation aperture and ablation targets are mounted into one of the sapphire disc. The preparation of the ablation targets is described in Ch. B.3.

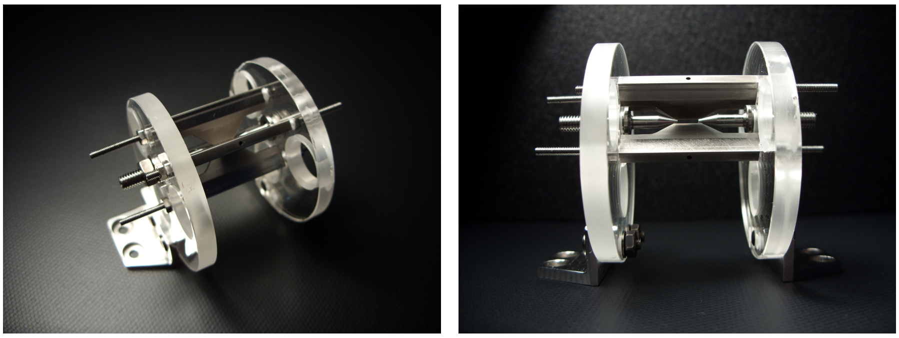

(a) **(b)**

Figure 3.1: Photos of the iQLOC 1 linear Paul trap without compensation electrodes.

3.2 Vacuum System

The linear Paul trap is mounted in an octagonal stainless steel[1] chamber with an inner diameter of 160 mm. It has optical access from eight CF35 windows in

---

[1] 316 LN.

the horizontal plane and a CF150 re-entrance window on the top[2]. The windows are mode of fused silica with an MgF_2 anti-reflective coating[3] centered at 280 nm giving a reflectance of 1.7 % at 267 nm and around 2.1 % at 397 nm. All window- and vacuum flanges are made from stainless steel[4].

The vacuum system is depicted in Fig. 3.2 (b). It has been refurbished in late 2020, because the vacuum pressure limited the performance of the experiment. Our design goal was a reduced and smaller system with shorter distance and direct line of sight between ion trap and pumps in order to increase the effectiveness of the pumps in a vacuum system with smaller volume. We use two pumps[5], which are a combination of ion pump[6] and non-evaporative getter (NEG[7]) pump. They are connected by CF35 flanges to custom-made steel parts[8]. We abstained from installing a dedicated pressure meter such as for example an ion gauge. Instead we use the current/pressure readings of the ion pump controllers [9], capable of measuring down to 0.1 nA (0.1 nPa). Typical indicated pressure readings are ≈ 0.5 nPa. Because of possible miscalibration and other error sources we take those pressure readings as indication and infer the "real" pressure inside the chamber by two-ion-crystal position swap rates, see Ch. 5.1.1. The low final pressures have been accomplished by a 42 days long bake-out process described in the appendix Ch. B.4.

Electrical access is accomplished by a dc[10] and an RF[11] feedthrough.

The old system included a ZnSe window which allowed to transmit higher wavelength spectra useful for the evaluation of the BBR shift in the trap (Doležal et al., 2015). During the refurbishment, we noticed it was leaky and the coating of it was brittle, falling to small pieces. Therefore, it was removed.

---

[2] 6.4 mm glass thickness, 35.2 mm total thickness of window and flange and 28.8 mm from the top air-side of the flange to the air-side window surface.

[3] Windows from *MPF*.

[4] 316LN.

[5] *SAES* NEXTorr® Z100.

[6] Diode ion pump with a pumping speed of 6 L/s (Ar).

[7] The getter material consists of ZAO® sintered getter discs. High pumping speed of 150 L/s.

[8] Stainless steel, 316LN. Produced by *Vacom*.

[9] Coldion-CU-100-3M, product of *Vacom*.

[10] *Vacom* CF35-MPC2-19-SE-CE-SSG, 32 pins.

[11] *Vacom* CF35-MHV-4-GS-SE-CE-SS, 4 pins.

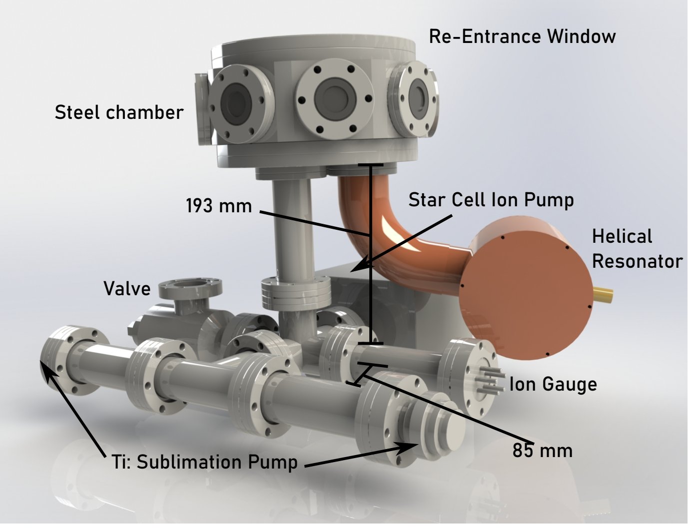

(a) Old system.

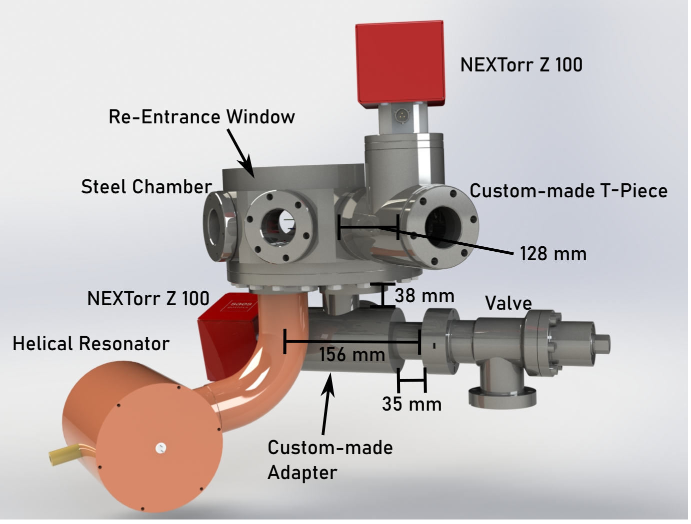

(b) New system.

Figure 3.2: CAD drawings of the iQLOC 1 vacuum system. (a) The old system, already described in Ref. (Wübbena, 2014), comprises several tube pieces and turns. A Star Cell ion pump (*Vacom)* in combination with a Ti-Sublimation pump maintain the vacuum in the chamber. The pressure was monitored by an ion gauge and showed typical values of 7.5 to 11 nPa. (b) The new system has a smaller footprint. Two NEXTorr® Z100 pumps provide a lower background pressures than in the old system, indicating ≈ 0.5 nPa.

3.3 Trap Drive

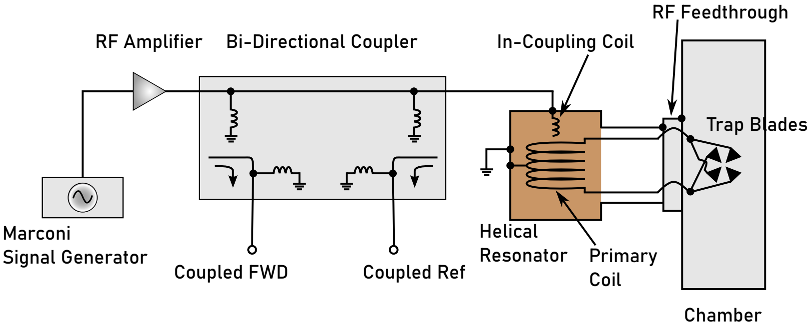

Figure 3.3: Schematic diagram of the RF circuit providing the signal for the trap drive quadrupole electric field.

The linear Paul trap is driven by the RF circuit shown in Fig. 3.3, which is a symmetric trap drive scheme, see Ch. 2.2. This means that all blades are connected to the RF signal, with neighboring blades being out of phase by 180°. A frequency synthesizer[12] is remotely controlled from a PC and powers the system consisting of an amplifier[13] (40 dB), bi-directional coupler[14], a HRR, RF feedthrough[15] and the four Paul trap blades. The amplified signal is set to the resonance frequency of the HRR, which acts as passive filter and step-up transformer with quality factor Q. The in-coupling coil is connected to the HRR's copper housing, hence they share the same electric ground. The HRR, the steel surrounding of the RF feedthrough and the steel chamber are grounded to the optical table. The transmitted and reflected power can be monitored by the respective outputs of the bi-directional coupler, using a spectrum analyzer, oscilloscope or power meter.

The high peak voltages required on the Paul trap blades are provided by the frequency synthesizer and RF amplifier. An HRR between amplifier and blade trap allows for impedance matching between these parts, which maximizes the power transmitted to the trap. The peak voltage is given by $V_{\text{peak}} \approx \kappa\sqrt{2PQ}$, with κ being determined by inductance and capacitance of the circuit and P the input power (Siverns et al., 2012). An impedance matched circuit has a high quality factor $Q = f/\text{FWHM}$, with f the resonance frequency and FWHM the full-width-at-half-maximum of the power spectrum resonance of the HRR[16]. Since the HRR is a $\lambda/4$ resonator it can be said that the smaller the HRR's geometrical dimensions, the higher the resonance frequency. A small FWHM ensures a high suppression of the noise that the active amplifier introduces into the system. Residual noise can lead to motional heating of the ions (Siverns et al., 2012).

A high trap drive frequency can be beneficial, because it pushes the micromotion sidebands further away from the carrier resonance. But it entails smaller

---

[12] *Marconi* with high stability quartz oscillator. A RF attenuator from *Mini Circuits* reduces the power of the Marconi directly behind its output by 10 dB (not shown in Fig. 3.3).

[13] Mini-Circuits ZHL-5W-1.

[14] Mini-Circuits ZFBDC20-62HP+.

[15] Vacom CF35-MHV-4GS-SE-CE-SS.

[16] When measuring Q with a voltage signal, the angular resonance frequency ω has to be divided by the total width $\delta\omega$ at $1/\sqrt{2}$ of the peak voltage (Siverns et al., 2012).

radial secular frequencies, because with given Q the trap's q parameters scale with Ω^{-2} according to Eq. (2.8) to (2.13). Therefore, a compromise has to be found, where a two-ion crystal can be stably trapped in a linear configuration and the carrier-to-micromotion sideband distance is high enough to not suffer from heating on micromotion sidebands. The reflected part of the HRR must be smaller than 5 % at the used input powers in the of range of 1 to 8 W in order to prevent damaging of amplifier and frequency synthesizer.

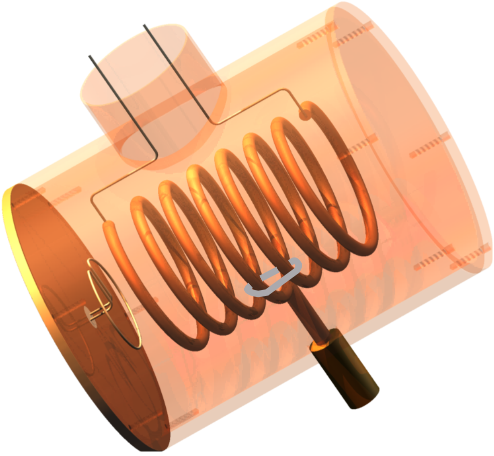

Figure 3.4: Rendered CAD drawing of the iQLOC 1 helical resonator. A silver coated copper wire is used to short two windings of the primary coil on one side. The picture without this wire was already published in (Wübbena, 2014).

The iQLOC 1 HRR, which is depicted in Fig. 3.4, comprises of a 120 mm diameter copper cylinder with a length of ≈ 150 mm. The primary coil has 7 windings of 5 mm thick bent copper wire up to a total height of ≈ 91 mm and an outer diameter of ≈ 65 mm. A thick copper rod is soldered at the center point of the primary coil and connects it to the copper housing. This puts the center of the primary coil on ground, a necessity for the symmetric drive. Two thinner copper wires with a diameter of 1 mm are soldered at the respective ends of the primary coil and lead to the electric feedthrough at the chamber. A BNC connection at the top lid is soldered to the in-coupling coil on the inner side of the helical and provides the input signal to it.

Using a symmetric trap drive reduces axial micromotion as the electric fields of neighboring blades cancel out. This can be seen by the high axial symmetry of electric field strength along the trap axis in Fig. 3.5. However, the high symmetry of the trap drive resulted in degenerate radial secular motional frequencies, which made them impossible to Doppler cool from a single laser direction, since one of the radial modes would align to be perpendicular to the cooling beam and thus evade being cooled. As it can be seen in Fig. 3.4 a small copper wire shorts together two windings of the primary coil on one side, effectively shifting the RF ground and peak voltage of this side. This symmetry breaking introduced slightly different peak voltages between left and right blade pairs and therefore split the radial secular frequencies further apart to a typical value of ≈ 19 kHz. A negative impact such as additional axial micromotion has not been observed. An increase in the micromotion amplitude has to be expected, when there is a phase-lag between opposing

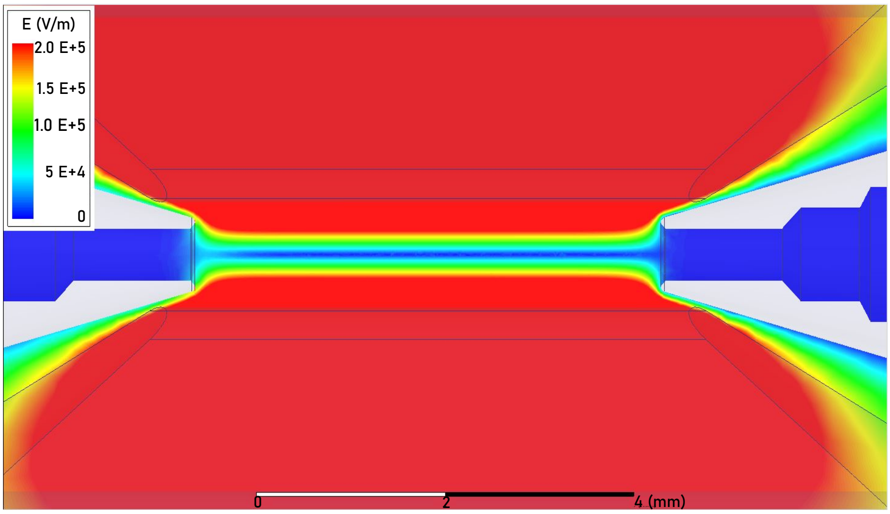

Figure 3.5: Electric fields in the iQLOC 1 Paul trap (Doležal, n.d.).

blades (Berkeland et al., 1998), which is not the case since all blades are on their peak voltages at the same time.

The Q factor of the loaded HRR, i.e., when it is connected to the trap, is dependent on the effective capacitance of trap and its connection to the HRR, as well as on the parameters of the in-coupling coil in the HRR. These *impedance-match* parameters include position, number of windings and distance between windings.

We used a network analyzer[17] to optimize the input coupling coil diameter and distance from the main HRR coil for low reflection and high Q factors. The network analyzer powered the loaded HRR. The transmitted signal was picked-up with a self-built antenna, whereas the reflected signal was obtained from the bi-directional coupler. The in-coupling coils are silver-coated copper wires held in place by a 3D printed support[18] and formed to a single turn. The distance from the in-coupling coil to the grounded cover of the HRR was varied, see Fig. 3.6. The insertion of the in-coupling coil into the 3D printed holder could in principle lead to additional capacitances, due to the dielectric nature of this material. But no significant impact on the Q factor or the resonance frequency was noticed. We chose a final in-coupling coil distance of 14 mm.

It must be noted that the Q factor and the reflection are highly dependent on the connection of the copper tube between HRR and chamber. The copper tube acts as well as a shield around the stiff output wires of the HRR and as ground connection between HRR and chamber. Care has been taken to arrange these wires inside the copper tube symmetrically in the center. By fine-tuning the position and tightening the shortening wire inside the HRR, we achieved a final $Q \approx 230$, see the fit in Fig. 3.7, and a reflection of $\approx 0.4\,\%$, which we could infer from the ratio of input and reflected power, measured by the network analyzer.

---

[17] *Anritsu* Network Analyzer.

[18] Polylactic acid (PLA).

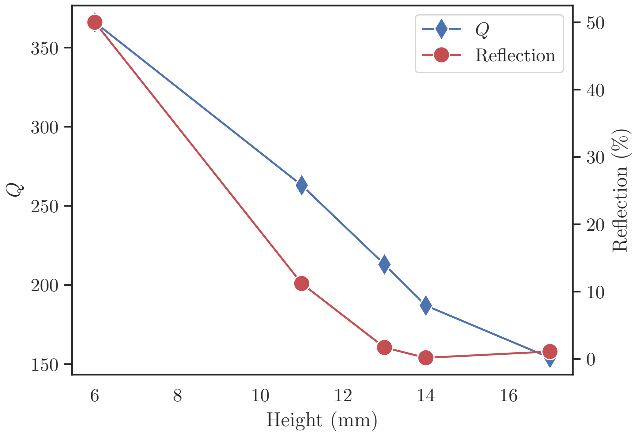

Figure 3.6: Measured Q (blue) and reflection in % (red) in dependence of the in-coupling coil distance from the HRR's cover. The Q factor drops with increasing distance together with the reflection. A good working point is where the reflection is below 1 to 2 % with maximum achievable Q. Other parameters have not been optimized when producing this graph. Therefore, the final Q value is not shown.

When the system is driven at usual power levels the components heat up and the reflection can go up to $\approx 3\,\%$. Temperature variations of the components result in variations of the trap voltages, and with them the secular frequencies (Ch. 5.4) and RF-induced shifts (Ch. 7.7.2). During the preparation of this manuscript an active stabilization of the trap drive power was implemented following Ref. (Johnson et al., 2016). A small pick-off antenna at the inner side of the bottom lid of the HRR cylinder is used to detect the power in the HRR. After this change, the in-coupling coil and the shortening wire position have been re-optimized and a $Q \approx 270$ at a resonance frequency of 28.0843 MHz was reached. This setting only influences the heating rate measurements in Ch. 5.5. We plan to reevaluate the trap-induced ac Zeeman shift (Ch. 7.7.2.1) when the active trap drive stabilization is fully operational.

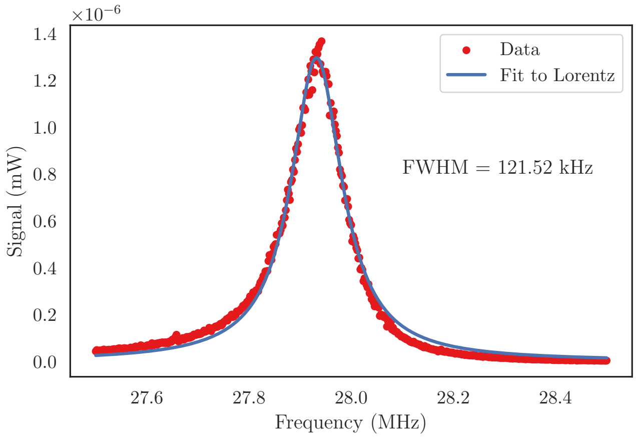

Figure 3.7: Loaded HRR transmission picked up by antenna (red dots) and Lorentzian fit (blue line). The resonance frequency is 27.95 MHz.

3.4 DC Electrodes

The axial trapping potential on the endcap electrodes is generated by a low noise high voltage supply[19]. Typical endcap voltages are 400 to 1500 V. On the dc electrodes used for EMM compensation, voltages of −200 to −600 V are applied.

The stability of the voltages is specified with a few 1×10^{-5} ($\approx$ mV) at 1 s, which was confirmed in measurements using a 6-digit multimeter[20]. In Ch. 5.4 it will be shown that the axial secular frequency averages with a 21 $\text{Hz}/\sqrt{\tau}$, where τ is the averaging time, down to 1.5 Hz at 200 s before it starts to drift.

3.5 Imaging System

All experiments are based on internal state discrimination using fluorescence on the $^{40}\text{Ca}^{+}$ $^{2}\text{P}_{1/2} \leftrightarrow {}^{2}\text{S}_{1/2}$ transition. The $^{40}\text{Ca}^{+}$ fluorescence is focused by a multi lens system[21] with a magnification of $\approx$ 17 (Benhelm, 2008; Wübbena, 2014) onto an EMCCD camera[22]. An electronic flip-mirror can direct the beam path onto a photo-multiplier tube (PMT[23]) for single photon counting and quantitative data analysis. The imaging system is depicted in Fig. 3.8. The $\approx$ 1.1 m beam path behind the lenses is folded inside a light-tight box above the vacuum chamber. The multi-lens objective has an antireflective coating for 397 nm and 729 nm and the spherical aberration due to the 6 mm width of the re-entrance window has been considered in the design of the objective. From the distances given in Fig. 3.8, a numerical aperture of NA$\approx$ 0.31 is estimated. In (Wübbena, 2014) a quantum detection efficiency of 0.44 %

---

[19] *ISEG* EHS 8 240x; CH0-CH3: +4 kV / 2 mA, CH4-CH7: −4 kV / 2 mA.

[20] *Keysight* 34410A.

[21] Manufactured by *Sill Optics, Germany* in cooperation with the University of Innsbruck.

[22] *Andor* iXon 885.

[23] *Hamamatsu* H10682.

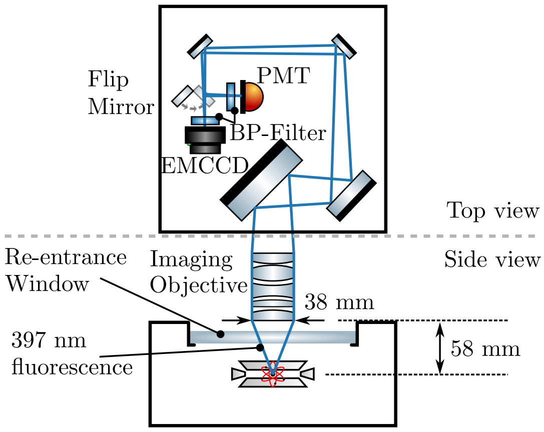

Figure 3.8: Used imaging system. A set of lenses focuses the $^{40}\mathrm{Ca}^+$ fluorescence at 397 nm either on a photomultiplier tube (PMT) or an EMCCD camera. Narrow bandpass filters (BP-Filter) suppress detecting scattered photons from other lasers and room light. This imaging system has been already described in (Wübbena, 2014; Benhelm, 2008).

has been calculated[24]. The camera is used for identification of ion crystal configurations and measuring reordering rates, see chapter 5.1.1.

Planned Imaging System With the upgrade of the vacuum system we exchanged the top re-entrance window, giving the opportunity to use a new imaging lens with a shorter distance from the ion to the first lens surface of 36.6 mm and a higher effective objective diameter of 42.6 mm. The aspheric lens was designed in the work for the iQLOC 2 experiment and has been described in Ref. (Hannig, 2018; Hannig et al., 2019). By this we expect an increase in detection efficiency because of the higher numerical aperture of NA$\approx$ 0.51 (Hannig, 2018).

3.6 Loading ^{27}Al and ^{40}Ca

Neutral Ca and Al clouds can be produced by thermal evaporation of small grains in an oven tube (oven loading) or by laser ablation. The old and the new iQLOC 1 setup feature an oven and an ablation target for both atomic species. The description of the loading setup in this thesis is focused on the new setup.

3.6.1 Oven Loading

The ovens in this experiment are small ceramic tubes with a height of 6 mm and a diameter of 4.3 mm, see Fig. 3.9. A single oven includes five outer holes and a central hole, each with a diameter of 0.75 mm. A tantalum wire is threaded through the outer holes which is used to heat the compressed metal grains of either pure Ca or Al metal probes inside the central hole. The bottom side of

---

[24] Considering saturated 397 nm $^{40}\mathrm{Ca}^+$ detection, the scattering rate is 32 kcounts/ms (Wübbena, 2014) and thus at best the PMT records 140 counts/ms. In the presented experiments in this thesis we use detection parameters, that give 100 to 120 counts/ms.

the central hole is sealed by a ceramic glue[25] in order to prevent the metal probes to leave the oven. Choosing tantalum as wire over tungsten, which would also have been a valid choice, has the advantage of a high melting point of 3290 K and a resistivity, that is high enough such that currents of only 1 to 2.5 A within the specifications of the dc feedthrough are required. The ovens are placed in titanium oven mounts, which also serve as heat-shields keeping the heat in the oven. With increasing temperature, the partial pressure of Ca and Al is growing and a continuous cloud of atoms is evaporated towards the trap center. Typical sublimation temperatures for Ca are 500 to 600 K at partial pressures between 1 to 15 000 nPa. Aluminum needs higher temperatures to evaporate, i.e., ≈800 to 900 K. When the partial pressure around the heated Al exceeds ≈200 nPa Al begins to melt at around 933 K. As mentioned above, for this reason the oven's central hole is closed in order to prevent the melted Al to drip out. Especially when the Al oven is run for the first time, the temperature has to be increased carefully, because the Al oxide layer has a much higher melting point than the pure metal of more than 2000 K. If the temperature is increased too fast, it can happen, that the melted aluminum inside the oven bursts through the oxide layer, depositing large amounts of this metal into the chamber.

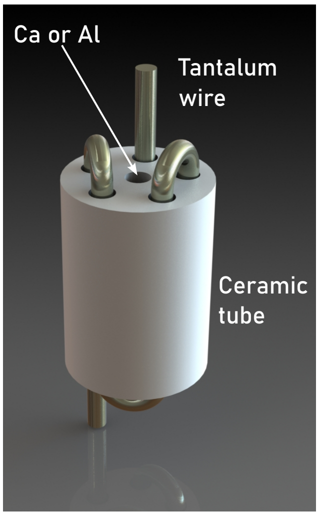

Figure 3.9: Drawing of an oven. The central hole contains metal probes of either Ca or Al. A tantalum wire heats the ceramic tube and the metal probes.

Both ovens are placed below the Paul trap, aligned along the trap axis with their central holes, oriented towards the trap center. The outgoing atom beam passes an aperture of 1 mm diameter to shield the trap electrodes from the atomic beam and finally crosses the trap center.

The high temperatures needed for oven loading heat the trap and its surrounding. It takes seconds to minutes until a significant cloud of atoms is evaporating from the oven, and turning it off does not stop the production immediately, since the oven stays warm for some time. This can lead to unwanted loading of more atoms if the ionization lasers are not turned off quickly enough and a drift

---

[25] *Ceramabond.*

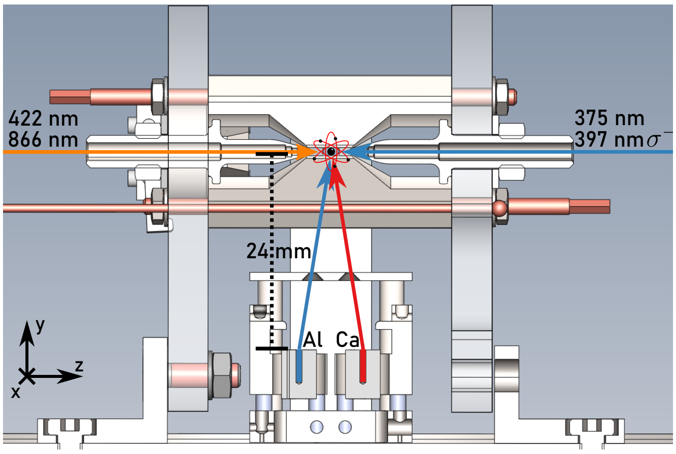

Figure 3.10: Oven loading geometry. The ovens are placed 24 mm below the trap center. The Ca ionization beams are entering axially, while the Al ionization beam is coming in diagonally (not shown here - see Fig. 3.11).

of the ion position on the timescale of minutes to hours. The latter effectively leads to a drift of the ion's micromotion amplitude after loading.

Even though oven loading is more and more superseded by ablation loading, which beats the two aforementioned drawbacks, it stays a reliable loading method for atomic clocks. For this reason the iQLOC 1 chamber includes an oven for each species as a fallback solution.

3.6.2 Ablation Loading

In this experiment, preparation of ^{40}Ca$^+$ and ^{27}Al$^+$ crystals is routinely achieved by ablation loading (Ashfold et al., 2004; Zimmermann et al., 2012). In contrast to the loading process with a resistively heated oven, ablation loading can be accomplished by a single laser pulse. We use a frequency doubled, flash-light pumped and Q-switched pulsed (ns) Nd:YAG laser[26]. The pulse energy is coarsely tuned to 400 to 600 µJ by hand and then fine-tuned by altering the Q-switch delay between 150 µs (maximum) and 300 µs (minimum power). The pulsed laser is focused on a Ca or Al sample, called ablation target, where it produces very high temperatures concentrated at the point of impingement. For ablation of Ca typical a pulse energy of ≈ 140 µJ and for Al ≈ 265 µJ are used. The temperature at the ablation spot is largely dependent on the laser intensity, i.e. the beam waist at the target. The laser is focused to a waist of roughly 200 µm using lenses. On a ps timescale a plasma plume consisting of atoms, molecules, ions and electrons is formed and ejects this material in cosine-squared dependence from the surface's normal vector towards the trap center (Ashfold et al., 2004). Therefore, the ablation target holder is designed such that the ablation target surface is pointing towards the trap center. The distance from target surface to trap center is 15.8 mm for the inner-lying Al target at an angle of 29.4° with respect to the trap axis and at 38.1° for the outer-lying Ca target, respectively. Between target and trap center

---

[26] *Amplitude* Minilite ML I X, pulse width 5 ± 2 ns, maximum pulse energy 44.1 mJ (13 mJ) at 1064 nm (532 nm). Maximum repetition rate 15 Hz.

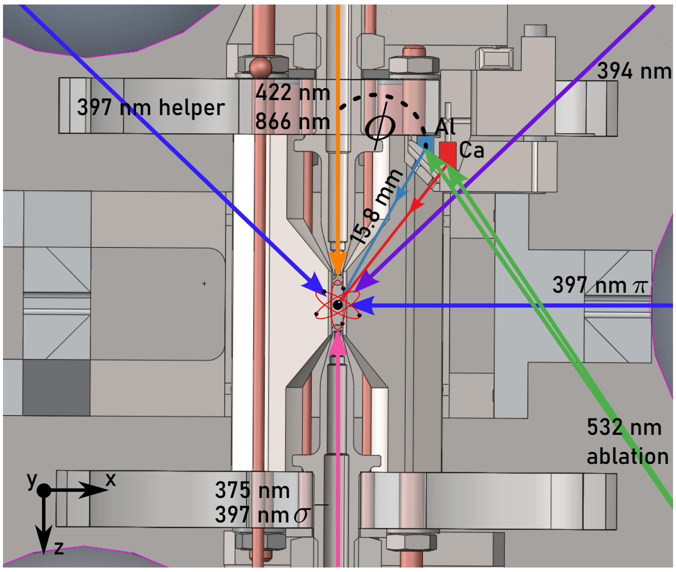

Figure 3.11: Ablation loading geometry. A motorized mirror is steering the ablation laser either onto the ^{27}Al or ^{40}Ca ablation target. The target's surfaces are designed such that they point towards the trap center with angles ϕ =29.4° for the Al and ϕ =38.1° for the Ca target, respectively.

is a cover made from Ti-6Al-4V with two apertures of 0.5 mm diameter and approximately 0.8 mm thickness, which protects the trap's endcaps and blades from getting coated with the target metals. The cover is electrically isolated from the target by ceramic tubes[27] and can be set to a static voltage in order to push away fast electrons inside the plasma plume. A photo[28] of the installed ablation targets is depicted in Fig. 3.12. A CAD drawing of the ablation target holder and aperture is shown in Fig. B.3 in the appendix Ch. B.3.

The generation of an atomic beam of finite length enables to time the ablation pulse with the ionization laser. In the experiment we set a delay between Q-switch trigger pulse and the turning-on of the Al ionization laser. In the old setup a time-of-flight measurement of neutral Al fluorescence using the ionization beam at 395 nm was conducted. This was possible since this wavelength is within the bandwidth of the optical filter in front of the PMT. As shown in Fig. 3.13, a peak velocity of $\approx$ 3.3 km/s was measured. A significant amount of photon counts was apparent even with the ionization beam turned off. The origin of this peak may lay in already ionized Al ions inside the ablation plume, but could not be resolved completely. However, this motivated a design for the new setup in which an offset voltage could be applied to the ablation aperture, in order to slow down the electrons or even prevent them from entering the trap region at all. A test of this has not been conducted so far, since the observation of this neutral atom fluorescence requires much higher pulse energies than typically used for loading, from which we refrained so far to prevent the targets from potential damage.

The ablation process itself is altering the surface, see Fig. 3.14. Since the ablation plume is leaving the target perpendicularly to its surface, the ablation

---

[27] Macor.

[28] Taken with a long working distance microscope camera *Dino-Lite* AM4115TF EDGE.

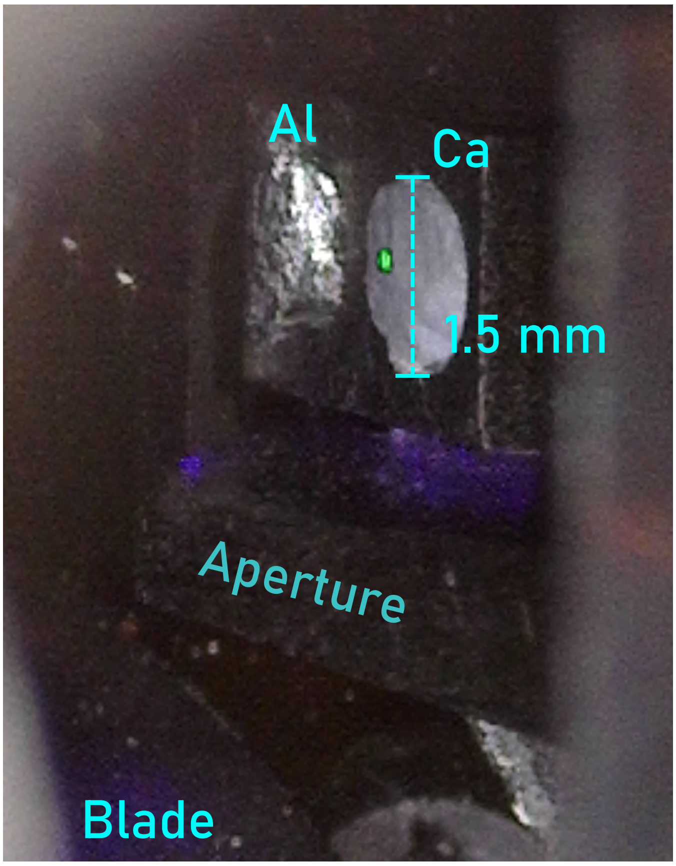

Figure 3.12: In-chamber photo of the two ablation targets, taken from about the same direction the ablation laser impinges onto the target (green laser spot).

loading efficiency can exhaust a single used ablation spot due to an increase in surface roughness. Recovering the loading efficiency can be achieved by changing the spot, but other techniques such as a refurbishment of the surface by an even higher pulse train and thus smoothening of the target surface has been reported. Starting with a Q-switch delay that usually results in a single trapped ^{40}Ca^{+} ion after 2 to 20 shots, we observe a decline in laser ablation efficiency over periods of days. We then increase the ablation power in small steps by decreasing the Q-switch delay. At a certain value we suddenly again load more than one ion. A subsequent reduction of laser power results at roughly the starting Q-switch delay prior to this procedure.

3.6.3 Ionization

For ionization of Ca we use a two-photon ionization process (Sheridan, 2009; Wübbena, 2011). The first, resonant pulse at 422.8 nm excites Ca from $^1S_0$ to $^1P_0$. From there, a photon at 375 nm excites Ca above the photon-ionization threshold.

For Al ionization also a two-step process is used. Two photons from the laser at 759.9052 THz (394.5 nm) excite in the first step $^2P_{1/2}(F' = 3)$ - $^2S_{1/2}(F = 2)$ (Guggemos et al., 2015; Liu et al., 2018) and in the final step into the continuum.

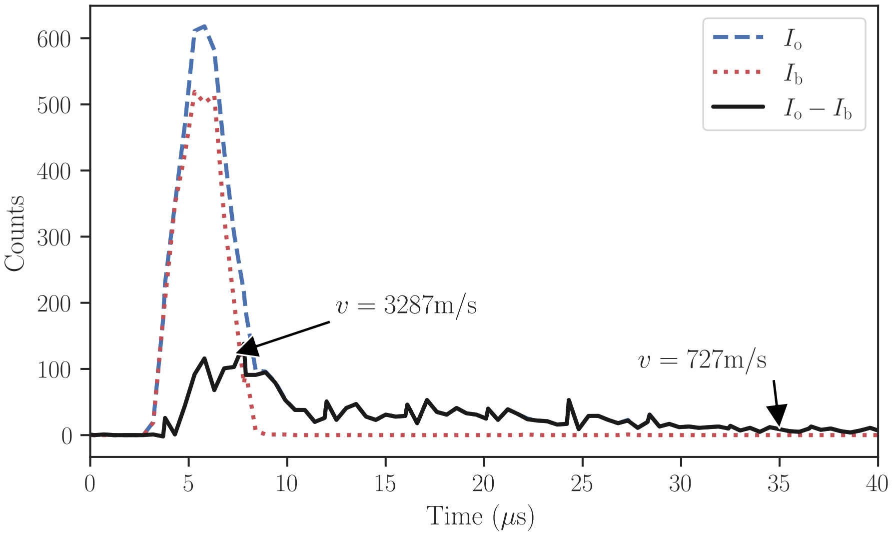

Figure 3.13: Aluminum time-of-flight measurement in the old setup. Measured PMT counts after the Q-switch opens at $t = 0$. There is a PMT signal even with blocked ionization beam I_b (blue). The difference between with unblocked ionization laser I_o (red) and I_b gives the black curve. The origin of I_b is not understand completely, but it may be a combination of ablation-ionized Al ions and the fact, that the ablation plume in the old setup was oriented towards the imaging lens.

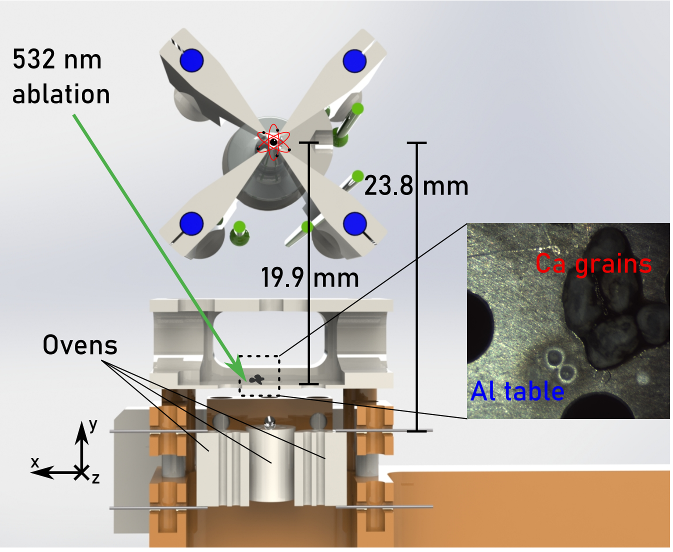

Figure 3.14: Old ablation target and ovens (removed in the new setup). Ablation loading was achieved by ablating from glued Ca grains and an Al made plate. After years of usage, including increased pulse energies for neutral Al fluorescence measurements, there are craters visible in the Al target.

3.7 Magnetic Field

A static magnetic field is necessary in order to lift the degeneracy of the fine-structure and hyperfine structure states of $^{40}\mathrm{Ca}^+$, and $^{27}\mathrm{Al}^+$ respectively, by the linear Zeeman effect. A low systematic shift and uncertainty of the $^{27}\mathrm{Al}^+$ clock transition and maximum coherence of the laser-ion interaction demand this field to be stable in time and, especially when trapping multiple ions, to be homogeneous over the spatial extend of the ions.

3.7.1 Quantization Magnetic Field

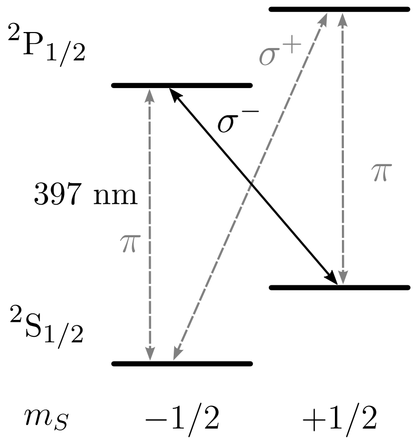

Figure 3.15: Alignment method for the σ^--polarized radiation at 397 nm for $^{40}\mathrm{Ca}^+$: For perfect polarization of the 397 nm σ^- beam (black) and alignment in respect to the bias magnetic field, all other polarization states of the ion vanish and the ion is trapped in the $m_s = -\frac{1}{2}$ state, from where it cannot scatter photons.

In this experiment we typically apply a bias quantization magnetic field of 0.15 mT along the trap axis direction, using a round coil pair[29] mounted at the chamber window flanges. Two coil pairs along the horizontal[30] and vertical[31] directions are used to null residual dc magnetic fields, as for example the earth magnetic field, and therefore redirect B_0 along the z direction. This calibration is routinely performed by minimization of 397 nm fluorescence of the σ^--polarized beam, scanning the two coil pairs in x and y (horizontal) direction. For perfect σ^--polarization of the beam and perfect parallel alignment between beam and direction of the magnetic field, the state population of $^{40}\mathrm{Ca}^+$ is trapped in the $|\,^2S_{1/2}, m_S = -\frac{1}{2}\,\rangle$ state, see Fig. 3.15. Using an axial 397 nm beam is here advantageous because it is naturally well aligned along the trap axis, see Ch. 4.7.

As current sources for the magnetic field coils, dc power supplies[32] are used, remotely controlled by the experimental control computer. Heating effects inside the power supplies and the coils themselves lead to settle-times between 5 to 15 min depending on the applied current value, as can be seen in Fig. 3.16

---

[29] For a bias field of $B = 0.15$ mT one has to put $I = 430$ mA on this coil pair.

[30] $I = 12$ mA.

[31] $I = 41$ mA.

[32] *TTi* QL355TP Power Supply.

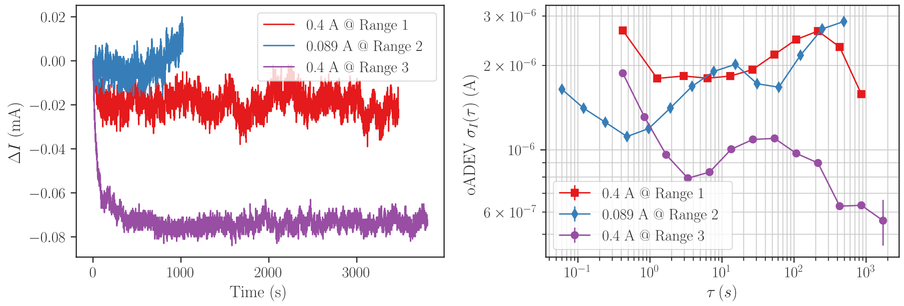

(a) Time trace. **(b)** oADEV.

Figure 3.16: Stability of the magnetic field current supply units mentioned in the text. (a) Time trace of the dc current supply. Higher applied currents increase the settle-time. (b) Stability in form of an oADEV of the data from (a). The violet data has been cut off to a start time of 350 s in order to infer the settled stability.

Table 3.1: Current ranges and stabilities of TTi QL355TP Power Supply.

Range	max. U (V)	max. I (A)	σ_y (1×10^{-6} A) at 1 s
1	15	5	2
2	35	3	< 2
3	35	0.5	1.3

(a). There, the current has been measured using a 6-digit multimeter[33]. The current stability is plotted as overlapping Allan deviations in Fig. 3.16 (b). Different range modes can be used, which differ in output current, voltage and achievable stability, see Tab. 3.1. All direction of the magnetic field coils are driven in mode 3.

3.7.2 Active Magnetic Field Stabilization

The instability of the quantization coil current is not the only source for magnetic field noise. External dc and ac magnetic fields are disturbing the total magnetic field seen by the Ca and Al ion on different time scales. Sources of varying magnetic fields are the earth's magnetic field[34] (slow drift), noise from the mains power line at frequencies of 50 Hz and harmonics, electronic devices as for example switching power supplies (several tens of kHz), the elevator in the stairwell 5 m away (slow drifts, static offset), see Fig. 3.17, and drifts of residual magnetization of steel components of and around the chamber.

As a first counter-measure to external magnetic field noise power supplies, amplifiers and supply line cables were placed as far away as possible from the vacuum chamber. Secondly, a magnetic field stabilization has been implemented into the experimental setup. It includes a self-built magnetic field stabilization

---

[33] *Keysight* 34410A.

[34] The earth magnetic field at PTB is continuously measured inside a small wooden hut. In December 2021 it was ≈ 49 571 nT ± 13 nT. Even though earth's magnet field is decreasing, in central Europe the magnetic field grows by 28 nT/yr (Harcken, n.d.).

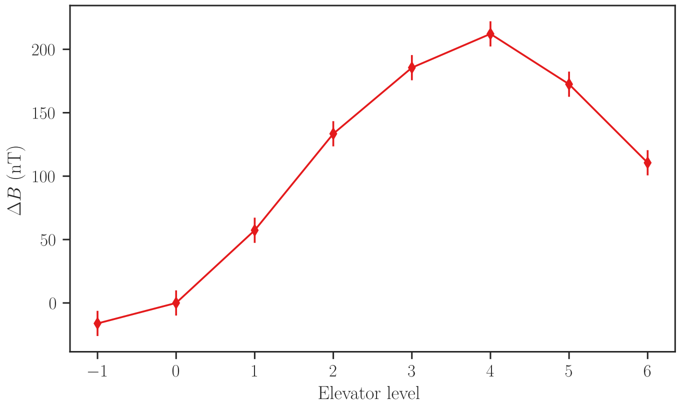

Figure 3.17: Magnetic field variation caused by the elevator as seen by the ion, probed by a change in the $^{40}\mathrm{Ca}^{+}$ $\mathrm{S}_{1/2}$, $m = -1/2 \leftrightarrow \mathrm{D}_{5/2}$, $m = 3/2$ transition frequency.

unit[35] which accepts input voltages in the range from −10 to 10 V from up to two magnetic field sensors[36] with a sensitivity of 0.04 V/μT. This unit allows for arbitrary mixing of both sensor signals for optimization of the transfer function between magnetic fields seen by ions and sensors. However, because of geometrical reasons in most experiments described here, only one sensor was used. It was placed as close to the ion as possible, usually on top of the chamber, centered along the quantization direction at $z = 0$ and $x = 8$ cm. Three dc voltage setpoints for the stabilization unit are provided by the experimental control's dc voltage outputs, which form the reference for a PID. The error signal is minimized by feeding back to three square compensation coil pairs with a side length of 60 cm and three windings of 1 mm thick copper wire, surrounding the chamber and the vacuum system. By measuring the magnetic field with an out-of-loop magnetic field sensor of similar type, a reduction of magnetic field noise up to a bandwidth of 500 Hz was measured using an electronic FFT. The noise peak at 50 Hz is reduced by at least 10 dB.

The achieved magnetic field stability on the ion is explored in Ch. 5.2.

3.8 Experimental Control System

The various laser sources brought to interact with the trapped ions or used for ionization have to be tuned in frequency and power rapidly and synchronously. This is accomplished by an experimental control system, which is driven by a software package called QFP. It comprises a field programmable gate array (FPGA)[37] clocked at 100 MHz, a *Python*-based sequencer and a *LabView* user front end. Together they control 16 direct digital synthesis (DDS) frequency sources, 32 TTL outputs, a PMT counter and a series of analogue voltage output ports, joint together in single rack device, called Paul's box. The experimental control system was developed at MIT and the University of Innsbruck (Pham, 2005; Schindler, 2008) and has been upgraded to control also the high voltage sources for the dc endcap and compensation electrodes, the current sources

---

[35] Designed and built by Tjeerd Pinkert and Nicolai Beev.

[36] *Sensys* three-axis fluxgate Sensor FGM3D/250, 2 kHz bandwidth.

[37] Altera Cyclone 1

for the quantization magnetic field coils (Wübbena, 2014), the 729 nm fiber switch and magnetic field stabilization unit.

The internal FPGA clock and DDS are referenced to a 10 MHz signal generated by an H-maser which is part of the SI-second infrastructure at PTB. The Paul's Box DDS chips[38] are clocked at 800 MHz and have a frequency resolution of ≈ 0.2 Hz because of a 32-bit phase register.

In the near future we plan to switch the experimental control system to *ARTIQ* which offers next to other advantages more sophisticated possibilities to implement the needed feedback from the clock interrogation onto the clock laser frequency.

There are also stand-alone[39] DDS implemented in the setup, which are used as static and stable RF frequency sources. They are referenced to the 10 MHz-H-maser signal as well. Their clock frequency is at 400 MHz and they feature a frequency resolution of 1.42 µHz.

---

[38] AD9910.

[39] Based on the DDS designs version 1.7 (2013), version 1.8.2 (2017) and version 44AH_0021_21 (2019) of department 4 at PTB Braunschweig.

4 Laser System

In the context of optical clocks lasers play a fundamental role, not only as local oscillator (LO) of the clock, but also as a tool for generating, preparing and detection of the clock's atomic reference. We have in total eleven laser systems in our laboratory distributed over several partially closed breadboards, which provide protection against temperature and air pressure fluctuations and dust, while at the same time ensuring laser safety. In Fig. 4.2 a map of the breadboards is shown. Excluding the frequency comb the experiment includes seven frequency doubling stages. Tab. 4.1 lists the used laser wavelengths and their application in the experiment. Most of the lasers are send to the trap center where they either interact with the $^{27}\mathrm{Al}^{+}$ or $^{40}\mathrm{Ca}^{+}$ ion, or with their neutral counterparts for photo-ionization, see Fig. 4.1

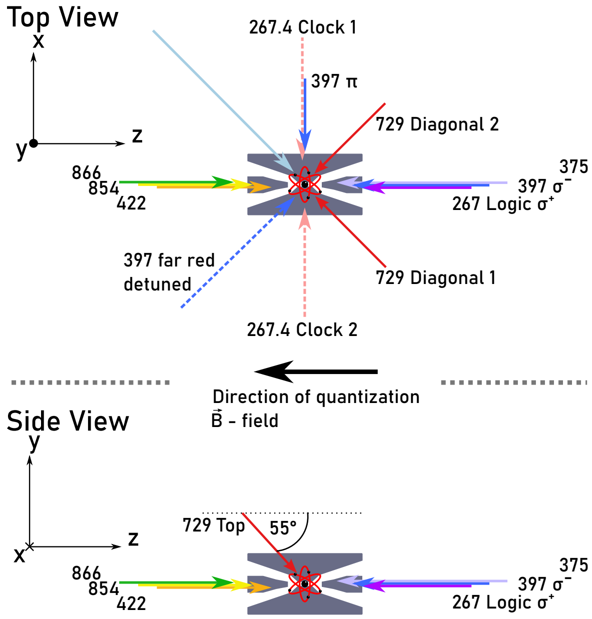

Figure 4.1: Laser beams impinging onto the trap center.

In this chapter the laser setups are described. For better readability these are simplified; more detailed drawings can be found in the appendix Ch. C. Throughout, reoccurring symbols are used in the drawings. They are listed in Fig. 4.3.

The chapter begins with general remarks on frequency doubling (Ch. 4.1), acousto-optical modulator (AOM) setups and intensity stabilization (Ch. 4.2), the frequency comb (Ch. 4.3), the transfer-lock technique (Ch. 4.4) and fiber noise cancellation (FNC) (Ch. 4.5). It then continues with presenting the laser breadboards of the $^{40}\mathrm{Ca}^{+}$ lasers, followed by the $^{27}\mathrm{Al}^{+}$ lasers.

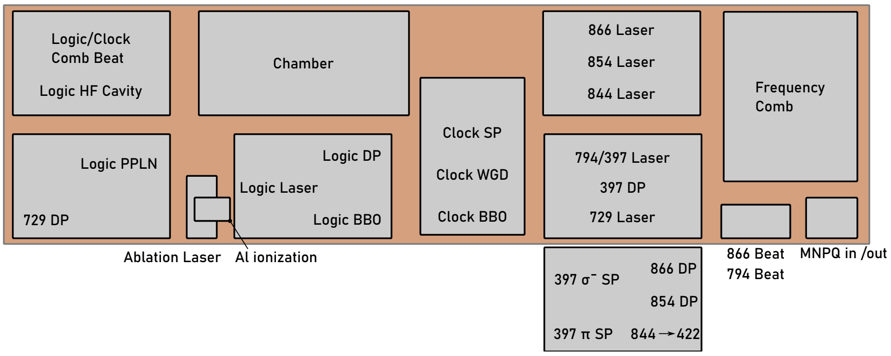

Figure 4.2: Map of optical breadboards. HF Cavity: High-Finesse cavity, SP: AOM single-pass, DP: AOM double-pass, WGD: waveguide doubler, BBO and PPLN: doubling cavities. The breadboard on the bottom side is mounted into a drawer system above the breadboard that is drawn on the top side of the respective breadboard, because of spatial constraints. The ablation laser is mounted on top of three posts with the Al ionization laser placed below.

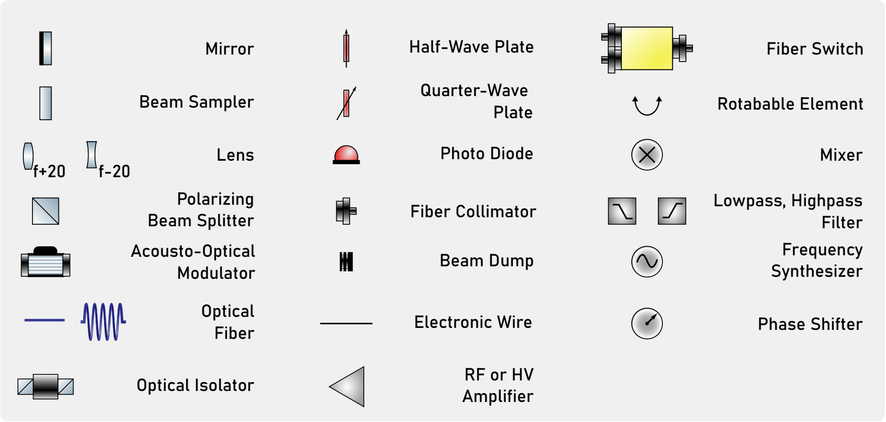

Figure 4.3: Used symbols in laser breadboard sketches (Franzen, n.d.). The annotation next to a lens is its focus distance in mm.

Table 4.1: Used Laser sources. Laser frequency observation by wavemeter (Wm) and/or frequency comb (Co). Applied second harmonic generations (SHGs): a) Monolithic bow-tie cavity (Hannig, 2018; Hannig et al., 2018), b) waveguide doubler (WGD) from *NTT*, c) single-pass provided by *Amplitude*, d) free-space bow-tie cavity (Wübbena, 2011; Wübbena, 2014), e) bow-tie cavity provided by *Toptica*. f) single-pass provided by *Menlo*.

λ (nm)	λ (nm) / SHG 1	λ (nm) / SHG 2	Application
1068[Wm,Co]	534 / PPLN[a]	267 / BBO[a]	^{27}Al^{+} logic
1069.6[Wm,Co]	534.8 / WGD[b]	267.4 / BBO[a]	^{27}Al^{+} clock
1064	532 / KTP[c]		Ca and Al ablation
866[Wm,Co]			^{40}Ca^{+} repumper
854[Wm]			^{40}Ca^{+} clear out
844[Wm]	422 / PPKTP[d]		Ca ionization resonant
794[Wm,Co]	397 / LBO[e]		^{40}Ca^{+} Doppler & EIT cooling, detection
729[Wm,Co]			^{40}Ca^{+} logic
395[Wm]			Al ionization resonant and into continuum
375			Ca ionization into continuum
1069, 1542	854, 866, 729, 794 / PPLN[f]		Frequency comb outputs
1542			MNPQ laser

4.1 Remarks on Frequency Doubling

Lacking availability of reliable and/or high power laser sources at the target frequencies in the UV make frequency doubling steps by SHG necessary. Additionally, the given frequency comb's output port frequencies require the $^{27}\mathrm{Al}^{+}$ logic and clock laser, and the $^{40}\mathrm{Ca}^{+}$ 397 nm laser to provide light in the infrared. The beat notes between the lasers and the frequency comb are required for transfer-locking and frequency comparisons. The ablation laser is frequency doubled[1] to the green, because of laser safety and alignment convenience.

Since SHG is a non-linear process, high laser intensities are needed in the crystals mentioned in the caption of Tab. 4.1 for high conversion efficiency. Therefore, the inputs of the doubling devices are usually amplified by tapered ampflifiers (TAs) or fiber amplifiers beforehand. The doubling crystals for the $^{27}\mathrm{Al}^{+}$ logic, the $^{27}\mathrm{Al}^{+}$ clock, the resonant Ca ionization and the $^{40}\mathrm{Ca}^{+}$ Doppler cooling laser are placed in the focus position of a bow-tie cavity. The cavity-lengths are stabilized in the case of the $^{27}\mathrm{Al}^{+}$ lasers by a Hänsch-Couillaud (HC) (Hänsch and Couillaud, 1980) and in all other case by Pound-Drever-Hall (PDH) (Drever et al., 1983; Black, 2001) locking scheme. The power enhancement in the cavity enables increased doubling efficiency compared to single-pass doubling. The BBO bow-tie cavities are flooded with clean oxygen[2], slightly above room pressure, and are temperature stabilized (Hannig, 2018; Hannig et al., 2018). This prevents UV-laser induced degradation of the BBO crystals (Sandberg, 1993).

4.2 Remarks on AOM setups and Intensity Stabilization

Within an experimental sequence, the lasers have to be turned on and off; their intensity steered; and their frequency tuned with <µs time resolution. All these tasks are accomplished by the usage of AOMs, which are controlled by the experimental control system described in Ch. 3.8. Laser beams in this experiment usually travel the AOM twice in double-pass (DP) setups, using the deflected AOM order there and back (Donley et al., 2019). This has the advantage that turning the AOM off results in a very high suppression of unwanted laser radiation, when properly blocking the non-deflected 0th order. Furthermore, frequency tuning does not change the position or angle of the output beam, in contrast to single-pass AOMs.

Intensity stabilization of the pulsed laser radiation is accomplished in a sample-and-hold fashion, where the beam intensity is sampled for typically 50 to 100 µs and an error signal is fed back onto the RF power of the respective AOM. The feedback signal is generated digitally and kept constant for the rest of the cycle, thus stabilizing the laser intensity for drifts between experimental cycles.

---

[1] Single-pass doubling using a potassium titanyl phosphate (KTP) crystal.

[2] Oxygen 5.0.

4.3 The Frequency Comb

Frequency combs are essential tools for the operation of optical clocks. In our setup we use a frequency comb for slow feedback by applying a transfer oscillator stabilization scheme, see Ch. 4.4, and for frequency measurements. Where required, the lasers are phase-stabilized via the frequency comb to an ultra-stable laser at 1542 nm, internally called MNPQ laser, residing in Paschen building at PTB. Its light is brought to the laboratory by a noise-canceled fiber using a multi-point extraction setup (Grosche, 2014). Furthermore, this and other frequency combs at PTB from the infrastructure for frequency comparisons between different lasers across the PTB campus.

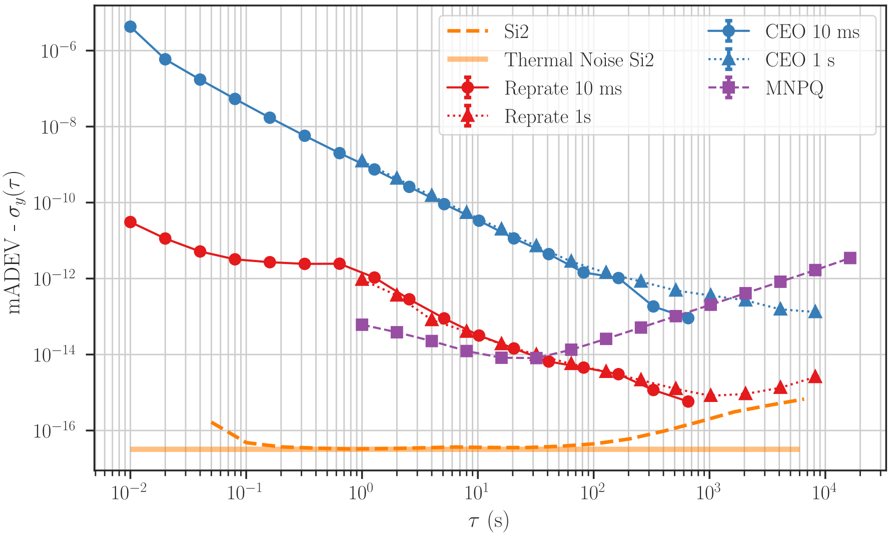

Figure 4.4: Statistical uncertainties as modified Allan deviations. The repetition rate (red, normalized to ≈ 1 GHz) is stabilized to the MNPQ laser (violet, normalized to 194.4 THz). The latter starts to drift at 20 s. This drift, measured versus the Si-cavity (orange, normalized to 194.4 THz), is subtracted electronically before stabilization of the repetition rate. The CEO frequency (blue, normalized to 40 MHz) is locked to a hydrogen maser signal. It should be noted, that only the absolute stability of the CEO signal is important, since it enters additive into the beat note of a laser with the frequency comb. The blue and red curves are both from two datasets with 10 ms (circles) and 1 s (triangles) Λ-averaged counter periods, see Ref. (Benkler, Lisdat, and Sterr, 2015).

The frequency comb[3] is a modelocked fs-pulse laser. It incorporates several Er^{3+}-doped fiber amplifiers and has output ports as given in Tab. 4.1. A built-in $f - 2f$ interferometer measures the CEO frequency at $\nu_{\mathrm{CEO}} = 40\,\mathrm{MHz}$, which is then stabilized to a 10 MHz signal derived from a hydrogen maser[4] by applying feedback onto the frequency comb's pump current. The repetition rate is at $\nu_{\mathrm{rep}} = 250.035\,136\,\mathrm{MHz}$ and is phase-locked to the MNPQ laser by feeding back onto the the comb's intracavity electro opitcal modulator (EOM) and piezo that is tuning the frequency comb's cavity length by moving a mirror.

---

[3] Optical Frequency Synthesizer FC1500-250-WG with intracavity EOM from *MenloSystems GmbH*.

[4] Maser H9 at PTB, which is steered by a Cs fountain clock on a daily basis, thus providing a SI second-derived wall plug signal to our laboratory.

The drift of the MNPQ laser against another more stable laser is subtracted in our laboratory electronically. The latter laser is stabilized to a Si-cavity at 124 K with a thermal noise limit of 3.2e-17 (Matei et al., 2017).

In Fig. 4.4 the achieved stabilities of the 4th comb tooth at $\approx$ 1 GHz, the CEO frequency and the MNPQ laser without drift correction is shown[5]. It is planned to upgrade the repetition rate stabilization by phase-locking it directly to the Si-cavity stabilized laser because of its superior stability.

4.4 Transfer-Lock

Coherent laser operations on the trapped ions require the lasers to be phase-stable over the period of the interaction time in Rabi and the dark time in Ramsey interrogations. Phase-noise with up to a few MHz offset from the applied frequency introduces decoherence, loss of SNR in the excitation probability, off-resonant excitation and frequency noise on the measured clock frequency. The clock laser has the highest demands on a narrow laser linewidth around the carrier frequency and is negligibly influenced by noise in the MHz range. In contrast to this, coherent operations with short (~µs) and higher power laser pulses, such as required for QL, have lower demands on the absolute carrier linewidth, but are negatively influenced by high-frequency laser noise. These noise contributions cause incoherent carrier excitation when driving sideband transitions, diminishing the quality of the coherent operations. Therefore, high frequency noise has to be suppressed in the $^{40}\mathrm{Ca}^+$ and $^{27}\mathrm{Al}^+$ logic lasers. When using double bright EIT cooling, the 866 nm and 397 nm lasers have to be only coherent, i.e., phase-stable to each other. For this reason it is possible to apply single EIT cooling on $^{40}\mathrm{Ca}^+$ using only a wavemeter frequency lock for the 397 nm laser, as long both EIT beams are derived from the same laser.

We use the frequency comb for stability transfer of a stable laser 2, see Fig. 4.5, to a pre-stabilized laser 1. Even though the repetition rate ν_{rep} and CEO frequency ν_{CEO} are phase-locked to the MNPQ laser and to a hydrogen maser respectively, a transfer-oscillator-locking scheme (Stenger et al., 2002; Scharnhorst et al., 2015) is applied. This stabilization scheme is implemented because the fiber comb exhibits residual noise contributions due to a limited locking feedback bandwidth. The short photon lifetime of the comb's cavity is related to increased amplified spontaneous emission noise, causing pulse time jitter in the laser pulses (Bao et al., 2014; Scharnhorst et al., 2015).

The main idea of the transfer-oscillator scheme is to generate a virtual beat which is free of the comb's parameters and thus immune to noise on these. Considering two lasers with frequencies ν_1 and ν_2 in beat note measurements with respective frequency comb outputs, the laser frequencies can be written as

$$\nu_1 = \nu_{\mathrm{CEO}} + n_1 \nu_{\mathrm{rep}} + \Delta\nu_1 \tag{4.1}$$

$$\nu_2 = \nu_{\mathrm{CEO}} + n_2 \nu_{\mathrm{rep}} + \Delta\nu_2 \ , \tag{4.2}$$

---

[5] MNPQ and Si data provided by department 4 at PTB.

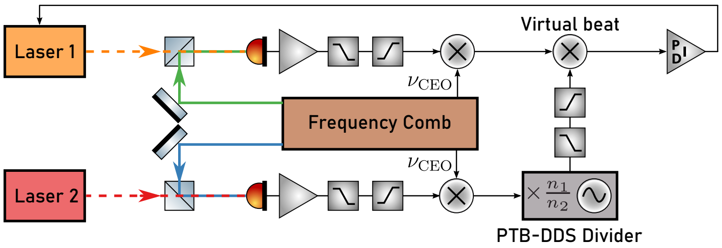

Figure 4.5: Transfer lock scheme. The colored laser beams generate beat note signals on photo-diodes which are processed by amplifiers and passive low- and high-pass filters. Laser 1 is then stabilized to laser 2 by a PID using the comb-free virtual beat.

where n_1 and n_2 are the integer numbers which specify the frequency comb's tooth generating the beat note frequencies $\Delta\nu_1$ and $\Delta\nu_2$, e.g. the difference frequency between laser and respective comb tooth.

In a first step, ν_{CEO}, available as an RF frequency, is subtracted from the beat notes using an electronic mixer and appropriate low-pass filters

$$\nu_1 = n_1 \nu_{\mathrm{rep}} + \Delta\nu_1 \tag{4.3}$$

$$\nu_2 = n_2 \nu_{\mathrm{rep}} + \Delta\nu_2 \ . \tag{4.4}$$

The CEO-free beat note from the stable laser 2 is further processed in a DDS whose output signal contains the input signal multiplied by a factor that is programmed[6] to be the comb tooth ratio n_1/n_2. This gives $\nu_2 = \frac{n_1}{n_2}(n_2\nu_{\mathrm{rep}}+\Delta\nu_2)$ which after sum/difference frequency generation with ν_1 in another mixer and electronic filtering results in the virtual beat

$$\nu_{\text{virt. beat}} = \Delta\nu_1 - \frac{n_1}{n_2}\Delta\nu_2 \ . \tag{4.5}$$

This virtual beat is free of comb parameters and is used to directly transfer the superior stability of laser 2 to laser 1 using a PID to generate feedback signals for example on laser current and/or laser diode grating.

The time required for signal processing and other phase delays reduce the achievable servo bandwidth. Typically, passive electronic attenuators and low and high-pass filters introduce substantial phase delays, in particular when used near the edges of their bandwidth. On the other hand, these are needed for removing unwanted frequency contributions naturally emerging from the mixing processes and especially at the output of the divider DDS. In order to subtract the frequency comb as well as possible, the virtual beat note must be generated in a phase coherent way, i.e., subtracting ν_{CEO} and ν_{rep} at the same phase in both signal paths. Therefore, additional delay lines have to be a implemented to synchronize the phase, which further diminishes the servo bandwidth.

However, frequency ratios of two lasers can be measured with relative uncertainties below 1×10^{-18} for averaging times of 100 s (Stenger et al., 2002). A high-bandwidth stability transfer to ion interrogating lasers in our

---

[6] The DDS is programmed to a frequency tuning word which approximates n_1/n_2 by $i/2^m$ where i is an integer and m the bit length of the tuning word. DDS devices in our laboratory have a bit length of $m = 48$ Bit and thus the error made by this approximation is negligible.

experiment have been proven in Ref. (Scharnhorst et al., 2015), where noise due to fluctuations in the repetition rate frequency of the frequency comb was canceled up to 3 dB within 1.8 MHz of the laser carrier frequency. This lead to a suppression of noise up to 200 kHz compared to the free-running external cavity diode laser (ECDL).

4.5 Fiber Noise Cancellation

Optical path length variations are induced by vibrations and thermal fluctuations on mirrors and optical fibers. They cause phase noise on the laser signal with bandwidths in the kHz range. Because this is slow compared to the phase evolution of the light, the accumulated phase noise can be suppressed by a path length stabilization setup. Several types of such fibre noise cancellation (FNC) setups exist, offering multi-point extraction (Grosche, 2014) or hundreds of km-long noise cancellation by bi-directional coherent signal amplification (Terra, Grosche, and Schnatz, 2010).

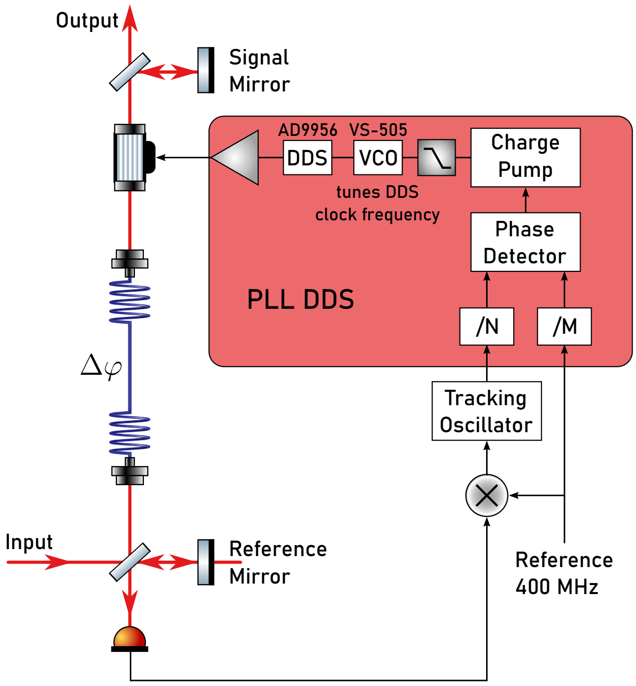

Figure 4.6: Fiber-noise cancellation setup using a phase-locked loop (PLL) DDS.

Owing to the short distances in this experiment, a simpler approach is implemented, which is sketched in Fig. 4.6. There, a heterodyne beat frequency is generated by reflecting the light at two signal/reference mirrors: One at a reference point near to the photo diode, the other at the far end of the path. The portion of light that is reflected by the far end mirror travels the path and the AOM twice, thus accumulating a phase noise amplitude of $2\Delta\varphi$ and a frequency offset of twice the AOM frequency. The beat frequency is mixed by a stable RF reference and tracked by a tracking oscillator. Its output and the reference signal are then fed into a PLL DDS. Both input frequencies can be divided by integer numbers to give the same frequency. Any phase deviation between the frequencies is detected in a phase detector and a voltage proportional to the difference is generated in a charge pump. The filtered output of the charge pump steers the clock frequency of a DDS by a voltage controlled oscillator (VCO). The corrected frequency is finally amplified and used as drive frequency for the AOM, closing the loop.

4.6 Chamber Breadboard

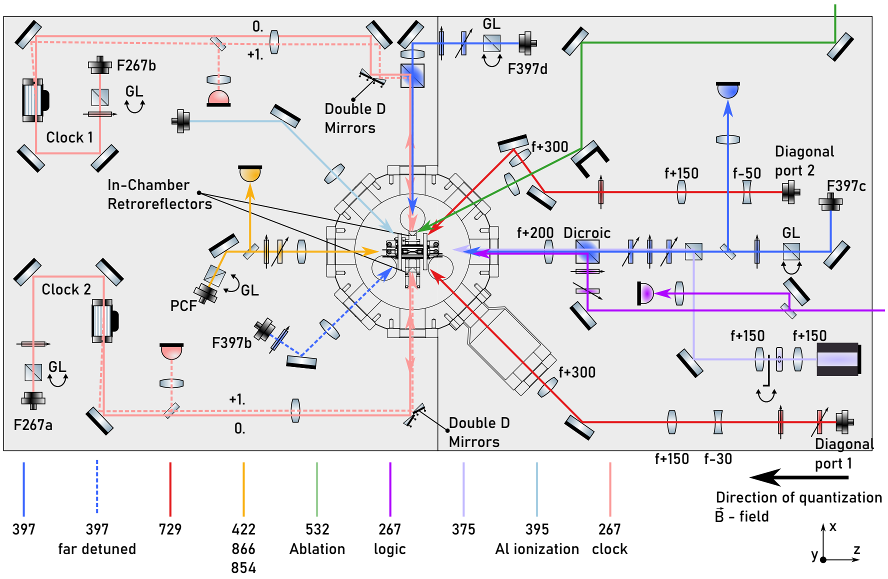

Figure 4.7: Chamber Breadboard. A description of the symbols can be found in Fig. 4.3. The 729 nm top port is shown in Fig. 4.9.

Laser beams are brought by free-space and fiber optics to the chamber breadboard, which is mounted 21.2(1) cm above the optical table. In Fig. 4.7 an overview of the chamber and all laser beams nearby is shown, with the exception of the 729 nm top port which is depicted in Fig. 4.9. All of them impinge on the ions in the trap center inside the vacuum chamber, except for the ablation laser (Ch. 3.6.2) which is focused onto the ablation targets. The latter is mounted in one of the holes in the sapphire disc of the trap.

4.7 ^{40}Ca^{+} Doppler Cooling, Repumper, Clear Out and Ionization Laser System

In Fig. 4.8 the ^{40}Ca^{+} lasers for state preparation and detection are shown. They include the lasers for ^{40}Ca^{+} ionization - 375 nm and 422 nm, Doppler cooling and detection - 397 nm, repumper - 866 nm, and clear-out - 854 nm.

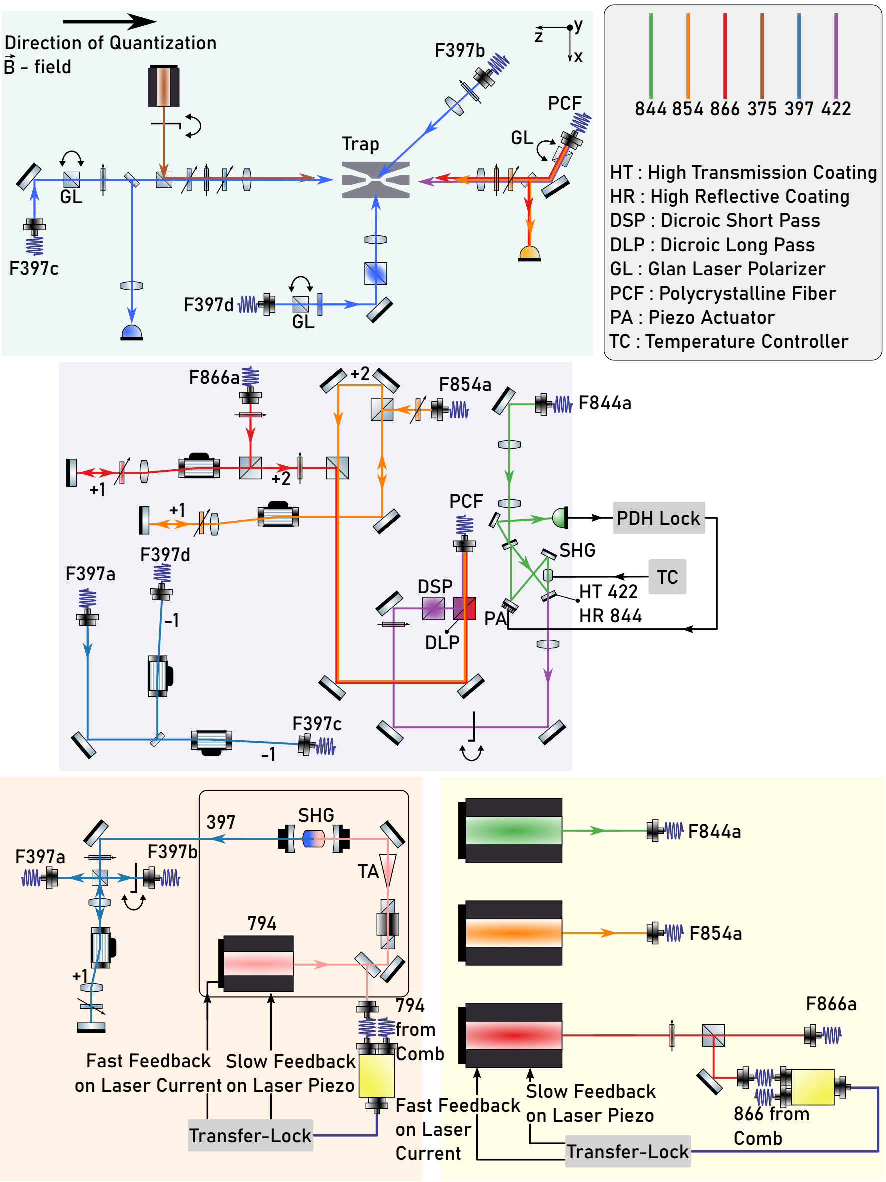

Figure 4.8: Simplified ^{40}Ca^{+} Doppler and ionization laser setup. The breadboard in the top is the chamber breadboard. Fiber collimators with the same name are connected by a PM fiber.

The ionization lasers are comprised of a frequency-doubled 844 nm ECDL[7] and a heated UV laser diode[8] at 375 nm. A mechanical shutter opens the beam path for ionization purposes.

While the 375 nm diode is directly mounted onto the chamber breadboard and overlapped with the axial 397 nm beam, the 844 nm laser is placed on the same breadboard as the 854 nm[9] and 866 nm[10] ECDLs. From there the laser outputs are brought by polarization maintaining (PM) fibers to an AOM breadboard. Here a PDH-locked free-space bow-tie cavity with a periodically poled potassium titanyl phosphate (PPKTP) crystal, heated to 77.0(5) °C [11] for non-critical phase-matching, doubles the laser frequency from 844 nm to 422 nm (Wübbena, 2011). Residual pump light at 844 nm at the output is removed by a dicroic mirror, passes a mechanical shutter, and is overlapped with the 854 nm and 866 nm laser beams before entering a photonic-crystal fiber (PCF).

The 854 nm and 866 nm beams on this breadboard both pass a DP AOM setup where the $2 \times (+1^{\text{st}})$ order is used and all other AOM orders are dumped. On the chamber breadboard all three beams counterpropagate the axial 397 nm beam. A beam sampler deflects a few hundred µW onto a photo-diode whose signal is used for intensity stabilization of the 854 nm and 866 nm beam in front of the chamber.

While the 844 nm and 854 nm frequency is only observed on the wavemeter[12], the 866 nm laser is stabilized by a transfer-lock scheme, see Ch. 4.4, enabling double bright EIT cooling (Scharnhorst et al., 2018).

The cooling and detection laser at 397 nm is a frequency-doubled ECDL[13] at 794 nm on the lower left breadboard in Fig. 4.8. It comprises a built-in TA with ≈1.2 W output power and a SHG stage. The doubling cavity is phase-locked using a PDH lock scheme.

A few mW of fundamental light at 794 nm before TA amplification are used to stabilize the laser by transfer-locking it to the MNPQ laser, see Ch. 4.4.

About 120(10) mW at 397 nm leaves the laser head and is split by a Glan-Laser polarizer into two paths. Most of the light is transmitted into a DP AOM[14] setup which gives the $2 \times (+1^{\text{st}})$ order. The reflection of the Glan-Laser of a few mW that is not entering the DP AOM and is therefore about 9 linedwidths red detuned to the Doppler-cooling transition[15]. This portion is fed into a PM fiber and brought to the chamber, where it serves as far-red detuned helper cooling beam, impinging onto the ^{40}Ca$^+$ ion from a diagonal direction.

The part of the light that went through the DP AOM is sent to the AOM breadboard in the center of Fig. 4.8. Here, the light is split into two equal parts and goes through individual single-pass (SP) AOM setups. The -1^{st} order of each beam is sent to the chamber breadboard, where the axial 397 nm

---

[7] *Toptica* DL Pro.

[8] NDU1113E from *NICHIA* mounted into a *Thorlabs* LDM21 controller.

[9] *Toptica* DL Pro.

[10] *Toptica* DL Pro.

[11] PT100 resistance 129.49 Ω.

[12] *High Finesse WS7*, resolution 10 MHz.

[13] *Toptica* TA SHG Pro.

[14] Usually run between 170 to 200 MHz.

[15] The unshifted 397 nm laser frequency is about 180 MHz red detuned from resonance, which has a linewidth of $\approx 2\pi \times 20$ MHz.

beam constitutes a σ^--polarized beam[16], mainly used for optical pumping (state preparation) into the $^2\mathrm{S}_{1/2}$, $m = -1/2$ ground-state and axial cooling. The radial beam is cleaned to linear polarization with the polarization vector pointing in axial direction, thus constituting a π-polarized beam, predominantly used for state detection and radial Doppler cooling.

The combination of a shared blue-detuned DP AOM and two individual SP AOM allows for two modes of operation. In both modes the π beam's SP AOM is fixed to 194 MHz and tuned via the DP AOM to the target frequency. The σ^- beam is tuned individually by it's SP AOM in a range of 0 to 4 MHz. In the first mode, the DP AOM is run at around 170 MHz which results in a total red-detuning of around one half linewidth away from resonance. This setting is used for Doppler cooling, optical pumping and detection. In the second mode, the DP AOM frequency is tuned to higher values shifting the laser frequencies to large blue detunings needed for EIT cooling. Maximum blue detunings of 5 to 6 linewidths can in principle be reached. The EIT cooling performance stability is dependent on stable laser power. Therefore, the 397 nm π- and σ^--polarized beams are intensity stabilized as well. For details on EIT cooling see Ch. 5.5.

The alignment of the axial 397 nm beam can be performed with high precision because the light must pass the two axial endcap electrode pinholes on the ion side of 0.5 mm diameter and have 5 mm minimal distance. The entrances of the endcap tips on the outer side have a diameter of 1.1 mm and a distance of 59.6 mm. The waist of the axial 397 nm beam before passing the $f = 200\,\mathrm{mm}$ focusing lens in front of the chamber is measured to be 915 µm. Thus at the center spot of the trap, the beam is focused to a waist of $w = 28\,\mu\mathrm{m}$. Simple geometrical considerations and the fact that misalignment causes measurable background scattering on the PMT, which is not apparent, constrain the angle between trap axis and 397 nm σ beam to be not bigger than 0.8°. The radial 397 nm beam is threaded through 2 mm wide holes in the in-chamber aluminum retroreflectors (Ch. 4.10) and vertically through the RF blades of the trap. Therefore it is constrained in the vertical direction to ±1° [17].

4.8 729 nm Laser

The $^{40}\mathrm{Ca}^+$ logic laser for driving $^2\mathrm{S}_{1/2} \leftrightarrow {}^2\mathrm{D}_{5/2}$ carrier and sideband transitions is an ECDL[18] at 729 nm with a TA that provides 190(10) mW output power. The laser head is located on the same breadboard as the 794 nm/397 nm laser. The layout is displayed in Fig. 4.9. A PM fiber guides the main part of the laser radiation to the double pass AOM breadboard where the $2 \times (+1^{\mathrm{st}})$ order is distributed by a fiber switch with up to three used fiber ports[19] around the chamber. Here, the light's polarization is cleaned, rotated and the beam is focused onto the $^{40}\mathrm{Ca}^+$ ion from two diagonal directions in the chamber's

---

[16] The magnetic field is oriented along the axial direction.

[17] $\tan\alpha = \frac{4\,\mathrm{mm}}{212\,\mathrm{mm}}$.

[18] *Toptica* TA 100.

[19] The fourth port is not used.

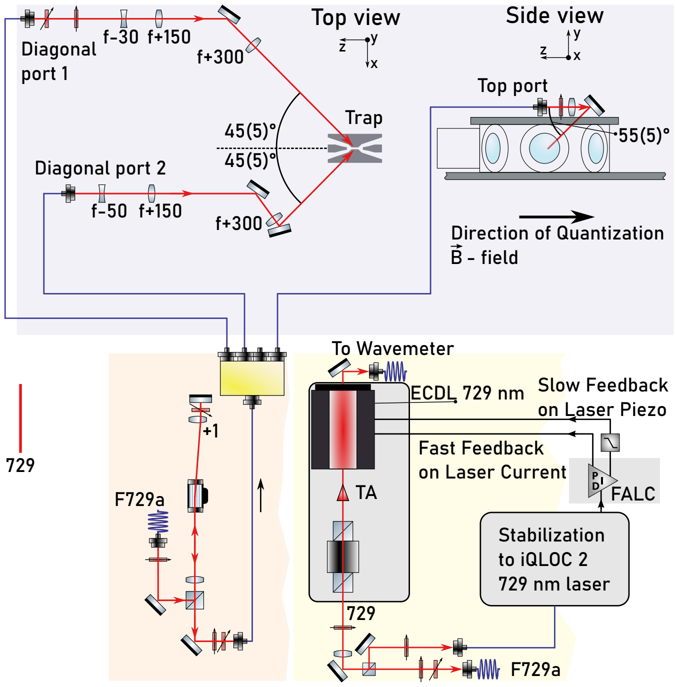

Figure 4.9: $^{40}\mathrm{Ca}^+$ logic laser at 729 nm. The orientation angles of the three laser ports at the chamber can be measured more precisely (Ch. 5.3), but due to occasional optimizing of beam pointing on the ion, a conservative estimate is assumed for the measurements, e.g. the evaluation of the excess micromotion (EMM) shift (Ch. 7.2).

horizontal plane and from a top port, which is mounted on a small breadboard on top of the chamber.

At the back-side of the laser head a few mW of 729 nm light is sent to the wavemeter. Next to the fiber coupler, which brings the main part of the laser light to the DP AOM breadboard, a 2nd fiber guides light to the frequency comb breadboard. Here, two options for phase-locking the laser are available.

Firstly, a beat note with the appropriate frequency comb's output can be used for a transfer lock onto the MNPQ laser/Si-cavity. However, when applying short laser pulses on motional sideband transitions, residual fast laser noise and locking servo bumps at Fourier frequencies around 1 to 2.5 MHz cause off-resonant carrier excitation, which reduces the achievable contrast.

Therefore, most experiments in this thesis use a second option, for which 729 nm light from a neighboring experiment provides another flexible stabilization option. This 729 nm laser system can either be tightly locked onto a high-finesse cavity by a PDH locking scheme using EOM generated sidebands at 12.4 MHz, or by an injection lock using the transmission of this cavity as seed for the TA of this laser. Either option provides a fiber-length stabilized frequency reference profiting from the fast-feedback with superior locking bandwidth of 1.5 MHz compared to the transfer lock of the iQLOC 1 laser onto the MNPQ/Si-cavity system. The three available 729 nm laser ports have no intensity or fiber-length stabilization.

4.9 $^{27}\mathrm{Al}^{+}$ Logic Laser

The laser for $^{27}\mathrm{Al}^{+}$ state preparation and $^{27}\mathrm{Al}^{+}$ QL operations is an ECDL[20] at 1069 nm, which gets frequency doubled twice to 267 nm. The laser setup is shown in Fig. 4.10.

The laser output on the lower right breadboard passes two 30 dB Faraday isolators, before entering a three port fiber coupling setup. The first coupler is seeding a fiber amplifier[21], which amplifies the signal from 5 to 10 mW to a typical output of 600 mW. The amplified light is sent to a SHG cavity using a periodically poled lithium niobate (PPLN) crystal as the non-linear medium. The other two fiber ports deliver light to a wavemeter and to the frequency reference breadboard in the upper-left of Fig. 4.10.

The PDH locking technique[22] is used to pre-stabilize the $^{27}\mathrm{Al}^{+}$ logic laser to a high-finesse cavity, in order to ensure high contrast in QL protocols. It consists of two concave mirrors[23] with radii of curvature of $R = 1000\,\mathrm{mm}$ and $R = 200\,\mathrm{mm}$, optically contacted onto a 100 mm long ultra-low expansion (ULE) spacer. The cavity is placed inside a vacuum chamber, where an ion pump maintains a pressure of about 10 µPa. Thermal isolation is accomplished by wrapping the vacuum chamber in styrofoam[24]. We infer a finesse of the cavity of $F \approx 350\,000$, see Fig. 4.11, by turning off the AOM in front of the cavity and observing the transmission of the cavity on a photo diode (cavity ring-down measurement). The free spectral range (FSR) of the cavity is

$$\mathrm{FSR} = \frac{c}{2L} \approx 1.5\,\mathrm{GHz}\,. \tag{4.6}$$

The half-width of one cavity resonance is given by $\mathrm{FSR}/F \approx 4\,\mathrm{kHz}$. The resonance frequency is coarsely tuned by two cooling Peltier elements at $T \approx 12.5\,^{\circ}\mathrm{C}$ mounted on the outside of the vacuum chamber of the cavity[25]. The increased frequency drift by operating the cavity not near the temperature of minimum thermal expansion at 20 °C is not limiting the performance of the laser due to the implemented transfer lock, which removes drifts.

This is implemented via a beat note with a frequency comb output at 1069 nm, which generates a virtual beat mixed down to dc to produce an error signal which is used as input for a Red Pitaya PID[26]. There a feedback signal in the range of 0 to 3.3 V is synthesized, which is brought to a customized DDS[27], called VCO DDS. Inside the DDS, a VCO chip[28] provides a 400 MHz clock signal. The feedback signal derived from the Red Pitaya is then used to tune this VCO within a range of ≈ ±100 kHz. By changing the clock frequency, the programmed output frequency of the DDS is tuned as well, with the tuning

---

[20] *Toptica* DL Pro.

[21] *NKT* Boostik.

[22] *Toptica* PDD 100 modulates the laser current at 20 MHz.

[23] Fused Silica substrate mirrors with coatings from *ATFilms*. Reflectivity ≥ 99.9985 % at 1070 nm.

[24] An inner heat shield is available but was not built into the chamber, because of production delays.

[25] Measured by thermistor resistance 17.194 kΩ.

[26] Customized device based on the Red Pitaya by *STEMLab* (Fenske, 2015).

[27] DDS chip AD9956.

[28] VS-505.

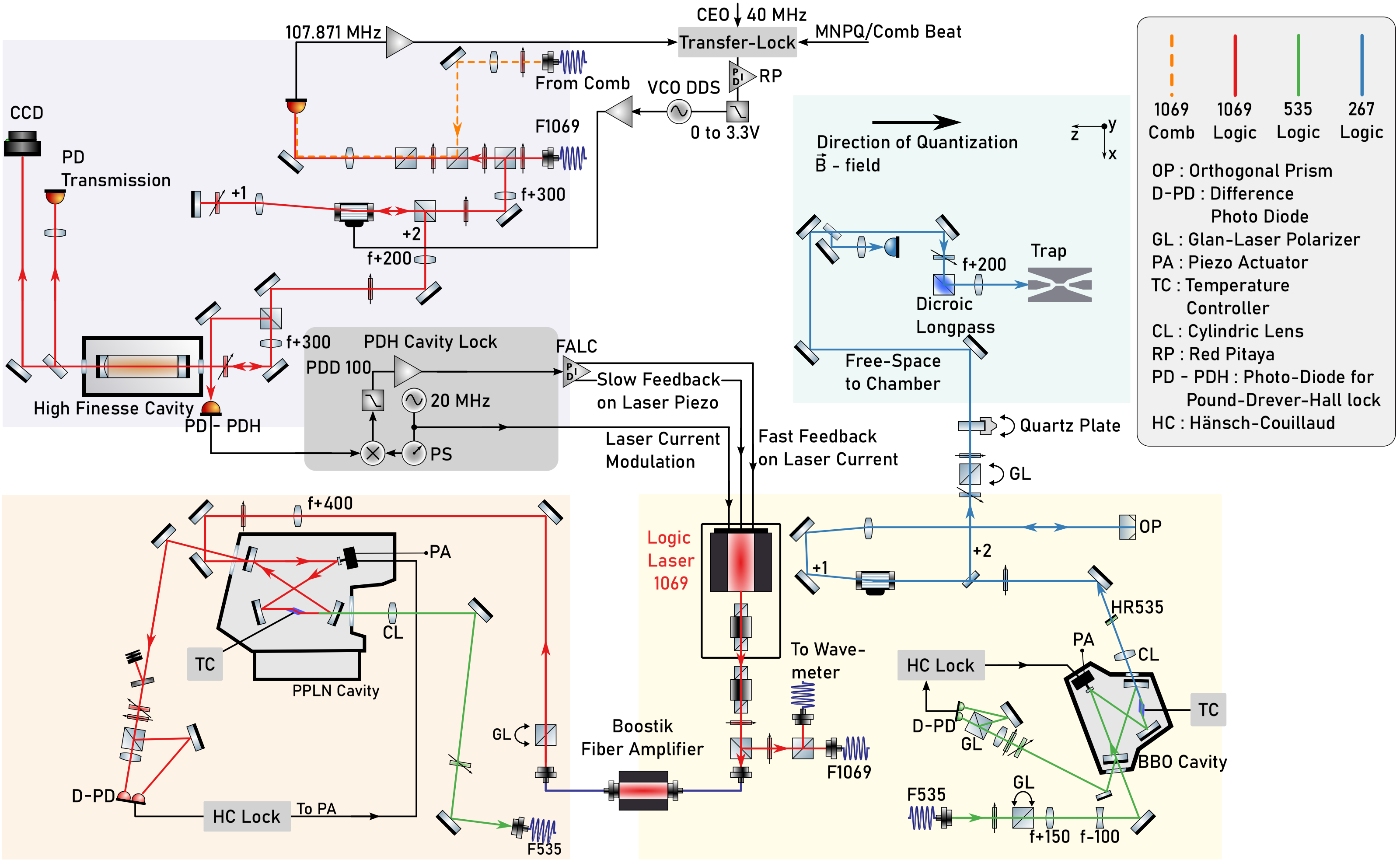

Figure 4.10: Simplified ^{27}Al^{+} logic laser setup. The ECDL laser at 1069 nm is located at the bottom-right breadboard.

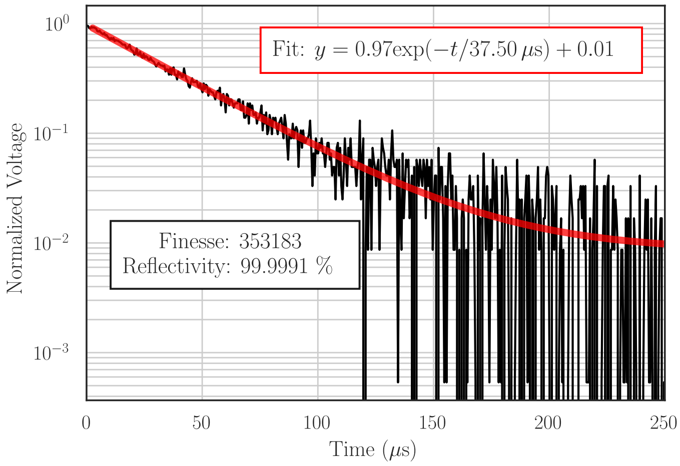

Figure 4.11: Cavity-ring-down measurement of the logic reference cavity. An exponential fit (red) to the normalized transmission photo diode signal (black), triggered by turning off the AOM.

range given by the ratio of output to clock frequency. A tuning range of ≈ ± (20 to 50 kHz) of the output frequency is typically reached.

The amplified fundamental laser radiation is frequency doubled in a bow-tie cavity[29] incorporating a PPLN crystal. The doubling crystal's temperature is stabilized to 84.1(2) °C for non-critical phase matching. Roughly 600 mW are converted to ≈ 250 mW at 535 nm. The cavity is locked by a HC locking scheme. A fiber is transferring the light back to the logic laser breadboard on the lower-right, which comprises a bow-tie cavity with a barium borate ($\beta - BaB_2O_4$) (BBO) crystal. Here, a pump power of ≈ 150 mW at 535 nm is converted to ≈5 to 7 mW UV light at 267 nm using critically phase-matched SHG, where the crystal is heated to 36.0(2) °C and the doubling efficiency is tuned by tilting the BBO crystal (Hannig, 2018; Hannig et al., 2018). This cavity is locked by a similar HC locking scheme as for the PPLN cavity. The cavity output enters a double-pass AOM setup optimized for UV light. The usual approach to separate the forward and backward traveling beam using a polarizing beam splitter after the light has passed a quarter-wave plate twice would be less efficient, because UV AOMs are based on fused silica, which exhibits a strong polarization-dependent diffraction efficiency. In order to overcome this issue, a right-angle prism is placed at the far end of the AOM as retroreflector, displacing the backward traveling beam vertically. The resulting $2 \times (+1^{\mathrm{st}})$ AOM order is then deflected into a free-space beam path towards the chamber breadboard.

For preparation of the two outer $^{27}\mathrm{Al}^+$ ground states with $m_F = \pm 5/2$, the polarization of the beam can be switched between σ^+ and σ^--polarized light using a zero order retardation plate[30] mounted in a fast switching galvanometer positioning system. A description of this retarder plate setup is given in Ch. 5.6. Switching between these polarization states is typically achieved between 1 to 2 ms, without ringing effects or drifts.

---

[29] Finesse≈ 124. The crystal is a 5 mm long, anti reflective (AR)-coated PPLN from *Covision*.

[30] AR coated quartz plate from *Bernhard Halle Nachfl. GmbH*, $10 \times 10\,\mathrm{mm}^2$, 1.6 mm thickness, $\lambda/2 \pm 2$ nm at $\lambda = 248$ nm. AR coating with 0.05% reflectivity at 267 nm.

Instead of generating the required circular light polarization already at this position, we chose to switch between two orthogonal linear polarization states of the light, which is less prone to residual birefringence of dielectric mirror coatings. On the chamber breadboard a fixed quarter waveplate is rotating the linear polarization vectors to $\sigma^{\pm}$-polarized light.

4.10 Clock Laser - 267 nm

The clock laser as the most demanding laser system resides in an own small laboratory in the basement of the Laue-building to avoid vibration-induced shifts from experimentalists and building vibrations. For compatibility with the frequency comb and because optics high-reflective mirrors are not available in the UV, the clock laser is operated at 1069 nm. The high powers needed for the required SHG steps are provided by fiber amplifiers. We chose a fiber laser[31] since those offer an out-of-the box instantaneous laser linewidth of a few kHz, which is substantial smaller compared to typical ECDL linewidths of < 1 MHz. To further improve the stability of the clock laser it is stabilized to an ultra-high Finesse cavity. The cavity and parts of the laser setup around it have already been described in Ref. (Amairi, 2014).

4.10.1 Clock Cavity

The basic principle of a cavity stabilization is to transfer the passive length stability between two mirrors to the laser wavelength. This can be stated as

$$\frac{\Delta\nu}{\nu} = -\frac{\Delta L}{L} \,, \tag{4.7}$$

where ν and L denote laser frequency and length of the cavity, respectively. State-of-the art cavities are operated at temperatures where the combination of mirror substrates and length of the spacer material has a zero-crossing with respect to temperature changes. A fundamental limit is the thermal noise of the spacer, mirror substrates and mirror coatings at finite temperatures. This thermal noise limit can be mitigated by increasing the cavity length (Jiang et al., 2011; Amairi et al., 2013; Häfner et al., 2015). For this reason two ULE spacers were optically contacted, giving a total length of 39.5 cm[32] and therefore a FSR of 380 MHz. The ULE spacers and mirrors have a combined coefficient of thermal expansion (CTE) zero-crossing temperature of 45.50(1) °C. However, the increased length renders the cavity more sensitive to vibrational noise. In order to compensate for this, the cavity is mounted on well-designed positions and the entire setup is placed on a passive vibration isolation platform[33].

The high Finesse of 650 000±6000 is reached by using high reflective mirrors[34] (Amairi, 2014).

---

[31] *NKT* Adjustik, 12.3 mW. Specified instantaneous laser linewidth of 6 kHz.

[32] The manufacturer could not guarantee well-oriented straight hole through a 40 cm long spacer.

[33] Minus-K 250BM-1.

[34] *ATFilms*, Fused Silica substrate, a plane and a 1 m radius of curvature mirror.

Three heat-shields, temperature stabilization and a vacuum chamber with an ion pump[35] provide further isolation from the environment. The cavity layout is depicted in Fig. 4.12. Two U-shaped Invar[36] profiles hold the cavity spacer in place on a 0.5 cm thick ULE base plate.

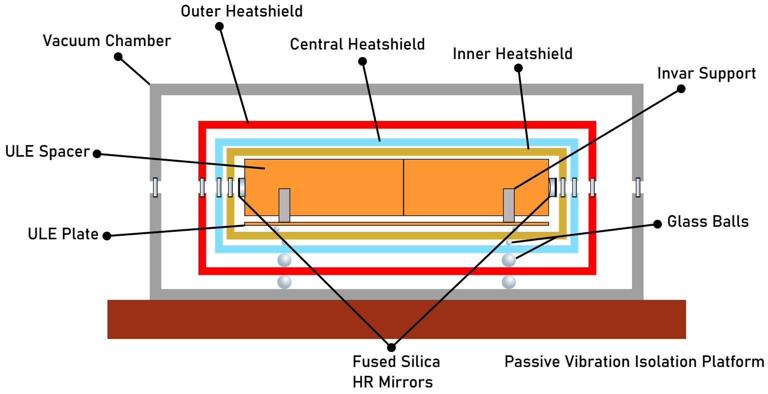

Figure 4.12: Sketch of the clock cavity.

In Ref. (Amairi, 2014) a thermal noise instability limit of 7×10^{-17} at 1 s was estimated from simulations. However, three-cornered hat measurements with a Si-cavity and another ULE-cavity stabilized laser (MNPQ) laser at PTB showed a minimum fractional statistical uncertainty of 1.1×10^{-15} at 1 s and a flicker noise floor at 1×10^{-15} afterwards (Amairi, 2014).

Several changes have been made to the cavity since then in order to improve the stability to the thermal noise limit, including the addition of a third heatshield, the replacement of the Teflon balls with glass balls between the heatshields, replacing heating wires with heating elements glued onto the heatshield, that are isolated with Kapton, and changing the horizontal symmetric contact points of the heatshields to an axially symmetric configuration. A final evaluation of the performance of the upgraded system is still ongoing.

4.10.2 Clock Laser Setup

The laser and cavity breadboard in the basement is shown on the right of Fig. 4.13. Directly at the fiber laser output the power is amplified[37]. Afterwards the laser is locked onto the high-finesse cavity using the PDH locking technique. For this, the cavity input light is phase modulated by an EOM at 95.66 MHz and the cavity reflection is observed on a photo diode. A PDH error signal is then synthesized, which is used as input for a PID[38]. This provides a fast feedback signal to the AOM with a locking bandwidth of 560 kHz (Amairi, 2014) and slow feedback to the piezo stretcher of the fiber laser's cavity. Intensity fluctuations result in thermally-induced length changes of the cavity, which compromise the phase stability of the clock light. Hence, the cavity transmission is stabilized using a photo diode and a PID that attenuates the RF power of the amplifier driving the aforementioned AOM. For adjustment

---

[35] *Agilent* StarCell pump, 25 L.

[36] Alloy of nickel and iron.

[37] *Keopsys*, 7000 mA.

[38] *Toptica* FALC110.

purposes the cavity transmission can be observed by a charged coupled device (CCD) camera or a photo diode.

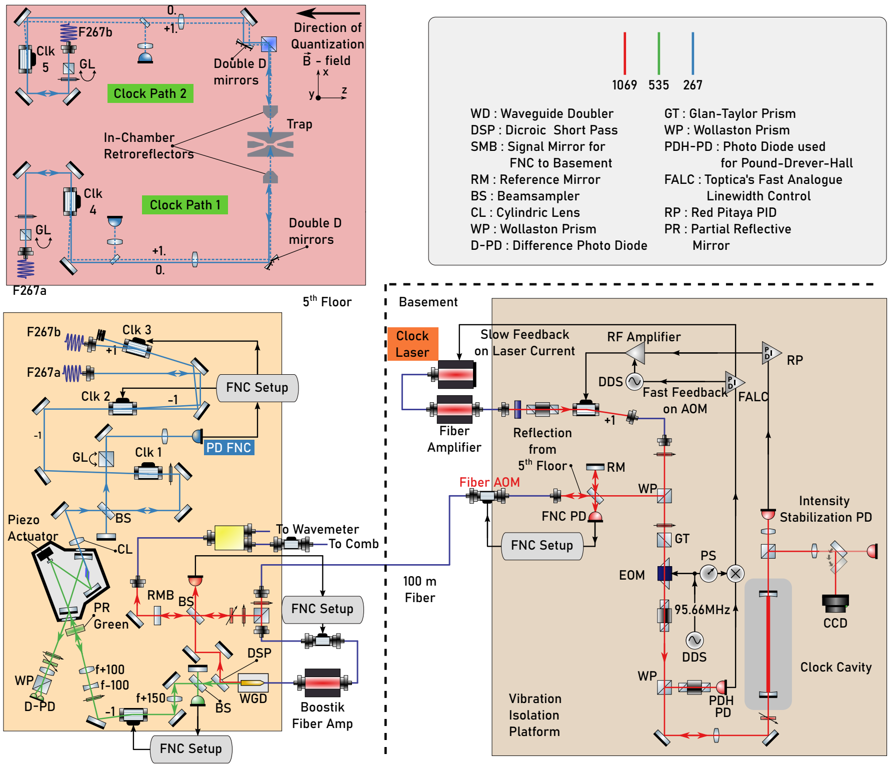

Figure 4.13: Simplified clock laser setup.

A 100 m fiber guides the light to laboratory in the 5th floor, depicted in the center of Fig. 4.13. The long path introduces substantial fiber noise to the laser phase. Therefore, the retroreflected light from mirror RMB travels back to the basement and a beat note with the light from the short reference path in front of the fiber coupler is used to measure fiber noise. A FNC setup, see Ch. 4.5, is then used, which feeds back on the AOM frequency, highlighted in red.

On the lower left breadboard in Fig. 4.13 (located on the 5th floor), the incoming light leaves the fiber and is split into a main part downwards and a reference and monitoring part to the left. A portion of the monitoring beam impinges onto the photo diode in the center, the other – transmitted – part is partially retro-reflected into the 100 m fiber, as mentioned above, and partially fed into a fiber splitter. From here the light is directed to a wavemeter and to the frequency comb breadboard. The main part of the incoming light is transmitted by the polarizing beam splitter cube is used for frequency doubling and later interrogation of the $^{27}\mathrm{Al}^{+}$ ion. The beam firstly passes through a fiber AOM and then seeds a fiber amplifier[39], before entering a WGD[40] that is temperature stabilized to 51.7 °C[41].

It is technically challenging to stabilize the laser phase through amplifiers and frequency doubling stages, because no backward traveling light is available.

---

[39] *NKT* Boostik, 2.4 A

[40] SP waveguide doubler, *NTT Advanced Technology Corporation* H-0534-000-A-B-C, 1 W maximum input power.

[41] R =3383 Ω at 10 kΩ NTC.

Amplifiers typically incorporate optical isolators for protection against reflections and doubling cavities in bow-tie configuration nominally only exhibit a forward propagating wave. For the clock laser we built a setup with the goal to suppress the noise through the single pass amplification and single pass frequency doubling steps. For this reason a dicroic short pass mirror deflects the non-doubled fundamental light at 1069 nm onto the center photo diode. There, the beat note between input and output of the WGD and fiber amplifier is used to synthesize a FNC error signal which feeds back on the fiber AOM in front of these devices. Light at 535 nm is transmitted by the dicroic, traveling through an AOM and entering a BBO - bow-tie cavity which is locked by a HC locking technique. Here, the light is converted to 267 nm. The total length of the cavity is phase locked on the phase of the 535 nm light by the HC lock. In order to reduce the uncompensated beam paths we place the reference mirrors as close as possible to the doubling cavity. For this reason a partial reflector in front of the cavity reflects light towards the WGD output, where it is sent onto a photo diode together with the reflection from a short reference-arm. The measured frequency noise is measured and the derived error signal is used for feeding back onto the AOM frequency, which is located between WGD and BBO cavity, constituting a FNC.

In order to compensate the 1st order Doppler shift when interrogating the clock transition, see Ch. 7.1, the ion is probed by two counter propagating beams. Therefore, the output of the cavity at 267.4 nm passes SP `Clk` AOM 1 before entering AOM `Clk` 2. Its first order is brought directly by a PM fiber to the clock breadboard (see the top left of Fig. 4.13), where it constitutes clock beam 1. The 0th order of clock AOM 2 passes AOM `Clk` 3 from which the 1st order diffracted beam is guided by a second PM fiber to the chamber breadboard, constituting clock beam 2. The two AOMs `Clk` 4 and `Clk` 5 are driven at two dissimilar frequencies, that give the same overall detuning for both beam parts. In case the used resonance frequency of cavity has to be changed from one mode to a neighboring mode – forcing a change of the laser frequency by the FSR – the AOM `Clk` 1 is implemented for flexibility. `Clk` 2 and 3 are for FNC and `Clk` 4 and 5 for shuttering the light.

As mentioned, residual phase noise from path length variations is a common issue in optical clocks. Here, we have the possibility to compensate the clock beams almost up to the ion by using two in-chamber retroreflectors[42]. For this reason we chose the lenses in clock path 1 and 2 to have a long focal length of 300 mm, which reduces the mismatch in focal position between the ion position and the mirror surface of 28 mm, due to the long Rayleigh lengths of 47 to 21 mm for input beam waists of 400 to 600 µm. Furthermore, the relative position of AOM and lens provides two well-separated AOM orders. On these surfaces the 0th-orders of `Clk` 4 and 5 are retroreflected into their fibers and two FNC beat notes at two dissimilar frequencies are generated at the photo diode which is labeled as `PD FNC` and highlighted by a blue box in Fig. 4.13. This scheme is possible because custom made and patented double-D mirrors[43] are used to separately steer the +1st order of AOM 4 and 5 onto the $^{27}\mathrm{Al}^{+}$ ion, and their 0th orders onto the in-chamber retroreflectors. The two

---

[42] Aluminum 6061 T6, 2.5 mm wide and 1.5 mm high pinhole.

[43] Design by F. Dawel, S. Hanning.

beat frequencies can be spectrally separated and used to compensate fiber noise in both paths from BBO cavity to the ion trap individually by feeding back on AOMs `Clk` 2 and 3. The functionality of this FNC has not been verified yet. A characterization of this setup is planned in the near future.

It should be noted that for the clock transition scans presented in Ch. 6, which were conducted in the old setup, the last mentioned part of the FNC was not set up and only `Clk` 1 and 2 of the UV AOMs were available.

As described in the beginning of the chapter, the frequency comb has no outputs at 267.4 nm or 535 nm (Tab. 4.1). Therefore, in order to be able to measure the change in clock laser frequency with the comb, one of the infrared AOMs at 1069 nm has to be scanned in the running clock.

4.10.3 Clock Laser Stability

Interrogation of the clock transition is performed with the aforementioned clock laser at 267.4 nm. When probing the clock transition, the stability of the interrogating laser must be better than the QPN during this time. The two frequency doubling stages required to generate this wavelength impose no limit on the achievable phase stability (Herbers et al., 2019). However, the free-space path in-between might (see previous section). The formula for Ramsey spectroscopy QPN Eq. (1.17) shows that the stability of a clock can be improved by increasing the probe time. A fundamental limit to the applicable probe time is the lifetime of the excited clock state, because for even longer times the coherence of the excited state is lost and the SNR decreases. In most experiments the maximum probe time is limited by the coherence time of the clock laser. Noting, that for single ion clocks several interrogations are necessary in order to generate a clock feedback signal, the coherence time of the laser must be even a few times the probe time.

To prevent cavity frequency drifts during ion interrogation, the light was transfer stabilized to the MNPQ laser using the frequency comb. This will also enable frequency comparisons with other clock experiments within PTB in the future. The applied transfer-lock setup is described in general in Ch. 4.4. The virtual beat between the MNPQ/Si cavity system and the clock laser is used to generate a control signal which feeds back onto the fiber AOM that is otherwise used for FNC of the 100 m fiber. The concerned AOM is highlighted with red color in Fig. 4.13. During this mode of operation the actual FNC setup is deactivated and the phase lock to the frequency comb suppresses also fiber noise.

In addition to this we use the beat with the frequency comb to evaluate the clock cavity performance. For these measurements the phase lock to the frequency comb was deactivated, and the FNC activated. We then tracked the CEO-subtracted beat between frequency comb and clock laser. This beat frequency was also counted when the transfer-lock was activated. The measured signal in this case is an in-loop signal, which benchmarks the quality of the phase-lock to the comb, and should not be falsely interpreted as stability of the clock laser. However, the electronic noise floor and problems in the stabilization can be revealed.

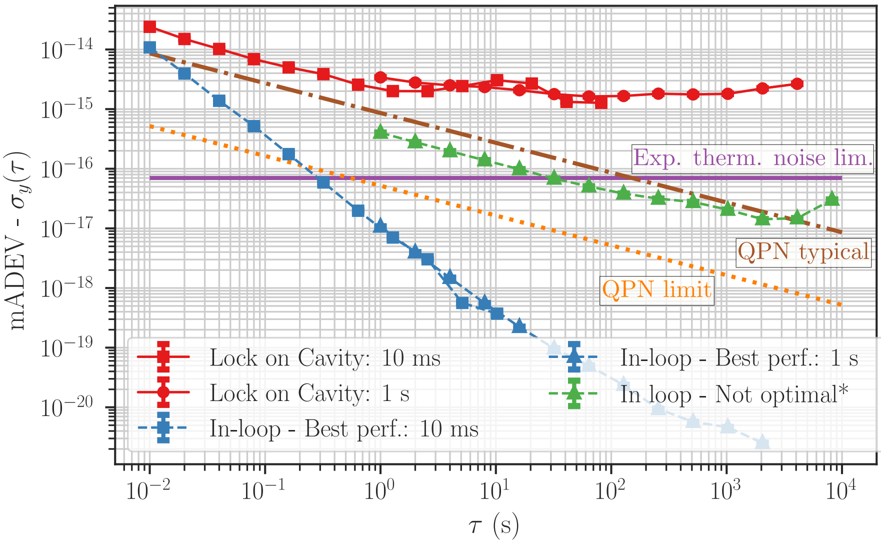

Figure 4.14: Statistical uncertainty of the cavity stabilized clock laser. Plotted is the modified Allan deviation, except for the expected thermal stability (purple, solid line, (Amairi, 2014)) and the QPN limits of the $^{27}\mathrm{Al}^{+}$ clock (orange and brown lines), which both are the standard Allan deviation using Rabi interrogation (Ch. 1.4.2). The orange QPN limit refers to the standard quantum limit, i.e., an interrogation time at the excited state lifetime of 20.6 s and zero dead time, whereas the brown curve is QPN at an interrogation time of 150 ms with 50% duty cycle. Lock on cavity (red solid line) means the clock laser is stabilized to the clock cavity only. Whereas the in-loop labeled data (green and blue dashed lines) refers to a clock laser which is stabilized on cavity and frequency comb. *The green in loop signal was counted at the time, when the clock transition data was measured that will be presented in Ch. 6. The best performance of the in-loop signal (blue) was counted at a different time, when no clock transition experiments were carried out. This signal shows the fast averaging $\propto \tau^{-3/2}$, typical for phase noise when using a modified Allan deviation (Rubiola, 2005; Benkler, Lisdat, and Sterr, 2015). In contrast to this, the transfer lock performance when the data for the $^{27}\mathrm{Al}^{+}$ clock transition was taken (green) has a slope $\propto \tau^{-1/2}$, which reveals frequency noise. The frequency noise was probably caused by a drop in SNR on the beat signal. The consequential low gain of the servo signal failed to suppress the phase excursions due to the noise on the 100 m fiber, which lead to cycle slips that manifested as frequency noise. Unfortunately, this was not noticed at this time. The red and blue curves were measured at different counter time windows of 10 ms (square markers) and 1 s (triangle markers) (Λ averaging).

In Fig. 4.14 the measured fractional frequency uncertainties in these two modes of operation are shown. It can be seen that the measured stability of the clock laser was at 2×10^{-15} at 1 s, which is comparable to the results from Ref. (Amairi, 2014). It must be noted that about 2 m of fiber length from the AOM breadboard to the frequency comb was not fiber length stabilized at this point. However, it appears that the clock cavity must be further improved, since in an interrogation of the clock transition with an interrogation time of 150 ms and a duty cycle of 50% the achieved stability will be limited by the local clock laser and not by the atomic reference. Comparing the best performance in-loop measurement, shown as blue curve, with the green curve, reveals that the lock performance was not optimal when measuring the clock transitions as presented in Ch. 6. This frequency noise, probably caused by an insufficient

SNR in the beat signal, was not noticed at this time. However this imposes limits on the achieved phase stability of the clock light at this time, since the noise in the 100 m long fiber was then not sufficiently suppressed. Assuming that in a not optimal operating transfer-lock the counted frequency deviations of the in-loop signals are on the order of the real clock laser frequency fluctuations this gives, extrapolating the green line to roughly 2×10^{-15} at 100 ms, about 9 Hz at 267.4 nm. This is on the same order as the observed minimum linewidth as will be shown in Ch. 6.

Finally, it should be noted that if in the future evaluation of the clock cavity the stability as measured in Fig. 4.14 is confirmed, further ways of improvements have to be discussed. Interrogating $^{27}\mathrm{Al}^{+}$ with the cavity-locked clock laser alone would result in a laser-limited and not QPN-limited short time stability as can be seen by comparing the red and brown curves. A transfer lock onto the Si-cavity stabilized laser could be sufficient for the clock operation when all fiber lengths from this reference laser to our laboratory and all fiber lengths from the clock laser starting from the transfer lock point to the ion are stabilized, as can be inferred from the stability of the Si-cavity laser in Fig. 4.4. The residual noise at high Fourier frequencies due to the transfer lock via the frequency comb should impose no limitation to the clock interrogation. However, the system would then be highly dependent on the performance of the transfer-lock and its locking bandwidth. The combination of a clock laser that is locked to the clock cavity with a stability as shown as red curve in Fig. 4.14, together with a slow lock on the Si-cavity laser would guarantee long probing times of the $^{27}\mathrm{Al}^{+}$ clock transition.

Part III

Measurements & Characterization

With the theoretical foundations and the technical setup described in the last parts, this part describes the measurements used to characterize the systematic shifts of the aluminum ion clock. It also presents the first observation of the clock transition in this experiment. Finally, the systematic shifts in this experiment are evaluated. The estimated systematic uncertainty budget is based on measurements conducted on a calcium ion and extrapolation.

5 Measurements for Setup Characterization

The following chapters benchmarks important physical features of the system. These include values which determine systematic shifts of the clock transition, as for example the background-gas pressure (Ch. 5.1), magnetic field stability (Ch. 5.2) and the motional heating rates (Ch. 5.5), as well as the ability to apply reliable QL pulses on stable sidebands (Ch. 5.4) and state preparation of the $^{27}Al^+$ transition by the usage of a fast polarization switcher (Ch. 5.6).

5.1 Residual Pressure in the Vacuum Chamber

Residual atoms and molecules in the vacuum chamber are detrimental for every ion clock experiment and for the $^{27}Al^+$ clock in particular:

1. Background-gas collisions provoke position swaps of the $^{27}Al^+$ and $^{40}Ca^+$ ion.
2. Background-gas collisions lead to heating and non-thermal states (Hankin et al., 2019).
3. High energy atoms can cause decrystallization of the two-ion crystal. Then seconds of recooling using a far red detuned helper beam is required, for the ion pair to recrystallize and reach a steady-state temperature (Wübbena et al., 2012).
4. Chemical reactions of the trapped ions with background gas molecules lead to effective ion loss. The aluminum ion in the excited ^{3}P-state is in particular reactive with hydrogen by the exothermic $Al^+\ (^3P)\ + H_2 \rightarrow AlH^+\ (X^2\Sigma^+) + H + 0.9\,\mathrm{eV}$ reaction (Müller and Ottinger, 1986).[1]
5. Ion loss due to a heavy collision.
6. Elastic collisions during the clock interrogation can impose a phase shift between the superposition of the ground and excited state, which results in systematic frequency shifts of microwave and optical frequency standards with uncertainties at the mid 10^{-19} level (Hankin et al., 2019).

Events 1 to 5 increase the statistical uncertainty due to the additional dead-time that is required for re-preparing the $^{27}Al^+$-$^{40}Ca^+$ crystal. The effect of 6 results in a systematic frequency shift, called collisional frequency shift (CFS). In order to suppress all of these effects a low background gas pressure is required.

---

[1] Photo-dissociation of AlH^+ is possible (Seck et al., 2014), but an additional 360 nm laser is needed for the first ionization step in this two-photon process. The second step is at 266 nm, which could in principle be reached by the aluminum logic laser.

5.1.1 Swaprate Measurements

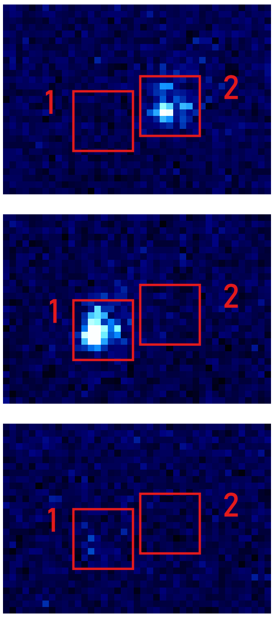

Figure 5.1: $^{27}\mathrm{Al}^{+}$-$^{40}\mathrm{Ca}^{+}$ crystal and regions of interest (ROIs) (red squares). $^{40}\mathrm{Ca}^{+}$ scatters 397 nm light and is thus visible on the EMCCD camera. The $^{27}\mathrm{Al}^{+}$ ion is dark and makes itself noticeable by pushing $^{40}\mathrm{Ca}^{+}$ away from the center. When the radial potential energy is higher than the axial, the crystal takes a linear axial ordering. The camera's horizontal axis is slightly tilted to the trap axis. Upon a collision, there is a probability for $^{40}\mathrm{Ca}^{+}$ and $^{27}\mathrm{Al}^{+}$ to swap their position (top to middle picture). Some collisions transfer enough kinetic energy to the ions such that they decrystallize (bottom picture).

Pressure values inferred from ion gauge or ion pump current are prone to large uncertainties, because in most setups they measure far away from the ion position, often in direct neighborhood to the vacuum pumps. In addition to that, the measured currents on the order of nA are tiny, such that electronic devices nearby can disturb the measurement, making the pressure readings dependent on the cable position. A more accurate technique is given by measuring the pressure directly with the ions, for example by observing position swaps in a two-ion crystal, see the supplemental material of Ref. (Rosenband et al., 2008).

In Ref. (Hankin et al., 2019) collisions of a single ion with H_2 are considered, as this is the dominant background-gas in ultra-high vacuum (UHV) experiments. The collisions are then treated as instantaneous changes to the velocity of one of the two ions, including Langevin-collisions as well as glancing collisions. The result of their calculations is a differential collision rate $\frac{\mathrm{d}\Gamma}{\mathrm{d}E_{\mathrm{kin}}}(E_{\mathrm{kin}})$, where E_{kin} is the gained laboratory frame kinetic energy of one ion upon a collision. The total collision rate is dependent on the density of background molecules and its kinetic energy distribution, i.e. the background pressure. An expression that connects the reorder rate with the differential collision rate is calculated to

$$\Gamma_{\mathrm{reorder}} = \sum_{i=1}^{2} \int_{0}^{\infty} P_{i,\mathrm{reorder}}(E_{\mathrm{kin}}) \frac{\mathrm{d}\Gamma_i}{\mathrm{d}E_{\mathrm{kin}}}(E_{\mathrm{kin}})\mathrm{d}E_{\mathrm{kin}} \ , \tag{5.1}$$

where the sum covers the two ions and $P_{i,\mathrm{reorder}}$ is the reorder probability for ion i. This probability can be assumed to be 0.5 when the kinetic energy is greater than the potential energy barrier

$$E_{\mathrm{reorder}} = \frac{3}{4}\left(\frac{\sqrt{m}\omega_z Q^2}{2\pi\epsilon_0}\right)^{\frac{2}{3}} \left[\left(\frac{2\left(\epsilon^2+\alpha-1\right)\left(\epsilon^2+\mu\left(\alpha-1\right)\right)}{\epsilon^2\left(\mu+1\right)+2\mu\left(\alpha-1\right)}\right)^{1/3} - 1\right] \ , \tag{5.2}$$

between ground-state axial and two-ion radial configuration (Hankin et al., 2019). Here $\mu = m_{\mathrm{Al}}/m_{\mathrm{Ca}}$ is the mass ratio between the two ions, ω_z is the single $^{40}\mathrm{Ca}^{+}$ axial secular frequency and $\epsilon = \omega_p/\omega_z$ with $\omega_p = \sqrt{(\omega_x^2+\omega_y^2+\omega_z^2)/2}$. The integral can then be approximated by

$$\Gamma_{\mathrm{reorder}} \lessapprox \frac{1}{2}\left(\frac{p}{902\,\mathrm{nPa}\cdot\mathrm{s}}\right)\left(\frac{E_{\mathrm{reorder}}}{1\,\mathrm{K}\times\mathrm{k_B}}\right)^{-0.278} \ , \tag{5.3}$$

with p being the H_2 pressure. This formula holds for an $^{27}\mathrm{Al}^{+}$-$^{40}\mathrm{Ca}^{+}$ crystal in 295 K H_2 background gas inside the bounds of $0.1\,\mathrm{K} < E_{\mathrm{reorder}} < 10\,\mathrm{K}$. We use this formula to calculate the background pressure in our chamber, noting that in Ref. (Hankin et al., 2019), which has similar conditions to our experiment, the pressure value using Eq. (5.3) and the results from a full symplectic integrator of 6th-order showed good agreement. We measured the reordering rate by counting position swaps of an $^{27}\mathrm{Al}^{+}$-$^{40}\mathrm{Ca}^{+}$ crystal and the energy barrier by measuring the single $^{40}\mathrm{Ca}^{+}$ secular frequencies.

5.1.2 Measurement Results

Measurements using a $^{27}\mathrm{Al}^{+}$-$^{40}\mathrm{Ca}^{+}$ crystal as a pressure "sensor" have been conducted prior and after the rebuilding of the vacuum system. A simple sequence was run in which the ion crystal was Doppler cooled by the 397 nm π- and σ^{-}-polarized lasers while applying 866 nm radiation for 2.5 ms. Additionally, a far-red detuned 397 nm beam was turned on continuously. The photon counts at two regions of interest (ROI) were monitored over longer periods of time T with an EMCCD camera – set to an exposure time of 0.1 s – throughout the whole sequence. A reorder event is apparent when the bright ($^{40}\mathrm{Ca}^{+}$) and dark ion ($^{27}\mathrm{Al}^{+}$) swap their position and thus the fluorescing region flips from one ROI to the other, see Fig. 5.1 top and center. When a decrystallization occurs, visible in the bottom of Fig. 5.1, both regions get dark and stay dark for a few seconds depending on the cooling efficiency of the far-red detuned 397 nm helper laser. An activation of the far red-detuned 397 nm radiation triggered by a decrystallization event was not possible using the experimental control system based on *QFP*. In the planned new experimental control system this would be more easily to implement. Using a threshold photon count allowed to count the number of reordering events N_{reorder}, i.e., when the fluorescent region swaps, and decrystallization events $N_{\text{decrystallization}}$, when both regions are below threshold. For two typical measurement results see Fig. 5.2.

The measured unbiased reorder rate is then given by

$$\Gamma_{\text{reorder}} = \frac{N_{\text{reorder}} + \frac{N_{\text{decrystallization}}}{2}}{T} , \tag{5.4}$$

where decrystallization events are assumed to have a probability of $1/2$ to provoke a reordering (Hankin et al., 2019).

Fig. 5.2 shows the result of a reordering measurement in the old and the new system. In the new system reordering events are drastically reduced, which is also apparent in Fig. 5.3, where the distribution of the time between two events is plotted for all measurements conducted in the old and the new setup.

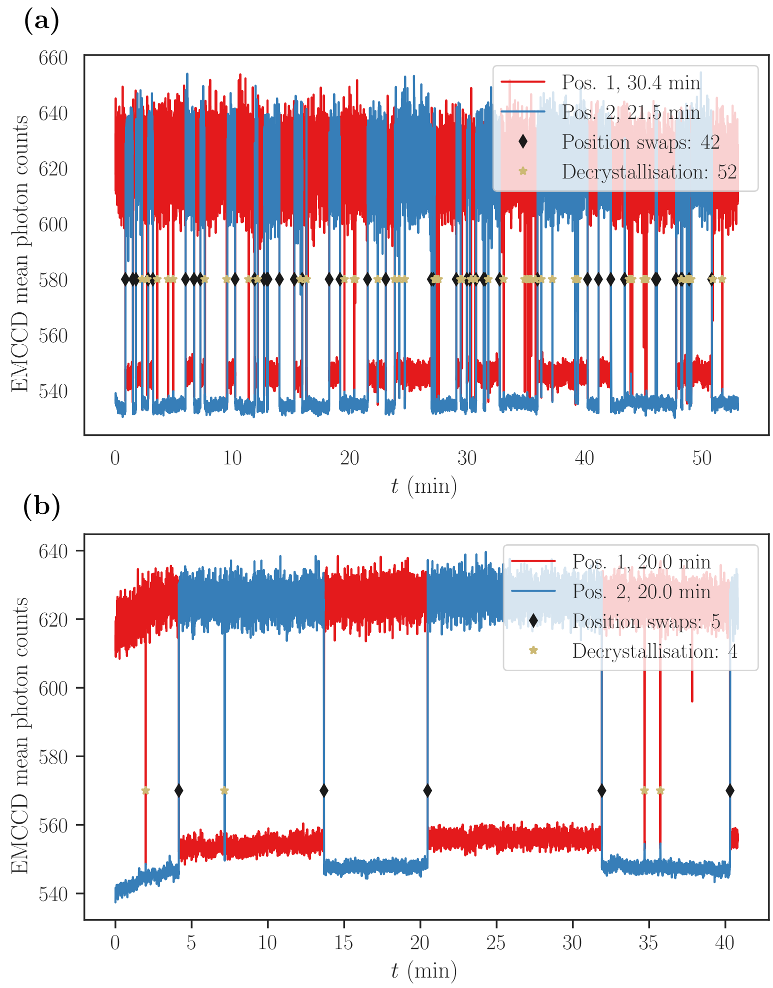

Figure 5.2: Collected fluorescence in two regions of interest by an EMCCD camera for the old (a) and the new (b) setup. The symbols indicating position swap and decrystallization events are placed on the corresponding photon count threshold.

The reordering rate has been measured at different potential energy barriers by varying dc endcap voltages and the radial trap drive power. Using Eq. 5.3 we infer 10.5 nPa background pressure in the new setup. For the evaluation of

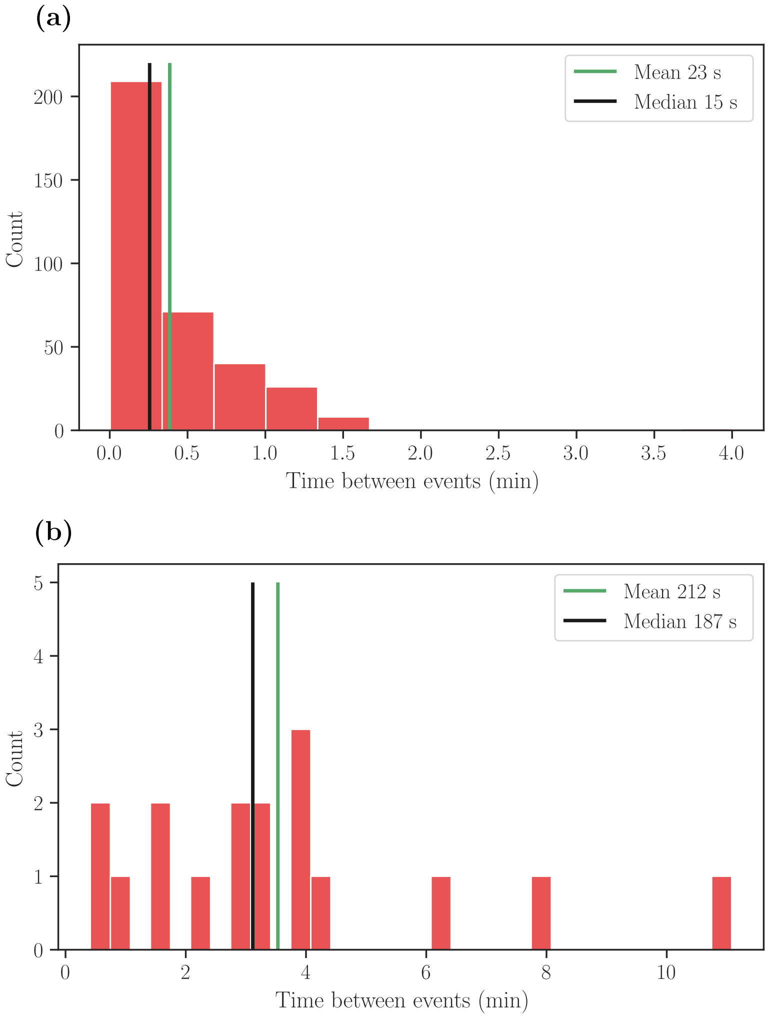

Figure 5.3: Distribution of time intervals between two events with no division made between reordering and decrystallization events for the old (a) and the new (b) setup. The bin-width is 20 s. Combined data from all measured potential energy barriers.

the background gas collisional shift (Ch. 7.6) we take this pressure value and half its magnitude as conservative estimate for its uncertainty, i.e., 11(6) nPa.

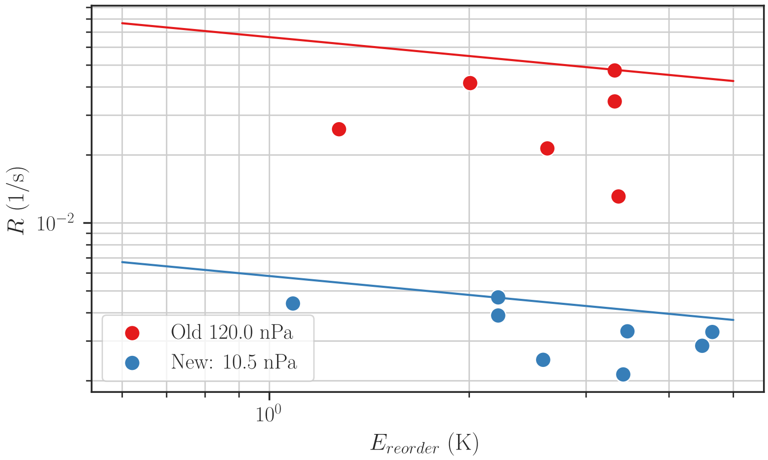

Figure 5.4: Measured reordering rates vs. potential energy barrier. Changes in the potential energy barrier were introduced by varying endcap electrode voltage and RF trap drive power. The solid lines are upper limits of the reordering rates that were calculated from the pressure values indicated in the legend using Eq. 5.3.

5.2 Magnetic Field Stability

As magnetic field noise directly affects the magnetic field sensitive energy levels of the ions, it leads to drifts of the transition frequencies and destroys the coherence of atomic states if the magnetic field changes within one or a few experimental cycles. Both effects are exploited in the following two subsections in order to quantify the achieved level of magnetic field stability in terms of slow magnetic field drifts, changing the energy level of probed atomic transitions and in terms of fast magnetic field noise, causing a decay of coherence over time. A detailed study of the magnetic fields induced by the high currents of the RF-blade trap at the trap drive frequency is elaborated in Ch. 7.7.2.

The applied magnetic field in this experiment can be tuned by a set of quantization magnetic field coils around the chamber. By probing different magnetic sublevels on the ions the magnetic field can be inferred. This can be performed during clock-operation by probing the $^{27}\mathrm{Al}^{+}$ clock transition on the two outer $m_F = -5/2 \leftrightarrow m_F = -5/2$ and $m_F = 5/2 \leftrightarrow m_F = 5/2$ magnetic sub state transitions (Ch. 7.7). For the measurements presented in this thesis, we measured the absolute magnetic field on $^{40}\mathrm{Ca}^{+}$ by probing the $\mathrm{S}_{1/2}$, $m = -1/2 \leftrightarrow \mathrm{D}_{5/2}$, $m = -5/2$ and the $\mathrm{S}_{1/2}$, $m = -1/2 \leftrightarrow \mathrm{D}_{5/2}$, $m = -1/2$ transitions with measured frequencies $\nu_{-5/2}$ and $\nu_{-1/2}$, respectively. This is beneficial since $^{40}\mathrm{Ca}^{+}$ is more sensitive to the magnetic field compared to $^{27}\mathrm{Al}^{+}$. Using the Landé g-factor for the $^{40}\mathrm{Ca}^{+}$ $3d^2\mathrm{D}_{5/2}$ level of $g_{5/2} = 1.200\,334\,0(3)$ (Chwalla et al., 2009) the absolute magnetic field can be calculated by subtracting the measured transition frequencies

$$B = \frac{\left(\nu_{-1/2} - \nu_{-5/2}\right) h}{2\mu_B g_{5/2}} , \tag{5.5}$$

where h is the Planck constant and μ_B the Bohr magneton. A direct observation of e.g. the magnetic field sensitive splitting of the ground state S-level of the $^{40}\mathrm{Ca}^+$ is also possible. But a suitable RF source and antenna are not implemented in the setup.

Ramsey experiments on $^{40}\mathrm{Ca}^+$ $\mathrm{S}_{1/2},\ m = -1/2 \leftrightarrow \mathrm{D}_{5/2},\ m = -5/2$ and the $\mathrm{S}_{1/2},\ m = -1/2 \leftrightarrow \mathrm{D}_{5/2},\ m = -1/2$ transitions were carried out. These transitions have a sensitivity

$$\mathrm{d}\nu_{-1/2}/\mathrm{d}B = 5.62\,\mathrm{Hz/nT}\ , \tag{5.6}$$

and

$$\mathrm{d}\nu_{-5/2}/\mathrm{d}B = 27.99\,\mathrm{Hz/nT}\ , \tag{5.7}$$

respectively, which makes the latter a factor of 5 more sensitive to magnetic field fluctuations. In both experiments described below, one experimental cycle included Doppler cooling of a single $^{40}\mathrm{Ca}^+$ ion and state preparation to $|{\downarrow}\rangle = \left|\mathrm{S}_{1/2},\ m = -1/2\right\rangle$ by optical pumping on the $\mathrm{S}_{1/2} \leftrightarrow \mathrm{P}_{1/2}$ transition with a σ^--polarized laser at 397 nm. This is followed by two $\pi/2$ pulses at 729 nm separated by a dark time t_d, driving transitions from $|{\downarrow}\rangle$ to $|{\uparrow}\rangle = \left|\mathrm{D}_{5/2},\ m = -1/2\right\rangle$ or $|{\uparrow}\rangle = \left|\mathrm{D}_{5/2},\ m = -5/2\right\rangle$, respectively. The first $\pi/2$ pulse[2] puts $^{40}\mathrm{Ca}^+$ into a superposition state

$$\psi(0) = \frac{1}{\sqrt{2}}\left(|{\downarrow}\rangle + |{\uparrow}\rangle\right)\ . \tag{5.8}$$

During the subsequent dark time t_d all lasers are turned off and the states accumulate a differential phase ϕ, yielding a state (Wineland et al., 1998; Riehle, 2004; Ruster et al., 2016)

$$\psi(t_d) = \frac{1}{\sqrt{2}}\left(|{\downarrow}\rangle + e^{i\phi(t_d)}\,|{\uparrow}\rangle\right)\ , \tag{5.9}$$

immediately before the second $\pi/2$ pulse. This state has a density matrix representation (Ruster et al., 2016)

$$\hat{\rho} = \frac{1}{2}\begin{pmatrix} 1 & Ce^{-i\phi} \\ Ce^{i\phi} & 1 \end{pmatrix}\ , \tag{5.10}$$

where the coherence $C = 2\,|\hat{\rho}_{12}|$, i.e., the magnitude of the off-diagonal matrix elements, has been added in order to account for dephasing due to magnetic field fluctuations. Thus, after the final $\pi/2$ rotation the probability to find $^{40}\mathrm{Ca}^+$ in the excited state is

$$p_\uparrow = \frac{1}{2}\left(1 + C\cos\left(\phi\right)\right)\ . \tag{5.11}$$

---

[2] The pulse can be described by a y-rotation operator like $R_y(\theta) = \begin{pmatrix} \cos(\theta) & -\sin(\theta) \\ \sin(\theta) & \cos(\theta) \end{pmatrix}$ with $\theta = \pi/2$.

State detection is accomplished on the $S_{1/2} \leftrightarrow P_{1/2}$ transition. One sequence cycle includes two Ramsey interrogations, the first on the insensitive and the second on the sensitive transition.

Magnetic field noise influences the achieved signal in two ways. Firstly, slow drifts in the magnetic field over many experimental cycles impose frequency shifts of the observed Ramsey structure, as shown in Fig. 5.5. There, Ramsey fringes are depicted which occur when the laser frequency is scanned. This frequency dependence can be used to probe the drifting magnetic field by repeating this experiment continuously. Secondly, fast magnetic field noise with periods shorter than the dark time introduces a dephasing of the coherence C in dependence of the applied dark time. Therefore, by measuring the decay of the coherence over time the rms value of the magnetic field fluctuations can be inferred (Monz, 2011; Ruster et al., 2016).

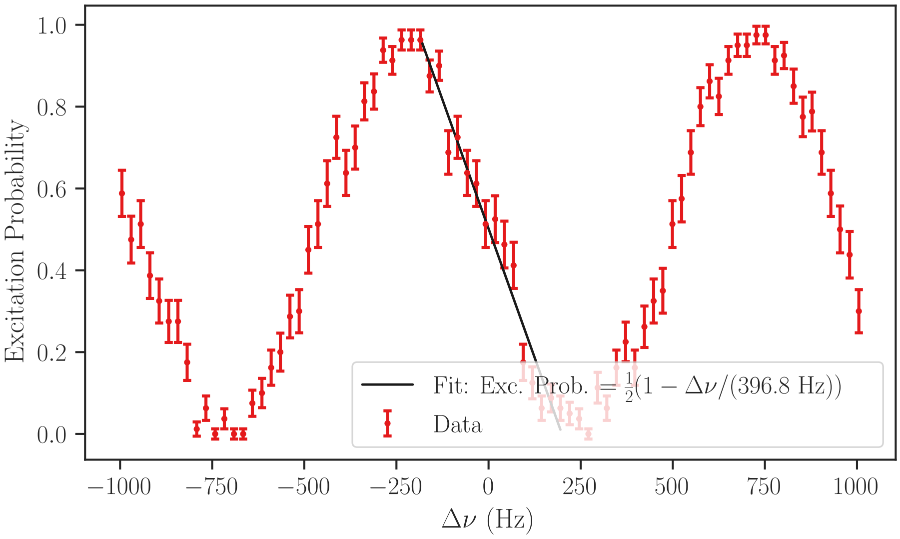

Figure 5.5: Measured Ramsey fringes occurring when scanning the 729 nm frequency over the $|\downarrow\rangle = |S_{1/2}, m_J = -1/2\rangle \leftrightarrow |\uparrow\rangle = |D_{5/2}, m_J = -1/2\rangle$ transition with a dark time of 500 µs. The fitted linear slope can be used to infer frequency changes by measuring the time-dependent variations of the excitation probability. The detuning $\Delta\nu = 0$ is here referring to an absolute frequency detuning that results in 50 % excitation probability when the measurement is started, as described in the text of the beginning of Ch. 5.2.1.

5.2.1 Magnetic Field Drifts

Slow magnetic fields drifts can be made visible by continuous observation of the $^{40}\mathrm{Ca}^+$ excitation probability, on a slope of a Ramsey fringe with constant dark time t_d. The 729 nm laser was detuned by half a Ramsey fringe linewidth, which gave a steep-slope excitation signal, see Fig. 5.5, proportional to the detuning from the transition frequency. The sequence is sketched in Fig. 5.6. In lowest order a linear dependence in the change of excitation probability due to magnetic field drifts is apparent. A calibration curve was previously taken from whose linear fit the excitation-to-frequency conversion factor was extracted. Using Eq. (5.5), the magnetic field B and the deviation from its average value were calculated, assuming that frequency excursions were caused solely by the magnetic field. In Fig. 5.7 the Allan deviations (ADEV) in nT of the magnetic field fluctuations is shown. A single data point is the average of 80 cycles. Scans where the excitation probability reached 0 or 1 were discarded in order to exclude Ramsey fringe hops. The results contain measurement where the start of each cycle was triggered on the phase of the 50 Hz power line (line trigger) and/or the active magnetic field stabilization was activated (Ch. 3.7.2).

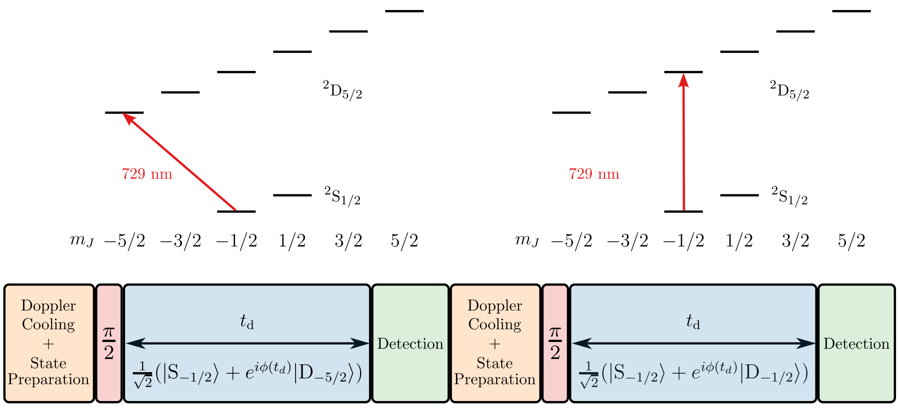

Figure 5.6: Ramsey sequence for measuring the magnetic field stability. After the Ca ion is Doppler cooled and prepared into the electronic ground state, a $\pi/2$ pulse on the $|\downarrow\rangle = |S_{1/2}, m_J = -1/2\rangle \leftrightarrow |\uparrow\rangle = |D_{5/2}, m_J = -5/2\rangle$ ($|\downarrow\rangle = |S_{1/2}, m_J = -1/2\rangle \leftrightarrow |\uparrow\rangle = |D_{5/2}, m_J = -1/2\rangle$) transition generates $\psi(0)$ as defined in Eq. (5.8). Then, the laser radiation is turned off for a dark time t_d. Finally, a 2^{nd} $\pi/2$ pulse on the same transition is applied and the state is detected.

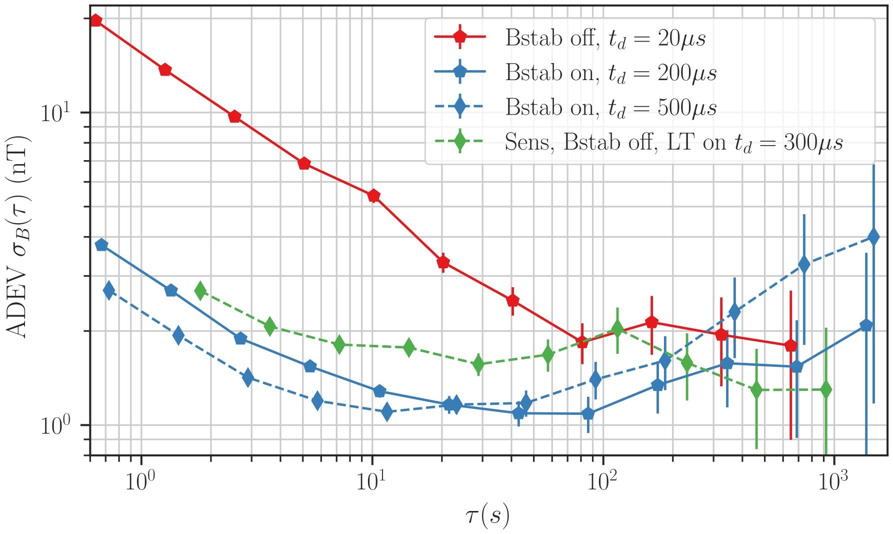

Figure 5.7: Magnetic field stability ADEV, inferred from single slope Ramsey spectroscopy of the $|S_{1/2}, m_J = -1/2\rangle \leftrightarrow |D_{5/2}, m_J = -1/2\rangle$ and $|S_{1/2}, m_J = -1/2\rangle \leftrightarrow |D_{5/2}, m_J = -5/2\rangle$ transitions. The red line is without magnetic field stabilization, whereas blue lines are stabilized. The green curve is without magnetic field stabilization, but triggered on the 50 Hz supply line. Also the magnetic field of the green line was measured only using the sensitive transition, and not as in all other cases using the difference of sensitive and insensitive transition. Without magnetic stabilization the dark time is limited to $t_d \approx 20\,\mu\text{s}$.

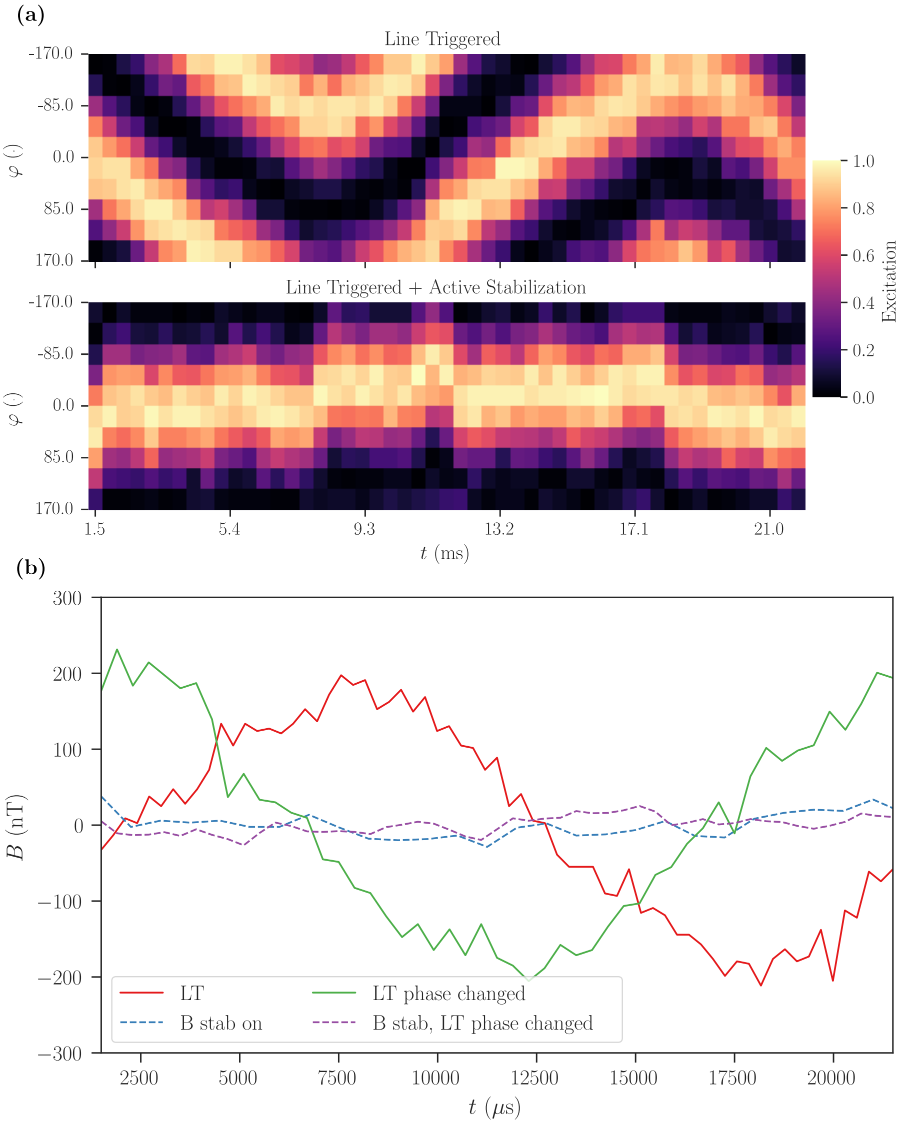

Figure 5.8: (a) 2D Plot of Ramsey phase φ vs. delay time t. Top: Without magnetic field stabilization, the phase of the 50 Hz line is directly visible. Bottom: The magnetic field stabilization unit suppresses power line noise. (b) 1D cuts through the scans shown in (a), transformed to B (nT). All curves were measured with activated line triggering. In the green and violet curves the phase-offset of the line trigger unit was deliberately changed. The apparent magnetic field fluctuations in the stabilized case are caused by the QPN-limited frequency resolution of the Ramsey experiments with a dark time of 150 µs.

Since the linewidth of the Ramsey fringes and therefore the sensitivity for magnetic field fluctuations increases with t_d, longer dark times are favorable. However, for the sensitive transition without magnetic field stabilization, it was not possible to use dark times longer than $t_d \approx 20$ µs without leaving the linear slope after a few interrogations, introducing fringe hops. QPN is dominating the short time behavior of these ADEV curves in two fashions. Firstly, for sufficiently short dark times the sensitivity to the magnetic field is so small, that the signal is dominated by QPN. This was confirmed by simulating QPN at $p = 0.5$ (not shown). In consequence, the data taken with shorter dark times start at higher lying points in the ADEV. Secondly, all curves average with $\propto \tau^{-\frac{1}{2}}$ in the beginning, which is typical for QPN. In the running clock, the magnetic field value will be inherently measured when probing both outer lying ^{27}Al^{+} clock transitions, see Ch. 7.7, hence a drift of the magnetic field can be compensated by randomizing the order in which the transitions are probed. At a typical clock transition Rabi interrogation time of 150 ms a QPN limited magnetic field noise is extrapolated from Fig. 5.7 to be ≈5 nT. Even though the magnetic field at these times was not measured, there is no obvious reason for higher noise at this time. Therefore, at the start of the averaging of the magnetic field using ^{40}Ca^{+}, the influence of the frequency shift of the ^{27}Al^{+} clock of 0.21 Hz due to this 5 nT is only a fraction of the observed linewidth of 5.3 Hz, which guarantees a fringe-hop free averaging of the ^{27}Al^{+} clock. A reasonable estimate of the clock cycle time is a few seconds. During this time no magnetic field drift is apparent and as proven by Fig. 5.7, a stability better than 2 nT can be expected when averaging up to 100 s with active magnetic field stabilization.

The highest noise contribution to the magnetic field is due to fluctuations on the 50 Hz power line. This can be inferred from the fact that triggering on the ac line has almost the same effect as the activated magnetic field stabilization as can be seen from the green curve in Fig. 5.7, and from the scans shown in Fig. 5.8. In Fig. 5.8 the aforementioned experiment was modified to a single Ramsey scan on the sensitive transition, where the start of the experiment was line triggered. A delay between the line trigger and the first $\pi/2$ laser pulse was added by varying the length of the Doppler cooling pulse. The sequence therefore effectively samples the phase of the 50 Hz power line. For visualizing the 50 Hz oscillation, the phase of the finishing 729 nm $\pi/2$ pulse was scanned in Fig. 5.8 (a). The magnetic field stabilization unit suppresses this effect, reducing the residual amplitude to a few nT as depicted in the lower panel of (a) and in the dotted, blue and violet lines in (b).

It should be noted that the line trigger is not canceling the 50 Hz noise amplitude, but making it the same at constant time points for every experimental run. Measuring the clock transition only with line-triggering activated would therefore be very detrimental for the error budget of the clock, since the amplitude of the 50 Hz magnetic field varies not fast enough that it could be considered as averaging to zero, especially for probe times of a few 10 ms. We therefore measure the clock transition only with activated magnetic field stabilization and note that it can be measured by averaging to a statistical uncertainty of 2 nT.

5.2.2 Coherences

Clock interrogations with typical probing times of a few hundred milliseconds are mostly sensitive at small Fourier frequencies up to a few ten hertz of the magnetic field noise spectrum (Al-Masoudi et al., 2015). However, fast magnetic field fluctuations in the kHz range contribute to a quadratic Zeeman shift of the clock frequency, which is evaluated in Ch. 7.7.2. In order to quantify these faster noise contributions compared to the slow drifts described above, coherence measurements were carried out. Instead of detuning the 729 nm laser, the phase of the last $\pi/2$ pulse was scanned for varying dark times. From the fitting of the observed signal to

$$p_{\uparrow}(t_d) = \frac{1}{2}\left(1 + C(t_d)\cos\left(\phi + \phi_0\right)\right) \ , \tag{5.12}$$

the decay of coherence $C(t_d)$ over time was measured through the decay of the fringe contrast. The coherence C is subject to magnetic field fluctuations ΔB by (Monz, 2011)

$$C(t_d) = \mathrm{Re}\left\langle \exp\left(-i\frac{\mu}{\hbar}\int_0^{t_d} \mathrm{d}t'\Delta B(t')\right)\right\rangle , \tag{5.13}$$

where here $\langle\ \rangle$ denotes an ensemble average over the random magnetic field fluctuations $\Delta B(t)$ and $\mu = h\mathrm{d}\nu/\mathrm{d}B$ is the magnetic field sensitivity of the used states. For Ramsey dark times shorter than the intrinsic decoherence time, which is roughly twice the excited state lifetime (Monz, 2011), the decay of C is of Gaussian shape and can be described by $e^{-t^2/(2\tau^2)}$, where τ is the decoherence time (Riebe, 2005; Monz, 2011; Ruster et al., 2016; Leopold et al., 2019). An exponential decay that scales with $\sim e^{-t/\tau}$ is expected when the intrinsic decoherence time is shorter than the experimental Ramsey dark time, which was not observed here.

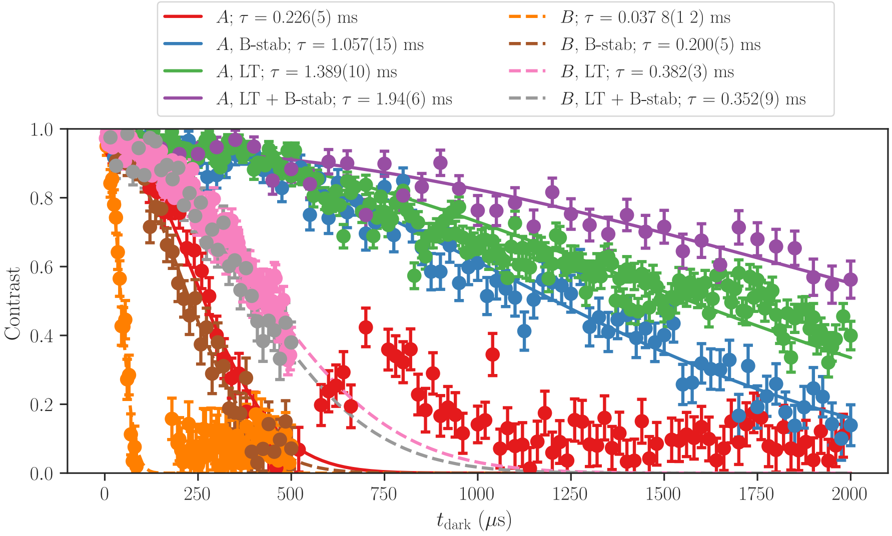

Figure 5.9: Coherences of the magnetic insensitive $m_{\mathrm{S}} = -1/2 \leftrightarrow m_{\mathrm{D}} = -1/2$ (named A) and the sensitive $m_S = -1/2 \leftrightarrow m_{\mathrm{D}} = -5/2$ (named B) transition of $^{40}\mathrm{Ca}^+$. Measurements labeled with LT are triggered on the ac line, those labeled with B-stab are performed with active magnetic field stabilization. Gaps in this plot are due to failure in fitting to Eq. (5.12).

The results of the measurements are shown in Fig. 5.9. As it can be seen, the active magnetic field stabilization (B-stab) and triggering on the ac power line (LT) are suppressing the noise by approximately one order of magnitude compared to the unstabilized case.

From the measured coherence time τ and the sensitivities $\mathrm{d}\nu/\mathrm{d}B$ from Eq. (5.6)-(5.7) the rms magnetic field fluctuations can be expressed as (Monz, 2011)

$$\sqrt{\langle \Delta B^2 \rangle} = \frac{1}{(2\pi\tau\frac{\mathrm{d}\nu}{\mathrm{d}B})} \; . \tag{5.14}$$

The resulting magnetic field rms values are listed in 5.1.

Table 5.1: Measured rms magnetic field fluctuations deduced from coherence time measurements.

Transition $m_S \leftrightarrow m_D$	Stabilization	$\tau_{\mathrm{insens}}/\tau_{\mathrm{sens}}$	$\sqrt{\langle \Delta B^2 \rangle}$ (nT)
$-1/2 \leftrightarrow -5/2$	-		150(5)
$-1/2 \leftrightarrow -5/2$	B-stab		28.4(7)
$-1/2 \leftrightarrow -5/2$	LT		14.88(12)
$-1/2 \leftrightarrow -5/2$	LT + B-stab		16.2(4)
$-1/2 \leftrightarrow -1/2$	-	6.1	125(3)
$-1/2 \leftrightarrow -1/2$	B-stab	5.3	26.8(4)
$-1/2 \leftrightarrow -1/2$	LT	3.6	20.39(15)
$-1/2 \leftrightarrow -1/2$	LT + B-stab	5.5	14.6(4)

Laser frequency noise can introduce a decoherence similar to those shown in Fig. 5.9 (Monz, 2011). However, the used 729 nm laser was locked to another stabilized 729 nm laser, see Ch. 4.8. Therefore, it can be assumed that magnetic field noise is the main contribution to the decoherence. The two used transitions have a magnetic field sensitivity ratio of 5. Thus in case the decoherence is solely caused by magnetic field noise the coherence times should scale also with 5, which is not fulfilled for the cases in absence of any magnetic field stabilization and line triggering without magnetic field stabilization. For the case of line-triggered experiments the main reason for the deviation may be found in the differently sampled 50 Hz noise amplitudes when the dark time is scanned. The deviations in the case without line trigger and magnetic field stabilization may be caused by different ambient noise due to the temporal separation of the measurements. The differences of rms B values between the two transitions for the case with active magnetic field stabilization outside the given standard deviations are small and can be attributed to the quality of the Gaussian fits to the coherence curves and small changes in the magnetic field fluctuations. The partial revival events, visible in Fig. 5.9 for the unstabilized and less pronounced for the case with activated magnetic field stabilization, occur at those times, where the experimental cycle time is a multiple of the 50 Hz period.

For estimations on the aluminum ion clock's error budget in Ch. 7.7.1 we take the average of the actively stabilized values without line triggering, labeled with *B-stab* in Tab. 5.1 and as uncertainty half the difference between these values: $\sqrt{\langle \Delta B^2 \rangle} = 27.6(8)$ nT.

5.2.3 Remarks on Improvements of the Magnetic Field Stability

As pointed out in the sections above, magnetic field noise is a limiting factor for coherence of the $^{40}\mathrm{Ca}^{+}$ qubits. However, as will be discussed in the systematic shifts analysis in chapter 7.7.1, the impact on the error budget of the $^{27}\mathrm{Al}^{+}$ clock is small due to the low sensitivity of the aluminum ion to the magnetic field. Nevertheless, further improvements on the stability of magnetic fields can be considered, since they influence the analysis of motional states and the contrast of QL pulses on $^{40}\mathrm{Ca}^{+}$ as will be pointed out in the next two chapters.

Experiments with the highest achieved coherence times of a few hundred microseconds to seconds comprise magnetic shields made of layers of μ-metal with attenuations 28 to 60 dB at frequencies between 0.01 to 1000 Hz (Ruster et al., 2016) and cryogenically cooled copper with attenuations between 30 to 40 dB at frequencies from 60 Hz to 1 kHz (Leopold et al., 2019).

5.3 Orientation of the radial modes

The Lamb-Dicke factors of the 729 nm laser ports have been measured by driving Rabi oscillations on GSC carrier and 1st-order BSB transitions on a single $^{40}\mathrm{Ca}^{+}$ ion and calculating the ratio of the measured Rabi frequencies. Using Eq. (2.49) the angles between laser and the orientations of the motional modes were inferred. In Tab. 5.2 the results for the three 729 nm laser ports, see Fig. 4.9, are shown.

Table 5.2: Lamb-Dicke factors and angle between laser beam and secular mode orientation of the 729 nm laser ports. The uncertainty of the Lamb-Dicke factors due to fitting errors is 3×10^{-4} and of the deduced angles 0.4°.

Mode	Diagonal 1	Diagonal 2	Top
Radial 1	0.0375 / 57.6°	0.0398 / 55.3°	0.0403 / 54.8°
Radial 2	0.0299 / 64.6°	0.0354 / 59.4°	0.0477 / 46.7°
Axial	0.0655 / 44.8°	0.0649 / 45.4°	0.0524 / 55.4°

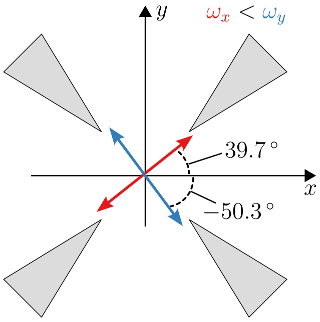

Figure 5.10: Orientation of radial modes inferred based on measurements of 729 nm Lamb-Dicke factors.

The deduced orientation angles and Lamb-Dicke factors are used as input for an optimization program, that calculates the orientation of the motional modes in the coordinate system of the linear Paul trap. The results are shown in Fig. 5.10. The radial modes are tilted by about 5 to 7° with respect to the RF blades, which are nominally oriented at 45° to the horizontal plane. When using the fitted radial mode directions with the best estimates on the laser beam orientations, deviations in the Lamb-Dicke factors of about 15 % are observed. Taking this uncertainty, as well as laser intensity fluctuations during the Rabi oscillation measurements and occasional re-aligning of laser beams onto the ions into account, a conservative estimate on the uncertainty of the laser beam orientations in the trap coordinate system is 5°, see Fig. 4.9 and Tab. 7.1.

5.4 Stability of Secular Frequencies

Coherent manipulations on the motional sidebands require these to be stable during experimental sequence. This is important for sideband cooling and quantum logic pulses, where a drifting sideband means a loss in fidelity of the respective operation.

In order to distinguish the instability of motional modes from other level-shifting effects, such as magnetic fields, a so-called Ramsey motion sequence is applied (Wineland et al., 1998). A coherent superposition of the 0 and 1 phonon Fock and electronic ground state $|\,{}^2\mathrm{S}_{-1/2}, n = 0\,\rangle + e^{i\phi(t)}|\,{}^2\mathrm{S}_{-1/2}, n = 1\,\rangle$ is used as starting state for a Ramsey interferometer measurement, which is depicted in Fig. 5.11. Because the superposition state has only contributions from a single internal energy level, its phase evolution $\phi(t)$ is only sensitive to the motional frequency ω_r, i.e. $\phi(t) = \omega_r t$. In consequence, the differential phase evolution between this state and the laser field is only sensitive to changes in the motional sidebands frequency. The excitation at the end of the Ramsey sequence has been monitored over a long period of time and has been pre-calibrated by a frequency scan, which gave the conversion factor from excitation to frequency excursion.

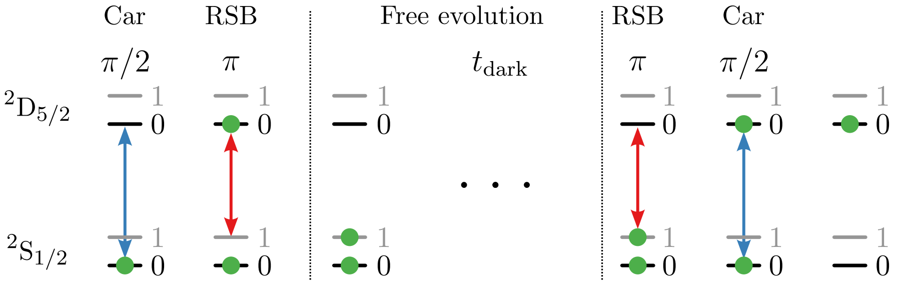

Figure 5.11: Ramsey motion sequence. Starting from a GSC $^{40}\mathrm{Ca}^+$ ion, a carrier $\pi/2$ pulse puts $^{40}\mathrm{Ca}^+$ in a superposition of ground and excited internal state. The subsequent π pulse on the RSB generates a superposition between the motional Fock states $|0\rangle$ and $|1\rangle$, whose phase evolution versus the laser phase during the dark time t_{dark} is largely independent of magnetic field noise. After the dark time the pulse sequence is reversed. All depicted lasers pulses are at 729 nm.

The results are shown in Fig. 5.12 as overlapping Allan deviations. For the radial sideband at longer times a stability curve has been added, which resulted from repeated scanning of the radial sideband frequency using Rabi interrogation. The stability of the radial modes is determined by the trap drive stability, which itself is limited by the temperature stability of the amplifier and Helical resonator in the RF signal chain. At best the radial sidebands are stable down to 100 Hz but start to drift away after 20 s. Over the course of a few days the radial frequency can drift by ≈ ±6.3 kHz. From these bounds we infer a rectangular uncertainty of 3.64 kHz[3] of the radial trap frequency (Metrology (JCGM/WG 1), 2008), which is equivalent to 0.07 dBm input trap drive power uncertainty around the typically applied value of 0.5 dBm before amplification. This is relevant for the assessment of the ac Zeeman shift in Ch. 7.7.2.1, where the trap drive stability is limiting the measurement accuracy of the shift. In order to improve on those values, an active trap drive stabilization is planned.

The axial sidebands inherit their stability from the low noise dc high voltage supplies, see Ch. 3.4.

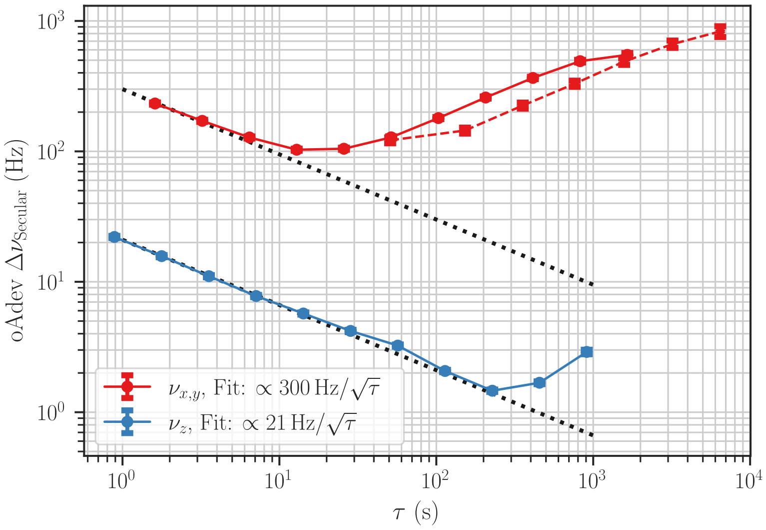

Figure 5.12: Stability of the radial (red) and axial (blue) secular frequencies from Ramsey motion experiments (solid line) and a resonance scan (dashed line). The radial x, y sidebands show the same stability.

Since the stability of the axial sidebands are superior to the radial, we use them for the QL operations.

5.5 Heating Rates

Ground-state cooling (GSC) is a necessary prerequisite for QL and for reducing the systematic shifts on the clock transition due to motion, see Ch. 6.1 and Ch. 7.4. The standard technique for GSC in this experiment is single EIT cooling, which was introduced in Ch. 2.4.3. An ideal GSC process cools the

---

[3] Some measurements indicated a correlation between a drifting room temperature in the laboratory and radial secular frequencies. The given uncertainty is $1/\sqrt{3}$ of the bounds given by the maximum measured secular frequency excursions.

^{27}Al$^+$-^{40}Ca$^+$ crystal into a thermal motional state with $\bar{n} \approx 0$. The population probability of $p(n = 0) \approx 1$ is particularly important for maximum contrast in QL spectroscopy, which will be described in Ch. 6.1. The systematic motional shifts in the absence of simultaneous sympathetic cooling are dominated by the heating rates $\dot{n}$ in this experiment.

The preparation of the ^{27}Al$^+$-^{40}Ca$^+$ crystal is achieved by Doppler cooling for 2 ms, followed by EIT cooling for 1.5 ms using a blue detuning with respect to the $m_S = -1/2 \to m_P = -1/2$ Doppler cooling transition of $\sim 3\Gamma$, where $\Gamma/(2\pi) = 20.7$ MHz. The temperature is either measured by fitting the RSB or BSB Rabi oscillations, using the property $p_{\mathrm{th}}(n+1) = p_{\mathrm{th}}(n)\bar{n}/(\bar{n}+1)$, to (Rasmusson et al., 2021)

$$P_{\uparrow}^{\mathrm{RSB}} = \frac{\bar{n}}{\bar{n}+1} \sum_{n=0}^{\infty} p_{\mathrm{th}}(n) \sin^2\left(\frac{\Omega_{n+1,n} t}{2}\right) \tag{5.15}$$

$$P_{\uparrow}^{\mathrm{BSB}} = \sum_{n=0}^{\infty} p_{\mathrm{th}}(n) \sin^2\left(\frac{\Omega_{n+1,n} t}{2}\right) , \tag{5.16}$$

with the thermal distribution $p_{\mathrm{th}}(n) = \bar{n}^n/(\bar{n}+1)^{n+1}$ and generalized Rabi-frequencies $\Omega_{n',n}$ (Eq. (2.39)), or by applying the ratio method using Eq. (2.57).

In Fig. 5.13 GSC cooled Rabi oscillations on the 1$^{\mathrm{st}}$-order BSBs are shown. The reached temperatures according to the fits of $\bar{n} = 0.16(1)$ and $0.13(1)$ for the in-phase (IP), and out-of-phase (OP) mode respectively, pose no significant limitation to the QL protocol. This can be seen by the reached contrast in excitation probability of $> 95\,\%$.

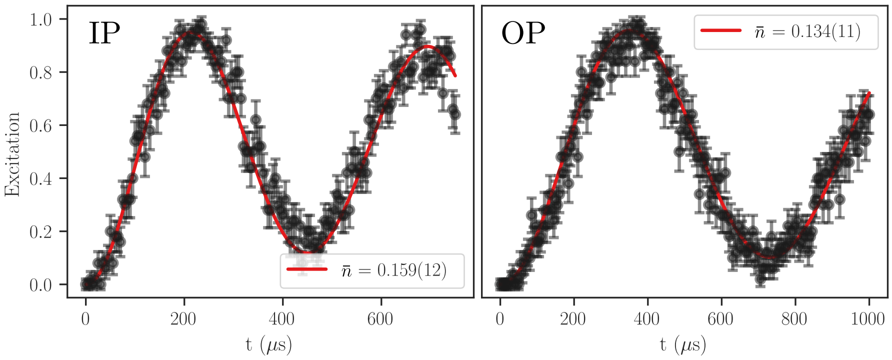

Figure 5.13: Rabi oscillations on the GSC axial IP and OP ^{27}Al$^+$-^{40}Ca$^+$ BSB of 1$^{\mathrm{st}}$-order.

The corresponding Rabi oscillations for the radial OP mode are shown in Fig. 5.14. We estimate temperatures of $\bar{n} = 0.45(25)$ from frequency scans over the RSB and BSB sidebands. The radial IP mode is difficult to measure as will be discussed below.

The heating rates are measured individually by at first GSC the respective mode, followed by measuring the 1$^{\mathrm{st}}$ order RSB and BSB excitation contrast after a delay time t. Using sideband ratio method Eq. (2.57) reveals $\bar{n}(t)$, which can be fitted by a linear function to give the heating rate $\dot{\bar{n}}$. In the upper panel of Fig. 5.15, the results for the axial modes of the ^{27}Al$^+$-^{40}Ca$^+$ crystal are shown.

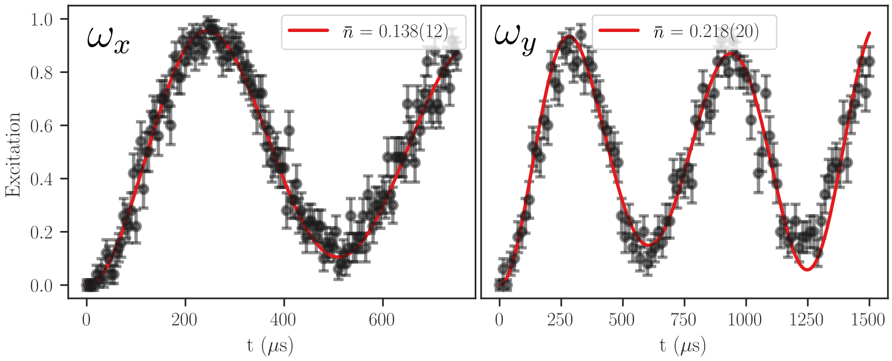

Figure 5.14: Rabi oscillations on the GSC radial OP ^{27}Al^{+}-^{40}Ca^{+} BSB of 1$^{\text{st}}$-order.

The measured axial heating rates of 56(5) ph/s for the IP, and 3.7(1.0) ph/s for the OP mode are comparable to the heating rates in a similar trap, where 70 ph/s and 0.8 ph/s have been measured (Guggemos et al., 2019). The x and y radial modes are almost degenerate in frequency, but show nevertheless dissimilar heating rates as can be seen in the middle and bottom panel of Fig. 5.15. The reason for this is currently unclear.

The radial IP mode is the most difficult to cool, because of the small contribution of the cooling calcium ion to this motion, see Tab. 2.3 in Ch. 2.5.2. The small mode amplitude of 0.157 also reduces the Lamb-Dicke factor of the 729 nm beam used for the temperature and heating rate measurements. In consequence, the required Rabi interrogation time of 1100 µs is on the order of the measured electronic coherence time and the total experimental data acquisition time of $\gtrsim$30 s exceeds the times during which the radial sideband start to drift away. An additional challenge is the small separation of the radial modes of 19 kHz, which causes off-resonant excitation of the neighboring modes at the laser powers used. High frequency laser noise also introduces off-resonant excitation on the carrier transition. Further improvements in magnetic field, trap drive power stability and laser noise reduction will improve the accuracy of the measurements of this mode.

The results of these measurements are summarized in Tab. 5.3. For the radial IP modes no reliable GSC BSB oscillations could be measured because due to small contrast on these sidebands. For the assessment of the time-dilation shift in Ch. 7.4 we therefore take a conservative estimate on the average motional occupation number of $\bar{n} = 0.45(25)$ for these modes, extrapolated from the heating rate measurements. In the future, the $\bar{n}$ of these modes will be assessed through sideband spectroscopy on the Al^{+} ion. It is important to note, that the motional state distribution after EIT cooling and in particular after typical clock interrogation heating times have to be studied in the future. As emphasized in Ref. (Hankin et al., 2019) and (Rasmusson et al., 2021) the motional state after a collision and after GSC, can become non-thermal. This has to be taken into account in the time-dilation evaluation. However, the proposed method in Ref. (Rasmusson et al., 2021) could not be applied with success in this experiment so far, because off-resonant excitation prevented coherent driving of higher-order GSC motional sidebands.

Lower temperatures can be reached when applying 1 to 5 SBC pulses after EIT cooling. This would lead to a higher QL contrast than that measured in

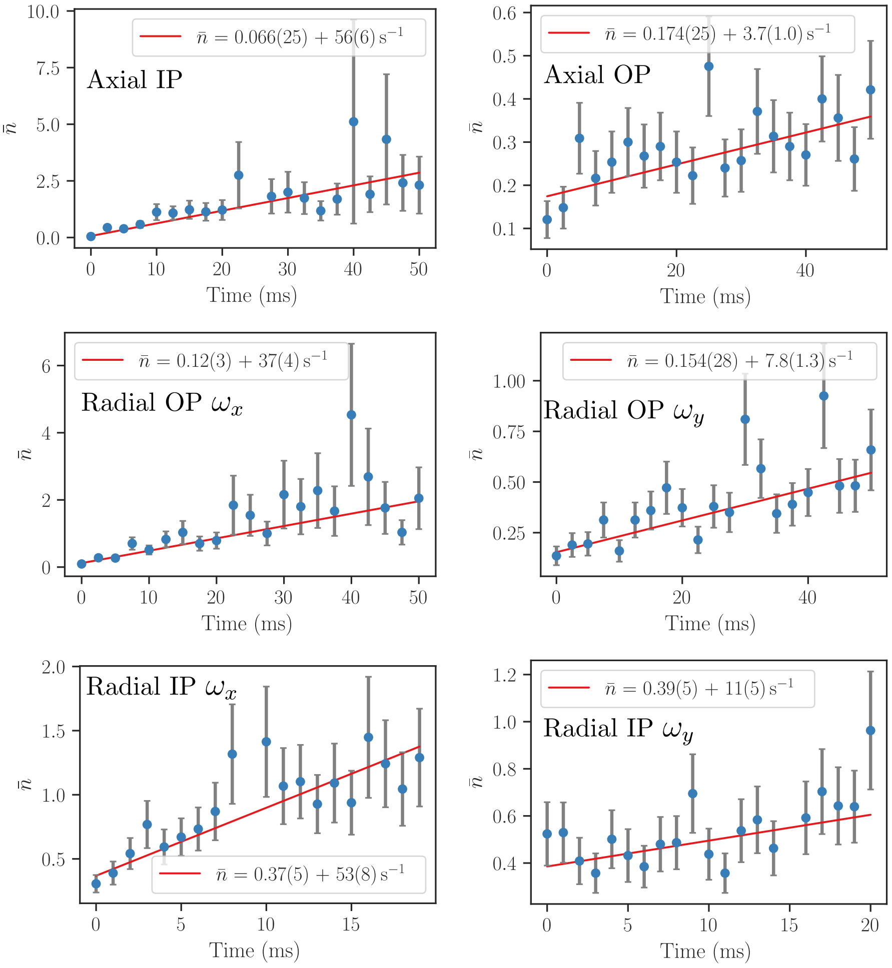

Figure 5.15: Heating rates of the ^{27}Al^{+}-^{40}Ca^{+} crystal. The top panels show the axial modes, the middle panel the radial OP modes, and the bottom panel the radial IP modes. The two radial modes are separated by 19 kHz with $\omega_x < \omega_y$. The given uncertainties are fitting errors.

Fig. 6.2. However, since the achieved contrast was sufficient to discriminate the ^{27}Al^{+} states, these additional pulses were not implemented. It should also be noted that the impact of the achieved $\bar{n}$ for the error budget is not significant, since the heating rates are on a level where they would cancel the benefits of a reduced initial time-dilation shift.

The heating rates in this experiment are slightly higher than those reported in other large ion traps (Brewer et al., 2019b) and significant higher than those that are reported in chip traps (Keller et al., 2015; Hannig, 2018; Kalincev et al., 2021). The latter often incorporate electronic filters on their in-vacuum carrier boards, which is an efficient way to reduce noise at the motional frequencies of the trapped ions.

Table 5.3: The ^{27}Al^{+}-^{40}Ca^{+} secular modes and their heating rates. IP = in-phase, OP = out-of-phase.

Mode	$\omega/(2\pi)$	$\bar{n}$	$\dot{n}$
axial IP	1.2 MHz	0.16(1)	56(6)
axial OP	2.15 MHz	0.13(1)	3.7(1)
radial OP x	1.72 MHz	0.14(1)	37(4)
radial OP y	1.739 MHz	0.22(2)	7.8(1.3)
radial IP x	2.76 MHz	0.45(25)	53(8)
radial IP y	2.779 MHz	0.45(25)	11(5)

5.6 Fast Polarization Switching

The linear Zeeman effect is eliminated in the clock cycle by probing the two outer $m_F = \pm 5/2$ ^{1}S$_0$ $\leftrightarrow$ ^{3}P$_0$ transitions. This is achieved through optical pumping via the ^{3}P$_1$ state of Al$^+$ and requires fast polarization switching of the corresponding logic laser beam (Ch. 4.9). "Fast" in this context means that this operation should not contribute to the dead time of the clock. Changing the polarization can be accomplished during those parts of the clock sequence that are carried out on the calcium ion. These are Doppler and EIT cooling as preparation for QL. Since the time needed for this is 2.5 to 10 ms, depending on the number of cooled modes, a switching speed faster than this is required. One possible alternative to the implemented method is a conventional quarter-wave plate that is installed in a rotation-mount. The required time for switching this plate exceeds 50 ms, due to the high inertia of the system and the long angle of 90° which must be traveled. Another alternative is to derive a second beam-path with rotated polarization from the logic lasers. This approach guarantees high switching speeds, but it requires separate AOMs and beam paths which is not cost and space efficient. UV Pockels cells are also available as a third alternative. These devices are resource-intensive as well and drifting of the polarization has been reported[4]. In the following, the fast polarization switch based on a galvanometer-driven rotation of a birefringent crystal is described. It is efficient since only one beam path is neccesary and the low-weighing crystal must only be rotated by angles of <20° and thus provides sufficiently high switching speeds.

The used zero-order wave plate[5] is made from two optically contacted quartz plates with 800 µm and 811.27 µm thickness. The fast axes of these y-cut plates are rotated by 90° to each other which results in a configuration where with normal incidence the retardation only depends on the thickness-difference of the plates, similar to an Ehringhaus-compensator (Rath, 1960). When these plates are tilted this is no longer the case, because one plate is tilted around its

---

[4] Private communication from a neighboring experiment.

[5] AR coated quartz plate from *Bernhard Halle Nachfl. GmbH*. This idea for fast polarization switching originates from Markus Greiner at Harvard University.

slow and the other around its fast axis. In this case the retardation depends on the angle of incidence.

In clock operation the logic beam at 267 nm is passing this retardation plate with cleaned linear polarization by using the transmission of a Glan-Laser polarizer. The quartz plate is fixed[6] to a rotatable galvanometer[7] axle with its slow axis pointing in bottom-up direction. The linear polarization vector of the laser beam is carefully aligned to have an angle of 45° with respect to the plate's effective fast axis, see Fig. 5.16. A rotation of the crystal along its slow axis results in a retardation difference between the electric field components along the fast and slow axis of the retarder.

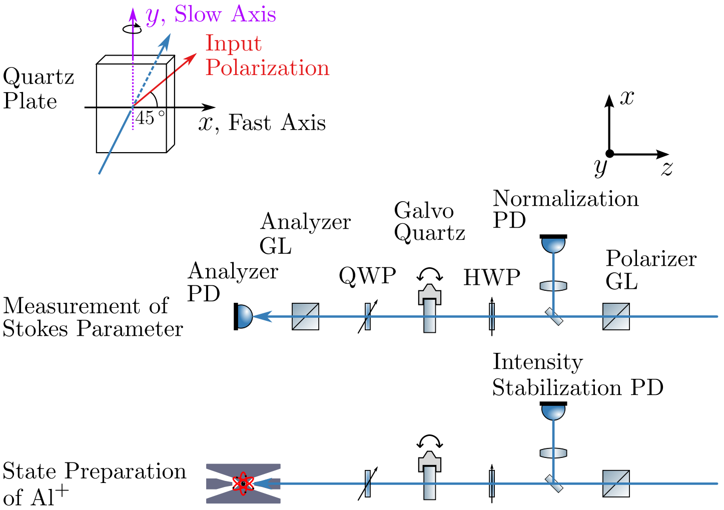

Figure 5.16: Setup for measuring the Stokes parameters of the polarization switcher and final setup for the state preparation of Al^+. The logic laser light (blue) is traveling from right to left. The quartz plate is mounted with its slow axis parallel to the rotation axis y. HWP: half-wave plate, QWP: quarter-wave plate, GL Glan-Laser polarizer, PD: photo diode.

We adjusted the quartz plate that the input beam receives $\lambda/2$ retardation at 0 V (0°) and λ at 6.6 V (8.25°), in good agreement to the expected value of 8.3°.

After the adjustment of the crystal we measured the Stokes parameters as described in Ref. (Berry, Gabrielse, and Livingston, 1977) in order to quantify the polarization state of the output light. The Stokes parameters for the two mentioned voltages ($U = 0\,\mathrm{V}$, $U = 6.6\,\mathrm{V}$) on the galvanometer and without the

---

[6] Glued with TorrSeal®.

[7] *Thorlabs* GVS 0.8 V/°.

quartz plate are inferred from fitting the Stokes parameters to the transmitted intensity

$$\begin{aligned} I_T(\alpha,\beta,\delta) = \frac{1}{2}\left[I + \left(\frac{M}{2}\cos(2\alpha) + \frac{C}{2}\sin(2\alpha)\right)(1+\cos(\delta))\right] \\ + \frac{1}{2}\left[S\sin(\delta)\sin(2\alpha - 2\beta)\right] \\ + \frac{1}{4}[(M\cos(2\alpha) - C\sin(2\alpha))\cos(4\beta) \\ + (M\sin(2\alpha) + C\cos(2\alpha))\sin(4\beta)]\,(1-\cos(\delta)) \;, \end{aligned} \tag{5.17}$$

with $\alpha = -45°$ (input polarization) and $\delta = 90°$ (retardation quarter-wave plate) and β the angle of the quarter-wave plate. The measurement outcome, depicted in Fig. 5.17, is that $S/I \approx 0$ which means the polarization is linear to a high degree.

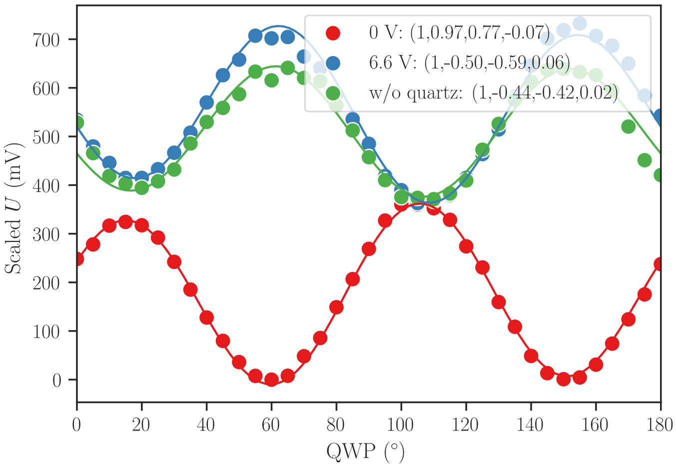

Figure 5.17: Normalized Stokes parameters (I, M, C, S) fitted to measured data for two quartz plate angles and without quartz. The parameter S quantifies the circularity of the polarization state of the light. As in all configurations shown the parameters is ≈ 0 the polarization is linear to a high degree.

We tested the switching speed of the galvanometer in the high precision mode[8]. We used an arbitrary waveform generator to trigger the galvanometer to move by 5 V. A speed of 1.9 V/ms has been measured, which means the galvanometer needs about 3.4 ms for the rotation of 8.25°.

Therefore, the installed polarization switch enables reliable generation of two orthogonal polarization states needed for the preparation of the aluminum ground state without introducing any additional dead time in the clock cycle. It should be noticed that the two linear polarization states of the logic light and the derived circular polarizations must be optimized on the Al^+ ion in the future.

---

[8] The galvanometer speed can be increased at the cost of smaller angle resolution.

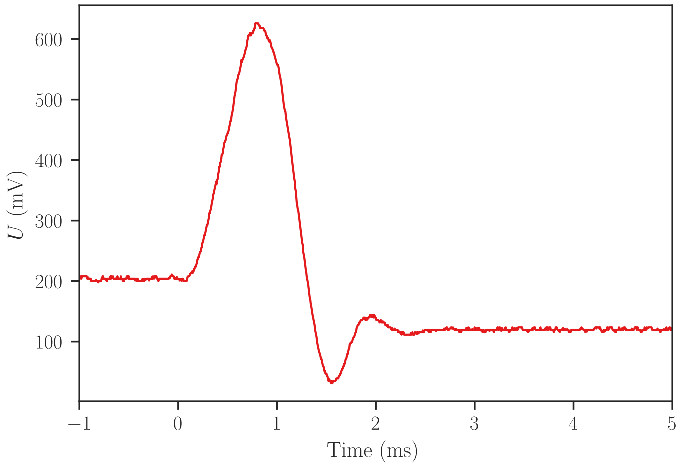

Figure 5.18: Switching time measurement. A TTL pulse triggers the galvanometer to move by 5 V which changes the transmission through an analyzer Glan Laser polarizer. The transmission is recorded on a photo diode. The slope is not linear because the light is elliptical when passing the GL.

6 Quantum Logic Spectroscopy of the ^{27}Al^{+} Clock Transition

This chapter presents the results of observing the ^{27}Al^{+} clock transition and coherent driving of it. The measurement has been conducted in the *old* vacuum system. The trap remained untouched during the work on the vacuum system, thus we expect a similar behavior in the upgraded vacuum system. The ^{27}Al^{+} clock laser at that time was referenced to the frequency comb, but not all fiber paths were phase stabilized. The quantization magnetic field at the time was 0.468 mT.

The chapter starts with a description of QL spectroscopy and how it was implemented for the observation of the ^{27}Al^{+} clock transition. Then the measurement results are presented in Ch. 6.2, followed by a brief discussion of QPN in Ch. 6.3. State detection errors are elaborated through *QuTiP* simulations in the beginning of Ch. 6.3.2 and a quantum non-demolition (QND) analysis is performed in Ch. 6.3.3.2.

6.1 Quantum Logic Spectroscopy

The lack of an accessible detection transition in ^{27}Al^{+} is overcome by employing a quantum logic (QL) protocol (Schmidt et al., 2005). This method consists of a sequence of 1$^{\text{st}}$-order blue sideband (BSB) and red sideband (RSB) laser pulses on the clock and the logic ion. These logic pulses thus add and remove one phonon from the shared motional system in dependence of the electronic state of the clock ion. This enables the transfer of electronic state information from the clock ion (here ^{27}Al^{+}) to the logic ion (here ^{40}Ca^{+}).

The QL protocol that we use to interrogate the ^{27}Al^{+}-^{40}Ca^{+} crystal is depicted in Fig. 6.1. The ions start in their electronic ground states and are cooled to their motional ground-state with $\bar{n} \approx 0$. A clock laser at 267.4 nm (violet) is attempting to excite ^{27}Al^{+} to the ^{3}P$_{0}$ clock state.

In the upper lane the clock excitation failed, leaving the ^{27}Al^{+} ion in its electronic ground state. A BSB pulse on the axial IP mode using the 267 nm laser excites in this case the ^{27}Al^{+} logic state ^{3}P$_{1}$ and adds at the same time a phonon to the ions' shared motional mode. A subsequent RSB pulse on ^{40}Ca^{+} with the 729 nm laser excites ^{40}Ca^{+} to the long-lived ^{2}D$_{5/2}$ state. In this state ^{40}Ca^{+} is dark for a final detection with the 397 nm laser, as depicted by the histogram of detected photons.

The bottom panel shows the protocol for a successful excitation of the ^{27}Al^{+} clock state. In this case the BSB excitation on ^{27}Al^{+} and RSB excitation on ^{40}Ca^{+} fails. The concluding state detection through the cycling transition on ^{40}Ca^{+} is successful and scatters photons with a high rate. Given our detection efficiency of 0.44 % (Ch. 3.5) and a detection time of 300 µs, the PMT records on average 25 photons for a bright Ca^{+} ion.

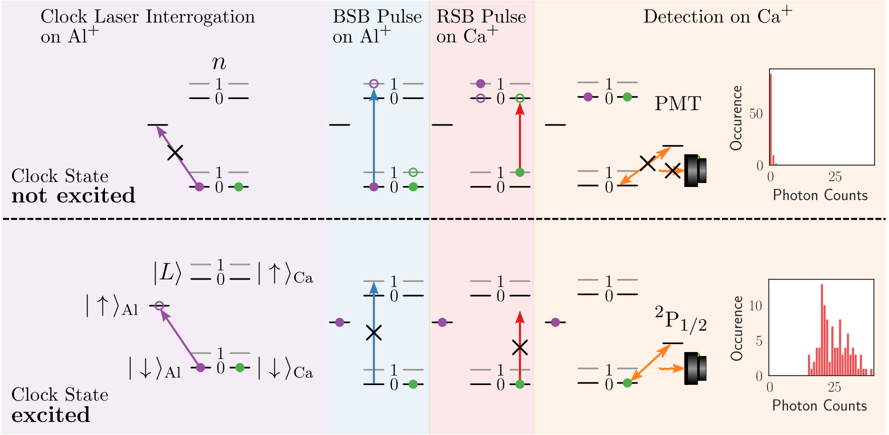

Figure 6.1: Quantum logic sequence used for interrogating and detecting the ^{3}P$_0$ clock state of the ^{27}Al$^+$ ion (purple dots). For better readability the energy levels are only drawn once in the lower panel. A series of sideband pulses transfers the internal state information from ^{27}Al$^+$ to the shared motional system with phonon number n and finally to the internal state information on ^{40}Ca$^+$. The clock laser at 267.4 nm (purple arrow) interrogates the ^{27}Al$^+$ clock transition ($|{\downarrow}\rangle_{\mathrm{Al}} \leftrightarrow |{\uparrow}\rangle_{\mathrm{Al}}$). The ^{27}Al$^+$ logic laser at 267 nm (blue arrow) drives the first BSB on the ^{27}Al$^+$ logic transition ($|{\downarrow}\rangle_{\mathrm{Al}} \leftrightarrow |L\rangle$). On ^{40}Ca$^+$ (green dots) a RSB is driven ($|{\downarrow}\rangle_{\mathrm{Ca}} \leftrightarrow |{\uparrow}\rangle_{\mathrm{Ca}}$) using 729 nm light (red arrow) if the previous BSB excitation was successful. A 397 nm laser (orange arrow) drives the cycling ^{2}S$_{1/2} \leftrightarrow {}^2P_{1/2}$ on ^{40}Ca$^+$ from which fluorescence is detected by a PMT. Repeating the experiments under the same conditions several times results in the shown histograms.

Fig. 6.2 shows a Rabi oscillation on the axial in-phase BSB on the ^{27}Al$^+$ logic transition with the ^{27}Al$^+$ initially prepared in the ground state. When the laser interrogation time is tuned to the π time of $\approx 35\,\mu$s, the QL contrast reaches more than 70 %. This is taking into account the excitation offset of roughly 8 % at 0 µs.

To summarize, in the implemented QL and detection sequence the PMT detects no photons, if the ^{27}Al$^+$ clock state is not excited and it detects many photons, if the clock state is excited. For the measurements presented in the following a QND detection protocol was applied. For this the described QL sequence including GSC, sideband transitions and detection was repeated ten times (ten QND detection cycles), which is possible since these operations do not disturb the excited clock state.

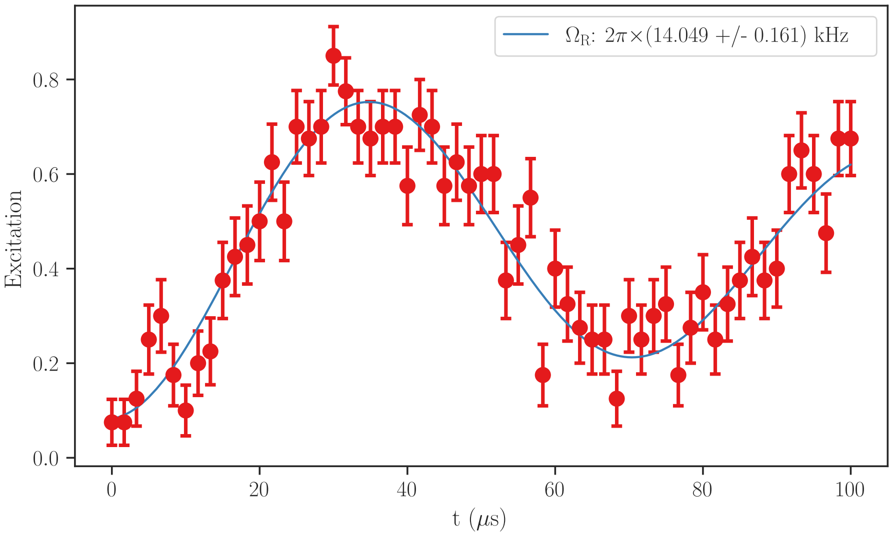

Figure 6.2: Scan of the $^{27}\mathrm{Al}^+$ logic laser Rabi time on the axial IP BSB. The Rabi oscillation was made visible by the subsequent 729 nm π-pulse on the axial IP RSB.

6.2 Observation of the Clock Transition

In this chapter the results of the clock transition frequency scans are presented.

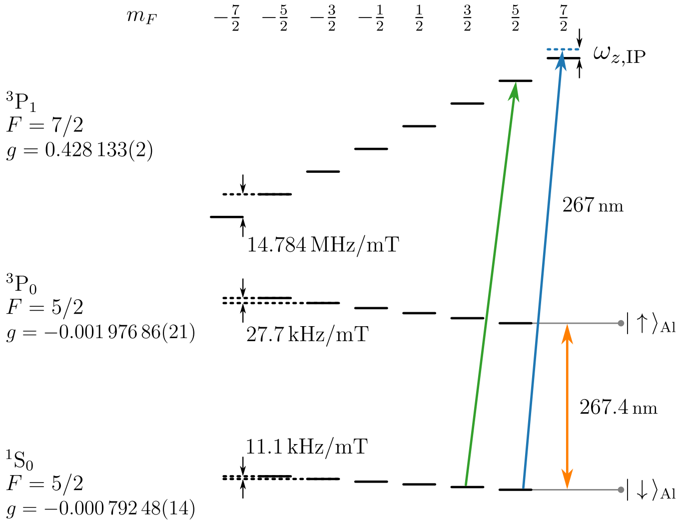

Figure 6.3: Level scheme of $^{27}\mathrm{Al}^+$ (not to scale). The $^1\mathrm{S}_0 \leftrightarrow {}^3\mathrm{P}_1$ $^{27}\mathrm{Al}^+$ logic transition enables $^{27}\mathrm{Al}^+$ state preparation (green) and QL pulses on the axial in-phase BSB (blue) with $\omega_{z,\mathrm{IP}} \approx 2\pi \times 1.1$ MHz detuning from the closed σ^+ $m_F = 5/2 \leftrightarrow m_F = 7/2$ transition. In this experiment the outer lying $m_F = 5/2 \leftrightarrow m_F = 5/2$ clock transition between $^1\mathrm{S}_0 \leftrightarrow {}^3\mathrm{P}_0$ has been probed (orange). Also shown are the Zeeman splittings, which are small for the ground and excited clock state, and the Landé g-factors, which have been taken from Ref. (Rosenband et al., 2007) for the excited clock and ground state and from Ref. (Guggemos et al., 2019) for the logic state.

In Fig. 6.4 the sequence used for detection of the clock transition is shown and in Fig. 6.3 the relevant energy levels of $^{27}\mathrm{Al}^+$ are depicted. The sequence is built on the repetitive detection of the $^{27}\mathrm{Al}^+$ state using the QL sequence

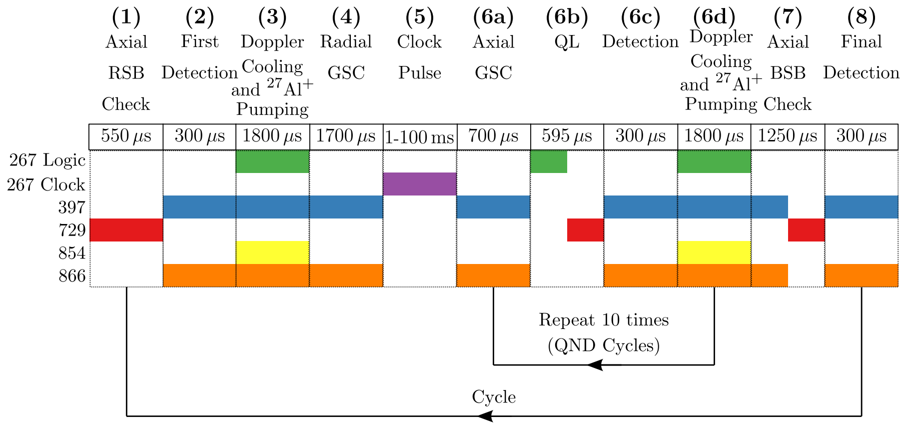

Figure 6.4: Clock interrogation cycle sequence.

described above. The following experiment was repeated 40 times at a fixed laser frequency and interrogation time.

(1) The sequence starts with testing, if the ^{27}Al$^+$-^{40}Ca$^+$ crystal is still apparent in the trap and ready for interrogation by a 729 nm RSB pulse on the axial in-phase RSB (550 µs).

(2) A signal of approximately 50 % sideband excitation is usually detected (300 µs), because the ions are at Doppler temperature.

(3) The preparation for the clock interrogation begins with sympathetic Doppler cooling of ^{27}Al$^+$ by the two orthogonal 397 nm laser beams on ^{40}Ca$^+$ (1800 µs) (Ch. 4.7). During this Doppler cooling, a series of 20 σ^+-polarized ^{27}Al$^+$ logic light π-time pulses on the $\left|^1\mathrm{S}_0\,, m_F = +3/2\right\rangle \longrightarrow \left|^3\mathrm{P}_1\,, m_F = +5/2\right\rangle$ carrier transition pump the ^{27}Al$^+$ population into the $m_F = 5/2$ state.

(4) Two consecutive single EIT pulses cool the radial modes to $\bar{n} \approx 0.2$ (700 µs+1000 µs). The axial modes are pre-cooled by these pulses.

(5) Then all lasers are turned off and the clock laser is turned on for an interrogation time t_{clk} (1 to 100 ms). For the data presented here, only the $|\,^1\mathrm{S}_0\,, m_F = +5/2\,\rangle \leftrightarrow |\,^3\mathrm{P}_0\,, m_F = +5/2\,\rangle$ transition was investigated, because in-sequence polarization switching, see Ch. 5.6, was not implemented at this time. The clock laser excitation pulse puts ^{27}Al$^+$ into a superposition state

$$|\psi\rangle_0 = \alpha\,|{\downarrow}\rangle_{\mathrm{Al}} + \beta\,|{\uparrow}\rangle_{\mathrm{Al}} \quad . \tag{6.1}$$

(6) After clock state interrogation, the clock laser is turned off and a repetitive sequence of cooling and detection is applied.

(6a) It starts with axial ground state cooling by a single EIT pulse on the axial in-phase (ax IP) sideband with $\omega_{\mathrm{ax\ IP}} \approx 2\pi{\times}1.1$ MHz, preparing the ions in the axial ground state $\bar{n}_{\mathrm{ax\ IP}} \approx 0$ (700 µs).

(6b) A BSB pulse on the $\left|^1\mathrm{S}_0\,, m_F = +5/2\right\rangle \leftrightarrow \left|^3\mathrm{P}_1\,, m_F = +7/2\right\rangle$ transition using the 267 nm ^{27}Al$^+$-logic laser and a subsequent RSB pulse at 729 nm (45 µs+550 µs) on the same motional mode are used for the QND detection protocol. An ideally working QL operation creates an entangled state between ^{27}Al$^+$ and ^{40}Ca$^+$:

$$|\psi\rangle_{\mathrm{QL}} = (\alpha\,|{\downarrow}\rangle_{\mathrm{Al}} + \beta\,|{\uparrow}\rangle_{\mathrm{Al}})\,|{\downarrow}\rangle_{\mathrm{Ca}} \rightarrow \alpha\left|^3\mathrm{P}_1\right\rangle_{\mathrm{Al}}|{\uparrow}\rangle_{\mathrm{Ca}} + \beta\,|{\uparrow}\rangle_{\mathrm{Al}}\,|{\downarrow}\rangle_{\mathrm{Ca}} \quad . \tag{6.2}$$

Since the RSB pulse time exceeds the natural lifetime of the $^3\mathrm{P}_1$ state of $\approx$305 µs, $^{27}\mathrm{Al}^+$ will already be decayed to the $m_F = 7/2$ ground state before detection. Therefore, the following state is subject to detection on the Ca^+ ion

$$|\psi\rangle_{\text{Before Detection}} = \alpha\,|{\downarrow}\rangle_{\text{Al}}\,|{\uparrow}\rangle_{\text{Ca}} + \beta\,|{\uparrow}\rangle_{\text{Al}}\,|{\downarrow}\rangle_{\text{Ca}}\ . \tag{6.3}$$

(6c) As consequence of this QND detection sequence, $^{40}\mathrm{Ca}^+$ will be detected to be *dark* (*bright*) if the $^{27}\mathrm{Al}$ clock state has (not) been excited (300 µs). A threshold of 11 photon counts was applied in order to discriminate between the two events. This projective state detection of $^{40}\mathrm{Ca}^+$ collapses Eq. (6.3) to

$$|\psi\rangle_{\text{After Detection}} = |{\downarrow}\rangle_{\text{Al}}\,|{\uparrow}\rangle_{\text{Ca}} \tag{6.4}$$

or

$$|\psi\rangle_{\text{After Detection}} = |{\uparrow}\rangle_{\text{Al}}\,|{\downarrow}\rangle_{\text{Ca}}\ , \tag{6.5}$$

depending on what was measured by the PMT.

(6d) After detection, both ions are Doppler cooled and $^{27}\mathrm{Al}^+$ is re-prepared as in step (3) (1800 µs). Due to the limited fidelity of the overall readout process a single sequence of (6) gives a detection error of $\approx$10 to 20 %. Repeating step (6) 10 times reduces the $^{27}\mathrm{Al}^+$ state detection fidelity to on average 0.051 % using a QND analysis method, see Ch. 6.3.3.2.

(7) In order to check if $^{27}\mathrm{Al}^+$-$^{40}\mathrm{Ca}^+$ is still present in the trap and GSC is working, a sequence of a single EIT cooling pulse on the axial in-phase sideband followed by a 729 nm BSB pulse on $^{40}\mathrm{Ca}^+$ is applied (700 µs + 550 µs).

(8) A final detection pulse gives a positive result ($^{27}\mathrm{Al}^+$-$^{40}\mathrm{Ca}^+$ ion crystal healthy) if $\approx$ 0 photons are counted (300 µs). This signal acts at the same time as an estimate on the achievable contrast during the QL sequences.

A technical challenge in measuring the clock transition by QL in $^{27}\mathrm{Al}^+$ is a lack of electronic state reinitialization, e.g. through repumping. Therefore, once excited, $^{27}\mathrm{Al}^+$ will stay in the $^3\mathrm{P}_0$ state, unless it spontaneously decays with a rate of $\sim 1/20.6\,\mathrm{s}$, given by the natural lifetime of the transition, or by deexcitation through the clock laser. One way to deterministically prepare the electronic ground state is via a RSB pulse on the clock transition with a ground state cooled $^{27}\mathrm{Al}^+$-$^{40}\mathrm{Ca}^+$ crystal. Subsequent GSC and repetition of the sequence can prepare the Al^+ $^1\mathrm{S}_0$ state with high fidelity. However, the clock transition frequency and RSB π times need to be well known to be efficient.

For the observations of the clock transition presented in this thesis, this was not the case. In order to avoid waiting for $^{27}\mathrm{Al}^+$ to decay to its ground state by spontaneous emission, the resonance signal was extracted from state changes between the ground state and excited state of $^{27}\mathrm{Al}^+$. This is also preferred for clock operation, because of the reduced dead-time.

We evaluated the collected data in the following way: In cycle c we counted the number of *dark* n^c_{dark} and *bright* n^c_{bright} events at (6c)[1]. Histograms of these events, depicted in Fig. 6.5, show a significant difference away and near the estimated transition frequency. It can be seen that it is highly probable to

---

[1] In Fig. D.3 and D.4 in the appendix Ch. D two collections of these measured photon-count-sets at detunings far away and near the clock resonance are shown.

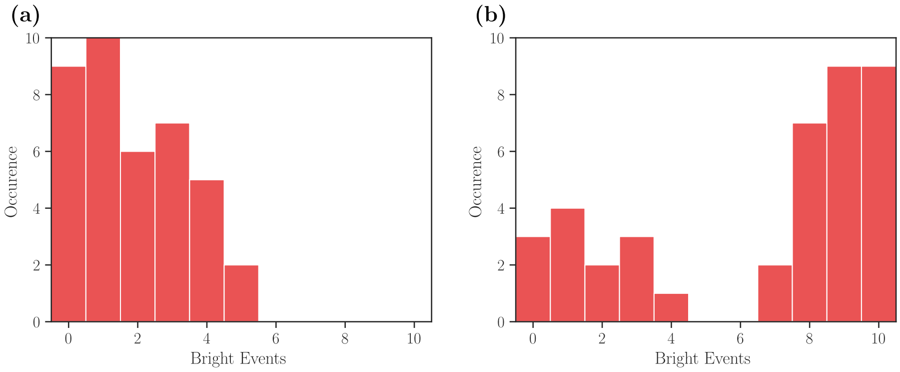

Figure 6.5: Histograms of counted bright states at constant clock laser frequency, summed over all $N = 40$ cycles, (a) away from the resonance and (b) near the resonance. There is a separation at 6 gates, which suggests to use this as a threshold in order to decide if the Al^{+} ion was excited or not.

observe ≥6 *bright* events near the resonance and <6 far away. We therefore counted ^{27}Al^{+} to be excited if $n^{c}_{\text{bright}} \geq 6$. In this case the cycle is flagged as $F_c = 1$, otherwise $F_c = 0$. A different approach of determining the state is presented in Ch. 6.3.3.2, where instead of using a threshold as discriminator between the two events, a conditional probability analysis of the measured PMT counts is applied (QND evaluation method). Assuming that the state of ^{27}Al^{+} is preserved either in the excited state, if it was previously detected to be in that state, or to be again prepared in the correct $\left|{}^{1}\mathrm{S}_0, m = +5/2\right\rangle$ state, we calculate the overall state-changing laser-atom interaction probability by taking the mean of the occurrence of state changes between *excited* ⟶ *not excited* and *not excited* ⟶ *excited*, i.e.,

$$P(\text{excitation}) = \frac{1}{N-1} \sum_{c=1}^{N-1} \delta_{(F_c + F_{c+1}),1} \,, \tag{6.6}$$

with $\delta_{i,j} = 1$ for $i = j$, and $= 0$ else and $N = 40$ in the conducted measurements.

Using this sequence and evaluation scheme we observed the clock transition $\left|{}^{1}\mathrm{S}_0, m = +5/2\right\rangle \leftrightarrow \left|{}^{3}\mathrm{P}_0, m = +5/2\right\rangle$ with linewidths down to $\approx$10 Hz, as shown in Fig. 6.6. The linewidth was likely limited by uncompensated fiber noise and insufficient transfer-lock performance as described in Ch. 4.10.3. We expect a significant improvement on this in the near future, aiming at linewidths of $\approx$1 Hz and below. In Fig. 6.7 coherent Rabi oscillations on this clock transition are shown, taken at different laser powers compared to the frequency scan in Fig. 6.6.

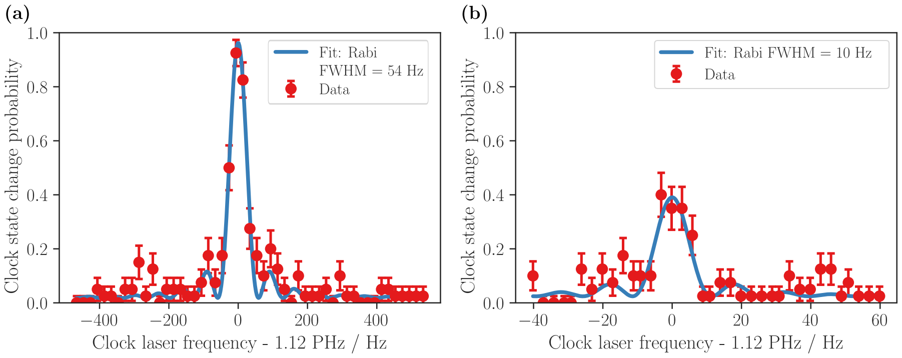

Figure 6.6: Clock transition data with different clock laser interrogation times: (a) 15 ms, (b) 75 ms. Data points (red) are fitted to a Rabi lineshape (blue) with a linewidth of 54 Hz and 10 Hz. The error bars correspond to QPN of the $^{40}\mathrm{Ca}^{+}$ detection of the bright state using the threshold technique for $^{40}\mathrm{Ca}^{+}$ and evaluation of the clock state change probability.

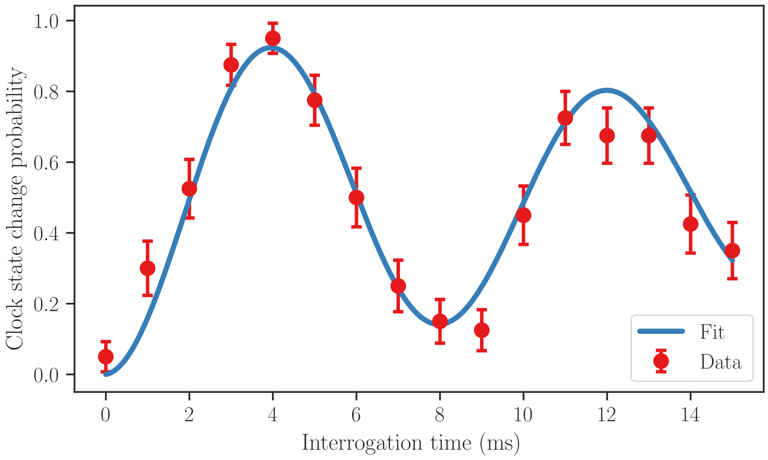

Figure 6.7: Rabi oscillation data (red) on the clock transition, fitted to a Rabi oscillation with frequency $\Omega \approx 2\pi \times 125$ Hz (blue). The error bars correspond to QPN of the $^{40}\mathrm{Ca}^{+}$ detection of the bright state using the threshold technique for $^{40}\mathrm{Ca}^{+}$ and evaluation of the clock state change probability.

6.3 Error of State Detection

Because of the quantum nature of this experiment, the measurement outcome is subject to quantum projection noise (QPN) (Itano et al., 1993), i.e., it is random to which state the ion collapses in a single detection cycle. That means, even though $^{27}\mathrm{Al}^{+}$ was excited to the clock state, detection can project into either Eq. (6.4) or (6.5). The experiment has therefore to be repeated to decrease the QPN, see Ch. 6.3.1.

The projection to Eq. (6.4) or (6.5) only holds in a closed system with flawlessly working state preparation, QL and detection steps. Even though this experiment is approximating this situation very well, it is not perfect. Noise, decoherence processes and leakage to other states have an influence on the measured signal, as well as on the effect the detection has on the state of $^{27}\mathrm{Al}^{+}$ before the next cycle. The remainder of this chapter is dedicated to elaborate on this and to provide estimated numbers on the detection fidelity.

In the following Ch. 6.3.2 *QuTiP* simulations suggest that the repetitive measurement in some circumstances even can change the projection of the partially collapsed state. In Ch. 6.3.3 the errors for the indirect, repeated detection of the ^{27}Al$^+$ clock state using QND protocols on the ^{27}Al$^+$-^{40}Ca$^+$ ion pair, as presented in Ch. 6.2, are elaborated. The analysis is based on QND measurement theory, briefly introduced in the Ch. 6.3.3, closely following (Hume, 2010). Subsequently QND concepts are applied on ^{40}Ca$^+$ and ^{27}Al$^+$ state detection.

6.3.1 Quantum Projection Noise

The error bars on data points achieved by projective measurements onto the ground state $|\downarrow\rangle_{\mathrm{Ca}}$ of ^{40}Ca$^+$ with the projection operator $\hat{P}_{\downarrow_{\mathrm{Ca}}} = |\downarrow\rangle\,\langle\downarrow|_{\mathrm{Ca}}$, are QPN. This includes all measurements on single ^{40}Ca$^+$ and ^{40}Ca$^+$-^{27}Al$^+$ crystals, based on collected 397 nm photons by the PMT. QPN can be calculated from the variance of the projective measurement (Itano et al., 1993; Ludlow et al., 2015). With $|c_{\downarrow_{\mathrm{Ca}}}|^2 = p_{\downarrow_{\mathrm{Ca}}}$ being the expectation value and the probability to find ^{40}Ca$^+$ in the ground state the variance is given by

$$\langle(\Delta\hat{P}_{\downarrow_{\mathrm{Ca}}})^2\rangle = p_{\downarrow_{\mathrm{Ca}}}(1 - p_{\downarrow_{\mathrm{Ca}}}) \ . \tag{6.7}$$

The uncertainty in measuring a state population due to the standard error $u(\hat{P}(\downarrow_{\mathrm{Ca}}))$ connected to the variance in Eq. (6.7) averages down with the standard error of the mean by $u(\hat{P}_{\downarrow_{\mathrm{Ca}}})/\sqrt{N}$ with N the number of experiments. For the error bars in this work, a tiny correction to this QPN due to quantization noise from finite number of experimental trials has been added

$$\text{Error} = \sqrt{\frac{p_{\downarrow_{\mathrm{Ca}}}(1 - p_{\downarrow_{\mathrm{Ca}}})}{N} + \frac{1}{N^2}}\ , \tag{6.8}$$

preventing the measurement error to become zero for $p_{\downarrow_{\mathrm{Ca}}} = 1$ or 0.

In general, the projective measurement of an atomic system S that is in the state $|S\rangle$ gives e.g. the measurement result a_n. The measurement projects the state $|S\rangle$ onto the eigenstate $|u_n\rangle$ of the projector operator $\hat{P}_A$ that belongs to the measured (non-degenerate) eigenvalue a_n. This type of measurement is called direct measurement. Because of the collapse of the wavefunction any repetitive measurement on the already measured state would give the same result (a_n). This is not necessarily the case for the indirect measurement, where some property of the system S is measured by a measurement on an auxiliary (meter) system M.

6.3.2 QuTiP Simulations of the Clock Transition Measurement

In order to learn more about the applied detection scheme of the clock transition presented in Ch. 6.2 simulations with *QuTiP* (Johansson, Nation, and Nori, 2012; Johansson, Nation, and Nori, 2013) were carried out. *QuTiP* is a Python framework capable to simulate quantum dynamics in open systems. Before the simulation results are shown, a brief collection of expectations and information about how the simulation was set up is given. The result of this chapter includes the finding of conditional error probabilities, which are used for the QND evaluation of the clock transition in Ch. 6.3.3.2.

The *QuTiP* simulations will include non-perfect QL pulses and thermal distributions of the motional Fock states $|n\rangle_m$. The effect of non-ideal BSB and RSB QL pulses is that the state before detection can be written as a

$$\begin{aligned} |\psi\rangle = \tilde{\alpha}\ |0\rangle_m |\uparrow\rangle_{\mathrm{Al}} |\downarrow\rangle_{\mathrm{Ca}} + \alpha\beta\ |0\rangle_m |\downarrow\rangle_{\mathrm{Al}} |\downarrow\rangle_{\mathrm{Ca}} \\ + \alpha\tilde{\beta}\tilde{\gamma}\ |0\rangle_m \left|{}^3\mathrm{P}_1\right\rangle_{\mathrm{Al}} |\uparrow\rangle_{\mathrm{Ca}} + \alpha\tilde{\beta}\gamma\ |1\rangle_m \left|{}^3\mathrm{P}_1\right\rangle_{\mathrm{Al}} |\downarrow\rangle_{\mathrm{Ca}}\ . \end{aligned} \tag{6.9}$$

For perfect logic π pulses the coefficients $\beta = \gamma = 0$ and $\tilde{\beta} = \tilde{\gamma} = 1$ up to a phase factor, which is not relevant, since the two operations were made on different ions. After spontaneous decay of the ${}^3\mathrm{P}_1$ state the collapsed states after a projective measurement on ${}^{40}\mathrm{Ca}^{+}$ are

$$|\psi\rangle_{\text{collapsed}} = \tilde{\alpha}\, |0\rangle_m |\uparrow\rangle_{\mathrm{Al}} |\downarrow\rangle_{\mathrm{Ca}} + \alpha\beta\, |0\rangle_m |\downarrow\rangle_{\mathrm{Al}} |\downarrow\rangle_{\mathrm{Ca}} + \alpha\tilde{\beta}\gamma\, |1\rangle_m |\downarrow\rangle_{\mathrm{Al}} |\downarrow\rangle_{\mathrm{Ca}} \tag{6.10}$$

or

$$|\psi\rangle_{\text{collapsed}} = \alpha\tilde{\beta}\tilde{\gamma}\, |0\rangle_m |\downarrow\rangle_{\mathrm{Al}} |\uparrow\rangle_{\mathrm{Ca}}\ . \tag{6.11}$$

Therefore, when ${}^{40}\mathrm{Ca}^{+}$ is measured to be in its excited state, the combined state collapses state will be very likely a pure state with ${}^{27}\mathrm{Al}^{+}$ in its ground state, independent of the quality of the QL pulses. On the other hand detecting ${}^{40}\mathrm{Ca}^{+}$ in its ground state will project the total system to a pure entangled state between ${}^{40}\mathrm{Ca}^{+}$ and ${}^{27}\mathrm{Al}^{+}$ in its excited state.

More realistic assumptions about the motional state include thermal or double thermal distributions, see Ch. 2.4, which can be caused by sideband cooling (Rasmusson et al., 2021) or collisional heating (Hankin et al., 2019). It is expected that these effects have little influence on the efficiency of the applied QL pulses since the probability of the motional $n = 0$ state is still the highest and small linewidth lasers make couplings to higher Fock states, which are resonant at higher detunings from the carrier, very small, even if there is significant population.

The starting state of the simulations is set to the product state with the motion and ${}^{27}\mathrm{Al}^{+}$ and ${}^{40}\mathrm{Ca}^{+}$ in their ground states.

$$|\psi(t = 0)\rangle = |0\rangle_m |\downarrow\rangle_{\mathrm{Al}} |\downarrow\rangle_{\mathrm{Ca}}\ . \tag{6.12}$$

The dimension of the motional state, i.e., the number of accessible Fock states can be defined. In this simulation the maximum Fock state number is set to five. Coherent interaction between laser and ions are defined by Hamiltonians given by Eq. (2.45) to (2.47).

Incoherent processes are taken into account in *QuTiP* by expanding the Hilbert space of the system to that including the environment, such that the total density matrix is governed by the von Neumann equation (Schwabl and Brewer, 2006)

$$\dot{\hat{\rho}}_{\mathrm{tot}} = -\frac{i}{\hbar}\left[\hat{H}_{\mathrm{tot}}, \hat{\rho}_{\mathrm{tot}}(t)\right] \ , \tag{6.13}$$

where $\hat{H}_{\mathrm{tot}} = \hat{H}_{\mathrm{sys}} + \hat{H}_{\mathrm{env}} + H_{\mathrm{int}}$ is the total Hamiltonian, comprised of Hamiltonians of the system of interest, the environment and the interaction between system and environment. Tracing out the environment such that $\hat{\rho} = \mathrm{Tr}_{\mathrm{env}}(\hat{\rho}_{\mathrm{tot}})$ gives the Lindblad master equation

$$\dot{\hat{\rho}}(t) = -\frac{i}{\hbar}\left[\hat{H}(t), \hat{\rho}(t)\right] + \sum_n \frac{1}{2}\left[2C_n\hat{\rho}(t)C_n^\dagger - \hat{\rho}(t)C_n^\dagger C_n - C_n^\dagger C_n\hat{\rho}(t)\right] \ . \tag{6.14}$$

The environment and system are coupled by collapse operators $C_n = \sqrt{\gamma_n}\hat{A}_n$ defined by $\hat{H}_{\mathrm{int}}$, where γ_n is a rate and $\hat{A}_n$ describes the coupling. In *QuTiP* we define heating of 80 phonons/s by

$$\begin{aligned}\hat{C}_{\mathrm{heating},1} &= \sqrt{80/\mathrm{s}}\ \hat{a}\\ \hat{C}_{\mathrm{heating},2} &= \sqrt{80/\mathrm{s}}\ \hat{a}^\dagger \ ,\end{aligned} \tag{6.15}$$

and spontaneous emission of for example the ^{27}Al$^+$ ^{3}P$_1$ logic state to the ground state by

$$\hat{C}^{\mathrm{Al}}_{\mathrm{spont.\ emission}} = \sqrt{1/300\,\mu\mathrm{s}}\ \hat{\sigma}^{\mathrm{Al}}_- \ , \tag{6.16}$$

with $\sigma^{\mathrm{Al}}_- = |{\downarrow}\rangle\left\langle {}^3\mathrm{P}_1\right|_{\mathrm{Al}}$. The repreparation of the electronic ^{40}Ca$^+$ ground state after detection is performed with a similar collapse operator, where the rate has been set to a high value, which models the situation where the clear-out laser at 854 nm deexcites $|{\uparrow}\rangle_{\mathrm{Ca}}$. The logic pulses and heating will increase the motional quantum number of the system, therefore GSC after clock laser interrogation and detection was implemented by collapse operators

$$\begin{aligned}\hat{C}_{\mathrm{cooling},1} &= \sqrt{1\times 10^5/\mathrm{s}}\ (1 + n_{\mathrm{init}})\hat{a}\\ \hat{C}_{\mathrm{cooling},2} &= \sqrt{1\times 10^5/\mathrm{s}}\ n_{\mathrm{init}}\hat{a}^\dagger \ ,\end{aligned} \tag{6.17}$$

where this definition of collapse operators ensures to reprepare the target GSC $\bar{n}$ which is denoted n_{init} here and which was tested in the simulation.

The program flow is depicted below.

1. Set a clock laser detuning and define all laser pulse times.
2. Time evolution with carrier clock laser Hamiltonian.
3. Time evolution with cooling collapse operator.
4. Time evolution with BSB Hamiltonian interaction on ^{27}Al$^+$.
5. Time evolution with RSB Hamiltonian interaction on ^{40}Ca$^+$.

6. Measurement, in which *QuTiP* chooses the projection of the evolved state onto $|\downarrow\rangle\langle\uparrow|_{\mathrm{Ca}}$ or $|\uparrow\rangle\langle\uparrow|_{\mathrm{Ca}}$ according to their probability.
7. Time evolution with cooling and spontaneous decay collapse operators to model cooling and repreparation of ^{40}Ca$^+$ to its ground state.

Table 6.1: Decoherence settings in the *QuTiP* simulations for producing Fig. 6.10. The π-times for the BSB pulse and RSB pulse are 50 µs and 550 µs, respectively.

Setting	Motional state	Spont. emiss. during BSB	Heating	Pulse time BSB / RSB
1	Fock $|0\rangle$	No	No	π
2	Fock $|0\rangle$	Yes	No	π
3	Fock $|0\rangle$	No	Yes	π
4	Fock $|0\rangle$	No	No	0.8π / 0.91π
5	thermal $\bar{n} = 0.15$	No	No	π
6	thermal $\bar{n} = 0.15$	Yes	Yes	0.8π / 0.91π

The simulation tries to mimic the experiment by repeating steps (3) to (7) 10 times before another clock laser interrogation in step (2) and with a given detuning, 40 clock laser interrogations were simulated. Several simulation parameters have been varied in order to study the influence of different decoherence processes. In total 6 settings have been tested. They are listed in Tab. 6.1. They range from the most ideal situation (setting 1), which represents Eq. (6.3), over non-ideal QL pulses (setting 4/5) which mirror Eq. (6.9), to a situation with all decoherence sources turned on in setting 6, which we then use to calculate the conditional probabilities for the QND analysis in the next section. Because *QuTiP* is not throwing away information when calculating expectation values, any expectation values of operators can be calculated while the wavefunction evolves. This allows to observe all state expectation values over the course of the simulation.

Fig. 6.8 shows the expectation values for the ^{27}Al$^+$ clock and the ^{40}Ca$^+$ excited states over the duration of the clock laser interaction and 10 times repetition of QND and detection. It can be seen that under ideal conditions the ^{27}Al$^+$ state after the first detection (that is immediately after the first drop to zero of the red line) is in a stable state with almost unity probability for the clock state to be excited or not excited. With full decoherence and imperfections taken into account the ^{27}Al$^+$ clock excitation does not collapse immediately to a state with unit or zero probability. As the ^{40}Ca$^+$ detection collapses the state to a linear combination of eigenstates of the measured eigenvalue, the ^{27}Al$^+$ excitation evolves through a random-walk like path to either side. Therefore, the QND requirement that ^{27}Al$^+$ once it is projected into one state stays in this state over the course of the measurements may not be fully satisfied under realistic conditions.

The result of a frequency scan simulating setting 6 is shown in Fig. 6.9. The parameters used in the simulation were approximately the same as used in the laboratory, producing Fig. 6.6 (a). The clock state excitation probability

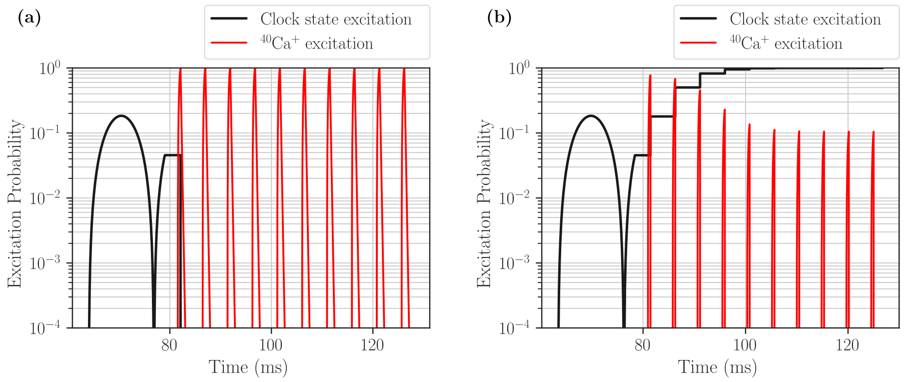

Figure 6.8: Expectation value of ^{27}Al$^+$ clock state and ^{40}Ca$^+$ $D_{5/2}$ state during clock pulse and following 10 QND cycles for two different decoherence/imperfection settings as given in Tab 6.1. Both graphs are taken at the same detuning and clock interrogation cycle, in (a) under ideal conditions (seeting 1), and in (b) under least ideal conditions (setting 6). With more decoherence channels and imperfections the state after detection can show a random-walk-like evolution, which collapse with non-zero probability into an excited state. The beginning of the black curves shows the Rabi oscillation on the clock transition with a maximum excitation probability of 20 % due a detuning of 441 Hz from resonance. In (b) the imperfections and non-zero population of the $n = 1$ Fock state due to heating cause the ^{40}Ca$^+$ excitation probability to become non-zero even though the ^{27}Al$^+$ clock state is excited.

after clock laser interrogation (blue line) shows the typical Rabi-lineshape and the calculated excitation probability (red dots), when applying the swap rate evaluation process described in Ch. 6.2. This demonstrates that the swap method is a valid evaluation scheme. The mean number of *bright* detected states (^{27}Al$^+$ clock state is excited) (green line) is a fuzzy signal away from resonance, due to occasional off-resonant excitation and de-excitation and reaches 0.5 at resonance where the probability for a state swap reaches 1.

The effect of the different decoherence processes can be visualized by the detection errors they introduce into the system. As described above, upon realistic assumption of imperfect QL pulses there will be a non-zero probability to measure a *bright* (*dark*) ^{40}Ca$^+$ even though the clock state of ^{27}Al$^+$ was not excited (was excited). Motional heating and thermal states are described by mixed states, which cause the coherences, i.e., the off-diagonal elements of the density matrix, to decrease. All these effects will give rise to finite probabilities that the wrong state is detected. We calculate the error probabilities by the following projector expectation values

$$P_{\text{False-Excited}} = \mathrm{Tr}\left[\hat{\rho}^{\text{Al,Ca}} \left(|\uparrow\rangle\langle\uparrow|_{\text{Al}} \otimes |\uparrow\rangle\langle\uparrow|_{\text{Ca}}\right)\right] \tag{6.18}$$

$$P_{\text{False-not excited}} = \mathrm{Tr}\left[\hat{\rho}^{\text{Al,Ca}} \left(\left(|\downarrow\rangle\langle\downarrow|_{\text{Al}} + \left|{}^3\text{P}_1\right\rangle\left\langle{}^3\text{P}_1\right|_{\text{Al}}\right) \otimes |\downarrow\rangle\langle\downarrow|_{\text{Ca}}\right)\right], \tag{6.19}$$

where $\hat{\rho}^{\text{Al,Ca}} = \mathrm{Tr}_{\text{motion}}(\hat{\rho})$ is the reduced density matrix with the motional states traced out and $\otimes$ denotes the tensor product.

In Fig. 6.10 the error probabilities averaged over all repetitions and detection gates for the decoherence settings from Tab. 6.1 are shown. We used here the mean, since the errors were symmetrically distributed. It can be seen that

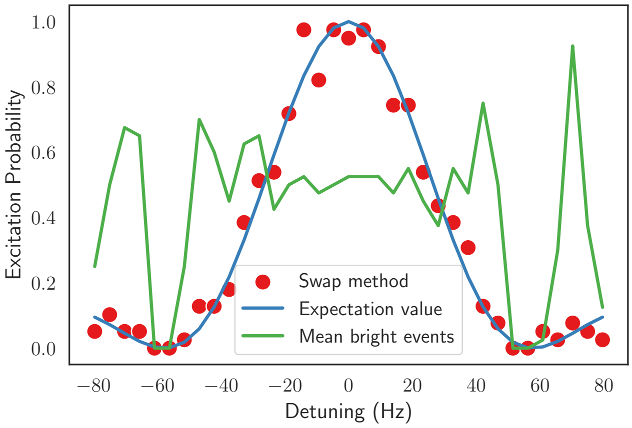

Figure 6.9: Simulated clock transition with setting 6 from Tab. 6.1 (most realistic setting). The expectation value of clock state excitation after clock laser interrogation (blue line) is shown together with evaluation using the swap method (red dots). The green line is the result when naively the mean number of all *bright* events (^{27}Al$^+$ clock state excited) are taken as signal.

for measurements with ideal and imperfect QND pulses (settings 1, 2 and 4) the average error probability is unevenly distributed, with the false negative probability being much greater than the false positive probability, as it is predicted by Eq. (6.10) and (6.11). However, for an ideal QND measurement the error probability is below 0.3 %. This deviation from zero can be explained by not entirely perfectly simulated π-times. Motional decoherence increases the false positive error probability as these processes mix the states with different n (setting 3 and 5). With all decoherences turned on in setting (6), the error probabilities are $P_{\text{False-Excited}} \approx 0.05$ and $P_{\text{False-not excited}} = 0.11$.

These probabilities of false occurrences describe in terms of classical probabilities the probability of the combined events denoted as $P(\text{Ca}_\uparrow \wedge \text{Al}_\uparrow)$ and $P(\text{Ca}_\downarrow \wedge \text{Al}_\downarrow)$, where the first term is the combined probability that the ^{40}Ca$^+$ and ^{27}Al$^+$ ion are both in their electronic excited and the second term where both ions are in their ground states, respectively. The conditional probability of detecting a specific ^{40}Ca$^+$ state Ca$_i$, given that ^{27}Al$^+$ was in the state Al$_j$ is then given by

$$P(\text{Ca}_i|\text{Al}_j) = \frac{P(\text{Ca}_i \wedge \text{Al}_j)}{P(\text{Al}_j)} \,. \tag{6.20}$$

For the following QND analysis in Ch. 6.3.3.2 we use the values from decoherence setting (6) and the conditional probabilities read to be $P(\text{Ca}_\downarrow|\text{Al}_\downarrow) = 0.206$, $P(\text{Ca}_\uparrow|\text{Al}_\downarrow) = 0.794$, $P(\text{Ca}_\downarrow|\text{Al}_\uparrow) = 0.861$, $P(\text{Ca}_\uparrow|\text{Al}_\uparrow) = 0.139$.

6.3.3 Quantum Non-Demolition Measurements

QND measurements are usually referred to measurements in which a division is made between a *signal* quantum system S and an auxiliary quantum system, called *meter* M. Measurements are carried out only on M, implying that S is

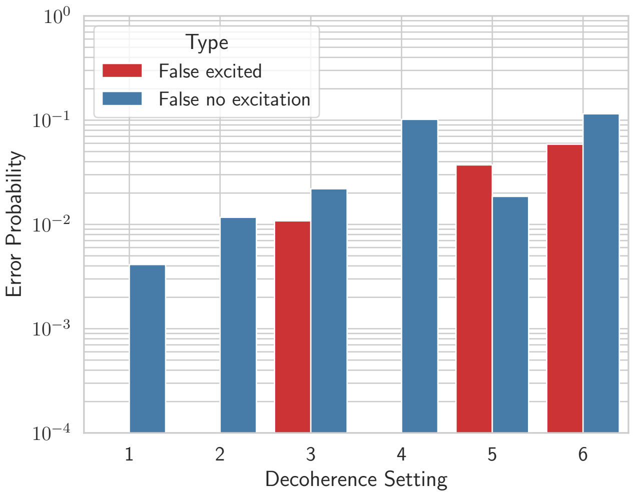

Figure 6.10: Averaged error probabilities defined by Eq. (6.18) and (6.19) for different simulational decoherence/imperfection settings listed in Tab. 6.1. Not visible red error bars are below 4×10^{-11} and thus in the range of computational errors.

preserved and available to repetitive measurements. During the repetitions the measurement error probability due to noise on M decreases, giving an increase in SNR, while noise on the quantum system S, for example spontaneous state decay, increases the error probability with time. Thus, an optimum detection time with minimum error probability is apparent. The concept of QND was originally invented in the 1980's in the context of gravitational wave detection (Caves et al., 1980).

To put the term quantum non-demolition measurement into perspective: Every measurement on a quantum system can be treated as a QND measurement as it does not imply any specific measurement devices or quantum system, nor does it add something new to quantum theory, reinforced by almost perfect agreement between experiments and theory. That is, firstly, a quantum state's wavefunction evolves coherently and time reversible according to the Schrödinger equation. Secondly, measuring the quantum system brings the system to collapse into one of the possible eigenstates of the projector operator that implements the measurement and every succeeding measurement using the same measurement setting results into giving exactly the same result without changing the quantum state. A QND measurement does not change any of these two statements. This is why there is an on-going debate how useful QND concepts are and if they not only introduce confusing terminology (Monroe, 2011; Grangier, 2012). However, QND concepts can help to better understand and "engineer" chains of measurement events, especially in the case of QL measurement schemes.

There are three basic requirements which may be more or less fulfilled in the measurements. For completeness they are given below, again closely following (Hume, Rosenband, and Wineland, 2007; Hume, 2010), noting that more details are given in (Caves et al., 1980; Braginsky and Khalili, 1996).

Firstly, being interested in the observable $\hat{O}_S$ of system S and being able to directly measure the observable $\hat{O}_M$ of system M, the interaction Hamiltonian $\hat{H}_{SM}$ with

$$\left[\hat{O}_M, \hat{H}_{SM}\right] \neq 0 \tag{6.21}$$

ensures that there is an interaction between S and the observable of M. Secondly, the interaction must not be separable, that is

$$\hat{H}_{SM} \neq \hat{H}_S \otimes \hat{H}_M \,. \tag{6.22}$$

If they would be separable the state of M would evolve independently of S. Finally, to be able to measure repetitively it must hold

$$\left[\hat{O}_S, \hat{H}\right] = 0 \,, \tag{6.23}$$

with $\hat{H} = \hat{H}_{SM} + H_0$ and $\hat{H}_0$ the free evolution Hamilton operator of the system. This guarantees that S, once projected into a state, remains in this state over the course of the measurements. A real measurement cannot fulfill these requirements perfectly. A characterization of how well a measurement satisfies these requirements can be carried out following (Ralph et al., 2006).

6.3.3.1 Direct Measurement

The detection of $^{40}\mathrm{Ca}^{+}$ can be considered as a direct QND measurement, identifying it as S. The meter M is not further specified but it includes the modes of the light field that interacts with the PMT. Let S_i be a particular state from all possible states. There are N_S states, i.e., for two states $i = 0, 1$ and $S_i \in \{|{\downarrow}\rangle_{\mathrm{Ca}} = \left|{}^2\mathrm{S}_{1/2}, m = -1/2\right\rangle, |{\uparrow}\rangle_{\mathrm{Ca}} = \left|{}^2\mathrm{D}_{5/2}, m = -1/2\right\rangle\}$. The measured observable of this quantum system can be written as an operator $\hat{O}_S = \sum_{i=1}^{2} \lambda_i \left|S_i\right\rangle \left\langle S_i\right|$ with λ_i being the eigenvalue of this observable. Let further be p the number of detected photons and $P(p|S_i)$ the probability of observing p photons given the ion is in the state S_i. The counted photons follow a Poissonian statistic

$$\mathcal{P}(p, \mu_i) = \frac{\mu_i^p}{p!} e^{-\mu_i} \,, \tag{6.24}$$

with μ_i the mean number of counted photons and $\mu_0 \gg \mu_1$, that is $^{40}\mathrm{Ca}^{+}$ is in the ground state, S_0 scatters much more photons as in the excited state S_1. Bayes' theorem gives the probability that the ion is in state S_i when p photons were detected

$$P(S_i|p) = \frac{P(p|S_i)P(S_i)}{\sum_k P(p|S_k)P(S_k)} = \frac{P(p|S_i)}{\sum_k P(p|S_k)} \,. \tag{6.25}$$

The a priori probabilities $P(S_i)$ are assumed to be $1/N_S$, i.e., $1/2$ for two states. Suppose the measurement outcome is that the ion was in state $S_{i'}$. That outcome depends on p and was chosen by picking $S_{i'}$ from all possible states for which $P(p|S_{i'})$ is the greatest. Then, the probability of having deduced the false state from the observed photon counts is given by

$$P_{\mathrm{err}}(p) = 1 - P(S_{i'}|p) \ . \tag{6.26}$$

The mean error probability is then

$$\overline{P_{\mathrm{err}}} = \sum_{p=0}^{\infty} P_{\mathrm{err}}(p) \left[\sum_{k=1}^{N_S} P(S_k) P(p|S_k) \right] \tag{6.27}$$

Setting the a priori probability $P(S_k) = 0.5$ simplifies Eq. (6.26) to

$$\overline{P_{\mathrm{err}}} = \frac{1}{2} \sum_{p=0}^{\infty} \sum_{k \neq i'}^{N_S} P(p|S_k) \ . \tag{6.28}$$

The index i' depends on p by picking the state with highest probability $P(p|S_{i'})$ or by applying a threshold p_{thresh} to the photon counts in order to discriminate which state was measured. In consequence, when calculating the sum in the Eq. (6.28) the index i' changes during summation.

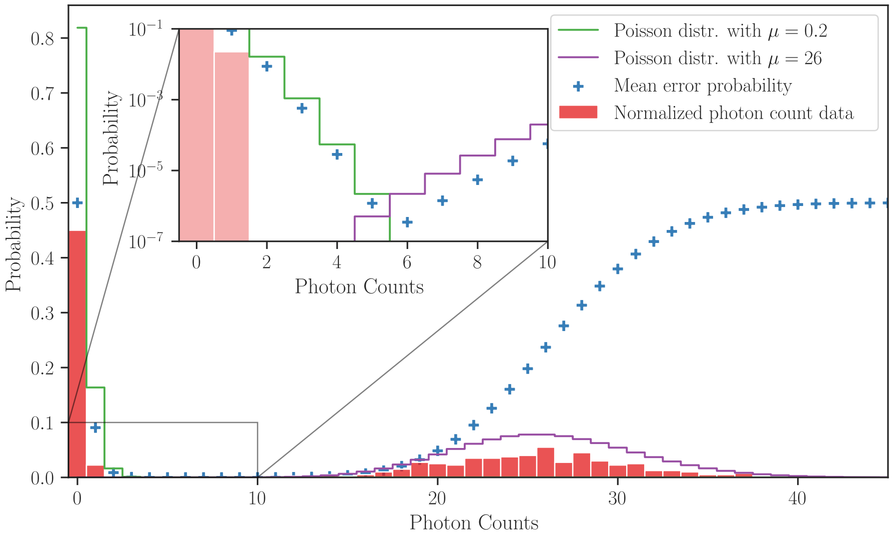

Figure 6.11: Direct measurement photon statistics. Summed collection of ^{40}Ca$^+$ photon counts at 397 nm received from the point of highest excitation in Fig. 6.6, here normalized to unit probability (red histogram). The mean error probability (blue crosses) is calculated using Eq. (6.28) using the photon counts on the x axis as threshold count number. Poisson distributions with fitted $\mu = 0.2$ (green line) and $\mu = 26$ (purple line) are crossing at the point of minimum mean error probability, reaching 1×10^{-6} at a state discrimination threshold of 5 counts.

Experimentally acquired photon counts from data that produced Fig. 6.6 are plotted in Fig. 6.11, together with two theoretical Poisson distributions $P(p|S_k) = \mathcal{P}(p, \mu = 0.2 \text{ or } 26)$ (fitted μ values) and the average error probability inferred from these two statistics. A comparison between the threshold and QND approach reveal that by setting the threshold to 5 counted photons, the mean detection error probability reaches a minimum value of 1×10^{-4} %, which it the same as for picking instead the state with highest likelihood probability. Such small errors make clear why electron shelving is such a high powerful tool for state detection. The model here is also applicable to more than a single ion. For two ions, the distribution would show peaks for the cases when 0, 1 or 2 ions are bright. State discrimination in this case, is typically achieved by applying two thresholds or choosing the state with highest likelihood probability.

6.3.3.2 Indirect Measurement

As in the case for the $^{27}\mathrm{Al}^+$-$^{40}\mathrm{Ca}^+$ clock, the information is at first transferred from the quantum system $^{27}\mathrm{Al}^+ = S$, with $S_0 = |{\downarrow}\rangle_{\mathrm{Al}}$ and $S_1 = |{\uparrow}\rangle_{\mathrm{Al}}$, to the system $^{40}\mathrm{Ca}^+ = M$ with $M_0 = |{\downarrow}\rangle_{\mathrm{Ca}}$ and $M_1 = |{\uparrow}\rangle_{\mathrm{Ca}}$ via QL before detection of the state. This enables to repeatedly perform QL and to detect the state of M without disturbing S. In Ch. 6.3.2 *QuTiP* simulations of the measurement procedure show that the repeated measurement can indeed have a back-action onto S as information about its state builds up. However, in any realistic experiment the requirements for a QND measurement are never perfectly met. In the following we assume that the back-action on S is small. The measurement signal will be a series of photon counts $\{p\} = \{p_1, \ldots, p_c\}$, if repeated c times (c QND measurement cycles). The probability of observing the photon-count set $\{p\}$ is

$$P(\{p\}\,|S_i) = \prod_{j=1}^{c} P(p_j|S_i) \ . \tag{6.29}$$

Again Bayes' theorem gives the probability of detecting the state S_i, if the set $\{p\}$ has been measured

$$P(S_i|\,\{p\}) = \frac{P(\{p\}\,|S_i)}{\sum_k P(\{p\}\,|S_k)} \ , \tag{6.30}$$

and the probability of the error when the measured state is $S_{i'}$ is therefore

$$P_{\mathrm{err}}(\{p\}) = 1 - P(S_{i'}|\,\{p\}) \ . \tag{6.31}$$

The mean error can be calculated as in Eq. (6.28), replacing p with $\{p\}$. The sum then contains an infinite number of summands, each a particular set $\{p\}_l$ with $l = 0, \ldots, \infty$. As in the case above, the sum can be truncated at a number, here $p_{\mathrm{max},c}$, defined by the maximum number of photon counts and maximum possible sets. Therefore the mean error probability can be written as

$$\overline{P_{\mathrm{err}}} = \frac{1}{N_S} \sum_{l=1}^{p_{max,c}} \sum_{k \neq i'} P(\{p\}_l\,|S_k) \ . \tag{6.32}$$

Detection errors made by discriminating between a *dark* and *bright* M signal are neglectable, as pointed out in Ch. 6.3.3.1. But the QL protocol is not perfect. For example the finite lifetime of the $^3\mathrm{P}_1$ states constrain the achievable fidelity during the BSB pulses and heating can cause the RSB excitation to change the state of the Ca^+ ion even though the BSB on the Al^+ did not change its state. We model the QND measurement therefore by (classical) conditional probabilities. These probabilities are assumptions and (reasonable) guesses based on experimentally acquired fidelities and *QuTiP* simulation results. In Fig. 6.12 the tree-diagram of used conditional probabilities is shown.

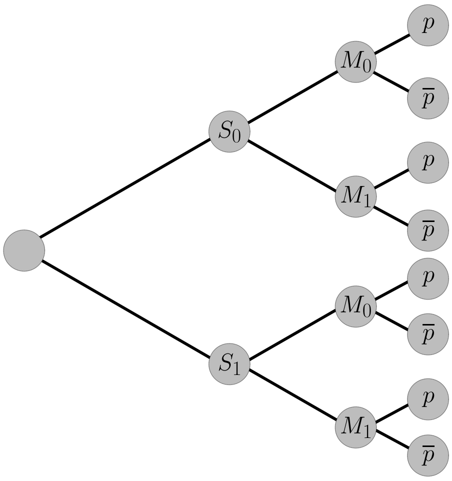

Figure 6.12: Clock excitation tree diagram for illustrating the conditional probabilities for the cases that the clock ion is in the ground state (S_0) or in the excited state (S_1), leading to the events the meter ion is in the ground (M_0) or excited state (M_1), which results in measuring p photon counts or not ($\overline{p}$).

The conditional probability that a certain event S_1 produced the observed photon count number p_j is therefore given by

$$\begin{aligned} P(p_j|S_1) &= P(M_0|S_1)P(p_j|M_0) + P(M_1|S_1)P(p_j|M_1) \\ &= P(M_1|S_1)\mathcal{P}(p_j, \mu_1) + P(M_0|S_1)\mathcal{P}(p_j, \mu_0) \ . \end{aligned} \tag{6.33}$$

Bayes' theorem then gives the probability $P(S_1|p_j)$ of detecting S_1, given that p_j photons have been registered

$$P(S_1|p_j) = \frac{P(p_j|S_1)P(S_1)}{P(p_j|S_0)P(S_0) + P(p_j|S_1)P(S_1)} \ , \tag{6.34}$$

with equal prior probabilities $P(S_0) = (S_1)$. For $P(S_0|p_j)$ we find equivalently

$$P(p_j|S_0) = P(M_1|S_0)\mathcal{P}(p_j, \mu_1) + P(M_0|S_0)\mathcal{P}(p_j, \mu_0) \ , \tag{6.35}$$

and

$$P(S_0|p_j) = \frac{P(p_j|S_0)P(S_0)}{P(p_j|S_0)P(S_0) + P(p_j|S_1)P(S_1)} \ . \tag{6.36}$$

As conditional probabilities we take those found in Ch. 6.3.2, e.g. $P(M_0|S_0) = 0.206$, $P(M_1|S_0) = 0.794$, $P(M_0|S_1) = 0.861$, $P(M_1|S_1) = 0.139$ for our experimental settings. In order to account for the finite lifetime of S_1, we introduce an exponential decay to Eq. 6.34 and a respective exponential growth to Eq. (6.36), using the ^{27}Al$^+$ clock state lifetime of 20.6 s.

In the evaluation of the clock transition in Ch. 6.2 a threshold of 6 bright events after 10 detection cycles has been used in order to discriminate between

^{27}Al^{+} in the ground or excited state. Here, the probabilities Eq. (6.33) and (6.35) are first calculated and then for progressing QND cycles multiplied as in Eq. (6.29). The most likely state after a certain number of QND cycles is then picked by choosing the one with the highest probability according to Eq. (6.34) and (6.36). The error probability is then given by Eq. (6.31). The frequency scans Fig. 6.6 (a) and 6.9 are reproduced by this QND method in Fig. 6.13 in good agreement with the threshold method from Ch.6.2.

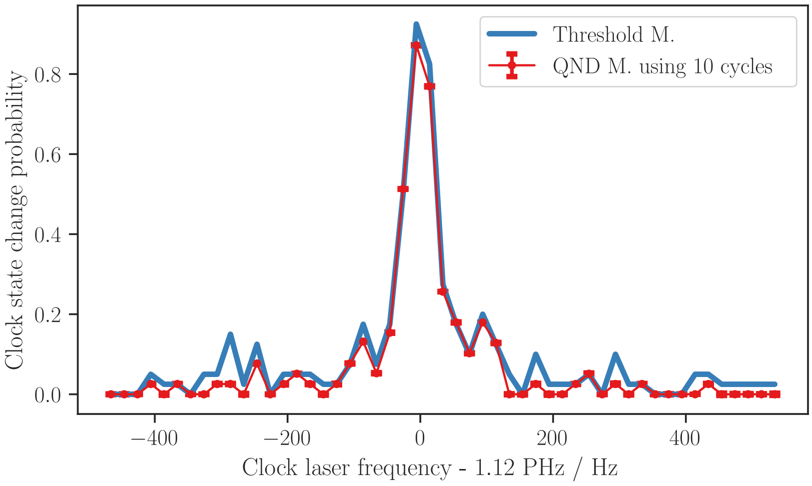

Figure 6.13: QND analysis method applied to the experimental acquired photon counts that produced Fig. 6.6 (a) (using all 10 gates) and threshold method (using ≥ 6 bright states as clock state excited) in comparison. In the QND method outliers with an error $> 1\,\%$ have been excluded and the error bars are mean values. Excluding the outliers a reduction in noise away from resonance can be seen when comparing to the threshold method.

A Monte-Carlo simulation of the QND evaluation method has been conducted. There S_0 (S_1) has been picked to produce a set of photon counts according to Eq. (6.35) (Eq. (6.33)). Using these sets of photon counts the evaluation procedure above was tested in order to find the error probabilities for increasing QND cycles and was compared to those acquired by measured photon counts. We are interested to see how the error probability over QND cycles decreases or increases. Therefore, for each QND cycle we discriminated between S_0 and S_1 which depend on the photon counts of the preceding QND cycle. In order to average the error probabilities over the different detunings and repetitions, we take the median of the distributions, since these are highly asymmetric over a few orders of magnitude, see Fig. D.1 and D.2 in the appendix Ch. D. This prevents over-estimation of the center position in these distributions.

Fig. 6.14 (a) shows how the error probability of detecting S_0 decreases with growing QND cycles to $\approx 0.002\,\%$ after 10 cycles. As already mentioned in (Hume, Rosenband, and Wineland, 2007), detecting S_1 is limited by the finite lifetime of 20.6 s, reaching a minimum error probability of $\approx 0.1\,\%$ in this case[2]. When the number of QND cycles is fixed, the error probability increases

---

[2] In a perfect measurement without detection errors the finite clock state lifetime and the time between clock interrogation and first QND cycle limits the error probability in detecting S_1 to $1 - 1e^{-2\,\mathrm{ms}/20.6\,\mathrm{s}} \approx 1 \times 10^{-4}$.

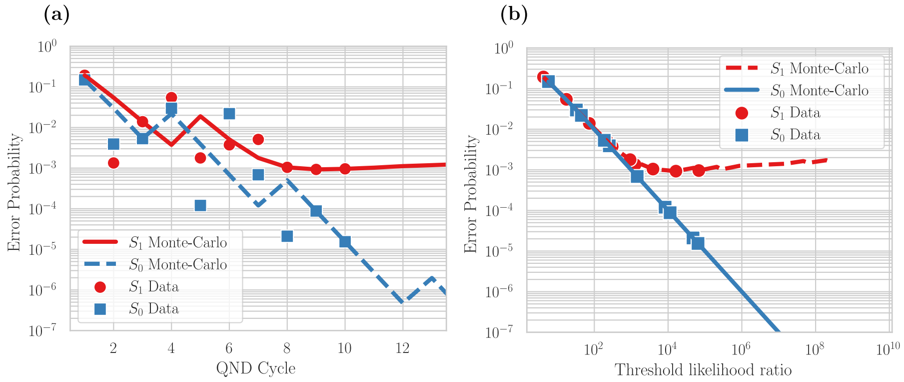

Figure 6.14: Error probability over (a) number of QND cycles and (b) achieved likelihood ratio, which is defined as the greater of the ratio of the product probabilities: $\max\left[P(\{p\}\,|S_1)/P(\{p\}\,|S_0), P(\{p\}\,|S_0)/P(\{p\}\,|S_1)\right]$. As described in the text, S_0 (blue) is the $^1\mathrm{S}_0$ $^{27}\mathrm{Al}^{+}$ ground and S_1 (red) is the $^3\mathrm{P}_0$ excited state. Measurement results are symbols and results from Monte-Carlo generated photon counts are lines. As mentioned in the text the values here are median values of the error probability and threshold likelihood ratio.

occasionally. This happens for example when a few S_1 events are followed by a few S_0 events and vice versa. See Fig. D.3 and D.4 in the appendix Ch. D for two sets of measured PMT counts.

A better detection method is the proposed *adaptive detection scheme* in (Hume, Rosenband, and Wineland, 2007), where the detection is only repeated until a specified error rate or probability likelihood ratio is reached. The probability likelihood ratio can be defined as

$$\max\left[\frac{P(\{p\}\,|S_1)}{P(\{p\}\,|S_0)}, \frac{P(\{p\}\,|S_0)}{P(\{p\}\,|S_1)}\right]. \tag{6.37}$$

This enables measuring with less QND cycles on average and also prevents the error probability to increase again. In our case, a likelihood ratio of 1×10^3 is optimal as this is the point where the error probability of S_1 detection settles and no further information can be gained by increasing the likelihood ratio, see Fig. 6.14 (b).

This method requires live update of PMT count histograms during detection cycles and feedback onto the experimental control program, which was technically not implementable in our system when the presented experiments were carried out. Using *Artiq* as experimental control in the future would allow for this detection scheme to be used. This is highly favorable, since it reduces the dead time between clock interrogations and therefore increases the feedback gain. Because of this benefit and the smaller achievable error probabilities the *adaptive* QND method is more effective as the simple threshold method.

7

Systematic Shifts and Uncertainty Budget Assessment

Compared to other clock species, the clock transition of $^{27}\mathrm{Al}^{+}$ is hardly influenced by external field shifts. Nevertheless, these shifts can surpass a level of 1×10^{-16}. Therefore, systematic deviations from the unperturbed atomic transition have to be assessed and subtracted from the measured transition frequency. The combined uncertainty of these corrections determines the accuracy of the clock. In the following, the relevant shifts of the $^{27}\mathrm{Al}^{+}$ clock transition are presented and their magnitude together with their individual uncertainty is evaluated. Here we take advantage of the co-trapped logic ion, $^{40}\mathrm{Ca}^{+}$, which is more sensitive to external perturbations compared to $^{27}\mathrm{Al}^{+}$. The chapter closes with the total systematic uncertainty budget and a brief discussion of unassessed shifts and possible improvements.

7.1 First-Order Doppler Shift

Relative motion between laboratory frame laser beam and the ion introduces a first-order Doppler shift. This shift is a direct consequence of special relativity theory, as the moving ion will sample another frequency as measured in the laboratory rest frame. When locking the laser onto the resonance, the servo will steer the laser frequency such that it matches in the atomic frame the atomic resonance at proper frequency ν. The relative frequency shift $\Delta\nu/\nu = (\nu_{\mathrm{lab}} - \nu)\nu$ is

$$\frac{\Delta\nu}{\nu} = \frac{\left\langle v_{\parallel} \right\rangle}{c} - \frac{\left\langle v^2 \right\rangle}{2c^2} + \frac{\left\langle v_{\parallel} \right\rangle^2}{c^2} + O(v/c)^3 \, , \tag{7.1}$$

with $v_{\parallel}$ the ion's velocity in the direction of the probe beam, v the total velocity of the ion, c the speed of light and $\langle \; \rangle$ denotes the averaging during the probe duration (Ludlow et al., 2015).

The first term of Eq. (7.1) is the 1st-order Doppler shift. The periodic motion of the ion in the Paul trap guarantees $\left\langle v_{\parallel} \right\rangle = 0$ over the probe duration. However, due to thermal drifts or the buildup of stray charges when probing the clock with light at 267 nm, the relative position between ion and probe beam can change over time and the residual shift can still be on the order of 10^{-17} (Brewer et al., 2019b) and must be canceled. This is typically achieved by probing the ion from two opposing laser beam directions. Using this technique in Ref. (Brewer et al., 2019b) the average 1st-order Doppler shift was estimated to be zero with a fractional frequency uncertainty of 2.2×10^{-19} and we expect to reach a comparable level in our setup.

The two following terms in Eq. (7.1) are referred to as time-dilation shifts. The ion in a linear Paul trap moves along different types of trajectories given by secular motion and intrinsic and excess micromotion. As the latter can be compensated to a high degree with the help of sensitive measurements, it is discussed separately in Ch. 7.2. The remaining motional shifts are then elaborated on in Ch. 7.4.

7.2 Excess Micromotion Shift

One important shift of the aluminum clock transition is caused by residual stray electric fields. Such fields push the ion out of the position where the RF quadrupole electric field is zero and therefore increase the motional amplitude. In order to study the change in motional energy by displacements, a revisiting of the motion defining the Mathieu equation is necessary.

A residual static electric field $\vec{E}_{\mathrm{dc}}$ at the ion's rest position will modify the Mathieu equation Eq. (2.7) to

$$\ddot{u}_j + \frac{\Omega_{\mathrm{rf}}^2}{4} u_j \left[a_j + 2q_j \cos\left(\Omega_{\mathrm{RF}} t\right)\right] = \frac{\vec{E}_{\mathrm{dc}} \cdot \vec{e}_j Q}{m} , \tag{7.2}$$

where $\vec{e}_j$ is the direction vector of the mode j, see (Berkeland et al., 1998). This alters Eq. (2.12) to

$$u \approx \left[u_{0j} + u_{1j} \cos(\omega_j + \phi_j)\right] \left(1 + \frac{q_j}{2} \cos\left(\Omega_{\mathrm{RF}} t\right)\right) . \tag{7.3}$$

As pointed out in (Berkeland et al., 1998), uniform static electric fields on the order of a few V/m can develop in the system by for example unevenly coating the trap electrodes with neutral atoms originating e.g. from ablation or oven loading, leading to contact potentials. Also charging of dielectric materials and oxide layers due to emittance of electrons and photo-ionization by intense UV radiation hitting the electrode structure is possible.

Once the ion is pushed away from the RF node, it senses a residual electric RF field $\vec{E}_{\mathrm{rf}}$, causing EMM. This micromotion brings additional kinetic energy E_{kin} into the system, which cannot be cooled since it is a driven motion. In fact, heating occurs when the laser frequency is tuned near, but above the center frequency of any sufficiently strong micromotion sidebands.

The additional kinetic energy gives rise to a relative time-dilation shift (Keller et al., 2015)

$$\left\langle \frac{\Delta\nu}{\nu} \right\rangle_{\mathrm{EMM}} = -\frac{\langle E_{\mathrm{kin}} \rangle_{\mathrm{EMM}}}{mc^2} = -\left(\frac{Q}{2mc\Omega_{\mathrm{RF}}} E_{\mathrm{RF}}\right)^2 \tag{7.4}$$

where the brackets denote a time average over the measurement interval, which is large compared to the time scales of secular and micromotion oscillation periods.

The ion's velocity due to excess micromotion (EMM) can be integrated by the equation of motion

$$m\dot{\vec{v}}_{\mathrm{EMM}} = Q\vec{E}_{\mathrm{RF}} \cos(\Omega_{\mathrm{RF}} t) \tag{7.5}$$

Following (Keller et al., 2015), EMM can be measured by the 1st-order Doppler shift of an ion undergoing periodic motion with $\vec{v}_{\mathrm{EMM}} = \vec{v}_0 \cos(\Omega_{\mathrm{rf}} t + \phi)$. In the rest frame of the moving ion the laser phase is modulated with the modulation index

$$\beta = \frac{\vec{k} \cdot \vec{v}_0}{\Omega_{\mathrm{RF}}} \ . \tag{7.6}$$

where $\vec{k}$ is the wave vector of the laser field $E(\omega_{\mathrm{L}})$ with probe laser frequency ω_{L}. Consequently the moving ion experiences a laser field that has sidebands at Ω_{RF}. For $\beta \ll 1$, which is fulfilled here, the resulting spectrum can be approximated using Bessel functions $J_k(\beta)$ of the first kind[1]

$$E(\omega) \propto J_0(\beta)\delta(\omega - \omega_{\mathrm{L}}) + J_1(\beta)\left[\delta(\omega - \omega_{\mathrm{L}} - \Omega_{\mathrm{RF}}) - \delta(\omega - \omega_{\mathrm{L}} + \Omega_{\mathrm{rf}})\right] \ , \tag{7.7}$$

where $\delta(\omega)$ denotes the Dirac-delta function and $E(\omega)$ is the amplitude of the laser field. The residual RF electric field can be expressed by using β.

$$E_{\mathrm{RF}} = \frac{m\Omega_{\mathrm{RF}}^2}{kQ}\beta \ . \tag{7.8}$$

Combining Eq. (7.4) and (7.8), the time-dilation shift due to EMM can be written as

$$\left\langle \frac{\Delta\nu}{\nu} \right\rangle_{\mathrm{EMM}} = -\frac{(\vec{v}_0)^2}{4c^2} \ . \tag{7.9}$$

Table 7.1: 729 nm laser directions used for 3D probing of the EMM shift. See also Fig 7.11(a) and Ch. 5.3. An uncertainty of 5° is attributed to each value.

Beam	θ	ϕ
Diagonal 1	134.4°	180°
Diagonal 2	135.2°	0°
Top	55.4°	270°

We use the resolved sideband method on the Ca$^+$ $^2S_{1/2} \leftrightarrow {}^2D_{5/2}$ transition at 729 nm with a linewidth of $\Gamma \ll \Omega_{\mathrm{RF}}$. According to Eq. (7.6) and (7.7), the ratio of EMM sideband Rabi-frequency $\Omega_{\pm 1}$, to carrier Rabi-frequency Ω_0 gives the β-component parallel to the wavevector $\vec{k}$ of the probing laser beam.

$$\frac{\Omega_{\pm 1}}{\Omega_0} = \frac{J_1(\beta)}{J_0(\beta)} \approx \frac{\beta}{2} \ . \tag{7.10}$$

In the assessment of the EMM shift in this experiment, a set of three non-coplanar dependent 729 nm beams has been utilized to do a full "tomography" of this shift. Defining $\vec{L}_1$, $\vec{L}_2$ and $\vec{L}_3$ as the dimensionless directional vectors

---

[1] If β is not significantly smaller than 1, higher order terms must be taken into account.

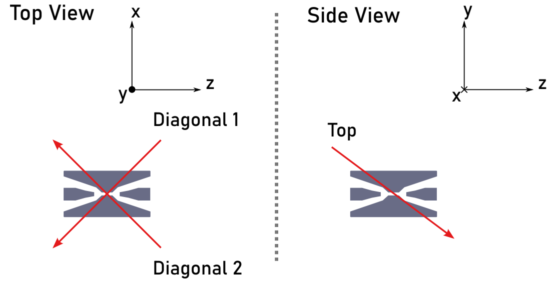

Figure 7.1: For measuring the EMM velocity amplitude, three 729 nm beams impinge onto a single trapped $^{40}\mathrm{Ca}^+$ ion. The standard spherical coordinates are used to define their orientation angles, which are listed in Tab. 7.1.

of three laser beams impinging onto the ion, which can be represented using spherical coordinates. For the 729 nm laser ports used in this experiment the corresponding angles are listed in Tab. 7.1 and sketched in Fig. 7.1.

$$\vec{L}_i = \begin{pmatrix} \sin(\theta_i)\cos(\phi_i) \\ \sin(\theta_i)\sin(\phi_i) \\ \cos(\theta_i) \end{pmatrix} \tag{7.11}$$

Equation (7.6) can be rewritten to

$$\beta = \frac{k}{\Omega_{\mathrm{RF}}} \vec{L} \cdot \vec{v}_0 \tag{7.12}$$

Probing the EMM modulation index from three non-coplanar directions, it is possible to reconstruct the micromotion amplitude. Noting that the projection of the velocity of the ion onto the laser direction is given by

$$\vec{L}_i \cdot \vec{v}_0 = L_{ix} v_{0x} + L_{iy} v_{0y} + L_{iz} v_{0z} = l_i \ , \tag{7.13}$$

where $l_i = \beta_i \Omega_{\mathrm{RF}}/k$ and $i = 1, 2, 3$. This equation can be written in matrix form

$$\vec{l} = A \cdot \vec{v}_0 \ . \tag{7.14}$$

The matrix A can be inverted. Therefore, the velocities can be calculated by $\vec{v}_0 = A^{-1} \cdot \vec{l}$.

The measurements were carried out on a single Doppler cooled $^{40}\mathrm{Ca}^+$ ion. The result of a typical Rabi frequency measurement is depicted in Fig. 7.2. In order to estimate the shift on the co-trapped $^{27}\mathrm{Al}^+$ ion during clock interrogation the time-dilation shift (Eq. (7.9)) is rescaled to

$$\frac{\beta_{\mathrm{Ca}}}{\beta_{\mathrm{Al}}} = \frac{u_0 q_{\mathrm{Ca}}}{u_0 q_{\mathrm{Al}}} = \frac{m_{\mathrm{Al}}}{m_{\mathrm{Ca}}} \Rightarrow \left\langle \frac{\Delta\nu}{\nu} \right\rangle_{\mathrm{EMM}} = -\frac{(\vec{v}_0)^2}{4c^2} \frac{m_{\mathrm{Ca}}^2}{m_{\mathrm{Al}}^2} \ . \tag{7.15}$$

In order to map the EMM shift in our trap, the dc voltages in the trap have been varied, as shown in Fig. 7.3 (a). The conversion factor of electrode voltage to ion position were inferred from the camera pixel distances using the

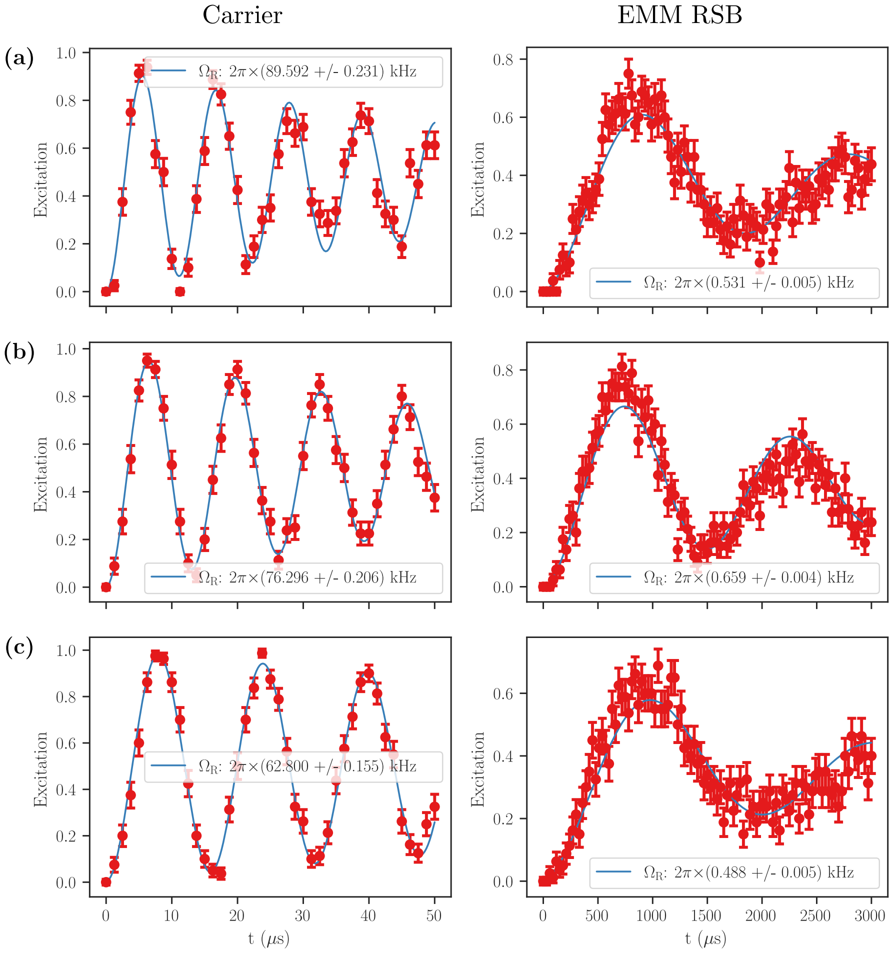
Carrier

EMM RSB

Figure 7.2: Typical results of the Rabi oscillation measurements on carrier and EMM RSB for determining EMM in the trap. All measurements were carried out on a single Doppler cooled ^{40}Ca^{+} on the magnetically less sensitive ^{2}S$_{1/2}$, $m = -1/2$ to ^{2}D$_{5/2}$, $m = -1/2$ transition, using three non-coplanar 729 nm beam directions: (a) Diagonal 1 ($\beta = 0.0119$), (b) Diagonal 2 ($\beta = 0.0173$), (c) Diagonal 3 ($\beta = 0.0156$).

known separation of a two-ion ^{40}Ca^{+} crystal. They are given by ≈ 0.65 µm/V for the endcap electrode and ≈ 0.1 µm/V for the compensation electrodes, respectively, when the voltages are increased from the setting where the ions are in the trap center. The conversion factor for the compensation electrodes which push the ion towards or away from the camera could not be measured, but are assumed to be the same as for the other compensation electrode pair which moves the ion orthogonal to the line of sight of the camera. Due to the large variations in the voltages on time scales exceeding the needed settle times for those electrodes the acquired values in Fig. 7.3 (a) indicate only an overall trend. Along the trap axis (Endcap 0 variation) EMM is comparably small and varying smoothly, while off-axis ion positions accompany steep changes in EMM amplitude.

In Fig. 7.3 (b) scans of the dc electrodes around positions with minimum EMM, taken in short measurement runs with settled dc voltages are shown. The data points for the shift and uncertainty are total values, i.e. the total shift has been evaluated from the different probing directions according to Eq. 7.12

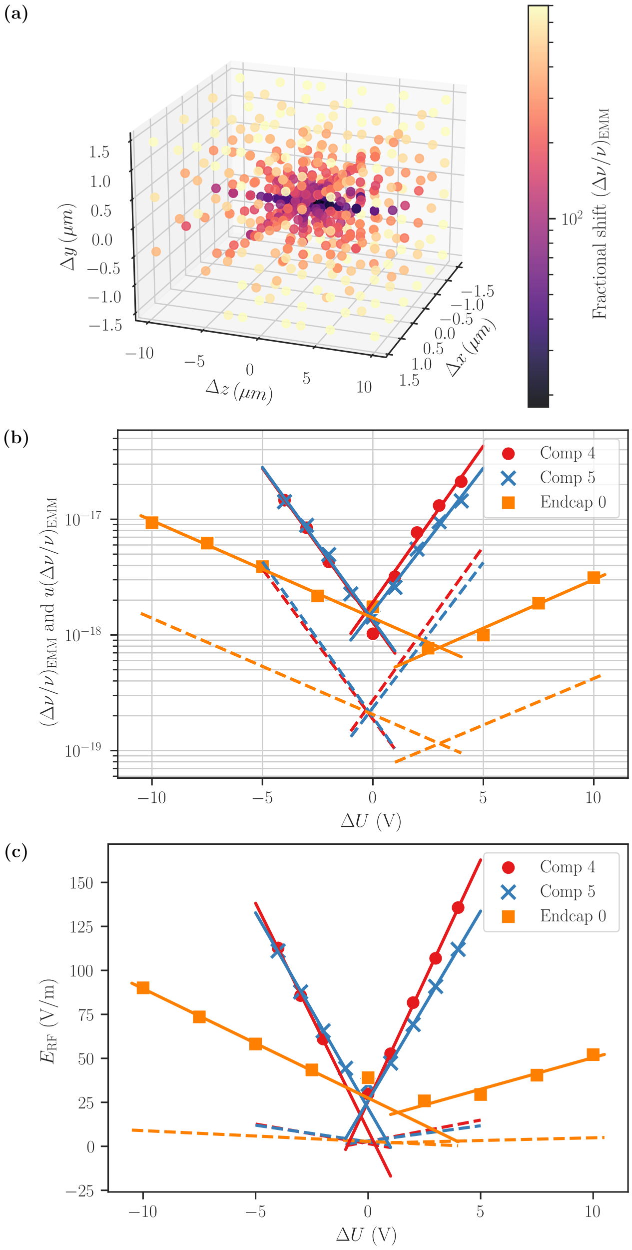

Figure 7.3: Results of the EMM shift measurement. (a) Total shift in fractional frequency units, measured over many days. The position in the trap has been estimated by using the conversion factors described in the text. (b) Total fractional frequency shift (symbols and solid lines) and uncertainty (dashed lines) around the best performing spot in the trap. (c) Residual RF electric field E_{RF} (Eq. 7.8), calculated from the same data as in (b). The lines are linear fits. The compensation electrodes have been scanned in the shown order beginning with Comp 4. As it can be seen, the optimal compensated voltage for the electrode Endcap 0 was off by ≈ 3 V. The dc electrode voltages at $\Delta U = 0$ V were (Endcap 0, Endcap 1, Comp 4, Comp 5)=(737.5 V, 800 V, 227.75 V, 223 V).

and in the uncertainty evaluation (rms of the individual contributions) the uncertainty of the probing beam directions has been considered. We take as value the crossing of the orange lines, since this value is typically reached, when scanning the voltages in the shown order. We estimate a frequency shift and uncertainty of the $^{27}\mathrm{Al}^{+}$ clock transition of

$$\left(\frac{\Delta\nu_{2D}}{\nu}\right)_{\mathrm{EMM}} = -7.8(1.2)\times 10^{-19}\ , \tag{7.16}$$

Because the presented measurements where carried out on a single $^{40}\mathrm{Ca}^{+}$, a co-trapped $^{27}\mathrm{Al}^{+}$ would experience the aforementioned shift only in the two-ion configuration where $^{27}\mathrm{Al}^{+}$ is placed at the point of compensated micromotion. A position swap of both ions can in principle be measured and the data can then be discarded and a reswap of the ions be provoked. Another possibility is to place the ion crystal centered on the point of compensated EMM. Then, as calculated in Ch. 2.5.1 $^{27}\mathrm{Al}^{+}$ will have its equilibrium positions at $d_{\mathrm{Al}} \pm 2.6\,\mu\mathrm{m}$ from the trap center, which corresponds to $\Delta U_{\mathrm{Endcap0}} \approx \pm 2\,\mathrm{V}$. From Fig. 7.3 (b) a shift of $-1.70(25)\times 10^{-18}$ can then be inferred at these symmetric positions around the axial compensation point.

Intrinsic micromotion (IMM) leads to a temperature-dependent offset in achievable micromotion compensation, which would express itself in deviations from the triangular shape of the fitted curves in Fig. 7.3 (b) and (c) at the region with lowest micromotion (Keller et al., 2015). As can be seen in Fig. 7.3 (c) there is still a residual $E_{\mathrm{rf}} \approx 20(3)$ V/m at the compensated point which must be attributed to IMM, because the micromotion in this trap has been measured at Doppler temperatures. A further evaluation with a GSC ion is planned for the future. The contribution of the IMM to the systematic uncertainty budget is discussed in Ch. 7.4.

The accuracy in measuring EMM shift was formerly (Scharnhorst, 2018) limited by technical limitations in the measurement method, where near the compensated point the Rabi times on the EMM sidebands became very long. This limitation was overcome here by increasing the laser intensity (higher power, smaller focus) and by improving the magnetic field stability to allow for longer probe times. Therefore, the uncertainty in this shift is currently limited by the uncertainty of the laser orientation angles as shown in Fig. 7.4. Assuming zero uncertainty in the angles, the curve gets flat at around 2.5×10^{-20}, which is then the limit given by the fitting errors of the Rabi frequencies. In the future, a measurement of EMM on $^{27}\mathrm{Al}^{+}$ directly, using the 267 nm logic laser, is planned. Furthermore the stability of the EMM within the clock interrogation sequence has to be studied in detail.

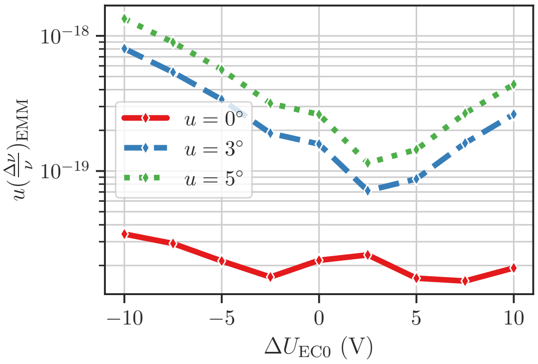

Figure 7.4: Influence of the laser orientation uncertainty u to the total EMM uncertainty when scanning the endcap 0 voltages. The curve with the angle uncertainty set to zero is flat and is given by the Rabi frequency fitting errors.

7.3 Trap Induced Second-Order AC Stark Shift

The electric quadrupole field of the Paul trap causes a 2nd-order ac Stark shift, because the mean-squared electric field does not vanish $\langle E^2 \rangle \neq 0$ across the wavefunction of the ion. The shift can be derived by averaging the quadrupole field over the ion trajectory (Keller et al., 2015), which yields

$$\left(\frac{\Delta\nu}{\nu}\right)_{\mathrm{S}} = \frac{\Delta\alpha(0)}{h\nu}\left\langle E^2 \right\rangle = \frac{\Delta\alpha(0)}{h\nu}\left(\frac{E_{\mathrm{rf}}^2}{2} + \frac{m_{\mathrm{Al}}\Omega_{\mathrm{rf}}^2}{Q^2} k_B T_{\mathrm{Al}}\right) , \qquad (7.17)$$

with $\Delta\alpha(0) = 7.02(94) \times 10^{-42}\,\mathrm{J\,m^2/V^2}$ the differential static polarizability (Brewer et al., 2019b). Because of the low differential polarizability of the clock transition of $^{27}\mathrm{Al}^+$, the shift and its uncertainty are small compared to other shifts, even at typically achieved Doppler temperatures[2] of $T = 650(70)\,\mu\mathrm{K}$:

$$\left(\frac{\Delta\nu}{\nu}\right)_{\mathrm{S}} = 7.138(19) \times 10^{-19} . \qquad (7.18)$$

7.4 Time-dilation Shift

The residual secular and intrinsic micromotion velocity of the clock ion during clock interrogation imposes also a 2nd-order Doppler shift on the clock frequency, which is called time-dilation shift. It must be noted that even a perfectly GSC ion, trapped in a linear Paul trap, has a finite velocity due to the zero point energy of the corresponding harmonic oscillator modes. This shift depends on the temperature of the ion, therefore laser cooling is needed to mitigate it.

There are two possible kinds of clock interrogation modes. The first is GSC of all motional modes before clock interrogation and then turning the cooling lasers off during the interrogation. The second is GSC of all modes

---

[2] The theoretical Doppler limit is $T = 497\,\mu\mathrm{K}$.

beforehand and then moderately continue with sympathetic laser cooling during interrogation. While in the first method the heating rates after GSC determine the shift by time-dilation only, the second method keeps the ion temperature at a low level and thus the time-dilation shift, but the cooling lasers impose an additional ac Stark shift.

In Ref. (Scharnhorst, 2018) both variants have been compared for this experiment, where in the latter case Double-Bright EIT cooling was assumed. A moderate cooling power resulting in a mean motional phonon occupation of $\overline{n} < 5$ and a strong cooling power with $\overline{n} < 0.2$ for all modes have been considered. The combination of expected time-dilation and calculated ac Stark shifts were then found to be $-0.2(4) \times 10^{-18}$ and $-1.1(5.3) \times 10^{-18}$ in fractional frequency units. These results will be briefly reviewed in the context of the total uncertainty budget in Ch. 7.10. The discussion here is restricted to the case without simultaneous cooling.

The time-dilation shift is given by the total kinetic energy of the clock ion divided by its rest energy

$$\left(\frac{\Delta\nu}{\nu}\right)_{\mathrm{2D}} = -\frac{\langle E_{\mathrm{kin}}\rangle}{m_{\mathrm{Al}}c^2} \ . \tag{7.19}$$

Following Ref. (Wübbena et al., 2012), the total kinetic energy of $^{27}\mathrm{Al}^+$ is given by the sum over all modes, including the intrinsic micromotion (IMM) of the radial modes, which contribute with approximately the same amount as the secular motion (Berkeland et al., 1998). Here, the total kinetic energy in a single mode is split between $^{40}\mathrm{Ca}^+$ and $^{27}\mathrm{Al}^+$ by $E_{\mathrm{kin}} = (b_1^2 E_{\mathrm{kin}})^{\mathrm{Ca}} + (b_2^2 E_{\mathrm{kin}})^{\mathrm{Al}}$ for the in-phase (IP), and $E_{\mathrm{kin}} = (b_2^2 E_{\mathrm{kin}})^{\mathrm{Ca}} + (b_1^2 E_{\mathrm{kin}})^{\mathrm{Al}}$ for the out-of-phase (OP) modes, respectively. The normalized mode eigenvector components b were defined in Eq. (2.67). The kinetic energy of $^{27}\mathrm{Al}^+$ can hence be written as

$$\begin{aligned} E_{\mathrm{kin}} = \frac{1}{2}\Bigg[& b_{xy,2}^2 \hbar\omega_{x,\mathrm{IP}} \left(\overline{n}_{x,\mathrm{IP}} + \frac{1}{2}\right)(1 + S_{xy,\mathrm{IP}}) \\ & + b_{xy,2}^2 \hbar\omega_{y,\mathrm{IP}} \left(\overline{n}_{y,\mathrm{IP}} + \frac{1}{2}\right)(1 + S_{xy,\mathrm{IP}}) \\ & + b_{xy,1}^2 \hbar\omega_{x,\mathrm{OP}} \left(\overline{n}_{x,\mathrm{OP}} + \frac{1}{2}\right)(1 + S_{xy,\mathrm{OP}}) \\ & + b_{xy,1}^2 \hbar\omega_{y,\mathrm{OP}} \left(\overline{n}_{y,\mathrm{OP}} + \frac{1}{2}\right)(1 + S_{xy,\mathrm{OP}}) \\ & + b_{z,2}^2 \hbar\omega_{z,\mathrm{IP}} \left(\overline{n}_{z,\mathrm{IP}} + \frac{1}{2}\right) + b_{z,1}^2 \hbar\omega_{z,\mathrm{OP}} \left(\overline{n}_{z,\mathrm{OP}} + \frac{1}{2}\right)\Bigg] \ , \end{aligned} \tag{7.20}$$

where the global factor of $1/2$ after the equal sign accounts for the fact that the energy of the harmonic oscillator modes $\hbar\omega(n + 1/2)$ is the kinetic plus potential energy. According to the equipartition theorem, only half of this total energy belongs to the kinetic energy. The IMM scaling factors S (Wübbena et al., 2012) are given by

$$S_{xy,\mathrm{IP}} = \frac{2\epsilon^2/\mu}{2\epsilon^2/\mu - 2\alpha - (1 - \sqrt{\mu} b_{x,1}/b_{x,2})} \tag{7.21}$$

$$S_{xy,\mathrm{OP}} = \frac{2\epsilon^2/\mu}{2\epsilon^2/\mu - 2\alpha - (1 + \sqrt{\mu} b_{x,2}/b_{x,1})} \ , \tag{7.22}$$

where $\mu = m_{\mathrm{Al}}/m_{\mathrm{Ca}}$ is the mass ratio of the two ions and all other terms[3] have been introduced in Ch. 2.5.2. It is usually assumed that IMM contributes with the same energy as the secular motion to the total kinetic energy in the radial modes (Berkeland et al., 1998). However, for $^{27}\mathrm{Al}^+$ $S_{xy,\mathrm{IP}} = 1.22$ and $S_{xy,\mathrm{OP}} = 3.18$.

During the probe time and without cooling, the mean motional phonon occupation $\overline{n}$ will increase linearly with the heating rate $\dot{\overline{n}}$. After the clock probe time T the average $\overline{n}$ of the respective mode can be calculated as the time averaged mean

$$\langle \bar{n} \rangle = \frac{1}{T} \int_0^T \left(\bar{n}_0 + \dot{\bar{n}} t \right) \mathrm{d}t = \bar{n}_0 + \frac{\dot{\bar{n}} T}{2} \ . \tag{7.23}$$

From sideband thermometry measurements (Ch. 5.5) the heating rates shown in Tab. 5.3 are deduced. As noted in Ref. (Hankin et al., 2019), background gas collisions (BGC) lead to significantly higher heating rates as measured by the sideband ratio method, because after a collision the motional distribution becomes non-thermal with contributions at higher n. It is also known that sideband cooling can lead to non-thermal states (Rasmusson et al., 2021). Therefore, the motional state distributions after EIT cooling and due to collisions during the clock interrogation have to be studied in the future, for example by the method proposed in Ref. (Rasmusson et al., 2021). The impact of these high energy contributions to the frequency shift is suppressed, because the time-dilation effect would shift the clock resonance completely off-resonance and because their coupling strengths, given by the Rabi frequencies, is suppressed by motional Debye-Waller factors (Hankin et al., 2019; Chen et al., 2017). To account for the unknown non-thermal distribution and measurement fluctuations of the heating rates, we add an uncertainty of 10 % of the respective measured heating rates to the uncertainty retrieved from the linear fits (Tab. 5.3).

The resulting time-dilation shift due to linear heating rates and their uncertainties is shown in Fig. 7.5. Because of the high uncertainty of the heating rates of the radial IP modes, the uncertainty grows faster than the shift, passing the uncertainty of the time-dilation shift of a continuously Doppler cooled ion crystal at 0.2 s. At a reasonable clock interrogation time of 150 ms the shift is

$$\left(\frac{\Delta \nu}{\nu} \right)_{\mathrm{2D}} = -3.65(55) \times 10^{-18} \ . \tag{7.24}$$

---

[3] $\alpha = 0.5$, $\epsilon = 1.879$, $b_{xy,1} = 0.157$, $b_{xy,2} = 0.988$, $b_{z,1} = 0.827$, $b_{z,2} = 0.562$.

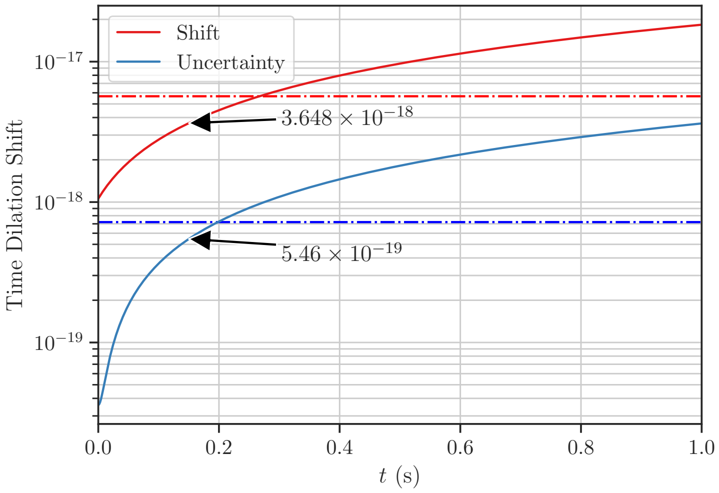

Figure 7.5: Probe-time dependence of the time-dilation shift due to heating rates in Tab 5.3. The heating rate uncertainty has been enlarged by 10 % of the heating rate value of the respective mode. Shown is the fractional frequency shift (red solid line) of the $^{27}Al^{+}$ clock transition and its uncertainty (blue solid line). The two horizontal lines refer to a Doppler cooled $^{27}Al^{+}$-$^{40}Ca^{+}$ crystal with an effective Doppler cooling linewidth of 1.2Γ, which corresponds to motional excitations of $\bar{n}_{\mathrm{ax,\,IP}} = 9.9$, $\bar{n}_{\mathrm{ax,\,OP}} = 5.3$, $\bar{n}_{\mathrm{rad,\,IP,\,xy}} = 4.0$, $\bar{n}_{\mathrm{rad,\,OP,\,xy}} = 6.7$ and an uncertainty of 25 %.

Ways to improve on this uncertainty are discussed in Ch. 7.10.

7.5 Blackbody Radiation Shift

Every body at a finite temperature emits so-called blackbody radiation (BBR). The states involved in the clock transition couple differently to these fields and hence experience a differential energy shift. It depends on the temperature of the surrounding material in the vicinity of the ion and its emissivity. The experiment is carried out at room temperature, but the high powers fed into the RF blades by the RF trap drive heat up the trap surfaces. The temperature rise is measured with a temperature sensor glued to one of the sapphire discs and at the position of the ion it had been characterized for this setup by thermometric measurements and simulations in Ref. (Doležal et al., 2015) to $\Delta T_{\mathrm{ion}} = (1.0 \pm 0.5)\mathrm{K}$.

The BBR shift caused by the temperature T can be calculated by

$$\left(\frac{\Delta\nu}{\nu}\right)_{\mathrm{BBR}} = -\frac{\pi\left(k_B T^4\right)\Delta\alpha(\lambda)}{60\epsilon_0\hbar^4 c^3 \nu}\ , \tag{7.25}$$

with k_B the Boltzmann constant, $\Delta\alpha(\lambda)$ the differential polarizability between the $^{27}\mathrm{Al}^+$ clock transition states $^1\mathrm{S}_0$ and $^3\mathrm{P}_0$, ϵ_0 the electric field constant and $\hbar$ the reduced Planck constant (Rosenband et al., 2006). At room temperature $T \approx 300\,\mathrm{K}$, $\lambda \approx 10\,\mu\mathrm{m}$ and the differential polarizability is $\Delta\alpha(10\,\mu\mathrm{m}) = 7.03(94) \times 10^{-42}\,\mathrm{J\,m^2/V^2}$ as measured in Ref. (Brewer et al., 2019b) and its supplemental material, which agrees well with a calculation (Safronova, Kozlov, and Clark, 2011).

The resulting shift and its uncertainty are

$$\left(\frac{\Delta\nu}{\nu}\right)_{\mathrm{BBR}} = -3.27(44) \times 10^{-18}\ . \tag{7.26}$$

The uncertainty is dominated by the uncertainty in the differential polarizability. An increased temperature uncertainty of 5 K leads only to $-3.27(49) \times 10^{-18}$.

7.6 Collisional Frequency Shift

Collisions of the $^{27}\mathrm{Al}^+$ ion with background gas particles can change the motional state distribution to non-thermal Fock states, if no sympathetic cooling of the clock ion is present during clock interrogation. This results in motional heating and therefore in Doppler shifts, which are elaborated on in Ch. 7.4. Chemical reactions and heavy collisions result in ion loss in most cases. These events are naturally excluded from the frequency data and the respective shift is therefore zero.

The main contribution of BGC to a systematic frequency uncertainty stems from changes in the phase of the atomic superposition between ground and excited state due to interactions during Langevin spiraling collisions (Hankin et al., 2019). This results in a systematic frequency shift, called collisional frequency shift (CFS). These collisions have small impact parameters such that the colliding particle spirals towards the ion in a classical picture where it samples different interaction potentials of ground and excited state of the clock ion. In general, glancing collisions also introduce a phase shift, because the ion is polarizing the colliding molecule, which results in an electric field that generates an ac Stark shift (Hankin et al., 2019). However, due to the small differential polarizability of $^{27}\mathrm{Al}^{+}$ (Brewer et al., 2019b) this phase shift is negligible compared to the phase shift due to Langevin spiraling collisions (Hankin et al., 2019). The value of this phase shift depends on the potential energy curves of the $^{27}\mathrm{Al}^{+}$ states experienced by the colliding particle. In addition, the probability of a collision event, described by the collision cross section, also depends on the potential energy curves. Therefore the phase shifts have to be weighted by their cross section (Davis, Dubé, and Vutha, 2019). In previous evaluations the phase shifts were estimated to be $\pi/2$ per collision (Rosenband et al., 2008; Chou et al., 2010; Brewer et al., 2019b; Hankin et al., 2019), which is a conservative approach that overestimates the CFS and its uncertainty. The CFS evaluation was therefore limited by the applied collision model.

Since the most dominant background gas particles in UHV experiments are H_2 and He (Hankin et al., 2019; Davis, Dubé, and Vutha, 2019), the discussion here is restricted to these. In Ref. (Davis, Dubé, and Vutha, 2019) a theoretical framework was developed, which improves the accuracy of the evaluation of the CFS. A quantum master equation in Lindblad form is derived, whose Lindblad terms are the sums over partial wave phase-jump operators and the Hamiltonian is corrected by an additive mean field Hamiltonian. The CFS can then be extracted from the additional phase growth in the coherences (non-diagonal elements) of the equation of motion of the system compared to the evolution without collisions. The individual phase shifts of the partial waves are calculated using coupled-cluster methods. Averaging the kinetic energy of colliding particles over the Boltzmann energy distribution at 295 K they arrive at the following expressions for the CFS and its uncertainty

$$\begin{aligned}\langle\delta\omega_{\mathrm{He}}\rangle &= 2\pi(14\pm32)\mathrm{pHz}\left(\frac{n_{\mathrm{bg}}}{\mathrm{cm}^3}\right)\\ \langle\delta\omega_{\mathrm{H}_2}\rangle &= 2\pi(12\pm161)\mathrm{pHz}\left(\frac{n_{\mathrm{bg}}}{\mathrm{cm}^3}\right)\ ,\end{aligned} \tag{7.27}$$

in terms of the unit particle density n for helium and hydrogen. In Ch. 5.1 a H_2 background pressure value of 11(6) nPa was estimated from measured reordering rates. Therefore, the absolute frequency shift is 32 µHz, (2.9×10^{-20} in fractional units) and is zero within its uncertainty. We therefore evaluate the fractional frequency shift due to H_2 BGC to

$$\left(\frac{\Delta\nu}{\nu}\right)_{\mathrm{CFS}} = 0.0(3.9)\times10^{-19}\ . \tag{7.28}$$

Assuming that the entire measured background gas pressure is from He atoms, the fractional frequency shift is $3(8)\times10^{-20}$ and hence negligible.

As pointed out in (Hankin et al., 2019) the CFS due to phase shifts is approximately constant for clock interrogations with increasing probe durations, because for increasing probe time, the probability for phase-shifting Langevin collision increases but is approximately balanced by the decrease in linewidth and in consequence a smaller possible phase shift. This is in contrast to the time-dilation component, which is increasing linearly with time.

In the future a full application of the proposed models in Ref. (Davis, Dubé, and Vutha, 2019; Hankin et al., 2019) in simulations of the collision events during the clock interrogation will allow to bound the uncertainty to even lower values.

7.7 Zeeman Shifts

Shifts arising from the magnetic field $\vec{B}$ are called Zeeman shifts. Linear contributions cause a splitting of hyperfine structure states $|\alpha F m_F\rangle$ used for the $^1\mathrm{S}_0 \leftrightarrow {}^3\mathrm{P}_0$ transition. They are averaged to zero by probing at least two Zeeman transitions with opposite m_F sign. Since the Zeeman hyperfine states are individually addressable, this could for example be accomplished by interleaved probing of $\left|^1\mathrm{S}_0, F = 5/2, m_F = -5/2\right\rangle \leftrightarrow |\,^3\mathrm{P}_0, F = 5/2, m_F = -5/2\,\rangle$ and $\left|^1\mathrm{S}_0, F = 5/2, m_F = +5/2\right\rangle \leftrightarrow |\,^3\mathrm{P}_0, F = 5/2, m_F = +5/2\,\rangle$. Following Ref. (Brewer et al., 2019a), the obtained clock frequencies from probing these two outer transitions can be written as

$$\nu^{(+),(-)} = \nu_0 \pm \frac{5}{2}(g_p - g_s)\frac{\mu_B}{h}\langle B\rangle + C_2\langle B^2\rangle \,, \tag{7.29}$$

where ν_0 is the unperturbed clock frequency, g_s and g_p are the Landé g-factors of S and P state, μ_B is the Bohr magneton, and C_2 is the quadratic Zeeman coefficient, which has been measured in (Brewer et al., 2019a) to be

$$C_2 = -71.944(24)\,\frac{\mathrm{MHz}}{\mathrm{T}^2} \,. \tag{7.30}$$

Here, $\langle\ \rangle$ denotes the time average. Higher order terms in Eq. (7.29) are very small and can be neglected.

The clock servo will correct for changes in the mean of these frequencies, which is given by

$$\nu = \frac{1}{2}(\nu^{(+)} + \nu^{(-)}) = \nu_0 + C_2\langle B^2\rangle \,. \tag{7.31}$$

Systematic shifts due to the quadratic term do not average to zero. They split up into a static part and a time varying part $\langle B^2\rangle = B_{\mathrm{dc}}^2 + \langle B_{\mathrm{ac}}^2\rangle$. The first term is dominated by the quantization magnetic field B_0 and its slow time dependence due to drifts and fluctuations. The latter is called ac Zeeman shift and accounts for oscillating magnetic fields with periods much shorter than clock transition probe times. They are caused by power line noise and the oscillating currents of the RF part of the linear Paul trap. Trap drive induced fields are typically on the order of a few μT (Gan et al., 2018; Chou et al., 2010; Brewer et al., 2019b). In the following the individual shifts are being discussed.

7.7.1 DC Zeeman Shift

The following section describes the planned strategy for the running clock. In this experiment we apply a quantization magnetic field of $B_0 = 0.15\,\mathrm{mT}$ along the trap axis direction for lifting the hyperfine degeneracy (Ch. 3.7.2). Within one clock cycle the two Zeeman components $\nu^{(+)}$ and $\nu^{(-)}$ are measured and the magnetic field can be calculated by subtracting both frequencies. Therefore, the magnetic field value is measured in real time, depending on the clock cycle time. From the magnetic field stability measurements in Ch. 5.2.1 it follows that the magnetic field can be inferred by a rolling time-average up to 100 s to a statistical uncertainty of 2 nT before it starts to drift away. When inferring B_{dc} from $\nu^{(+)}$ and $\nu^{(-)}$ an uncertainty in the Landé g-factors (Rosenband et al., 2007)

$$(g_p - g_s) = -1.184\,37(8) \times 10^{-3}\ , \tag{7.32}$$

has to be taken into account. As can be seen in Fig. 7.6, under typical clock operation conditions the magnetic field cannot be determined to a better uncertainty value than 10 nT due to the uncertainty in the Landé g-factors. Since $^{27}\mathrm{Al}^+$ is insensitive to magnetic fields it is advantageous to use $^{40}\mathrm{Ca}^+$ as magnetic field sensor. For example, the magnetic field can be inferred by subtracting the carrier resonance frequencies of the $^{40}\mathrm{Ca}^+$ $|\mathrm{S}_{1/2}, m_J = -1/2\rangle \leftrightarrow |\mathrm{D}_{5/2}, m_J = -1/2\rangle$ and $|\mathrm{S}_{1/2}, m_J = -1/2\rangle \leftrightarrow |\mathrm{D}_{5/2}, m_J = -5/2\rangle$ transitions using Ramsey interrogation, as described in Ch. 5.2 and applying Eq. (5.5) for calculating the magnetic field strength, see Fig. 7.6. Due to the higher value and accuracy in the $^{40}\mathrm{Ca}^+$ Landé g-factor of the $\mathrm{D}_{5/2}$-state, a small reduction of the uncertainty is achieved. Fig. 7.7 shows, that in this case the dc Zeeman shift uncertainty is limited by the C_2 factor. Unless improved measurements or

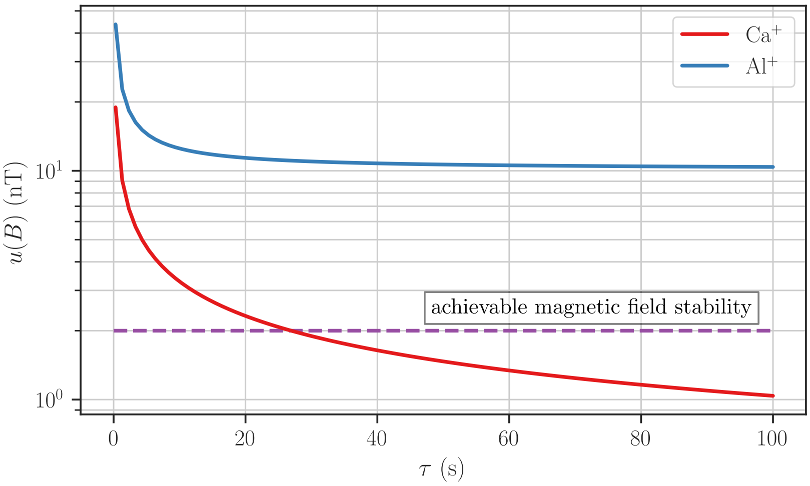

Figure 7.6: Magnetic field averaging estimated in the case for $^{40}\mathrm{Ca}^+$ by the QPN-ADEV with Ramsey interrogation with a dark time of $t_d = 500\,\mu\mathrm{s}$, and in the case for $^{27}\mathrm{Al}^+$ with a Rabi interrogation with a probing time of 150 ms. The cycle time is set in both cases to 0.6 s, which results in fractional frequency instability for the Al^+ clock of $1.2 \times 10^{-15}\ 1/\sqrt{\tau}$ (Brewer et al., 2019b). It can bee seen that the $^{27}\mathrm{Al}^+$ cannot average the magnetic field to the limit given by 2 nT (measured in Ch. 5.2.1), due to the uncertainty in the Landé g-factors.

calculations provide more accurate values for C_2, a reduction of the uncertainty of the dc Zeeman shift can only be achieved by reducing the magnetic field. A reduction of the dc magnetic field is accompanied by a potential overlap of motional secular frequency resonance of different $^{40}\mathrm{Ca}^+$ Zeeman states, which must be avoided to guarantee a high GSC efficiency. For the uncertainty budget of this clock we take the value obtained from measuring on $^{40}\mathrm{Ca}^+$. The additional dead-time, which is introduced by Doppler cooling, Ramsey interrogation of the two carrier transitions with 500 µs dark time and detection, is around 5 ms in total. This corresponds to 3 % of the clock interrogation time of 150 ms and becomes more negligible for longer interrogation times. Therefore, from Fig. 7.7 the dc Zeeman shift in this clock is estimated to be

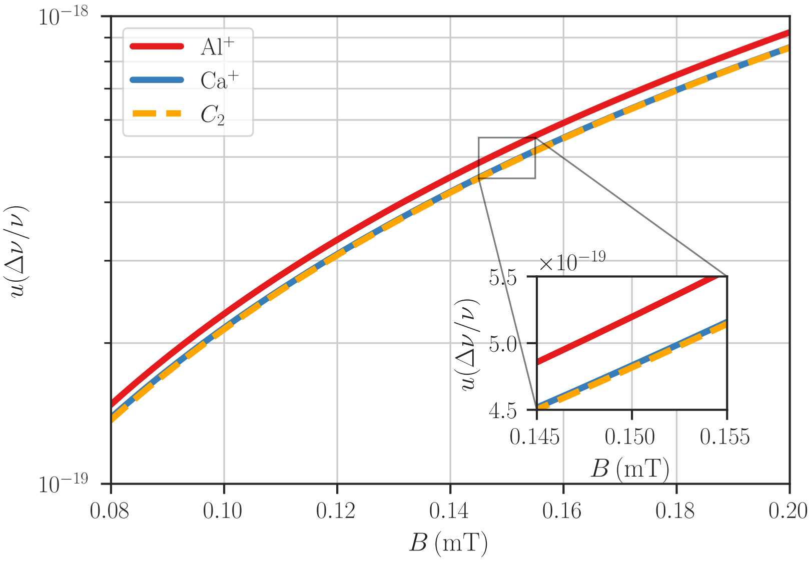

Figure 7.7: Dc Zeeman shift uncertainty in dependence of the magnetic field strength and ion used as magnetic field sensor. This assumes a 2 nT uncertainty limit for the $^{40}\mathrm{Ca}^+$ ion, since the magnetic field can only be averaged to this value. The other contributions in both ions are the systematic uncertainties in the Landé g- and C_2 factors. The contribution from the uncertainty of the C_2 factor is shown as the orange dashed line.

$$\left(\frac{\Delta\nu}{\nu}\right)_{\mathrm{Z,\,dc}} = -1.443\,99(48)\times10^{-15}\,, \tag{7.33}$$

using the uncertainty achieved by probing on $^{40}\mathrm{Ca}^+$.

7.7.2 AC Zeeman Shift

Oscillating magnetic fields are caused in a wide range of frequencies, where the main contributions are power line noise at 50 Hz and harmonics, switching power supplies in the range of a few 100 Hz to 1000 kHz and the magnetic field radiated by the RF Paul trap at 27.95 MHz.

Ac Magnetic field noise from power line and switching power supplies are one of the main reason for decoherence, next to laser noise. As described in Ch. 3.7.2 we use an active magnetic field stabilization and maximized the distances of noise-emitting devices to the ion. For the oscillating magnetic fields in this range, we inferred from coherence measurements an rms value of $\sqrt{\langle \Delta B^2 \rangle} = 27.6(8)$ nT (Ch. 5.2.2). The ac Zeeman shift and uncertainty connected to this contribution are $-4.9(3) \times 10^{-23}$ and thus negligible.

Charging and discharging the trap capacitance can induce high currents at the trap drive frequency Ω, which give rise to ac magnetic fields at the ion's position. In a perfectly symmetric and flawlessly machined trap all fields coming from the trap should sum up to zero at the trap center. Residual electric fields lead to excess and intrinsic micromotion, which can be partially compensated, see chapter 7.2. Ac magnetic fields induced by the RF part of the trap in contrast need to be characterized thoroughly, because they cannot be compensated nor shielded. They shift the clock transition by a quadratic Zeeman shift given by Eq. (7.31).

Following Ref. (Gan et al., 2018) the shift of a state $|a\rangle$ by a coupling of a magnetic field B with state $|b\rangle$ takes the form

$$\Delta E_a = -\frac{\langle B^2 \rangle}{2\hbar} \left(\frac{|\langle b|\vec{u} \cdot \vec{\mu}|a\rangle|^2}{\omega_{ba} - \omega} + \frac{|\langle a|\vec{u} \cdot \vec{\mu}|b\rangle|^2}{\omega_{ba} + \omega} \right), \tag{7.34}$$

in direct analogy to the ac Stark shift caused by an oscillating electric field, which is discussed in Ref. (Le Kien, Schneeweiss, and Rauschenbeutel, 2013). This formula is valid when the oscillation frequency is far detuned from the energy splitting between the states. Here the frequency ω_{ba} denotes the unperturbed energy splitting $E_b - E_a = \hbar\omega_{ba}$ of the states $|a\rangle$ and $|b\rangle$, $\vec{\mu}$ is the magnetic dipole operator, $\vec{u}$ the polarization vector of the magnetic field and $\langle \cdot \rangle$ denotes the time average.

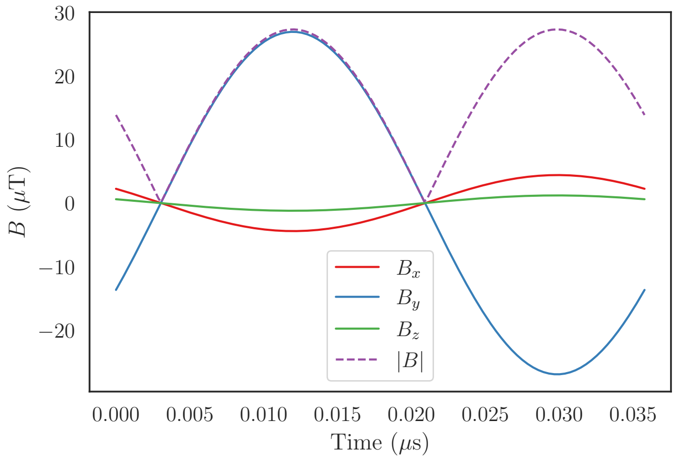

Figure 7.8: Simulation (Doležal, n.d.) of the trap induced ac magnetic field in the iQLOC 1 trap center at blade voltages of 225 V with symmetric drive, which corresponds to a radial secular frequency of $\omega_{\text{rad}} \approx 2 \times 1.589$ MHz or a trap drive input power before amplification of $P = -0.92$ dBm (Ch. E.4). The field components at the trap center have no phase lag at their nodes and the vertical magnetic field is dominating the total field amplitude.

Typical values of the ac magnetic field in other experiments are reported to be a few µT (Gan et al., 2018; Brewer et al., 2019a). For our linear Paul trap a simulation of the drive currents and the resulting magnetic field were performed to derive the ac Zeeman shift. Further details can be found in the appendix Ch. E.3. Fig. 7.8 depicts the result of a simulation at 225 V symmetric RF blade voltage amplitude. Event at this low trap drive power the magnetic field exceeds 27 µT, which is at least one order of magnitude higher than reported by other groups. As such strong fields would contribute significantly to the total systematic shift of the clock transition, a measurement of this shift was performed.

We measured the ac magnetic field using a method described in Ref. (Gan et al., 2018). It is based on detecting the Autler-Townes splitting γ of the $^{40}\mathrm{Ca}^{+}$ ground states induced by the trap magnetic field. Fig. 7.9 depicts the generation of Autler-Townes pairs in $^{40}\mathrm{Ca}^{+}$. The Autler-Townes splitting becomes apparent when the dc Zeeman splitting between these S-states is matched with the trap drive frequency Ω_{RF}. This splitting then constitutes a direct measurement of the ac magnetic field amplitude vector of $\vec{B}_{\mathrm{ac},\perp} \cdot \cos(\omega t)$, which is perpendicular to the quantization magnetic field.

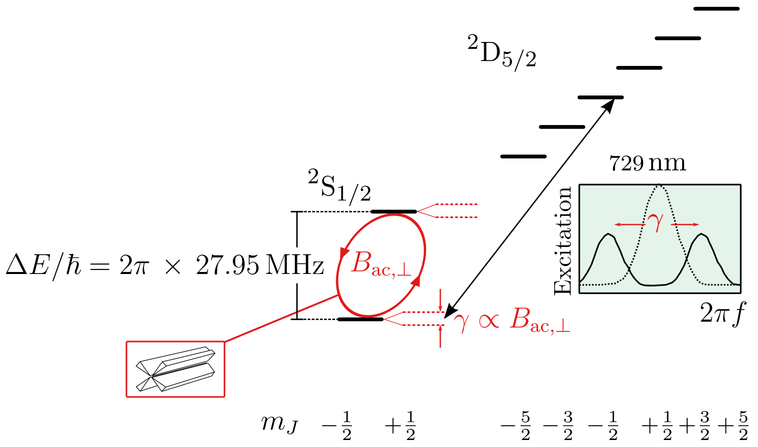

Figure 7.9: Measurement technique for the trap-induced ac magnetic field amplitude. For Zeeman splittings near the trap drive frequency $\Omega_{\mathrm{RF}} = 2\pi \times 27.95\,\mathrm{MHz}$, the $|\mathrm{S}_{1/2}, m_J = -1/2\rangle \leftrightarrow |\mathrm{D}_{5/2}, m_J = -1/2\rangle$ transition splits up into a spectrum of two Autler-Townes peaks separated by γ. The minimum splitting is at resonance and is a direct measurement of the state-coupling oscillating magnetic field $B_{\mathrm{ac},\perp}$ originated from the trap drive.

The analysis of this shift is structured as follows. In the appendix Ch. E.1 the relation between Autler-Townes splitting and trap ac magnetic field amplitude for the $^{40}\mathrm{Ca}^{+}$ $^2\mathrm{S}_{1/2}$ states is calculated and in Ch. 7.7.2.1 the measurement of these splitting frequencies is described. In Ch. 7.7.2.2 the inferred trap-induced ac Zeeman shift for the $^{27}\mathrm{Al}^{+}$ clock transition and its uncertainty are calculated. As mentioned above, the appendix Ch. E.3 gives more details on the simulations of the ac magnetic field in this experiment.

7.7.2.1 Measurement of the Perpendicular Magnetic Field

Following Ref. (Gan et al., 2018), the observed splitting γ is a direct measurement of the fast oscillating magnetic field $B_{\mathrm{ac},\perp}$, which is perpendicular to the static bias field B_0. At resonance, i.e., if the trap drive frequency is matched with the S-state Zeeman splitting, the Autler-Townes resonances are separated by

$$\gamma = \frac{g_J \mu_B}{2\hbar} B_\perp \,, \tag{7.35}$$

where g_J is the Landé g-factor of the S-states of $^{40}\mathrm{Ca}^+$, μ_B is the Bohr magneton and the index ac has been dropped from $B_{\mathrm{ac},\perp}$. A derivation of Eq. (7.35) is given in Ch. E.1.

Here, in order to match the Zeeman splitting of the S-states, which have a sensitivity of $\approx 28.037\,\mathrm{MHz/mT}$, with the trap drive frequency $\Omega_{\mathrm{RF}}/2\pi = 27.95\,\mathrm{MHz}$, a magnetic field $B_0 \approx 1\,\mathrm{mT}$ has to be applied. This is accomplished by placing two stacked neodymium magnets which produce a field of $\approx 0.8\,\mathrm{mT}$ near the chamber, with a distance of 20 to 30 cm from the ion. Fine-tuning of the Autler-Townes resonance is then accomplished by using the quantization field coil pairs, see Fig. 7.10.

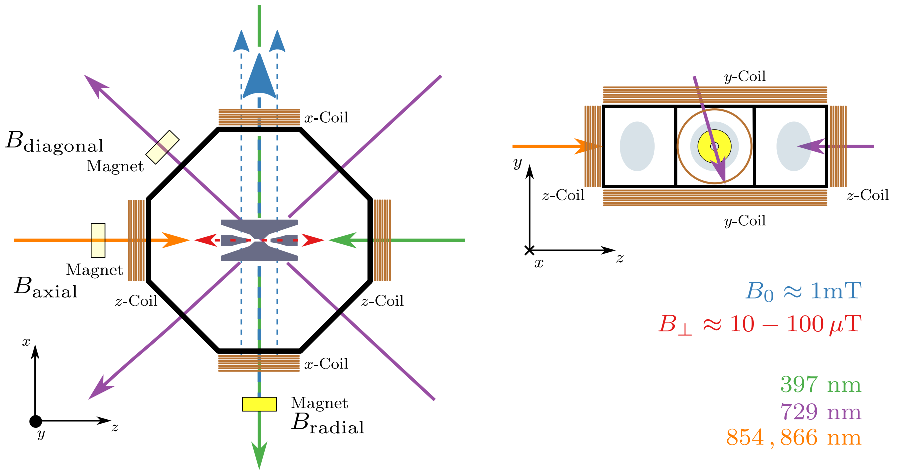

Figure 7.10: Schematic setup for measuring trap ac magnetic fields (red). The bias magnetic field $B_0 \approx 1\,\mathrm{mT}$ (blue), here displayed for the radial configuration, is produced by a stack of two neodymium magnets (yellow for radial and light yellow for axial and diagonal configuration) and the quantization coils. $^{40}\mathrm{Ca}^+$ Doppler-cooling, state preparation and detection lasers (green) impinge onto the ion in the center of the trap along the trap axis and along the radial direction. An Autler-Townes splitting is observed using 729 nm laser beams (violet), coming from the top port or from the diagonal windows. Clear-out and repumper beams (orange) enter the chamber along z. Measurements were conducted with B_0 pointing along four different directions, where for B_{top} (not shown) the magnetic field is tilted out of the horizontal plane by applying $B_y \approx 0.16\,\mathrm{mT}$ using the y-coils.

Since the ac Zeeman shift in $^{27}\mathrm{Al}^+$ is sensitive to the rms value of the total amplitude, i.e., $\langle(\vec{B}\cos(\Omega t))^2\rangle$, we measured $B_\perp$ from several directions by rotating the quantization field B_0, see Fig. 7.10 and 7.11(b). This enables a full "tomography" of the magnetic field vector amplitude, when using three

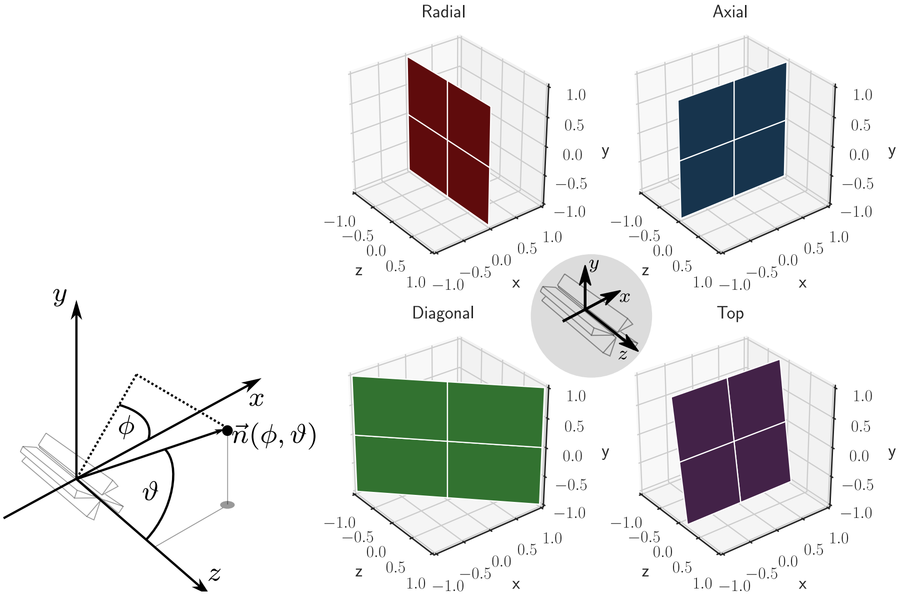

(a) (b)

Figure 7.11: (a) Definition of the spherical angles used throughout this thesis. ϕ is the azimuthal and ϑ is the inclination angle. (b) The oscillating magnetic field is probed as projection onto four planes, with their normal vector being defined by the direction of $\vec{B}_0$, see Tab. 7.2. Because of geometrical constrains no permanent magnet can be placed on top or below the vacuum chamber, which would provide a pure horizontal measurement plane.

non-coplanar directions. A measurement result $B_{\perp,i}$ is then the projection of the oscillating field amplitude $\vec{B}$ onto this plane:

$$B_{\perp,i} = \sqrt{|\vec{B}|^2 - \left(\vec{B} \cdot \vec{n}_i\right)^2}, \tag{7.36}$$

with $\vec{n}_i$ the normal vector of plane i. The normal vectors of the planes have been aligned along the corresponding direction by nulling the fluorescence of σ^--polarized 397 nm state preparation and Doppler-cooling laser beam, see Ch. 3.7.1. These were assumed to be perfectly aligned along the designated axis of the coordinate system as shown in Fig. 7.10. In Tab. 7.2 the measurement directions, their normal vectors and our uncertainty estimation on their alignment is listed. It must be noted, that the most precise alignment was possible along axial and top direction, radial alignment is intermediate and the least accurate along the diagonal direction. The latter has a higher uncertainty, since no pure σ-polarized beam for alignment was available. For the top measurement B_0 was tilted out of the horizontal plane by increasing the current on the y-coils. Comparing the 729 nm resonance before and after the increase, we inferred a magnetic field of $B_{0,y} = 0.160\,\mathrm{mT}$.

Quadratic Zeeman shifts of $^{40}\mathrm{Ca}^+$ are smaller than a few Hz and therefore neglected. A small tilt of the total quantization field B_0 during the scan of a single coil current in top and diagonal direction has been neglected. In the conducted measurements the magnetic field stabilization unit had to be turned off, otherwise it would have counteracted the scan of quantization coils.

Table 7.2: Measured ac Zeeman directions, their normal vector and spherical angles as defined in the coordinate system, shown in Fig. 7.11(a).

Direction	Normal vector	ϕ (°)	ϑ (°)	$\Delta\phi$ (°)	$\Delta\vartheta$ (°)
radial	$(1, 0, 0)$	0	90	1	1
axial	$(0, 0, 1)$	90	0	0.8	0.8
top	$(0, 0.160, 0.987)$	90	9.24	0.8	0.06
diagonal	$(-\frac{1}{\sqrt{2}}, 0, \frac{1}{\sqrt{2}})$	180	45	1	5

The measurement procedure was the same for all directions: After calibration of the magnetic field with the magnet installed, the current of the main quantization coil of the respective direction was increased until $B_0 \approx 0.97\,\mathrm{mT}$ was reached. This was verified by checking measured 729 nm resonances with theoretically calculated values and observing a decrease of excitation, as well the appearance of second peak. Near this point of the Autler-Townes resonance condition the following experiments were carried out: $^{40}\mathrm{Ca}^{+}$ was Doppler-cooled by π- and optically pumped into the $|\,^2\mathrm{S}_{1/2},\, m_J = -\frac{1}{2}\,\rangle$ state by σ^{-}-polarized 397 nm beams. Then, the 729 nm frequency was scanned over the $|\,^2\mathrm{S}_{1/2},\, m_J = -\frac{1}{2}\,\rangle \leftrightarrow |\,^2\mathrm{D}_{5/2},\, m_J = -\frac{1}{2}\,\rangle$ transition for increasing currents applied to the corresponding quantization coil pair (Fig. 7.12 (a)). Here, the detuning from the calculated unperturbed 729 nm transition versus the variation of B_0 for a top measurement are shown. One data point is the average of 80 to 100 experiments. The Rabi resonances have been fit and their center-frequencies were extracted. In Fig. 7.12 (b) the splitting frequencies (in Hz) of the Autler-Townes pairs, together with a fit to

$$f_{\mathrm{Split}} = \sqrt{(C\,(x - x_0))^2 + \tilde{\gamma}^2} \tag{7.37}$$

is shown. Here, x is a free parameter corresponding to the coil current/ΔB_0, while x_0, C and $\tilde{\gamma}$ are fitting parameters. From the minimal splitting $f_{\mathrm{Split,min}}$ the magnetic field can be inferred:

$$B_{\perp} = \frac{2h}{g_J \mu_B} f_{\mathrm{Split,min}}\,. \tag{7.38}$$

The Landé g-factors for the $^{40}\mathrm{Ca}^{+}$ ground state $g_J = 2.002\,256\,64(9)$ (Tommaseo et al., 2003) is known with high accuracy, such that it does not influence the uncertainty of $B_{\perp}$.

The Autler-Townes splitting on the $|\,^2\mathrm{S}_{1/2},\, m_J = -\frac{1}{2}\,\rangle \leftrightarrow |\,^2\mathrm{D}_{5/2},\, m_J = -\frac{5}{2}\,\rangle$ transition has also been measured. They show the same Autler-Townes splitting, but are more prone to magnetic field fluctuations. For this reason all following measurement results were inferred from $|\,^2\mathrm{S}_{1/2},\, m_J = -\frac{1}{2}\,\rangle \leftrightarrow |\,^2\mathrm{D}_{5/2},\, m_J = -\frac{1}{2}\,\rangle$ transition frequencies.

It is expected that the strength of $B_{\perp}$ is proportional to the power of the trap drive. The collected data of all conducted measurements is shown in Fig 7.13.

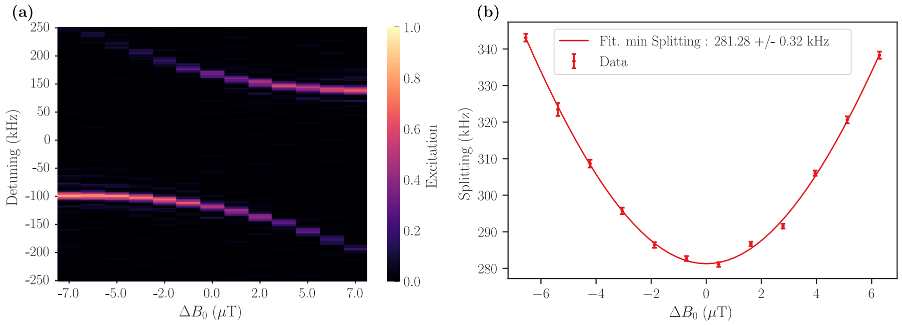

Figure 7.12: Typical measurement results for an Autler-Townes scan with B_0 in top configuration. (a) Observed Autler-Townes resonances as a function of B_0 (varied current through the z-coils). The frequency is shown as a detuning from the calculated $m_J = -\frac{1}{2} \leftrightarrow m_J = -\frac{1}{2}$ transition frequency at a magnetic field $B_0 = 0.9969\,\mathrm{mT}$. (b) Splitting frequency of the Autler-Townes resonances are fit Eq. (7.37). The minimum splitting frequency is proportional to $B_\perp$.

This includes variation of the dc tip and compensation electrodes. Note, that the following findings can be concluded from this plot.

1. The measured B field values are quite high compared to these reported in (Gan et al., 2018; Brewer et al., 2019a).
2. The measured B fields at a particular trap drive power are quite similar in all horizontal measurement directions. Thus it can be inferred that the magnetic field vector has its main component in B_y. Unfortunately, the neodymium magnet couldn't be placed in top direction due to spatial restrictions.
3. The error bars on individual data points are on the order of $0.02\,\mu\mathrm{T}$, while the maximum spread of measurement results with comparable trap settings goes up to $0.134\,\mu\mathrm{T}$.
4. Miroslav Doležal provided HFSS simulation data of magnetic fields at the ion position, extracted from simulated currents in the chamber for different trap drive voltages. The trap drive voltages have been transformed as described in Ch. E.4. The simulated data also confirm that the magnetic field vector mainly points along the y direction, see Fig. 7.8 and Fig E.3. The simulated magnetic fields are however larger compared to the measured values at comparable trap drive power. The reason for this may be found in the different positioning and orientation of the RF carrying copper stripes with respect to the trap center in the simulations and in the experimental setup.

From the linear part of the polynomial fit, Fig. 7.14, and from the considerations in Ch. 5.4, where a trap drive stability of $\pm 0.07\,\mathrm{dBm}$ at $0\,\mathrm{dBm}$ has been inferred, we expect a worst-case B-field variation of $\pm 0.17\,\mu\mathrm{T}$ due to trap drive instability. In fact, the fluctuations in the trap drive power are limiting the accuracy to which the ac Zeeman shift can be quantified. As pointed out in Ch. 5.4 a trap drive stabilization is a planned improvement on the experiment and thus we expect to further reduce the uncertainty of this shift in the future.

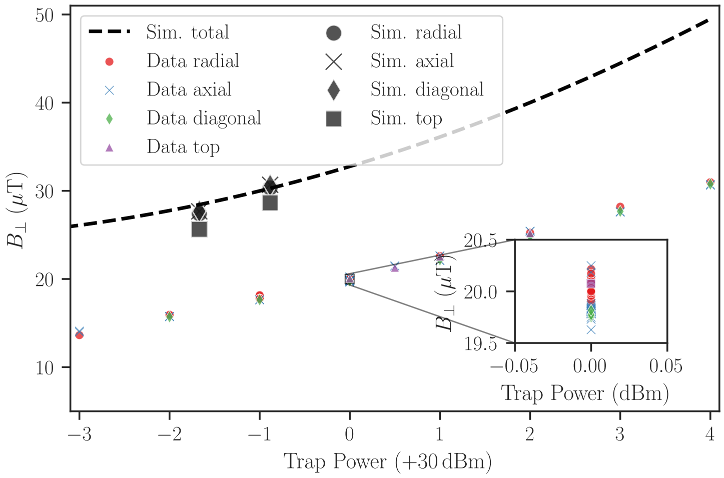

Figure 7.13: Measured (colored symbols) and simulated (black symbols and black dotted line) trap-induced magnetic fields in dependence of trap drive power. For better readability the error bars are not shown in the measured data.

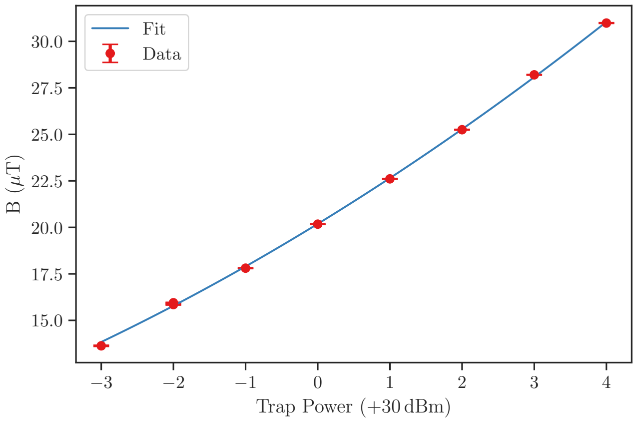

Figure 7.14: Polynomial fit of $B_\perp$ in radial measurement direction. $B_{\perp,\mathrm{rad}} = 0.085\,\mu\mathrm{T/dBm}^2 \cdot P^2 + 2.374\,\mu\mathrm{T/dBm} \cdot P + 20.189\,\mu\mathrm{T}$. An estimate on the sensitivity to trap drive power fluctuations can be inferred.

In order to answer the question if changes of the ion position or the level of micromotion have an impact on B_{ac} the dc electrode voltages were varied (Fig. 7.15). The scanned voltages are beyond the range needed for everyday micromotion compensation, see Ch. 7.2. From this measurement we deduce that $B_\perp$ shows no significant variation on the ion position or micromotion inside this range. This is also confirmed by HFSS simulations, see Fig. E.2 in the appendix.

The measurement results (Fig. 7.16) are the same within their uncertainties, and therefore little can be said about the changes in the small B_x and B_z components of the ac magnetic field. However, the absolute value of the magnetic field can be extracted from the evaluation process with relatively high accuracy. The high directionality along the y direction is surprising. The simulations (Ch. E.3) suggest that the position of the RF copper stripes and

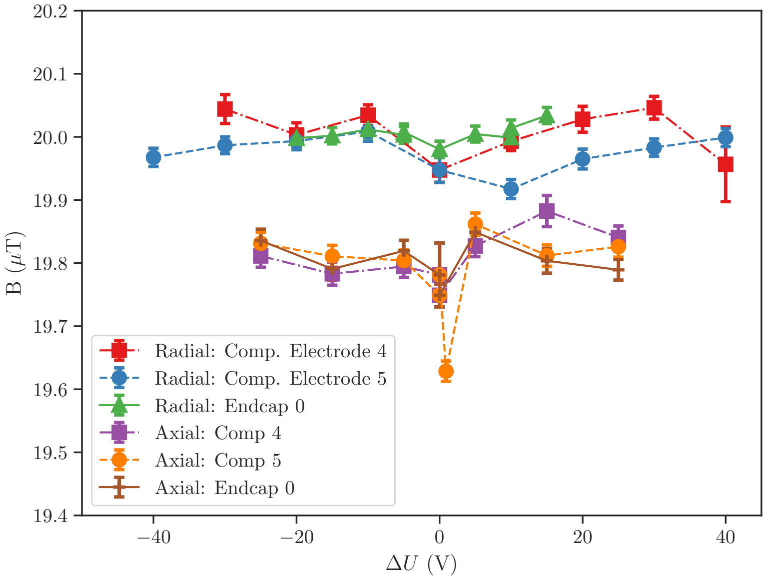

Figure 7.15: Measured $B_\perp$ in radial and axial direction in dependence of dc electrode voltages. For the endcaps it is $\approx 0.65\,\mu$m/V and for the compensation electrodes $\approx 0.09\,\mu$m/V. Compensation electrode 4 moves the ion in the y direction and electrode 5 in the x direction.

the compensation electrodes break the symmetry of the electrode geometry and result in the high vertical directionality.

7.7.2.2 Magnitude of B_{ac}

We implement a two-step evaluation process in order to extract values on the total amplitude B_{ac} and its orientation. For this it is necessary to have a model which relates a measurement outcome and parameters including their uncertainty to a value of $B^2_{\text{ac}} \pm u(B^2_{\text{ac}})$.

At first we used the data at 0 dBm to estimate the magnetic field vector orientation. This was achieved by fitting the data from all directions to Eq. (7.36). This is the biggest data set and it is close to the trap drive power of 0.5 dBm (ω_{rad} =1.92 MHz), which we plan to use during clock operation. In this fit, we vary the magnetic field vector's absolute value, its ϑ and ϕ angle to fit to the measurement results inside their bounds. The angles of the measurement normal vector are kept fixed. Second, noting that some measurement directions contain all information needed if the orientation of B_{ac} is known, we reverse Eq. (7.36). We take the orientation and the uncertainty of the field vector from step one and calculate the absolute value of B_{ac} using a simple model and data from the top direction measurement at 0.5 dBm. This is chosen because in the top direction, the magnetic field orientation is well-known.

Fig. 7.16 shows the data used for fitting the magnetic field vector direction. In the axial histogram measurement dates have been annotated to illustrate that drifts in trap drive power and laboratory temperature shift the ac Zeeman magnetic field. Consequently, a normal distribution of measurement results cannot be justified. Following the advises in the Guide to the Expression of

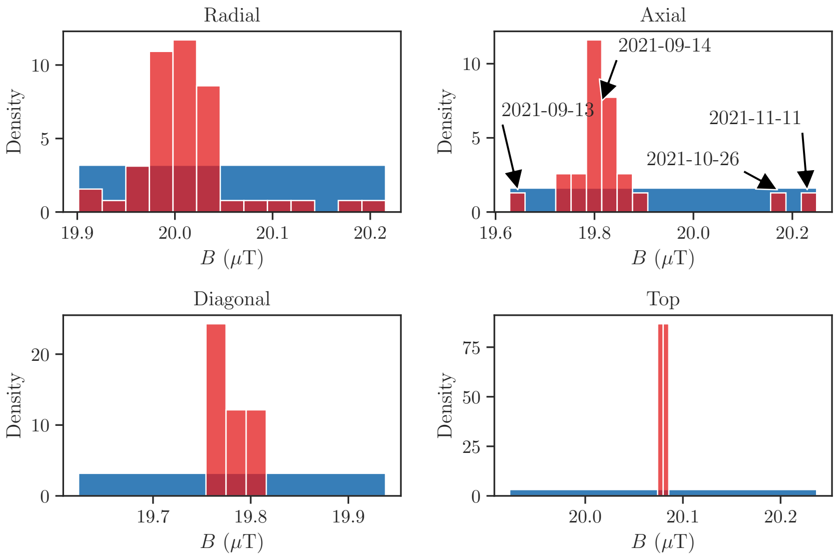

Figure 7.16: Histograms of all measured data at a trap drive power of 0 dBm (red). The bins are normalized to unit area. Even though the measurement outcomes may be normally distributed, when measured over a short period of time, i.e., at the same trap drive power and lab temperature, on long time scales they spread over certain ranges. This is indicated by the measurement dates added to the axial histograms. To account for this spread we assume rectangular distributions (blue); also normalized to unit area. In diagonal and top direction the rectangles have the width of the radial direction to account for the small number of measured values in these directions. From the rectangular distributions, we deduce the following measurement results, which will be used for fitting: radial: 20.06(9) µT, axial: 19.94(18) µT, diagonal: 19.78(9) µT, top: 20.08(9) µT.

Uncertainty in Measurement (GUM) (Metrology (JCGM/WG 1), 2008), we account for the fact that the magnetic field is somewhere between certain bounds by using rectangular distributions, depicted as blue areas in Fig. 7.16. The standard uncertainty of a measurement is then the half width of the rectangular distribution divided by $\sqrt{3}$ (Metrology (JCGM/WG 1), 2008). Applying a non-linear least-square minimization (Newville et al., 2021) using this data to the set of equations (7.36) gives the following results:

$$
\begin{aligned}
(B &= (20.11 \pm 0.08)\ \mu\mathrm{T}) \\
\phi_B &= (84.8 \pm 3.0)\ ^\circ \\
\vartheta_B &= (98.9 \pm 2.5)\ ^\circ \\
r(\phi_B, \vartheta_B) &= 0.429\,,
\end{aligned}
\tag{7.39}
$$

where $r(\phi_B, \vartheta_B)$ is the correlation between the angles of B. The parenthesized value of B is not used in the following analysis.

We now reverse Eq. (7.36) to

$$
B = \frac{B_{\perp,\,\mathrm{top}}}{\sqrt{1 - \left[\vec{e}\,(\phi_B, \vartheta_B) \cdot \vec{n}\,\left(\phi_{\mathrm{top}}, \vartheta_{\mathrm{top}}\right)\right]^2}}\,. \tag{7.40}
$$

$\vec{e}$ and $\vec{n}$ are the unit vectors of the magnetic field and the normal vector of the top plane. The combined uncertainty can be found in the appendix, see Eq. (E.16).

We take $B_{\perp,\mathrm{top}}$ =21.265(90) µT, measured in top direction at 0.5 dBm and assume full correlation $r(B_{\perp,\,\mathrm{top}}, \vartheta_{\mathrm{top}}) = 1$ and $r(B_{\perp,\,\mathrm{top}}, \phi_{\mathrm{top}}) = 1$. Using the values, uncertainties and correlations from Eq. (7.39) and Tab. 7.2 for the angles of $\vec{e}$ and $\vec{n}_{\mathrm{top}}$ results in an ac magnetic field of $B_{\,\mathrm{ac}}$ =21.266(91) µT. The described analysis steps are even more well-suited when the trap drive power fluctuations are suppressed by the active trap drive stabilization. However at this time, this has not been implemented and for the uncertainty budget of this clock we want to be conservative. In consequence, we enlarge the uncertainty to the value that was inferred from the trap drive fluctuations, i.e., $u(B_{\mathrm{ac}}) = 0.17$ µT. Combined, this results in an rms value of $\sqrt{\langle B_{\mathrm{ac}}^2\rangle} = 15.04(12)$ µT. The fractional clock frequency shift is hence

$$\left(\frac{\Delta\nu}{\nu_0}\right)_{\mathrm{Z,\,ac}} = -1.452(23) \times 10^{-17} \,. \tag{7.41}$$

In contrast to the dc quadratic Zeeman shift the main contribution here comes from the uncertainty in B_{ac}. The applied measurement technique however reduces the uncertainty due to this shift into the low 10^{-19} regime, even though the ac magnetic field in this trap is unusually high. The active trap drive stabilization will further improve on this uncertainty contribution. Assuming a reduction of trap drive drifts and corresponding magnetic field uncertainty by a factor of 5, that is 0.034 µT, the uncertainty in this shift would be as low as 5×10^{-20}.

7.8 Electric Quadrupole Shift

At the position of the clock ion significant electric field gradients can couple to the quadrupole moment of $^{27}\mathrm{Al}^{+}$. The gradients can be caused by a static axial field and due to the charge of the neighboring logic ion. Yet, both $^{27}\mathrm{Al}^{+}$ states involved in the clock transition it is nominally $J = 0 \leftrightarrow J = 0$ states, which means that the electrons due to their symmetrical symmetry do not support a quadrupole moment Θ. Interaction with the nucleus introduces hyperfine mixing, which enables to drive the clock transition at all and could in principle lead to a non-negligible Θ. However, in Ref. (Beloy, Leibrandt, and Itano, 2017) theoretical calculations give a small quadrupole moment of the excited clock state of $\Theta_{\mathrm{P}} = -1.7(6) \times 10^{-6} e a_B^2$ and $\Theta_{\mathrm{S}} < 1 \times 10^{-8} e a_B^2$ for the ground state, respectively. Here, e is the elementary charge and a_B is the Bohr radius. The clock ground state's quadrupole moment is negligible compared to that of the excited state. Following Ref. (Beloy, Leibrandt, and Itano, 2017) the energy shift for $^{27}\mathrm{Al}^{+}$ can be written as

$$\Delta E = \frac{1}{2}\frac{\partial^2\Phi}{\partial z^2}\frac{3m_F^2 - F(F+1)}{F(2F-1)}\Theta \,, \tag{7.42}$$

with F the total angular momentum and m_F the corresponding projection onto the quantization axis. The dependence on m_F^2 allows to cancel this shift by averaging all $m_F = -5/2, -3/2, \ldots, 5/2$ transitions (Dubé et al., 2005). The gradients of the two aforementioned potentials can be evaluated to (Beloy, Leibrandt, and Itano, 2017)

$$\frac{\partial^2\Phi_{\mathrm{Trap}}}{\partial z^2} = \frac{2U_0}{d^2}\left(\frac{3\cos^2(\theta)-1}{2} - \left(\alpha - \frac{1}{2}\right)\sin^2(\theta)\cos(2\phi)\right) \tag{7.43}$$

$$\frac{\partial^2\Phi_{\mathrm{Ion}}}{\partial z^2} = \frac{2U_0}{d^2}\frac{3\cos^2(\theta)-1}{2} \tag{7.44}$$

$$\frac{U_0}{d^2} = \frac{m_1\omega_{z,\mathrm{IP}}^2}{2e}\frac{\mu}{1+\mu-\sqrt{1-\mu+\mu^2}}\,, \tag{7.45}$$

where m_1 is the mass of $^{40}\mathrm{Ca}^+$, $m_2 = \mu m_1$ the mass of $^{27}\mathrm{Al}^+$ and $\omega_{z,\mathrm{IP}}$ the axial in-phase secular frequency. The angles between magnetic field quantization direction and the coordinate system are defined by the standard spherical polar and azimuthal angle and are $\theta = 0.0(8)^\circ$ and $\phi = 45.0(8)^\circ$ for the magnetic field direction pointing along the trap axis. Together with $\alpha = 1/2$, $\omega_{z,\mathrm{IP}} = 1.196\,\mathrm{MHz}$ the shift calculates to

$$\left(\frac{\Delta\nu}{\nu_0}\right)_{\text{el. quad.}} = -2.05(72)\times 10^{-20}\,, \tag{7.46}$$

which is only a negligible contribution to the uncertainty budget. The contribution of the gradients from the compensation electrodes have been discarded so far. It is worthwhile to note that the shift can also be canceled by interrogating with three different quantization magnetic field directions, due to the $3\cos(\theta) - 1$ dependence (Itano, 2000).

The quadrupole field of the RF trap drive is averaging to zero during clock interrogation.

7.9 Unassessed Shifts

Clock Laser ac Stark shift The clock laser can introduce an ac Stark shift by coupling the clock ground and excited states non-resonantly to other levels. Considering the low powers of nW to pW needed for clock interrogation, the shift is small. It was measured in (Chou et al., 2010) to be $0.0(2)\times 10^{-18}$ by comparing two $^{27}\mathrm{Al}^+$ clocks, where in one of them the clock laser intensity was increased by 40 dBm.

AOM Phase Chirp When shuttering the clock interrogation light with an AOM, the abruptly turned on RF drive of the AOM will heat the AOM crystal and lead to a phase chirp of the clock light passing through the AOM, which results in a frequency chirp (Degenhardt et al., 2005). This effect can be reduced by using low RF powers on the AOM. We did not measure this phase-chirp so far, but in Ref. (Chou et al., 2010) it was reported to be $0(2)\times 10^{-19}$ by limiting the power on the AOM to $< 1\,\mathrm{mW}$. Additionally, it is planned to detune the AOM frequency such that it is not resonant with the clock transition while keeping the AOM at constant power. Doing this, the AOM phase chirp is reduced, but a probe beam ac Stark shift has to be taken into account.

Gravitational Red-Shift Clocks at larger gravitational potential tick at lower rates. This effect is called gravitational red-shift and has been proposed by Einstein in 1911 in his general theory of relativity (Einstein, 1911). The shift on the earth's surface can be written as (Mehlstäubler et al., 2018)

$$\left(\frac{\Delta\nu}{\nu}\right)_{\mathrm{GR}} = \frac{g\Delta H}{c^2}\,, \tag{7.47}$$

with $g = 9.812\,51(1)\ \mathrm{m/s^2}$ the local gravitational acceleration or equivalently by using the gravity potential ΔW_p

$$\left(\frac{\Delta\nu}{\nu}\right)_{\mathrm{GR}} = \frac{\Delta W_p}{c^2}\,. \tag{7.48}$$

It has been verified in optical atomic clock networks on earth (Takamoto et al., 2020) and satellites (Herrmann et al., 2018; Delva et al., 2018). In the latter case two Galileo satellites, accidentally brought to elliptic orbits in 2014 and each carrying a hydrogen maser, confirmed the shift on the 10^{-5} level. Recently, the gravitational red-shift was measured within a single mm-scale ^{87}Sr sample (Bothwell et al., 2022). Today's clocks contributing to TAI (Temps Atomique International), with an uncertainty of 10^{-15} or better, require their geodetic height to be known within 1 m or better (Mehlstäubler et al., 2018).

Table 7.3: Leveling marks at PTB campus and expected gravitational red-shift of the $^{27}\mathrm{Al}^+$ clock in Laue Bau, here given by marker LB02 (Denker et al., 2014). The uncertainty in height is 2 to 3 mm.

Point no.	Description	Normal height H (m)	Geopotential number $C_p = W_0 - W_p$ (m²/s²)	$(\Delta\nu/\nu)_{\mathrm{GR}}$ (10^{-18})
LB01	v.-Laue-Bau, outside, wall marker	75.546	741.30	1640.96
LB02	v.-Laue-Bau, inside 5th floor, wall marker	90.576	888.79	0
KB04	Kopfermann-Bau, inside $^{171}\mathrm{Yb}^+$ bench, no marker	77.828	763.70	1391.81

Tab. 7.3 shows some geodetic height reference on PTB campus. The heights were determined in respect to the existing height marks of DHHN92 (Deutsches Haupthöhennetz 1992) and thus are referring to the level of the "Normaal Amsterdams Peil" (NAP) tide gauge. Height-marker LB02 is placed in the corridor of the 5th floor of the von-Laue-Bau in PTB Braunschweig, which

is next to the iQLOC 1 laboratory. The relative height of the iQLOC 1 trap with respect to this point is around 1.5 m, but is yet to be measured accurately. Therefore, in Tab. 7.3 the gravitational red-shifts refer to height differences between the listed markers.

7.10 Total Estimated Systematic Uncertainty Budget

The total estimated systematic uncertainty budget of the $^{27}\mathrm{Al}^{+}$-$^{40}\mathrm{Ca}^{+}$ ion clock described in this thesis is shown in Tab. 7.4.

The exact sequence and timing of the clock cycle will determine the time-dilation shift, which has the biggest contribution to the uncertainty budget. Assuming a clock interrogation without simultaneous cooling, a reasonable interrogation time of ≈150 to 200 ms would be chosen to keep 2nd order Doppler shifts by motional heating low. At these times the uncertainty of the heating rates is limiting the accuracy of the time dilation shift. In this configuration this shift will profit from the trap drive stabilization and improvements on the magnetic field stability, as then the radial IP modes can be better characterized. Furthermore, using $^{27}\mathrm{Al}^{+}$ for characterizing those modes with higher motional amplitude on this ion will also improve these values. Additionally, a more intense modeling of the heating processes, including BGC, as presented in Refs. (Hankin et al., 2019; Davis, Dubé, and Vutha, 2019), would improve the error bars on the heating rates as well as on the CFS.

As mentioned in Ch. 7.4, in order to suppress the time dilation shift, it is also possible to probe with simultaneous Doppler or EIT cooling. Different cooling settings are possible. In Ref. (Scharnhorst, 2018) the possibility of Double-Bright EIT cooling was discussed. There, a moderately weak cooling setting with a resulting steady state $\bar{n} < 5$ for all modes was considered and resulted in an additional ac Stark shift due to the EIT lasers of $-2(4) \times 10^{-19}$. Insufficient knowledge about the oscillator strengths in $^{27}\mathrm{Al}^{+}$, which are needed for the calculation of the shifts, were limiting the accuracy. A cooling setting with higher cooling power was also considered, but there the uncertainty exceeded 5×10^{-18}, which is unfavorable. It would be challenging to evaluate a systematic shift on the 10^{-18}-10^{-19} level directly, but it might be feasible to measure the ac Stark shift of the cooling lasers by comparing to another clock. Another possibility is to reduce the axial confinement and thus increase the distance between the aluminum and the calcium ion. Tightly focusing the cooling lasers with waists of ≤5 µm onto only the calcium ion is feasible. In this configuration the ac Stark shift would be reduced significantly. However, in the current laser configuration EIT and Doppler cooling would not be applicable, since the strong σ-polarized EIT dressing laser is directed axially, which hits both ions and the π-polarized main Doppler cooling laser is entering from a radial direction and would therefore only cool the radial modes until $^{40}\mathrm{Ca}^{+}$ is pumped into a dark state. The only possible method at this time would be a series of SBC pulses from one of the diagonal 729 nm lasers, which have overlap with all motional modes. Using EIT or Doppler cooling with single ion addressing would only be possible by rotating the quantization magnetic

Table 7.4: The total estimated systematic uncertainty budget of the iQLOC 1 $^{27}\mathrm{Al}^+$ clock. All values in 10^{-18}.

Name	Shift	Uncertainty	Note/Limitation
1^{st}-order Doppler	0	0.22	Assuming same performance as in (Brewer et al., 2019b).
Time-dilation EMM	−0.78	0.12	Measured on single $^{40}\mathrm{Ca}^+$. Drifting has to be measured.
Time-dilation secular	−3.65	0.55	All modes EIT cooled; no cooling during 150 ms interrogation. Limited by heating rates.
BBR	−3.27	0.44	Uncertainty in $\Delta\alpha(0)$.
CFS	0.029	0.39	Model.
Dc Zeeman	−1443.99	0.48	Uncertainty in C_2 factor.
Ac Zeeman	−14.52	0.23	Trap drive stability.
2^{nd}-order ac Stark (trap)	0.7138	0.019	Negligible.
Electric quadrupole	−0.0205	0.0072	Negligible.
Clock laser ac Stark	0	0.2	Assuming same performance as in (Chou et al., 2010).
Phase chirp	0	0.2	Assuming same performance as in (Chou et al., 2010).
Total	**−1465.56**	**1.04**	

field by 45° to a diagonal configuration. Then, a set of cooling lasers would enter diagonally and be able to the cool all modes.

The second highest contribution to the uncertainty is due to the uncertainty in the C_2 factor of the dc Zeeman shift. With more accurate measurements or calculations of this quantity a significant improvement is to be expected. While the ac Zeeman shift due to the trap magnetic field is relatively high in this experiment, it can be measured with high accuracy. At this time, the instability of the RF drive power is limiting the uncertainty of this shift. A stabilization of trap drive power will further decrease its uncertainty.

The BBR shift uncertainty is the third highest systematic uncertainty budget contribution and is limited by the uncertainty of the static differential polarizability $\Delta\alpha(0)$. More accurate measurements or calculations in these values would further reduce the uncertainty.

Excess Micromotion can be measured and compensated with high accuracy. Most relevant for this shift is an assessment of its stability during clock operation. We measured the shift to be stable during the probe duration, but it drifts on an hour time scale and must therefore be regularly compensated. This is especially important after loading ions into the trap, since reloading, e.g. necessary due to ion loss, is typically performed at lower RF powers. This is connected to a drift of the trap temperature. Furthermore, it must be checked, if the achieved EMM suppression can be confirmed by measuring on $^{27}\mathrm{Al}^+$ directly using the aluminum logic laser. In addition, the clock laser light at deep UV can cause photo-emission and released electrons can cause fluctuating stray potentials, which cause the EMM to drift. Since the EMM shift has been assessed by probing sidebands at the trap drive frequency, the results could be biased by the sidebands which are caused by trap-induced magnetic fields (Meir et al., 2018). Probing the micromotion sidebands on different $^{40}\mathrm{Ca}^+$ Zeeman sub-states can be used to infer the contributions from the trap-induced electric fields and measure the component $B_{0,\mathrm{ac}}$ of the oscillating magnetic field in direction of the quantization magnetic field B_0 (Gan et al., 2018)

$$\beta_m = \frac{g_{\mathrm{D}_{5/2}} m_{\mathrm{D}} - g_{\mathrm{S}_{1/2}} m_{\mathrm{S}}}{\hbar\Omega_{\mathrm{RF}}} B_{0,\mathrm{ac}} \,, \tag{7.49}$$

where β_m is the modulation index, similar to Eq. (7.10). Due to the high vertical directionality of the trap-induced magnetic field in this trap the influence of these sidebands on the EMM assessment is expected to be small. Assuming an oscillating magnetic field in quantization direction that is $\approx 1/10$ of the measured magnitude value, i.e. $\approx 2\,\mu\mathrm{T}$, and driving the $m_{\mathrm{S}} = -1/2 \leftrightarrow m_{\mathrm{D}} = -1/2$ transition, which was used in the EMM evaluation, a modulation index of $\beta_m \approx 0.0004$ is estimated, which is smaller than the measured modulation indices.

Overall, the estimated uncertainty of 1.04×10^{-18} proofs that this aluminum clock is competitive to the best performing clocks in the world and has the potential to be further reduced to below 1×10^{-18} in the future.

Part IV

Summary & Outlook

8 Summary

In this thesis the aluminum ion clock at PTB has been characterized towards its ability to probe the clock transition of $^{27}\mathrm{Al}^+$ with low systematic uncertainties.

One result of this work is the observation of the clock transition in $^{27}\mathrm{Al}^+$. Using a QL protocol that maps on a the internal state population of the $^{27}\mathrm{Al}^+$ to the $^{40}\mathrm{Ca}^+$ ion, the outer lying $|\,^1\mathrm{S}_0, m_F = +5/2\,\rangle \leftrightarrow |\,^3\mathrm{P}_1, m_F = +5/2\,\rangle$ clock transition of $^{27}\mathrm{Al}^+$ was driven. In frequency scans, minimal linewidths of the clock transition on the order of a few tens of Hz were measured, limited so far by uncompensated fiber noise. Coherent operations on $^{27}\mathrm{Al}^+$ were demonstrated by driving Rabi oscillations between ground and excited clock state. Two evaluation methods for state detection have been studied, where the QND method in combination with the adaptive detection protocol (Hume, Rosenband, and Wineland, 2007) has the perspective of reduced clock dead-time compared to a detection method with fixed detection gates.

Another technical achievement is the installation and characterization of a polarization switcher for the state preparation laser of $^{27}\mathrm{Al}^+$. This will allow to probe the outer two Zeeman transitions of the aluminum ion's clock transition without additional dead time and therefore enabling to measure the dc Zeeman-free clock transition.

The main result of this thesis is the compilation of a preliminary systematic uncertainty budget of this clock, which has been characterized by measurements mainly carried out on the auxiliary $^{40}\mathrm{Ca}^+$ ion, which has a higher sensitivity to external fields, and by drawing analogies to similar experiments. This includes an analysis of the trap-induced ac Zeeman shift, which has not been measured to this precision in other $^{27}\mathrm{Al}^+$ clocks so far. Even though the apparent trap-induced magnetic fields of $\sim 20\,\mu\mathrm{T}$ at the ion's position are higher than in other reported traps (Gan et al., 2018; Brewer et al., 2019b), its value was determined accurately enough to reduce its contribution to the uncertainty budget of the clock to 2.3×10^{-19}. The EMM shift was evaluated with improved accuracy since the last assessment in Ref. (Scharnhorst et al., 2015), reaching an uncertainty of 1.2×10^{-19}. Profiting from the improvements in theoretical models of background gas collisions and their impact on the $^{27}\mathrm{Al}^+$ clock transition, its contribution to the systematic uncertainty budget was estimated to 3.9×10^{-19}. This low inaccuracy was also only possible by the refurbishment of parts of the vacuum setup, that led to smaller background pressures of 11(6) nPa. A further reduction of the systematic uncertainty budget is discussed in this thesis, and is to be expected in the near future. In summary, a total systematic fractional frequency uncertainty of 1.04×10^{-18} has been evaluated, which makes this experiment comparable to today's most accurate clock (Brewer et al., 2019b).

9 | Outlook

This chapter describes the possible development of the experiment and discusses the prospect of a frequency comparison measurement at PTB and a compound single ^{27}Al^{+}/multi-ion ^{40}Ca^{+} clock.

9.1 Experimental Improvements

Clock Laser Stability The observed clock transition linewidths presented in this thesis were limited to ~10 Hz. A reason for this may be found in uncompensated fiber noise and an insufficiently performing transfer-lock of the clock laser to the Si-cavity-stabilized laser via the frequency comb at that time. Several improvements in this field are to be expected in the future. The technical requirements for a path-length stabilization of the 267.4 nm clock laser up to the ion trap have been prepared and will be implemented and tested in the next months. Furthermore, a new characterization of the clock cavity is planned. In particular, it will be tested if the theoretical predicted thermal noise floor of 7×10^{-17} at 1 s (Amairi, 2014) can be reached. The transfer-lock infrastructure will also be refurbished by direct transfer-locking to the Si-cavity-stabilized laser (Matei et al., 2017), instead of the currently employed two-stage stabilization scheme through the MNPQ-cavity-stabilized laser. This will improve the performance and reliability of the transfer-locked lasers in the laboratory, in particular the short-term stability.

New Reference Cavities for the 729 nm and 1068 nm Logic Laser Currently, a shared stable reference cavity for the 729 nm and the 1069 nm ECDLs is set up and characterized. Using the cavity transmission for injection locking (Akerman et al., 2015) will suppress high frequency noise of these lasers. This will allow for shorter QL pulses with increased contrast, thus potentially decreasing clock dead time and clock state detection errors. Also the accuracy of thermal sideband measurements will benefit, because the off-resonant scattering is further suppressed. This enables to apply the methods in Ref. (Rasmusson et al., 2021) for a characterization of the Fock state distribution of the motional modes in our setup.

Generating an effective $m_F = 0 \leftrightarrow m_F = 0$ Clock Transition A tool for fast in-sequence polarization switching of the 267 nm logic laser polarization was built, that will allow to prepare the outer $|\,^1\mathrm{S}_0\, m_F = -5/2\,\rangle$ and $|\,^1\mathrm{S}_0\, m_F = +5/2\,\rangle$ ground states alternately, such that a magnetic field-independent "virtual" $m_F = 0 \rightarrow m_F = 0$ clock transition frequency can be synthesized while simultaneously measuring the magnetic field for second order Zeeman shift assessment. This frequency will be used to stabilize the clock laser and distributed for frequency comparisons to other frequency standards at PTB.

Ion Loading Efficient loading of 27Al+ has to be established. Up to now, the total time from a single trapped $^{40}\mathrm{Ca}^{+}$ to a confirmed $^{27}\mathrm{Al}^{+}$ - $^{40}\mathrm{Ca}^{+}$ ion crystal can take minutes to hours. This is a big issue for clock operation, because in this downtime the clock laser cannot be steered by feedback from the ion. Currently loading of dark ions or molecules with masses $> 40\,u$ limits the loading efficiency. An "ablation" cleaning of the ablation target surface should happen over time, but it might be possible to speed up the process by carefully increasing the ablation power to higher values as usually applied for loading.

Trap Drive Stabilization The trap drive stability was limiting the accuracy of the ac Zeeman shift evaluation. The planned trap drive stabilization will reduce the drift of the power on the RF blades. This will improve the magnetic field amplitude part of the uncertainty of the ac Zeeman shift. Furthermore, the radial motional modes will also gain in stability, which has impact on two aspects of the clock. Firstly, this will eventually improve the GSC efficiency, because after EIT cooling a few sideband cooling pulses can be applied to cool to lower temperatures. Apart from potentially further reducing motional shifts, this opens the possibility to use the radial sidebands for QL. Secondly, the unstable radial sidebands were limiting the accuracy of the heating rate measurements of the motional modes. Hence, with the trap drive stabilization an improvement on the validity of the time-dilation shift can be expected. These results will decide if it is necessary to consider to rotate the quantization magnetic field to a diagonal configuration for single-ion addressed laser cooling during clock interrogation.

Magnetic Field Stability A magnetic shield for this experiment has not been considered yet, but could in principle reduce magnetic field noise. Currently, the magnetic field stabilization is taking out most of the noise up to a maximum bandwidth of 500 Hz. But compared to shielded experiments (Monz, 2011; Ruster et al., 2016) an improvement in coherence times by two orders of magnitude is possible. This would not immediately reduce the uncertainty of the 2nd order dc and ac Zeeman shifts dramatically, since the contribution due to the uncertainty in the 2nd order Zeeman constant C_2 is currently mainly limiting the total achievable accuracy in these shifts and the trap magnetic field cannot be shielded. But when the accuracy of the C_2 factor increases, this becomes more relevant. Additionally, longer $^{40}\mathrm{Ca}^{+}$ coherence times would enable to measure the radial temperatures and heating rates with higher accuracy, because due to the small 729 nm Lamb-Dicke factors for these modes, the applied π-times are exceeding the current coherence times. An improved characterization of the radial in-phase modes could also be accomplished by measuring on $^{27}\mathrm{Al}^{+}$, because of the higher motional amplitude of this ion in these modes compared to $^{40}\mathrm{Ca}^{+}$. More easily to implement than a magnetic shield is a 50 Hz feed-forward from the power line to the magnetic field coils (Flühmann et al., 2019). Such a feed-forward line-noise-suppression-unit is currently developed at our institute. Worthwhile considering is also the installation of permanent magnets to replace the coils for the quantization field, since these are not subject to 50 Hz line noise and its harmonics (Ruster et al., 2016).

New Experimental Control System During the next months a new experimental control system will be implemented. The combination of new hard- and software[1] will expand and improve the capabilities of this experiment. Apart from a future-proof hardware maintainability, this incorporates features that are in particular beneficial for clock operation. An increased DDS frequency resolution[2] of 8 µHz allows for finer frequency scans of the clock transition. In-sequence data acquisition avoids delay times, thus reduces clock dead time, and enables faster clock frequency steering, due to the capability of the FPGA to directly change sequence parameters. Furthermore, it improves the ability for automation, which is relevant for ion loading and calibration tasks.

9.2 Prospects of Measurements

The high density of high-accuracy and stable optical clocks at PTB is remarkable. The aluminum clock described in this thesis will soon contribute to this group of clocks. Of particular interest is a clock frequency ratio measurement with the ^{87}Sr (Schwarz et al., 2020; Lisdat et al., 2021), ^{171}Yb$^+$ (Lange, 2021) and ^{115}In$^+$ clocks at PTB. This measurement could be put in context to the frequency comparisons of Al$^+$/Sr, Al$^+$/Yb and Sr/Yb measured at NIST (Beloy et al., 2021). There, the frequency ratios including Al$^+$ deviated by more than 3σ from previously measured values. The frequency ratio of respective clocks at PTB and at other places in Europe may help to solve these discrepancies. Another prospect of these frequency ratio measurements is a possible validation and improvement of the constraints on the masses of potential dark matter particles (Beloy et al., 2021) and temporal variation of fundamental constants (Rosenband et al., 2008; Godun et al., 2014; Huntemann et al., 2014).

The aluminum ion clock described here is built to achieve highest accuracy. However, being a single-ion clock the averaging time for reaching inaccuracies of 1×10^{-17} and below can take thousands of seconds due to the QPN-limited SNR of a single interrogated quantum absorber. For example, the most accurate clock at this time (Brewer et al., 2019b) uses also a single aluminum ion and reaches a local oscillator-limited stability of $1.2 \times 10^{-15}\ 1/\sqrt{\tau}$, which means that this clock needs almost 17 d to reach an accuracy of 1×10^{-18}. This is highly impracticable for all sorts of frequency comparison, e.g., in geodetic experiments, where a gravitational potential should be measured within hours or maybe a day, or in the search for variation of fundamental constants or dark matter, when the expected modulation frequency of the clock frequency is faster than the averaging time. One possibility to overcome this challenge is to pre-stabilize the clock laser by a faster averaging clock (Dörscher et al., 2020).

The neighboring laboratory's ^{40}Ca$^+$ clock uses a continuous dynamical decoupling scheme (Pelzer et al., 2021) to generate protected clock states

---

[1] *ARTIQ* software and *Sinara* hardware (Bourdeauducq, 2016).

[2] AD9912, 48 bit DDS chip.

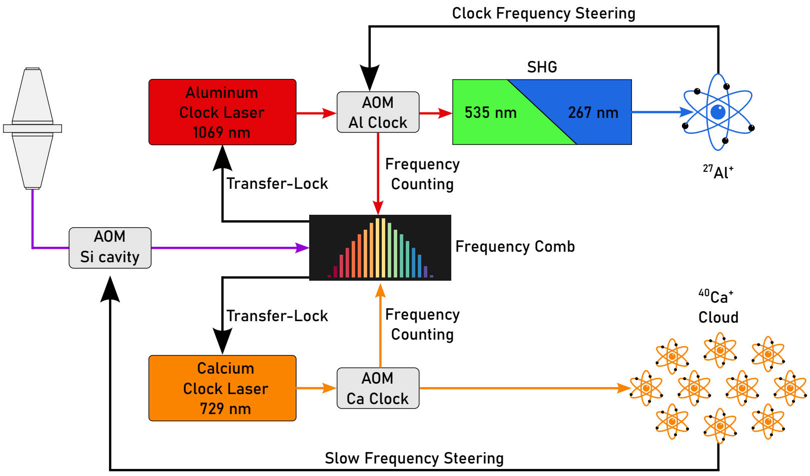

Figure 9.1: Compound clock, comprised of a single aluminum and a multi-ion calcium clock. The clock lasers are both pre-stabilized to high finesse cavities and additionally referenced by a transfer-lock onto laser light derived from a Si-cavity. The cloud of ^{40}Ca$^+$ ions is interrogated at their natural lifetime of ~1 s and feeds back onto the AOM of the Si-cavity light, correcting its frequency drift. The aluminum clock profits from this by a better stabilized clock laser for interrogating the ^{27}Al$^+$ ion.

(Aharon et al., 2019). This technique allows to suppress the quadrupole, linear Zeeman and tensor ac Stark shifts, which are usually inhomogeneously distributed over the extend of large ^{40}Ca$^+$ crystals. With the prospect of trapping > 10 ions simultaneously, this offers a system with a higher SNR than the described single ion clock. Since both experiments have direct access to the same frequency comb, the 729 nm clock laser of the ^{40}Ca$^+$ multi-ion clock could be used to pre-stabilize the clock laser of the ^{27}Al$^+$ ion clock, hence forming a compound clock which benefits from the low statistical uncertainty of the multi-ion ^{40}Ca$^+$ and the low systematic uncertainty from the ^{27}Al$^+$ clock. One possible configuration of this envisioned compound clock is depicted in Fig. 9.1. Here, the Si-cavity stability is transferred to the clock lasers of the aluminum and the calcium clock using the transfer-oscillator technique. The multi-ion calcium clock is operated close to the natural lifetime of ^{40}Ca$^+$ of ~1.1 s using Ramsey or Rabi spectroscopy. An error signal is derived and corrects the drift of the Si-cavity light to our system. In consequence, the stability of the aluminum clock laser is increased and faster frequency averaging is enabled.

The achieved gain in stability can be determined by the laser probe times (Peik, Schneider, and Tamm, 2006), the noise properties of the LO and the servo parameters of the pre-stabilization to the Si-cavity-stabilized laser and the multi-ion clock (Leroux et al., 2017). Setups with LOs that show laser noise on a much higher level than the QPN of the multi-ion clock will benefit more than setups, where the LO is already on a comparable stability level (Aharon et al., 2019). Comparing the QPN ADEVs in Fig. 9.2 with the shown LOs performances, the gain could be small. Therefore, a full simulation of the running compound clock including laser noise and servo parameters has to be performed in order to reasonably estimate the expected gain in stability for this setup (Leroux et al., 2017). However, the envisioned single-Al$^+$/multi-Ca$^+$

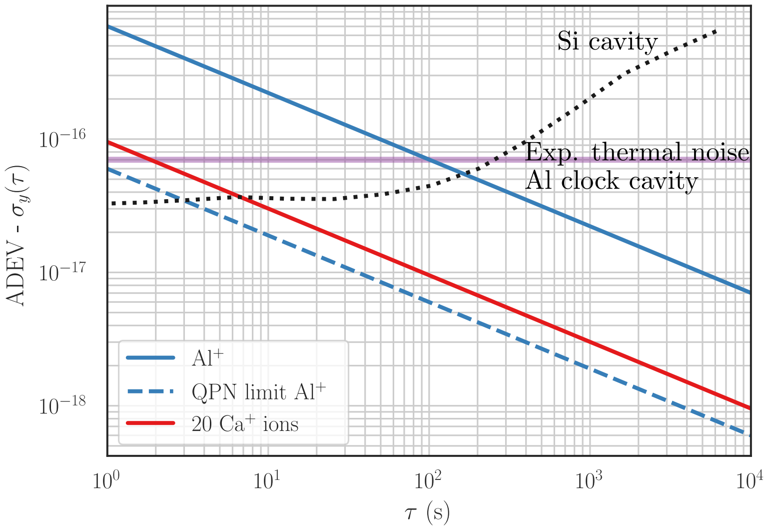

Figure 9.2: QPN stability limits of a single ion and a multi-ion clock. All clocks operate with a duty cycle of 75 %. Shown are the ADEVs of a single ion aluminum clock interrogated with a Rabi probe time of 150 ms (solid blue line) and 20.6 s (dashed blue line). The ^{40}Ca$^+$ clock is operated with 20 ions using a Ramsey dark time of 1.1 s (solid red line). The Si2 cavity is calculated by the modified ADEV and the expected thermal noise limit of the ^{27}Al$^+$ clock cavity is a simulated value (Amairi, 2014).

clock is a well-suited test bed for benchmarking such compound clock schemes taking advantage of the available options to pre-stabilize the LO.

Part V

Appendix

A Typical Lineshapes

The Rabi lineshape (Eq. (2.25) in Ch. 2.3.1) can be written as a function of the frequency detuning $\Delta\omega = \omega - \omega_0$ with $\omega = 2\pi\nu$

$$P_{\mathrm{Rabi}}(\Delta\omega) = \frac{\Omega_0^2}{\Omega_0^2 + \Delta\omega^2} \sin^2\left(\frac{\sqrt{\Omega_0^2 + \Delta\omega^2}}{2}\tau_i\right) , \tag{A.1}$$

with Ω_0 the on-resonance Rabi frequency and τ_i the interrogation time. The excitation probability P reaches 100 % for a π-pulse, i.e. $\tau_i = \pi/\Omega_0 \ll \tau$, where τ is the natural lifetime. Under these conditions the sidelobes nearest to the central peak are at $P \approx 11.6\,\%$ excitation probability.

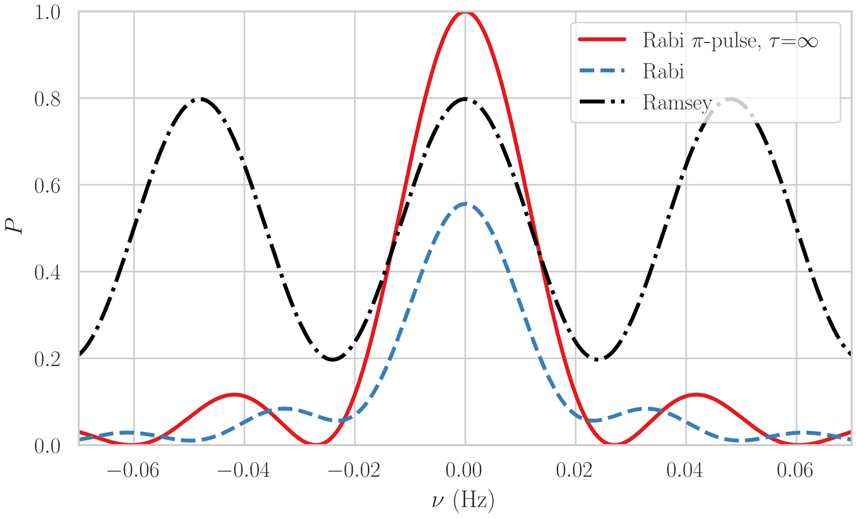

Figure A.1: Perfect π-pulse Rabi lineshape for $\tau_i = 32.038\,\mathrm{s}$ and $\tau = \infty$ (red). Considering $^{27}\mathrm{Al}^{+}$'s finite lifetime of $\tau = 20.6\,\mathrm{s}$ the optimum interrogation time for the highest stability is $\tau_i = 1.88\tau$ for the Rabi pulse (blue-dashed) and dark time $t_{\mathrm{dark}} = \tau$, for the Ramsey interrogation respectively (black-line-dots) (Peik, Schneider, and Tamm, 2006). The Rabi frequency is set to $\Omega_0 = 2.02/\tau$ and laser noise is neglected $\Gamma_L = 0$.

Integrating the optical Bloch equations (Peik, Schneider, and Tamm, 2006; Riehle, 2004)

$$\dot{u} = \Delta\omega v - \frac{1}{2}(\Gamma + \Gamma_L)\, u \tag{A.2}$$

$$\dot{v} = -\Delta\omega u - \Omega_0 w - \frac{1}{2}(\Gamma + \Gamma_L)\, v \tag{A.3}$$

$$\dot{w} = \Delta\omega v - \Gamma\,(w + 1) \ , \tag{A.4}$$

for the excitation probability $P = (w + 1)/2$ enables to consider the influence of the finite lifetime $\Gamma = 1/\tau$ and laser noise Γ_L for Rabi and Ramsey interrogations. An interrogation longer than the natural lifetime is possible and even favorable for highest stability performances when laser noise can be neglected (Peik, Schneider, and Tamm, 2006). In Fig. A.1 lineshapes for the $^{27}\mathrm{Al}^{+}$clock transition are shown. Assuming an infinite lifetime and a perfect π-time results in the Rabi lineshape (red). When considering the finite lifetime smaller linewidths can be achieved at the cost of reduced signal contrasts as can be seen for Rabi (blue-dashed) and Ramsey (black-line-dots) interrogation.

For interaction times $\tau_i \ll \frac{\pi}{\Omega_0} \ll \tau$, the observed linewidth when scanning the laser frequency over the resonance is given by the laser pulse's Fourier transform. This limit to the frequency resolution is called interaction time or Fourier broadening and arises from the finite interaction time between laser and atom. A rectangular pulse shape, i.e. instant turning on the laser at $t = -\tau_i/2$ and turning off the laser at $t = \tau_i/2$, will result in a power spectrum of the laser field $E_0 \cos(\omega_0 t)$ (Riehle, 2004)

$$S_{\mathrm{Fourier}}(\Delta\omega) = \left(\left[\frac{E_0\tau_i}{2}\right]\frac{\sin(\Delta\omega\tau_i/2)}{\Delta\omega\tau_i/2}\right)^2 . \tag{A.5}$$

This is a sinc-squared function, whose excitation spectrum for small pulse areas in comparison to the π-pulse can be approximated by

$$P(\Delta\omega) = \frac{\Omega_0^2\tau_i^2}{4}\mathrm{sinc}^2\left(\frac{\Delta\omega\tau_i}{2}\right) . \tag{A.6}$$

The full width at half maximum is FWHM$\approx 0.89/\tau_i$ and therefore slightly broader than that of a Rabi π-pulse. The sidelobes for a pulse with an interaction time of $\tau_i = \tau_\pi/10$ reach roughly 4.72 % of the main peak's amplitude.

Line broadening due to incoherent saturation of the transition is called power broadening. The excited state population saturates more quickly near resonance than at the sidelobes. The population ratio in the excited state governs the spectral shape

$$\frac{N_e}{N} = \frac{S_0}{2(1+S_0)\left(1+(2(\nu-\nu_0)/\tilde{\gamma})^2\right)} , \tag{A.7}$$

which is a Lorentzian with $S_0 = I/I_0$ being the on-resonance saturation parameter and a linewidth that is power broadened from the natural linewidth $\gamma = 1/(2\pi\tau)$ to $\tilde{\gamma} = \gamma\sqrt{1+S_0}$. The saturation intensity is given by $I_0 = \frac{2\pi^2 hc\gamma}{3\lambda^3}$ in the unit W/m^2 (Riehle, 2004).

B Vacuum Refurbishment

In the main text it is described that a refurbishment of the vacuum was necessary in order to improve the background gas pressure. This appendix provides more details on the performed vacuum work.

B.1 Aluminum Lifetime in Old Setup

The lifetimes and loss channels of trapped aluminum ions was recorded in the old setup and are shown in Fig. B.1 and B.2. A lifetime of 26 min is estimated by fitting an exponential decay function to the lifetime data. It is expected that the ^{27}Al^{+} lifetime decreases in clock operation, because in this case the ^{27}Al^{+} spends more time in the ^{3}P-states, in which it is more reactive with H_2 molecules (Ch. 5.1). Lifetimes during clock operation of 22 min are reported (Chen, 2017). Since here, the aluminum clock and logic lasers were only turned on occasionally for Rabi frequency scans, a clear correlation between observed lifetime and ^{27}Al^{+} laser interaction time could not be determined. However, the fact that in most cases the ^{27}Al^{+} was not even excited, the measured lifetime constituted a significant practical limitation. The most frequent reason for a necessary reloading was due to high energy collisions that removed ^{27}Al^{+} from the trap, followed by chemical reactions of ^{27}Al^{+} to unknown molecular ions. Losses of ^{40}Ca^{+} were observed as the third most common loss event, which can be caused by unlocked cooling lasers that heat ^{40}Ca^{+} out of the trap in combination with high energy collisions.

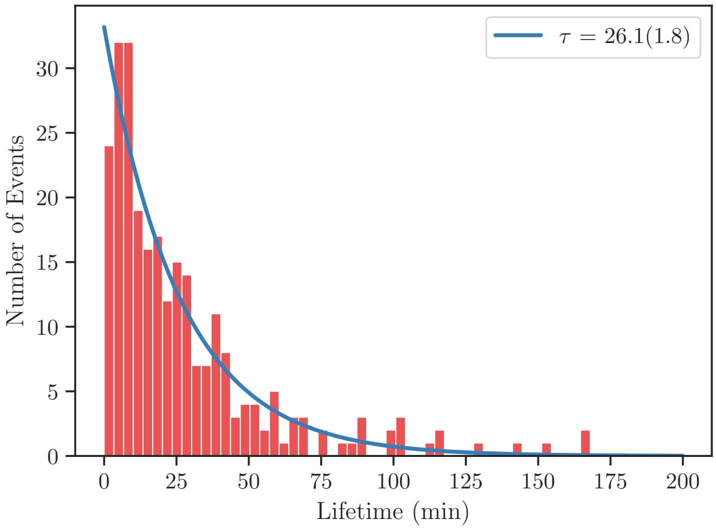

Figure B.1: Total observed lifetime of ^{27}Al^{+} in the old setup.

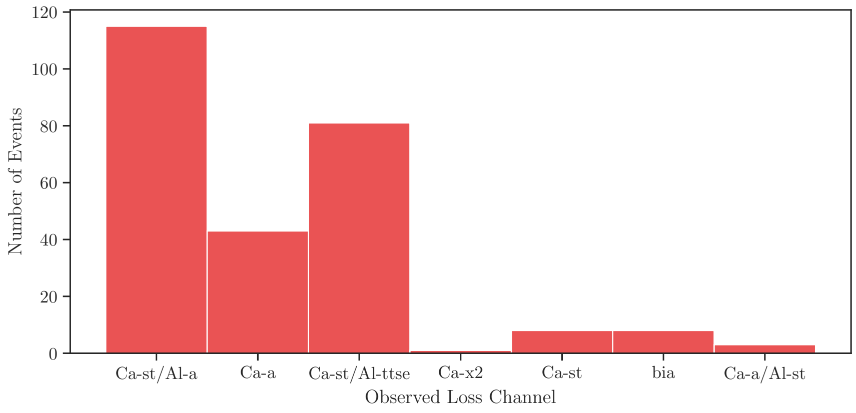

Figure B.2: Observed ^{27}Al$^+$-^{40}Ca$^+$ loss channels. Ca-st/Al-a: calcium still there/aluminum away, Ca-a: calcium away, Ca-st/Al-ttse: calcium still there/aluminum turned to something else, Ca-x2: 2nd calcium ion appeared, bia: both ions away, Ca-a/Al-st: calcium away/aluminum still there.

B.2 Cleaning

Where possible, in-vacuum parts have been cleaned by the usage of an ultrasonic bath flooded with water and different solvents for 15 min. We used only de-ionized water. A typical cleaning procedure started with coarse removing of dirt and fat particles in dish-washing/water mixture. Then the parts were put at first in an acetone, then rinsed with water, and finally put in an isopropyl alcohol bath. A clean dry-air gun was used to dry the parts. Cleaned parts were stored in aluminum foil, which was also used as clean working surface. We wore hairnets and latex or nitril gloves, as well as face-masks during handling cleaned parts and the installation into the opened vacuum chamber.

B.3 Preparation of Ablation Targets

Aluminium and calcium metallic samples were mounted into the ablation holder holes of 1.5 mm diameter, see Fig. B.3. The ablation targets were prepared in the following way. At first the titanium ablation target holder was cleaned as described above. Tools were cleaned in the same way. Those included, scalpel, Dremel fitting, file and a steal press. The steal press was also wrapped in several layers of aluminum foil.

The aluminum target was prepared from 1.5 mm diameter wire and the calcium target from small granule pieces [1]. The aluminum wire was at first cut into a small piece of several mm length with the tip sharpened like a pencil. Then it was pressed into the outer ablation holder hole using the press. On the back side the smooth wire was bent and filed down to a thin layer. The front was also filed to be parallel to the surface of the ablation holder. Calcium is a hard and non-flexible alkali earth metal. It is also very reactive with oxygen and water. Therefore the installation process was formerly trained in order to reduce

---

[1] Aluminum purity 99.999 %. Calcium purity 99.5 % and granule length 10 mm.

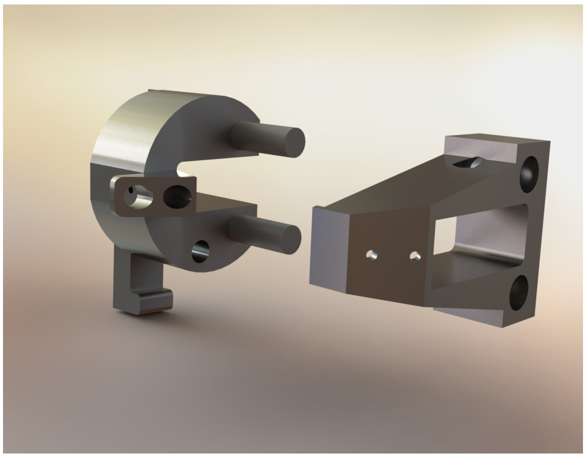

Figure B.3: CAD drawings of ablation target holder and aperture. All parts are titanium except for the two rods which are made from Macor.

the contamination time. At first a promising granule piece was eye-picked and then mounted into the Dremel fitting. The calcium particle was brought to rotation and filed to a round shape of 1.5 mm, with a sharpened tip on the one and a flat surface on the other side. Then the target was pressed into the target hole using the press, with the sharp tip pointing into the hole. Immediately before the target holder was installed into the sapphire disc, the surface of the calcium target was filed, in order to remove the oxidized layer and to make the surface parallel to the ablation holders surface.

B.4 Bake-Out

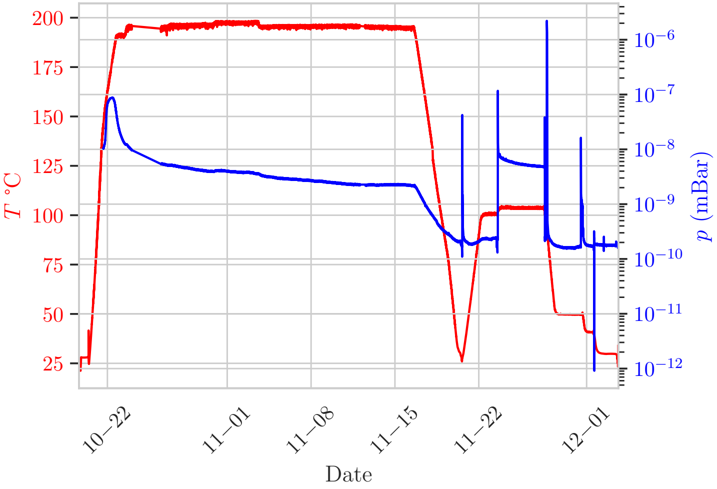

Figure B.4: Bakeout of the new setup. Pressure spikes on the right side were due to turning on and off ion pump and NEG conditioning and activation modes of the NEXTorr pumps. We attribute the slow pressure increase on the left side to an increase of residual solvent partial pressure, which is then pumped away.

For reaching UHV it is necessary to condition the vacuum chamber and its interior parts at high temperatures. Window coatings put constrains on the maximum temperature and temperature time gradients. We used a maximum temperature of ≈ 200 °C and temperature steps of 5 °C/h. The bake-out is depicted in Fig. B.4, where the pressure values were measured by an ion-gauge between turbo-pump and chamber valve. The small footprint of the setup allowed for putting it into a programmable oven with a turbo molecular pump connected to the chamber. For the high temperature phase the magnets of the ion pump were removed. After holding the maximum temperature for ≈ 24 d we ramped down the temperature and installed the magnets. We then put the NEG part of the NEXTorr pumps to condition mode and ramped the temperature to 100 °C and hold it for 4 d. Then we turned on and off the ion-pump several times before the NEG activation was started and held for 1 h. At the end of the activation the ion pumps were turned on and the temperature ramped down to room temperature.

C

Detailed Breadboard Drawings

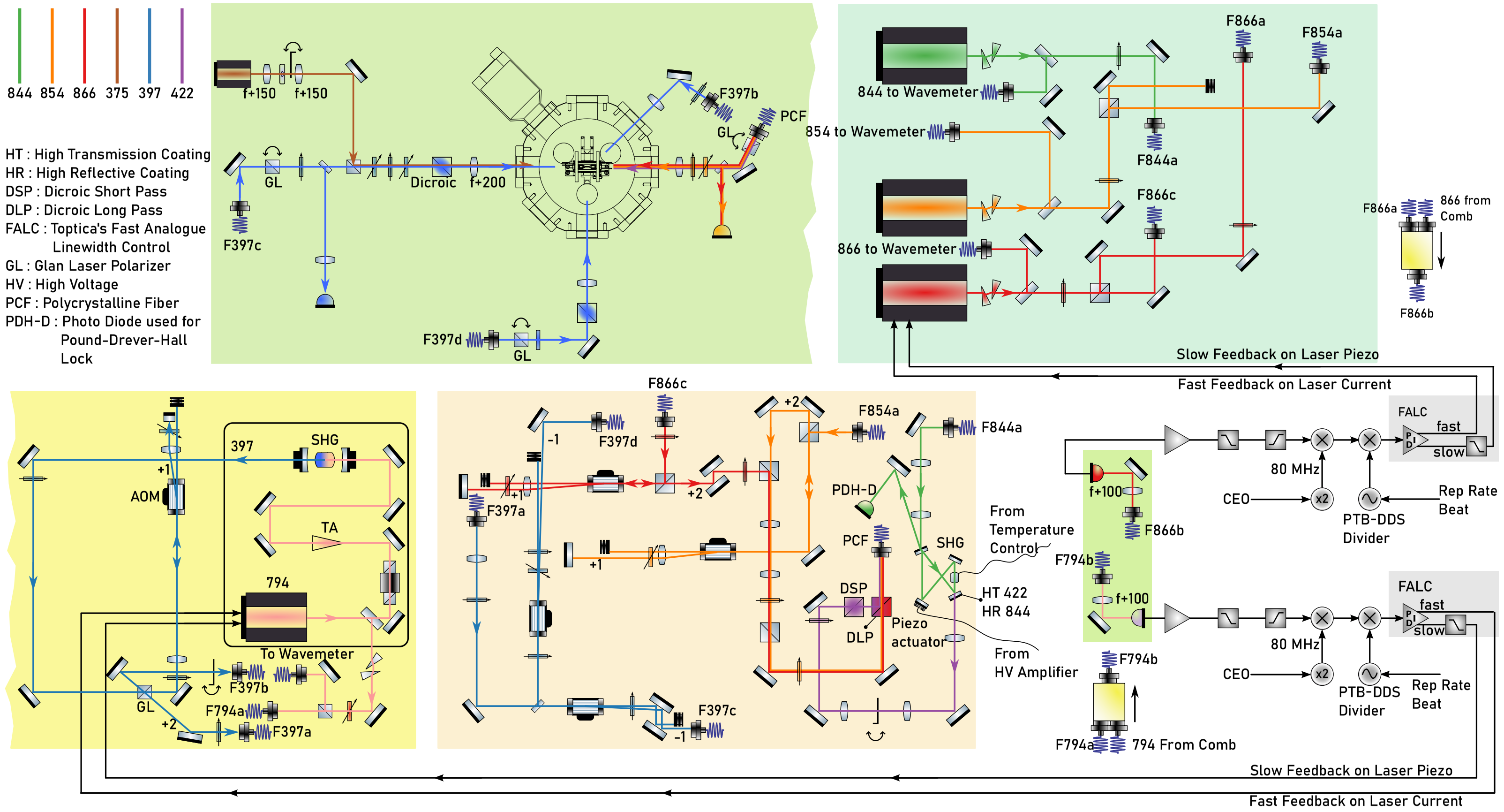

Figure C.1: ^{40}Ca^{+} Doppler and detection, repumper, clear out and ionization laser setup.

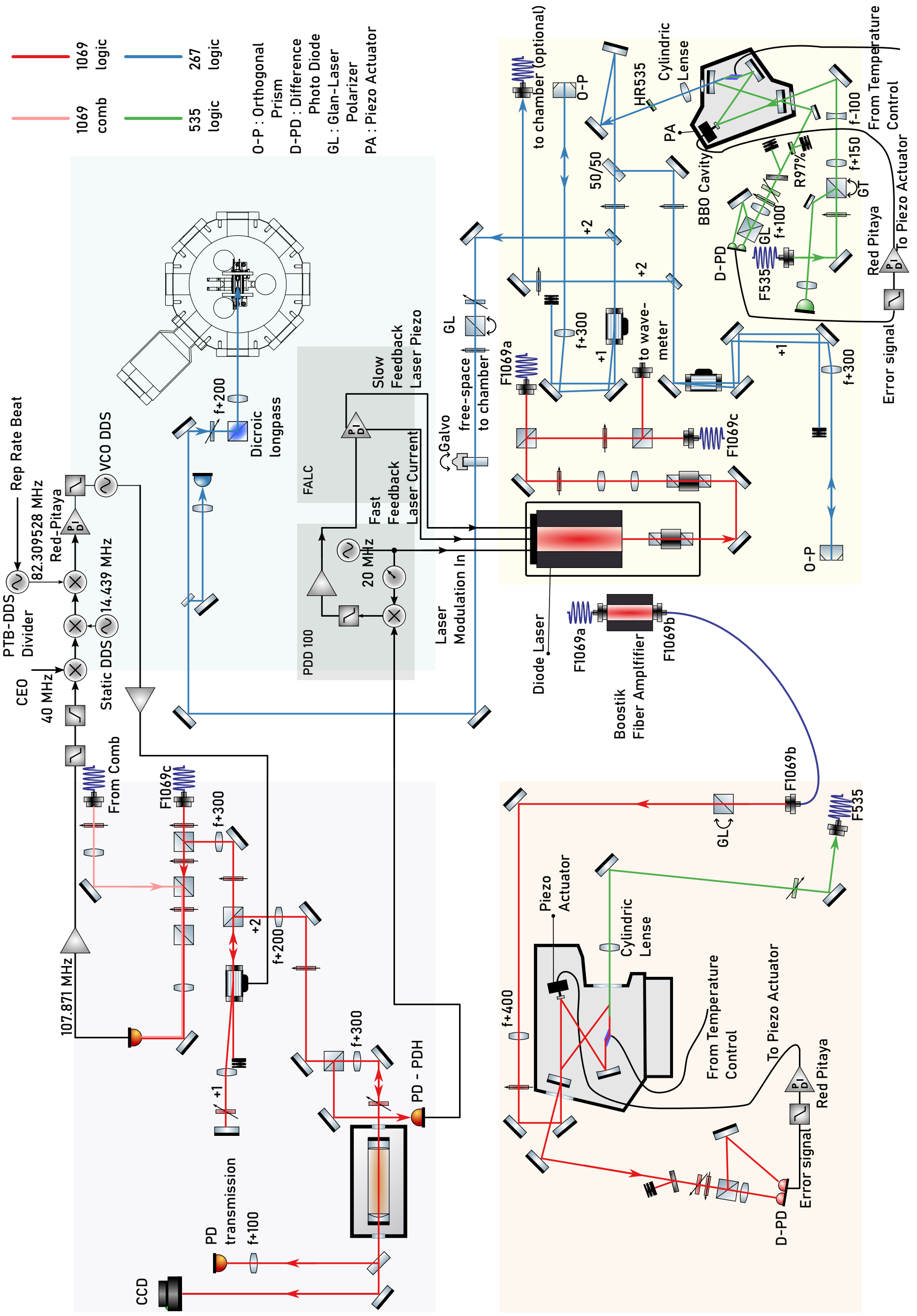

Figure C.2: $^{27}Al^{+}$ logic laser breadboards.

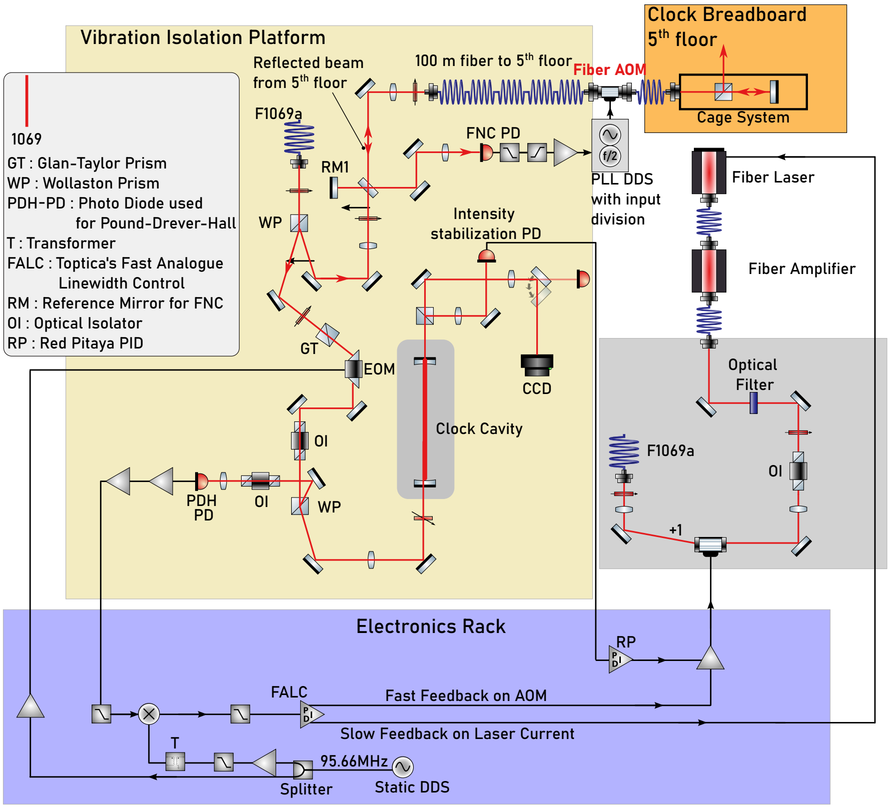

Figure C.3: Clock laser setup in the basement.

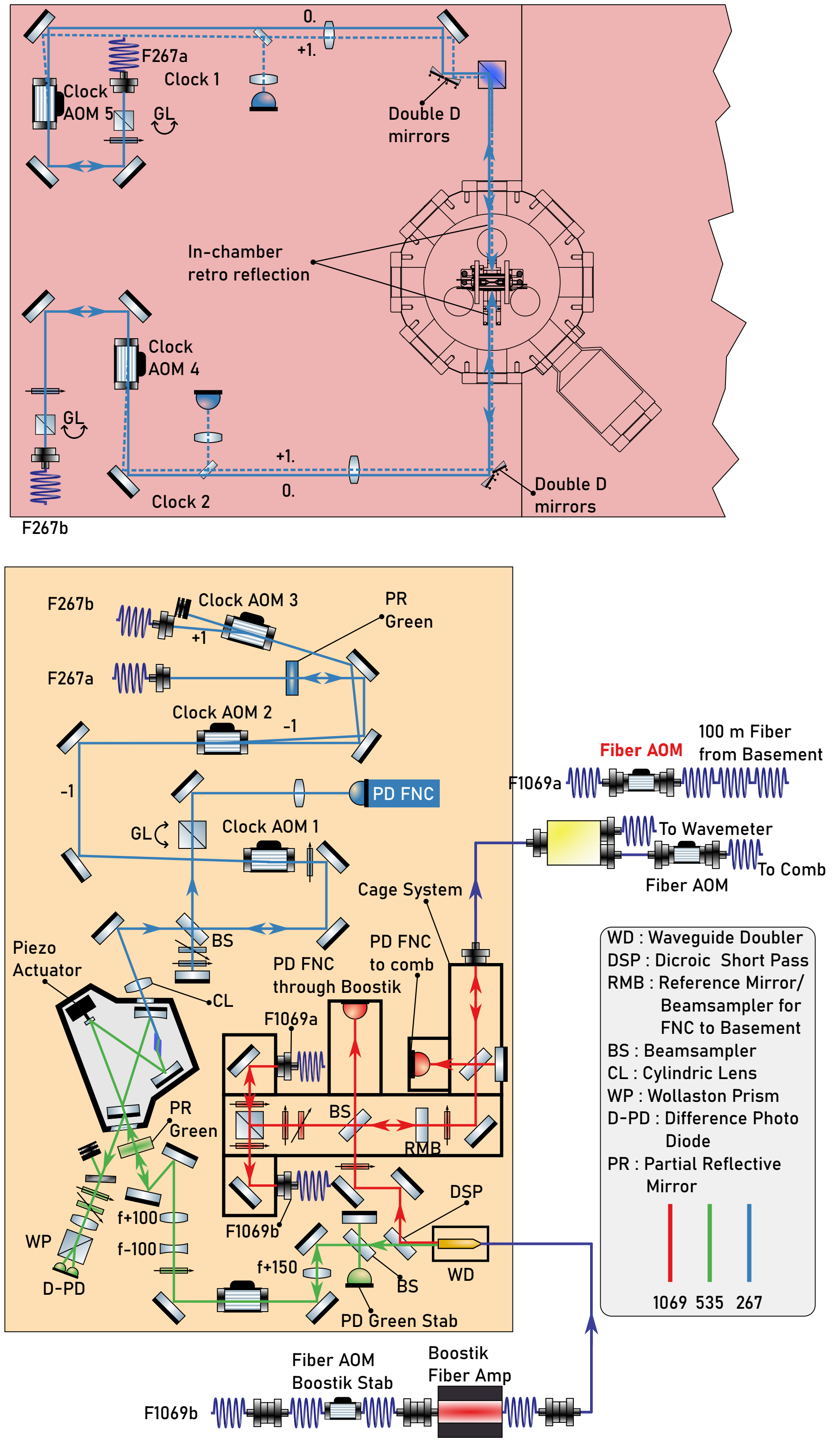

Figure C.4: Clock laser setup in 5^{th} floor. The beam is entering from the 100 m fiber on the right side.

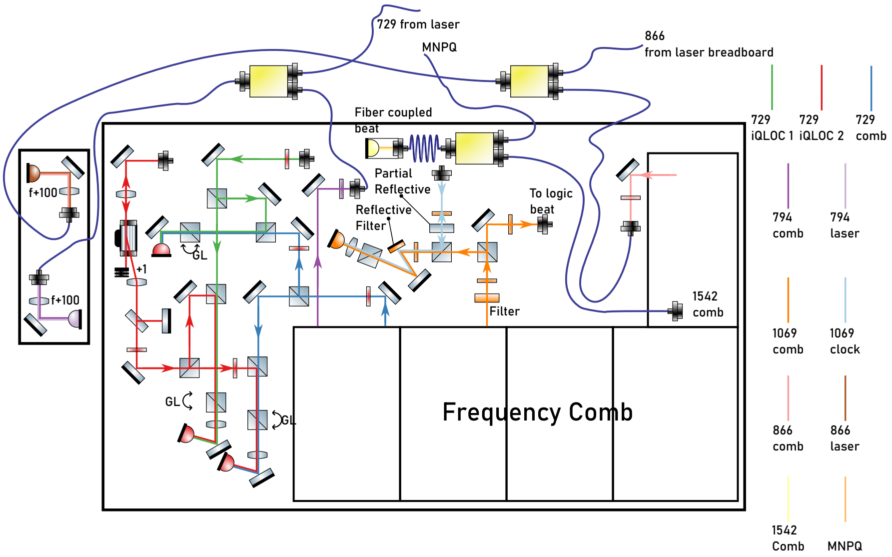

Figure C.5: Frequency comb breadboard.

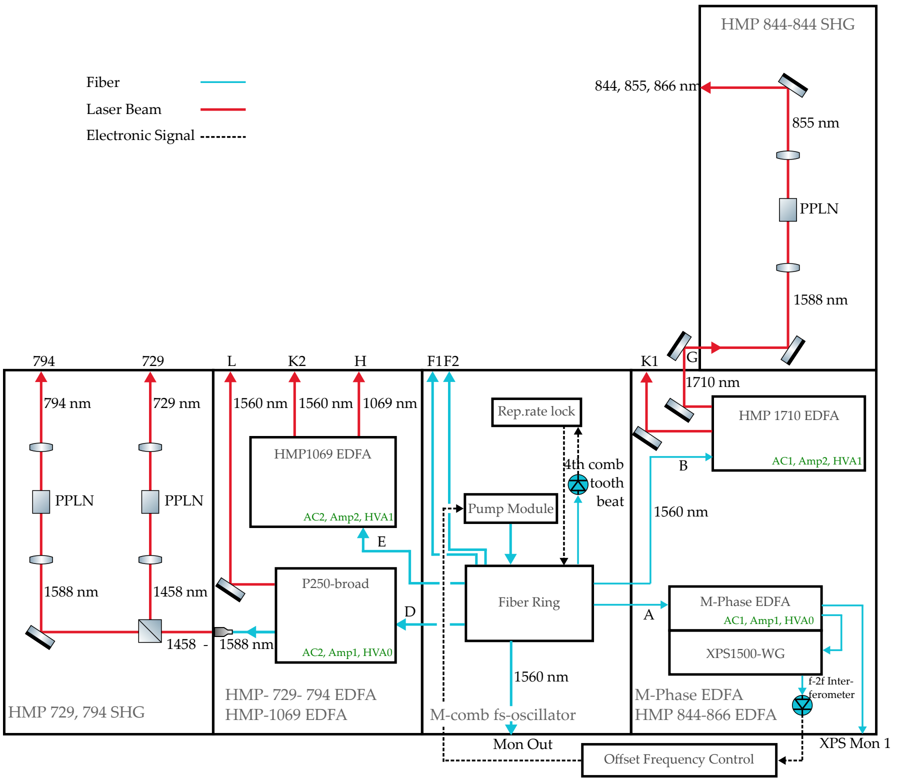

Figure C.6: Sketch of the frequency comb used in this experiment.

D Supplemental Material for the QND Analysis of Clock Transition Detection

This chapter discusses the error probabilities and their distribution from which appropriate estimators are required for the QND analysis in Ch. 6.3.3.2. In the second part of this appendix the exclusion of data with high error probabilities is described.

D.1 Estimator for the Average Error Probability

Applying the QND method as described in Ch. 6.3.3.2 to the measured PMT count data, that produced e.g. Fig. 6.6, results in certain average error probabilities for detecting $^{27}\mathrm{Al}^{+}$ in the ground S_0 or excited clock state S_1 (using the same notation as in Ch. 6.3.3.2). In order to calculate the average error probabilities for Fig. 6.14 a reasonable estimator for the average value has to be found. When averaging over all data points including all detunings, experimental repetitions and QL detection cycles the distributions can become asymmetric, see Fig. D.1 and D.2. As it can be seen, the frequency with small errors peak around 6000 while higher error probabilities are well below 900. In such asymmetric distributions the median gives a better estimator for a "typical" value. Therefore, in the results when averaging over all detunings and repetitions, leaving the QND detection cycle as free parameter, the median is used. On the other hand, the distributions become more symmetric for fixed detuning and when data points with an error probability of > 1 % are discarded. In consequence, the mean becomes a better estimator and for example in the frequency scan Fig. 6.13 the error bars were calculated by taking the mean.

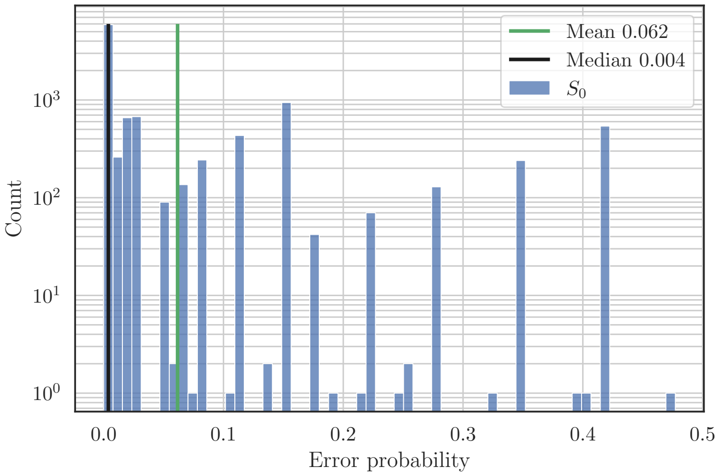

Figure D.1: Frequency of error probability when measuring $^{27}\mathrm{Al}^+$ in the ground state. Here for all detunings, measurement repetitions and detection gates. It can be seen that the distribution is highly asymmetric and spans over several orders of magnitude. Therefore, the median is a better estimator for the center of this distribution.

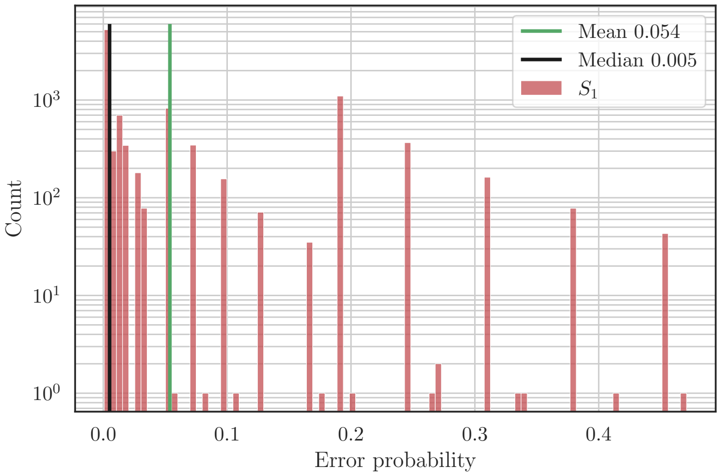

Figure D.2: Frequency of error probability when measuring $^{27}\mathrm{Al}^+$ in the clock state. Here for all detunings, measurement repetitions and detection gates. It can be seen that the distribution is highly asymmetric and spans over several orders of magnitude. Therefore, the median is a better estimator for the center of this distribution.

D.2 Excluding Data with high Error Probability

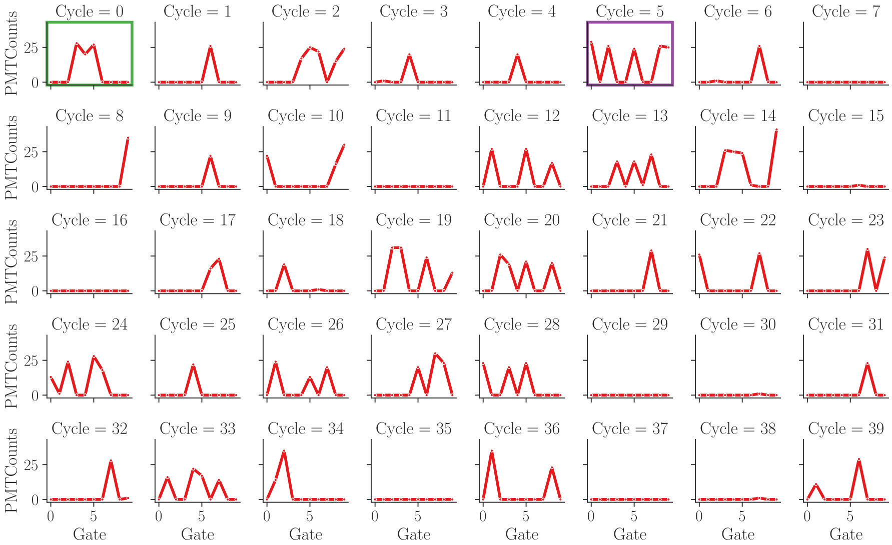

Figure D.3: Measured detection photon counts away from resonance. For better readability the QND cycles are labeled here as gates.

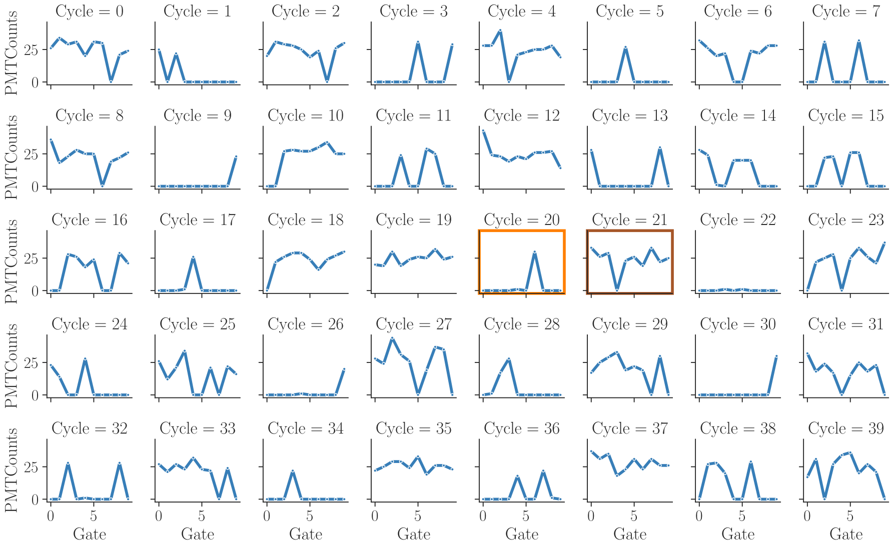

Figure D.4: Measured detection photon counts near resonance. For better readability the QND cycles are labeled here as gates.

It was mentioned above that certain measured series of PMT counts have a higher error probability compared to others. It is one of the benefits of the QND evaluation method that error probabilities can be calculated, based on which a decision can be made to discard these data points. In Fig. D.3 and D.4 the PMT counts for detecting the clock transition are shown; the first was measured at a detuning far away from resonance while the second is near the resonance. It can be see that there are "clean" and less "clean" cycles. The QND measurement evaluation method, presented in Ch. 6.3.3.2 can be used to calculate the error probability, which has been carried out here for the measurement cycles that are indicated by the colored boxes. The results are shown in Fig. D.5. It can be seen that signals with almost equal *bright* and *dark* PMT gates such as for example Cycle 5 (violet box) in Fig.D.3 result in high error probabilities and could therefore be counted as measurement error and be discarded. In the frequency scan in Fig. 6.13 that was evaluated with the QND method data points with and error probability of $> 1\,\%$ in the 10th QND detection cycle have been discarded. This reduced the noisy contributions further away from the resonance compared to the same frequency scan evaluated using the threshold method.

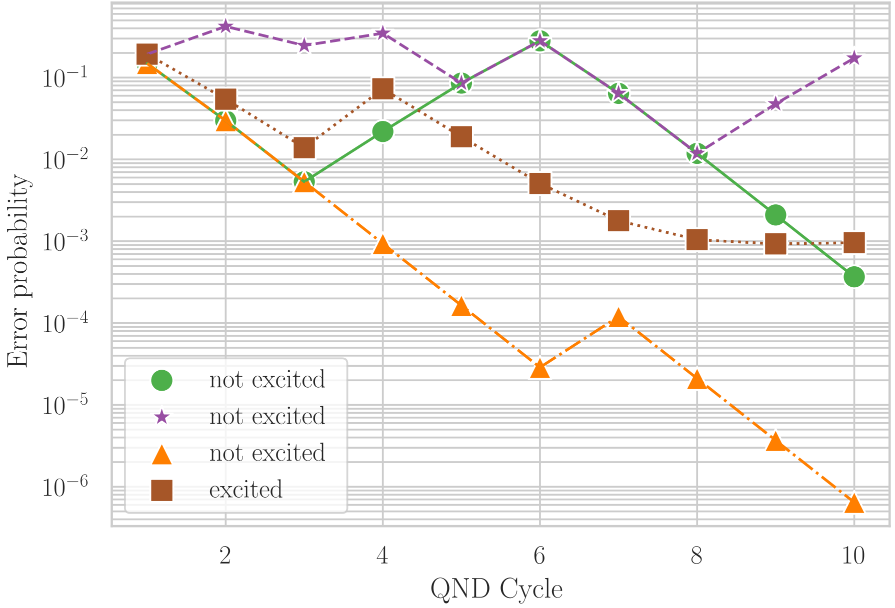

Figure D.5: QND analysis of the boxed detection cycles from Fig. D.3 and D.4. The same color represents the same measurement cycle from these figures. After 10 detection gates, those detection cycles were identified as indicated by the plot labels with their corresponding error probability.

E Supplemental Material for the AC Zeeman Shift

E.1 Autler-Townes Splitting in $^{40}\mathrm{Ca}^{+}$ $^{2}\mathrm{S}_{1/2}$ - States

When the frequency of the magnetic field ω is near or on resonance ω_{ba} on two states $|a\rangle$ or $|b\rangle$, the coupling induces a Larmor precession of the spin (Gan et al., 2018), which results in an Autler-Townes splitting. This can be observed, when a transition from one of the states $|a\rangle$ or $|b\rangle$ to a third state $|c\rangle$ is driven (Autler and Townes, 1955). In the following section, we calculate the Autler-Townes frequency splitting $\gamma = \gamma(B_{\perp})$ for the $^{40}\mathrm{Ca}^{+}$ S - Zeeman states $|a\rangle = |S = 1/2,\, L = 0,\, J = 1/2,\, m_J = -1/2\rangle$, $|b\rangle = |S = 1/2,\, L = 0,\, J = 1/2,\, m_J = +1/2\rangle$. As described in Sec. 7.7.2.1 $|c\rangle$ could be any of the $\left|^{2}D_{5/2}, m_J\right\rangle$ states.

Let β_{ab} be the the coupling strength between state $|a\rangle$ and state $|b\rangle$ due to a magnetic field $\vec{B}\cos(\omega t)$

$$\beta_{ab} = \frac{\left\langle a \middle| \vec{\mu}\cdot\vec{B} \middle| b \right\rangle}{2\hbar}\,. \tag{E.1}$$

Dropping the Js from m_J and where $\vec{\mu} = \vec{\mu}_L + \vec{\mu}_S = \vec{\mu}_J = -\frac{g_J\mu_B}{\hbar}\vec{J}$ is the total magnetic dipole operator of the atom with $\vec{J}$ the total angular momentum and μ_B the Bohr magneton. The states are given by $|a\rangle = |\alpha J m_J\rangle$ and $|b\rangle = \left|\alpha' J' m'_J\right\rangle$, where α denotes all other quantum numbers. The scalar product can be expressed as

$$\left\langle \alpha J m \middle| \vec{\mu}\cdot\vec{B} \middle| \alpha' J' m' \right\rangle = \left\langle \alpha J m \middle| \mu_0 B_0^{*} + \mu_{+} B_{+}^{*} + \mu_{-} B_{-}^{*} \middle| \alpha' J' m' \right\rangle\,, \tag{E.2}$$

where the vectors are written as spherical components $\mu_{+} = -\frac{1}{\sqrt{2}}\mu_x + \frac{i}{\sqrt{2}}\mu_y$, $\mu_{-} = \frac{1}{\sqrt{2}}\mu_x + \frac{i}{\sqrt{2}}\mu_y$, $\mu_0 = \mu_z$ and $B_{+} = -\frac{1}{\sqrt{2}}B_x + \frac{i}{\sqrt{2}}B_y$, $B_{-} = \frac{1}{\sqrt{2}}B_x + \frac{i}{\sqrt{2}}B_y$, $B_0 = B_z$ for the magnetic field vector respectively. Note that

$$\left\langle \alpha J m \middle| \mu_0 B_0^{*} \middle| \alpha' J' m' \right\rangle = 0\,, \tag{E.3}$$

for $\alpha \neq \alpha'$, $J \neq J'$ or $m \neq m'$. Here the coupling of two S states with $m = -\frac{1}{2}$ and $m' = \frac{1}{2}$ is considered, therefore this part is indeed zero.

For both vectors it is true, that the spherical components of the respective vector are the $q = +1, -1, 0$ components $T_q^{(1)}$ of the spherical tensor $T^{(1)}$; $T^{(1)} = \vec{\mu} = -\frac{g_J\mu_B}{\hbar}\vec{J}$ for the magnetic dipole moment, respectively the total angular momentum operator and $T^{(1)} = \vec{B}$ for the magnetic field. The Wigner-Eckert theorem gives

$$-\frac{g_J\mu_B}{\hbar}\left\langle \alpha J m \middle| J^{(1)}_{+1} \middle| \alpha' J' m' \right\rangle = -\frac{g_J\mu_B}{\hbar}\left\langle J'\,1\,m'\,1 \,|\, J\,m\right\rangle \cdot \left\langle \alpha J \middle\| \vec{J} \middle\| \alpha' J' \right\rangle . \tag{E.4}$$

$\langle J'\,1\,m'\,1\,|\,J\,m\rangle$ is the Clebsch-Gordan coefficient $\langle j_1\,j_2\,m_1\,m_2\,|\,j\,m\rangle$ and the reduced matrix element $\left\langle \alpha J \middle\| \vec{J} \middle\| \alpha' J' \right\rangle$ does not depend on angular momentum orientation, e.g. does not depend on m nor m'. This can be used to calculate the reduced matrix element from any known relation, for example

$$\begin{aligned}\left\langle \alpha J m \middle| J^{(1)}_{0} \middle| \alpha' J' m' \right\rangle &= m'\hbar\delta_{\alpha\alpha'}\delta_{JJ'}\delta_{mm'} \\ &= \langle J'\,1\,m'\,0\,|\,J\,m\rangle \cdot \left\langle \alpha J \middle\| \vec{J} \middle\| \alpha' J' \right\rangle ,\end{aligned} \tag{E.5}$$

which gives

$$\begin{aligned}\left\langle \alpha J \middle\| \vec{J} \middle\| \alpha' J' \right\rangle &= m'\hbar\frac{1}{\langle J'\,1\,m'\,0\,|\,J\,m\rangle}\delta_{\alpha\alpha'}\delta_{JJ'}\delta_{mm'} \\ &= m\hbar\frac{1}{\langle J\,1\,m\,0\,|\,J\,m\rangle}\delta_{\alpha\alpha'} \\ &= \hbar\sqrt{J(J+1)} .\end{aligned} \tag{E.6}$$

The Clebsch-Gordan coefficient here and the one appearing below can be found in (Bransden and Joachain, 2003). Inserting Eq. (E.6) in (E.4) and noting that $J = J'$ gives

$$\begin{aligned}&-\frac{g_J\mu_B}{\hbar}\left\langle \alpha J m \middle| J^{(1)}_{+1} \middle| \alpha' J' m' \right\rangle \\ &= -g_J\mu_B\sqrt{J(J+1)}\,\langle J\,1\,m'\,1\,|\,J\,m\rangle \\ &= -g_J\mu_B\sqrt{J(J+1)}\left(-\left[\frac{(J+m)\,(J-m+1)}{2J\,(J+1)}\right]^{\frac{1}{2}}\right) \\ &= \frac{g_J\mu_B}{2}\sqrt{(J+m)\,(J-m+1)}\end{aligned} \tag{E.7}$$

The minus component gives in analogy

$$-\frac{g_J\mu_B}{\hbar}\left\langle \alpha J m \middle| J^{(1)}_{-1} \middle| \alpha' J' m' \right\rangle = -\frac{g_J\mu_B}{2}\sqrt{(J-m)\,(J+m+1)} . \tag{E.8}$$

Substituting Eq. (E.7) and (E.8) into (E.2), respectively into Eq. (E.1), the coupling strength can be calculated to

$$\beta_{ab} = \frac{g_J\mu_B}{2\sqrt{2}\hbar}\left(B^*_+\sqrt{(J+m)\,(J-m+1)} - B^*_-\sqrt{(J-m)\,(J+m+1)}\right) \tag{E.9}$$

Noting that for the states $|a\rangle$, $|b\rangle$ considered here we have $J = J' = \frac{1}{2}$ and $m = \frac{1}{2}$ or $m = -\frac{1}{2}$. This results in

$$\beta_{ab} = -\frac{g_J \mu_B}{4\hbar}\left(B_x - iB_y\right) \tag{E.10}$$

$$|\beta_{ab}| = \frac{g_J \mu_B}{4\hbar}\sqrt{\left(B_x^2 + B_y^2\right)} = \frac{g_J \mu_B}{4\hbar} B_\perp \, . \tag{E.11}$$

Here $g_J = 2.003\,193$ (Ch. 2.1.2) because of the anomalous magnetic moment of the electron. For weak field strength $|\beta_{ab}| \ll \omega_{ab}$ the Autler-Townes splitting of $|a\rangle$ coupling to $|b\rangle$, observed when probing for example $|a\rangle \leftrightarrow |c\rangle$ is given by

$$\gamma = \sqrt{(\omega_{ab} - \omega)^2 + 4\beta_{ab}^2} \, , \tag{E.12}$$

(Autler and Townes, 1955). This approximation is justified, since for expected magnetic field strengths of $\lesssim 50\,\mu\mathrm{T}$ and a Zeeman splitting of $\omega_{ab} = 2\pi \times 27.95\,\mathrm{MHz}$, we have

$$\frac{|\beta_{ab}|}{\omega_{ab}} = 0.013 \, . \tag{E.13}$$

At resonance $\omega = \omega_{ab}$ the splitting is minimal and given by

$$\gamma = \frac{g_J \mu_B}{2\hbar} B_\perp \, . \tag{E.14}$$

The first order correction when including counter-rotating terms in the derivation of Eq. (E.12) is a Bloch-Siegert shift of the resonance condition

$$\frac{\omega}{\omega_{ab}} = 1 + \frac{\beta_{ab}^2}{\omega_{ab}^2} \, . \tag{E.15}$$

It has no impact on the splitting itself but it shifts the frequency at which the splitting occurs(Autler and Townes, 1955). It is small, and therefore can be neglected, .

E.2 Combined Uncertainty of the ac Zeeman Field

The combined uncertainty of B is given by

$$\begin{aligned} u(B) = \Bigg(& \left(\frac{\partial B}{\partial B_{\perp,\,\mathrm{top}}}\right)^2 u(B_{\perp,\,\mathrm{top}})^2 + \left(\frac{\partial B}{\partial \phi_{\mathrm{top}}}\right)^2 u(\phi_{\mathrm{top}})^2 \\ & + \left(\frac{\partial B}{\partial \vartheta_{\mathrm{top}}}\right)^2 u(\vartheta_{\mathrm{top}})^2 + \left(\frac{\partial B}{\partial \phi_B}\right)^2 u(\phi_B)^2 + \left(\frac{\partial B}{\partial \vartheta_B}\right)^2 u(\vartheta_B)^2 \\ & +2\left|\frac{\partial B}{\partial B_{\perp,\,\mathrm{top}}}\frac{\partial B}{\partial \phi_{\mathrm{top}}}\right| u(B_{\perp,\,\mathrm{top}})u(\phi_{\mathrm{top}})r(B_{\perp,\,\mathrm{top}},\phi_{\mathrm{top}}) \\ & +2\left|\frac{\partial B}{\partial B_{\perp,\,\mathrm{top}}}\frac{\partial B}{\partial \vartheta_{\mathrm{top}}}\right| u(B_{\perp,\,\mathrm{top}})u(\vartheta_{\mathrm{top}})r(B_{\perp,\,\mathrm{top}},\vartheta_{\mathrm{top}}) \\ & +2\left|\frac{\partial B}{\partial \phi_B}\frac{\partial B}{\partial \vartheta_B}\right| u(\phi_B)u(\vartheta_B)r(\phi_B,\vartheta_{\mathrm{top}})\Bigg)^{\frac{1}{2}} . \end{aligned} \tag{E.16}$$

E.3 Simulations of ac Magnetic Fields in the iQLOC 1 Trap

In a perfectly symmetric trap one would expect the magnetic field to cancel perfectly. The question arises where this symmetry breaking comes from that causes the comparable high ac magnetic fields in the described trap.

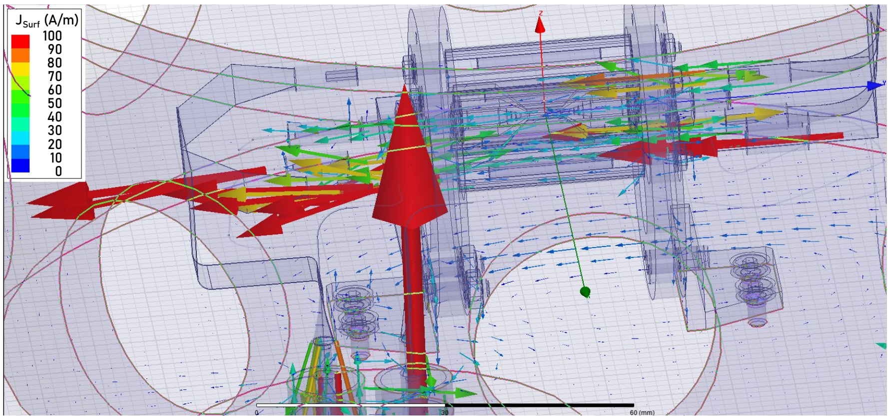

Figure E.1: Simulated surface current densities field for a symmetric drive at 2 × 500 V and a trap drive frequency at 27.95 MHz.

The simulations presented in this chapter are based on a model of the iQLOC 1 trap, which has been set up by Miroslav Doležal in the framework of heat distribution inside the chamber and the BBR shifts connected with it (Doležal et al., 2015). Starting point are HFSS simulations of the trap ac currents as source for the heating effects, see Fig. E.1. Having the simulated currents it was straightforward to extract the magnetic fields. The simulation included the steel chamber octagon, steel baseplate and fused silica top window, RF and dc feedthroughs, endcap and compensation electrodes including the wiring, RF blades and RF stripes, the two sapphire discs and a trap drive at a frequency of 27.95 MHz with varying power. Throughout this thesis, it was mentioned that part of the vacuum system of the experiment was rebuilt. It is therefore unlikely that the simulations cover the exact geometries of the trap's surroundings. Nevertheless simulation and experiment show the same qualitative properties and the same order of magnitude in ac magnetic field strengths.

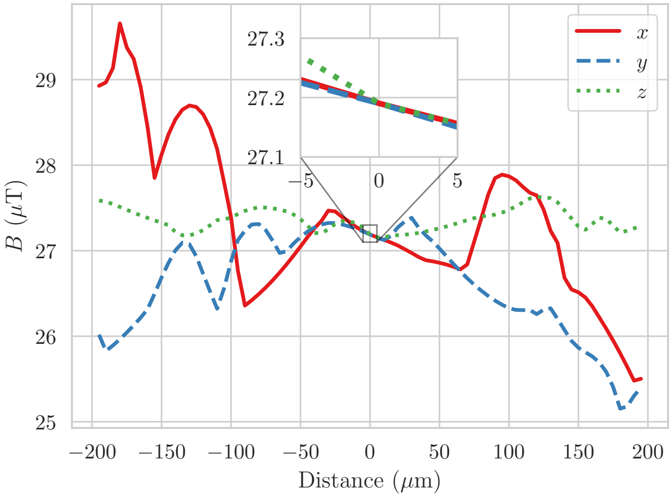

Figure E.2: HFSS simulations of the total ac magnetic field amplitude at 2×225 V trap drive voltage around the trap center. The plots are cuts through the center of the trap along the directions given.

In Fig. E.2 the total magnetic field amplitude B_{ac} in the trap is shown. In the vicinity of the trap center the magnetic field is relatively linear with a slope of −0.005 µT/µm in all directions. Over larger distances the magnetic field is relatively constant along the trap axis z, whereas in the radial directions the field is asymmetric and shows a non-monotonous behavior, likely caused by an insufficient mesh density. Fig. E.3 details the analysis by plotting the individual magnetic field components along the trap directions. It can be seen that the magnetic field orientation is pointing along the up-down y direction in the trap. A finding that has been confirmed by the measurements in Ch. 7.7.2.2. The field component B_z is the smallest and could be an artifact from the finite resolution grid used in the simulation [1].

Some qualitative changes to the simulated system have been tested, including an asymmetric trap drive, a different RF copper stripe geometry and a phase-lag between the blade pairs for the symmetric drive. The results are shown in Fig. E.4. As can be seen in Fig. E.5 a phase-lag between the two blade pairs in a symmetric drive, which is used in this experiment, has only a small impact on the magnitude and the direction of the ac B field. Conducting parts, as for example the compensation electrodes or the RF stripes, on the other hand have a more significant impact. Unfortunately a minimum simulation with only the RF blades and no RF power leadings cannot be conducted with the used HFSS software. A completely symmetric geometry of the copper bands leading the

---

[1] Private communication with M. Doležal.

RF drive from two orthogonal directions may be possible. In conclusion, a full explanation for the large ac magnetic field cannot be found. It is however likely that the copper stripes and the RF feedthrough, which lead the high currents to the trap and which are in the vicinity of one side of the trap, are the main cause of the high fields. The asymmetric position of the compensation electrodes, below and at the side of the trap, introduce also a symmetry breaking.

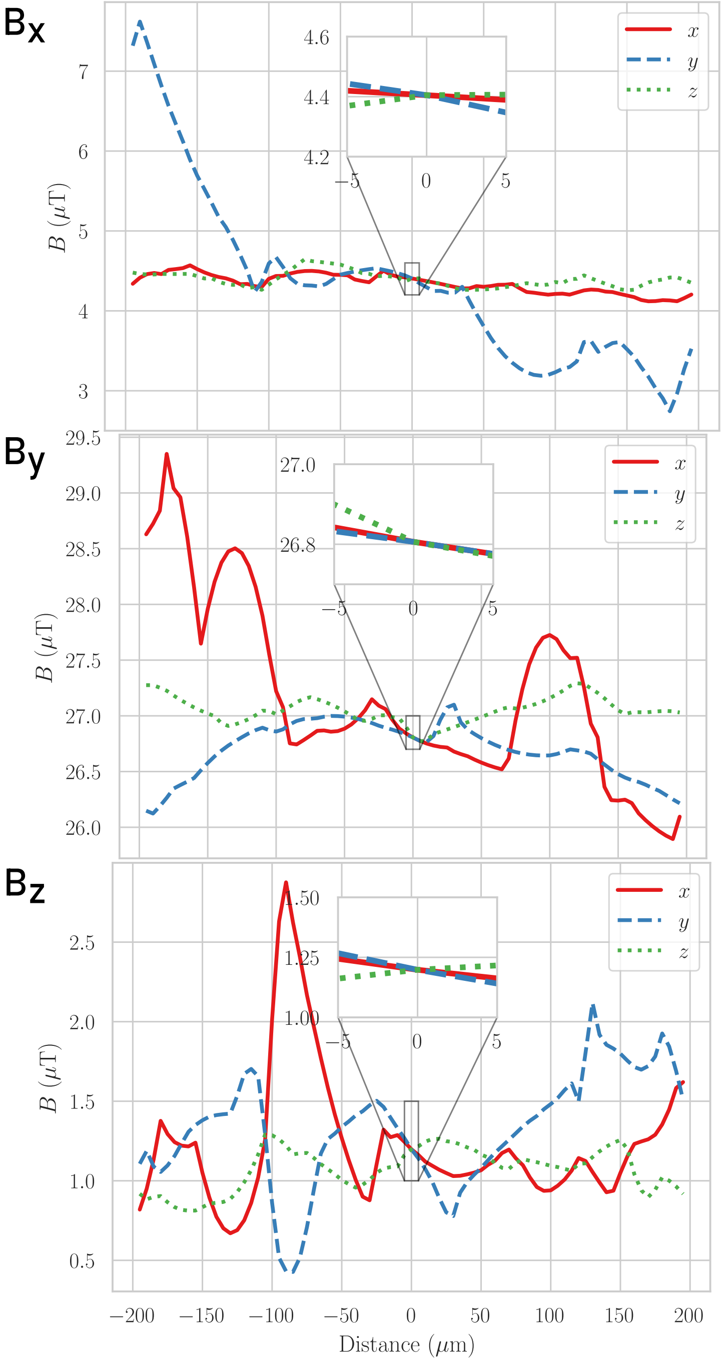

Figure E.3: HFSS simulations of the ac magnetic field amplitude components from top to bottom B_x, B_y, B_z at 2×225 V around the trap center. The plots are cuts through the center of the trap along the directions given.

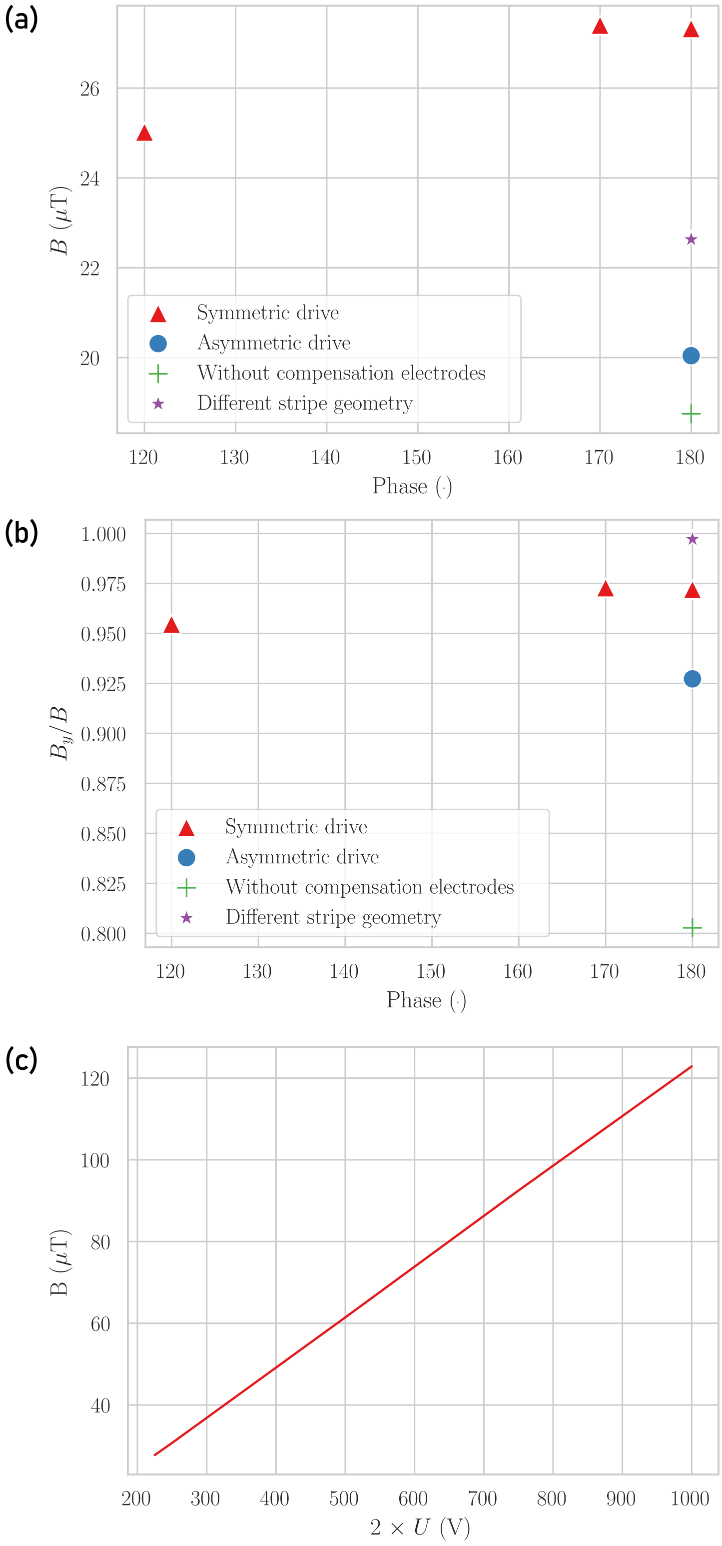

Figure E.4: (a) Magnitude of magnetic field in dependence of the phase of blade pair 1 vs. blade pair 2, for a symmetric trap drive at 2 × 225 V is displayed (red triangles). Additionally shown are an asymmetric drive at 1 × 225 V (blue dot), no compensation electrodes (green cross) and an RF stripes moved further away (purple star) as depicted in Fig. E.5. (b) Ratio of y component of B and magnitude of B for the parameters from (a). The compensation electrodes have a significant impact on the direction of B. (c) Magnetic field strengths in dependence of applied voltages to the RF blades. As expected a linear relationship is found.

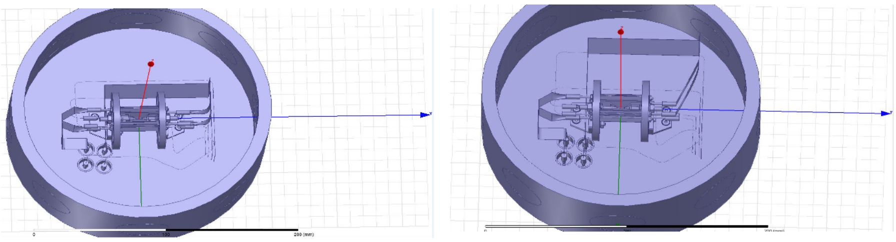

Figure E.5: Left standard simulated RF stripe geometry, on the right side one stripe has been placed farther away from the trap.

E.4 Conversion of Marconi Power to Trap Voltage

The applied Marconi power as input signal for the helical resonator is an appropriate measure for the applied trap power in the laboratory. However this makes comparisons to the simulations by Miroslav Doležal, who directly applied the voltages on the blades, and to other experiments difficult. Miroslav Doležal provided us also with $\vec{E}(x, y, z, t)$ data in a large region in the trap. From this time dependent phasor values it was possible to calculate the amplitude of the electric field $\vec{E}_0 = \vec{E}_0(x, y, z)$ from $\vec{E} = \vec{E}_0(x, y, z)\sin(\Omega_{\mathrm{RF}}t)$. The subsequent chapter describes the method for inferring the radial secular frequencies from this data.

This section is following the approach from Ref. (Splatt, 2009). The pseudopotential in eV can be written as

$$\Psi(x, y, z) = \frac{Q}{4m\Omega^2}\left|\nabla V_{\mathrm{RF}}(x, y, z)\right|^2 \ , \tag{E.17}$$

with the radial secular frequencies given by

$$\omega_{\mathrm{rad}}^2 = \frac{Q}{m}\frac{\partial^2\Psi}{\partial r^2} \ . \tag{E.18}$$

This shows that the pseudopotential Ψ is proportional to the square of the gradient of the electric potential. The electric field is the gradient of the electric potential. From this it follows $\Psi \propto |E|^2$. Furthermore, from Eq. (E.18) it follows that by calculating the Hessian matrix

$$H\left(\Psi_{i,j}\right) = \partial_i\partial_j\Psi \, , \qquad i, j = x, y, z \ , \tag{E.19}$$

and solving for its eigenvalues and eigenvectors, which are the principal curvatures $\kappa_{x'}, \kappa_{z'}, \kappa_{z'}$ and the principal axes x', y', z', respectively, the trap frequencies can be inferred from

$$\omega_i = \sqrt{\frac{Q}{m}\kappa_i} \, , \qquad i = x', y', z' \ . \tag{E.20}$$

The simulation includes only the dynamic part of the symmetric trap drive, i.e., the endcap voltages were put to ground. Therefore by fitting the fields at the trap center $|\vec{E}(x, y, z = 0)|^2$ to a quadrupole shape given by $A(x-x_0)^2+B(y-y_0)^2 =$

Table E.1: Radial secular frequencies ω_p due to the RF field, inferred from the fit of the simulated $|E|^2$ to a quadrupole shape. The factor of two at the trap voltages indicates that the two blade pairs are both at the respective voltage but with opposite phase for the symmetric trap drive.

Blade Voltage (V)	$\omega_{x'}/(2\pi)$ (MHz)	$\omega_{y'}/(2\pi)$ (MHz)
2×225	1.5892	1.5892
2×500	3.5734	3.5735

Ψ the Hessian matrix was calculated by a *Python* program. The result of this fitting is depicted in Fig. E.6. We inferred from this method the radial trap frequencies ω_p (Ch. 2.5.2), which arise from the RF quadrupole potential. The result is depicted in Tab. E.1. The actual radial frequencies in the linear Paul trap are influenced by the dc potential (Wübbena et al., 2012). Therefore, using an axial trap frequency of $\omega_z = 2\pi \times 1.1\,\mathrm{MHz}$ and assuming a full symmetric trap with $\alpha = 0.5$, the radial frequencies were calculated by applying Eq. (2.62). Since the radial trap frequencies scale linearly with the blade voltage, their value at other voltages can be extrapolated.

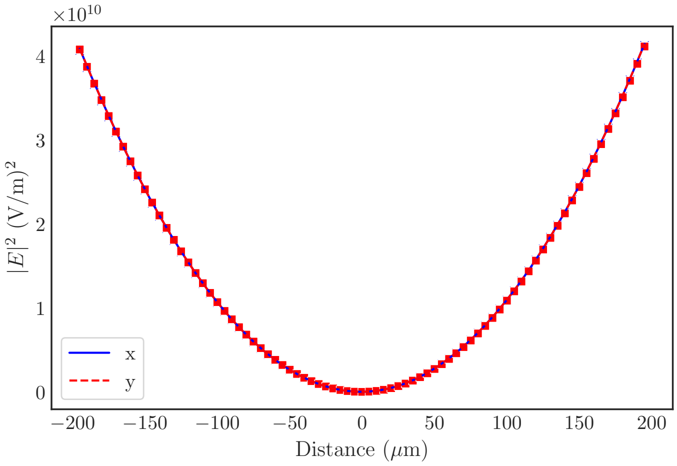

Figure E.6: Fitted squared electric field amplitude in the radial plane at $z = 0$ for a symmetric trap drive at 225 V. The fitted parameters are $A, B, x_0, y_0 = 1.0822 \times 10^{18}\,\mathrm{V^2/m^4}, 1.0822 \times 10^{18}\,\mathrm{V^2/m^4}, -6.9263 \times 10^{-7}\,\mathrm{m}, -4.4770 \times 10^{-7}\,\mathrm{m}$.

From a measurement of the radial secular frequencies in dependence of applied trap input power before amplification with +30 dB, a conversion between the three quantities input power P, blade voltage U and radial secular frequency $\omega/(2\pi)$ could be deduced. The results are depicted in Fig. E.7 and Tab. E.2.

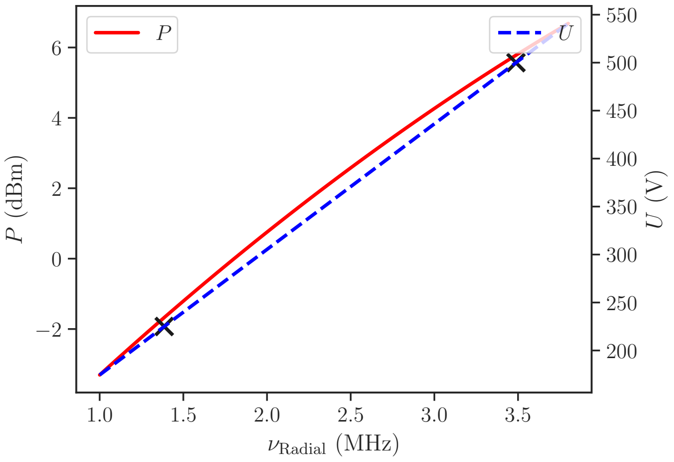

Figure E.7: Conversion graph which relates the helical input power P before amplification with +30 dB, blade voltage U and radial secular frequency $\nu = \omega/(2\pi)$ for the symmetrically driven Paul trap described.

Table E.2: Trap voltages for typical input powers before amplification.

P (dBm)	U (V)	ν_{Radial} (MHz)
−1.21	239.9	1.500
−0.92	249.3	1.571
−0.63	258.6	1.643
−0.35	268.0	1.714
−0.07	277.3	1.786
0.21	286.7	1.857
0.48	296.0	1.929
0.75	305.4	2.000
1.02	314.7	2.071
1.29	324.0	2.143
1.55	333.4	2.214
1.81	342.7	2.286
2.07	352.1	2.357
2.33	361.4	2.429
2.58	370.8	2.500

Curriculum Vitae

Curriculum Vitae

Personal Data

Name	Johannes Albrecht Kramer
Year of birth	1987
Born in	Schönebeck (Elbe)
Nationality	German

Employments

08/2011 – 10/2011	Academic Assistant, Otto-von-Guericke Universität, Magdeburg
09/2007 – 06/2008	Civil Service, Christliches Jugenddorfwerk (CJD) Schönebeck (Elbe)

Education

01/2015 – heute	PhD student, QUEST - Institute for Experimental Quantum Metrology, group of Prof. Dr. Piet O. Schmidt, Physikalisch-Technische Bundesanstalt, Braunschweig
10/2008 – 09/2014	Student of physics with degree *Diplom-Physiker*, Diploma thesis with the title "Zeitaufgelöste Simulationen der asymmetrischen Rückstreuung in einem dielektrischen Mikrodiskresonator", Arbeitsgruppe von Prof. Dr. Jan Wiersig, Otto-von-Guericke Universität, Magdeburg
12/2012	Pre-Diploma thesis (Forschungsbeleg) with the title "Bose-Einstein-Kondensat in einem Doppelmuldenpotential", Arbeitsgruppe von Prof. Dr. Jan Wiersig, Otto-von-Guericke-Universität, Magdeburg
07/2007	Abitur, Dr. Carl-Herrmann Gymnasium, Schönebeck (Elbe)

Braunschweig, March 10, 2023

Publications

Hannig, S., L. Pelzer, N. Scharnhorst, J. Kramer, M. Stepanova, Z. T. Xu, N. Spethmann, I. D. Leroux, T. E. Mehlstäubler, and P. O. Schmidt (2019). “Towards a transportable aluminium ion quantum logic optical clock.” *Review of Scientific Instruments* 90.5, p. 053204.

Leroux, Ian D., Nils Scharnhorst, Stephan Hannig, Johannes Kramer, Lennart Pelzer, Mariia Stepanova, and Piet O. Schmidt (2017). “On-line estimation of local oscillator noise and optimisation of servo parameters in atomic clocks.” *Metrologia* 54.3, p. 307.

Pelzer, L., K. Dietze, J. Kramer, F. Dawel, L. Krinner, N. Spethmann, V. Martinez, N. Aharon, A. Retzker, K. Hammerer, and P. O. Schmidt (2021). “Tailored optical clock transition in $^{40}\mathrm{Ca}^{+}$.” *Measurement: Sensors* 18, p. 100326.

Peng, Bo, Şahin Kaya Özdemir, Matthias Liertzer, Weijian Chen, Johannes Kramer, Huzeyfe Yılmaz, Jan Wiersig, Stefan Rotter, and Lan Yang (2016). “Chiral modes and directional lasing at exceptional points.” *Proceedings of the National Academy of Sciences* 113.25, pp. 6845–6850.

Scharnhorst, Nils, Javier Cerrillo, Johannes Kramer, Ian D. Leroux, Jannes B. Wübbena, Alex Retzker, and Piet O. Schmidt (2018). “Experimental and theoretical investigation of a multimode cooling scheme using multiple electromagnetically-induced-transparency resonances.” *Physical Review A* 98.2, p. 023424.

Scharnhorst, Nils, Jannes B. Wübbena, Stephan Hannig, Kornelius Jakobsen, Johannes Kramer, Ian D. Leroux, and Piet O. Schmidt (2015). “High-bandwidth transfer of phase stability through a fiber frequency comb.” *Optics Express* 23.15, pp. 19771–19776.

Bibliography

Aharon, Nati, Nicolas Spethmann, Ian D. Leroux, Piet O. Schmidt, and Alex Retzker (2019). “Robust optical clock transitions in trapped ions using dynamical decoupling.” *New Journal of Physics* 21.8, p. 083040 (cit. on pp. 16, 176).

Akerman, Nitzan, Nir Navon, Shlomi Kotler, Yinnon Glickman, and Roee Ozeri (2015). “Universal gate-set for trapped-ion qubits using a narrow linewidth diode laser.” *New Journal of Physics* 17.11, p. 113060 (cit. on p. 173).

Al-Masoudi, Ali, Sören Dörscher, Sebastian Häfner, Uwe Sterr, and Christian Lisdat (2015). “Noise and instability of an optical lattice clock.” *Physical Review A* 92.6, p. 063814 (cit. on p. 103).

Allan, D. W. (1966). “Statistics of atomic frequency standards.” *Proceedings of the IEEE* 54.2, pp. 221–230 (cit. on p. 10).

Amairi, Sana (2014). “A Long Optical Cavity For Sub-Hertz Laser Spectroscopy.” PhD thesis. Leibniz Universität Hannover (cit. on pp. 5, 30, 83, 84, 88, 173, 177).

Amairi, Sana, Thomas Legero, Thomas Kessler, Uwe Sterr, Jannes B. Wübbena, Olaf Mandel, and Piet O. Schmidt (2013). “Reducing the effect of thermal noise in optical cavities.” *Applied Physics B* 113.2, pp. 233–242 (cit. on p. 83).

Arnold, K. J., R. Kaewuam, A. Roy, T. R. Tan, and M. D. Barrett (2018). “Blackbody radiation shift assessment for a lutetium ion clock.” en. *Nature Communications* 9.1, pp. 1–6 (cit. on p. 14).

Arnold, K. J., R. Kaewuam, T. R. Tan, S. G. Porsev, M. S. Safronova, and M. D. Barrett (2019). “Dynamic polarizability measurements with ^{176}Lu^{+}.” *Physical Review A* 99.1, p. 012510 (cit. on p. 14).

Arnold, K.J., R. Kaewuam, S.R. Chanu, T.R. Tan, Zhiqiang Zhang, and M.D. Barrett (2020). “Precision Measurements of the ^{138}Ba^{+} $6s^2S_{1/2}$-$5d^2D_{5/2}$ Clock Transition.” *Physical Review Letters* 124.19. Publisher: American Physical Society, p. 193001 (cit. on p. 14).

Arvanitaki, Asimina, Junwu Huang, and Ken Van Tilburg (2015). “Searching for dilaton dark matter with atomic clocks.” *Physical Review D* 91.1, p. 015015 (cit. on p. 13).

Ashfold, Michael N. R., Frederik Claeyssens, Gareth M. Fuge, and Simon J. Henley (2004). “Pulsed laser ablation and deposition of thin films.” *Chemical Society Reviews* 33.1, p. 23 (cit. on p. 59).

Ashkin, A., G. Boyd, and J. Dziedzic (1966). “Resonant optical second harmonic generation and mixing.” *IEEE Journal of Quantum Electronics* 2.6, pp. 109–124 (cit. on p. 6).

Aspect, A., E. Arimondo, R. Kaiser, N. Vansteenkiste, and C. Cohen-Tannoudji (1988). “Laser Cooling below the One-Photon Recoil Energy by Velocity-Selective Coherent Population Trapping.” *Phys. Rev. Lett.* 61 (7), pp. 826–829 (cit. on p. 39).

Autler, S. H. and C. H. Townes (1955). “Stark Effect in Rapidly Varying Fields.” *Phys. Rev.* 100 (2), pp. 703–722 (cit. on pp. 197, 199).

BIPM (2019). *Le Système international d’unités / The International System of Units (‘The SI Brochure’).* Ninth. Bureau international des poids et mesures (cit. on p. 11).

Bao, Chengying, Andrew C. Funk, Changxi Yang, and Steven T. Cundiff (2014). “Pulse dynamics in a mode-locked fiber laser and its quantum limited comb frequency uncertainty.” *Opt. Lett.* 39.11, pp. 3266–3269 (cit. on p. 72).

Barber, Z. W., J. E. Stalnaker, N. D. Lemke, N. Poli, C. W. Oates, T. M. Fortier, S. A. Diddams, L. Hollberg, C. W. Hoyt, A. V. Taichenachev, and V. I. Yudin (2008). “Optical Lattice Induced Light Shifts in an Yb Atomic Clock.” *Phys. Rev. Lett.* 100 (10), p. 103002 (cit. on p. 15).

Barnes, James A., Andrew R. Chi, Leonard S. Cutler, Daniel J. Healey, David B. Leeson, Thomas E. McGunigal, James A. Mullen, Warren L. Smith, Richard L. Sydnor, Robert F. C. Vessot, and Gernot M. R. Winkler (1971). “Characterization of Frequency Stability.” *IEEE Transactions on Instrumentation and Measurement* IM-20.2, pp. 105–120 (cit. on p. 10).

Batori, Etienne, Nil Almat, Christoph Affolderbach, and Gaetano Mileti (2020). “GNSS-grade space atomic frequency standards: Current status and ongoing developments.” *Advances in Space Research* (cit. on p. 13).

Bauch, A., S. Weyers, D. Piester, E. Staliuniene, and W. Yang (2012). “Generation of UTC(PTB) as a fountain-clock based time scale.” *Metrologia* 49.3, p. 180 (cit. on p. 13).

Beloy, K., V. A. Dzuba, and S. M. Brewer (2020). “Quadruply Ionized Barium as a Candidate for a High-Accuracy Optical Clock.” *Phys. Rev. Lett.* 125 (17), p. 173002 (cit. on p. 15).

Beloy, K., D. R. Leibrandt, and W. M. Itano (2017). “Hyperfine-mediated electric quadrupole shifts in Al^+ and In^+ ion clocks.” *Phys. Rev. A* 95 (4), p. 043405 (cit. on pp. 162, 163).

Beloy, Kyle, Martha I. Bodine, Tobias Bothwell, Samuel M. Brewer, Sarah L. Bromley, Jwo-Sy Chen, Jean-Daniel Deschênes, Scott A. Diddams, Robert J. Fasano, Tara M. Fortier, Youssef S. Hassan, David B. Hume, Dhruv Kedar, Colin J. Kennedy, Isaac Khader, et al. (2021). “Frequency ratio measurements at 18-digit accuracy using an optical clock network.” *Nature* 591.7851. Number: 7851 Publisher: Nature Publishing Group, pp. 564–569 (cit. on pp. x, xii, 12–14, 175).

Benhelm, Jan (2008). “Precision spectroscopy and quantum information processing with trapped calcium ions.” PhD thesis. Institute fuer Quantenoptik und Quanteninformation der Österreichischen Akademie der Wissenschaften, Otto Hittmair-Platz 1, 6020 Innsbruck, Austria: University of Innbruck (cit. on pp. 56, 57).

Benkler, Erik, Christian Lisdat, and Uwe Sterr (2015). “On the relation between uncertainties of weighted frequency averages and the various types of Allan deviations.” *Metrologia* 52.4, pp. 565–574 (cit. on pp. 8, 71, 88).

Berkeland, D. J., J. D. Miller, J. C. Bergquist, W. M. Itano, and D. J. Wineland (1998). “Minimization of ion micromotion in a Paul trap.” *Journal of Applied Physics* 83.10, pp. 5025–5033 (cit. on pp. 54, 138, 145, 146).

Berry, H. G., G. Gabrielse, and A. E. Livingston (1977). “Measurement of the Stokes parameters of light.” *Appl. Opt.* 16.12, pp. 3200–3205 (cit. on p. 113).

Biedermann, G. W., K. Takase, X. Wu, L. Deslauriers, S. Roy, and M. A. Kasevich (2013). “Zero-Dead-Time Operation of Interleaved Atomic Clocks.” *Physical Review Letters* 111.17, p. 170802 (cit. on p. 16).

Black, Eric D. (2001). “An introduction to Pound–Drever–Hall laser frequency stabilization.” *American Journal of Physics* 69.1. Publisher: American Association of Physics Teachers, pp. 79–87 (cit. on p. 70).

Blythe, P., B. Roth, U. Fröhlich, H. Wenz, and S. Schiller (2005). "Production of Ultracold Trapped Molecular Hydrogen Ions." *Phys. Rev. Lett.* 95 (18), p. 183002 (cit. on p. 44).

Bollinger, J. J., W. M Itano, D. J. Wineland, and D. J. Heinzen (1996). "Optimal frequency measurements with maximally correlated states." *Physical Review A* 54.6, R4649–4652 (cit. on p. 11).

Bothwell, Tobias, Dhruv Kedar, Eric Oelker, John M. Robinson, Sarah L. Bromley, Weston L. Tew, Jun Ye, and Colin J. Kennedy (2019). "JILA SrI optical lattice clock with uncertainty of 2×10^{-18}." *Metrologia* 56.6. Publisher: IOP Publishing, p. 065004 (cit. on p. 15).

Bothwell, Tobias, Colin J. Kennedy, Alexander Aeppli, Dhruv Kedar, John M. Robinson, Eric Oelker, Alexander Staron, and Jun Ye (2022). "Resolving the gravitational redshift across a millimetre-scale atomic sample." *Nature* 602.7897. Number: 7897 Publisher: Nature Publishing Group, pp. 420–424 (cit. on pp. 15, 164).

Bourdeauducq, Sébastien et al. (2016). *ARTIQ 1.0. Zenodo. 10.5281/zenodo.51303*. `https://m-labs.hk/experiment-control/artiq/`. Accessed: 2022-04-14 (cit. on p. 175).

Brage, Tomas, Philip G. Judge, Abdellatif Aboussaid, Michel R. Godefroid, Per Jonsson, Anders Ynnerman, Charlotte Froese Fischer, and David S. Leckrone (1998). "Hyperfine Induced Transitions as Diagnostics of Isotopic Composition and Densities of Low-Density Plasmas." *The Astrophysical Journal* 500.1, pp. 507–521 (cit. on p. 20).

Braginsky, V. B. and F. Ya. Khalili (1996). "Quantum nondemolition measurements: the route from toys to tools." *Rev. Mod. Phys.* 68 (1), pp. 1–11 (cit. on p. 130).

Bransden, B.H. and C.J. Joachain (2003). *Physics of Atoms and Molecules*. Second. Pearson Education Limited (cit. on p. 198).

Brewer, S. M., J.-S. Chen, K. Beloy, A. M. Hankin, E. R. Clements, C. W. Chou, W. F. McGrew, X. Zhang, R. J. Fasano, D. Nicolodi, H. Leopardi, T. M. Fortier, S. A. Diddams, A. D. Ludlow, D. J. Wineland, D. R. Leibrandt, and D. B. Hume (2019a). "Measurements of $^{27}\mathrm{Al}^{+}$ and $^{25}\mathrm{Mg}^{+}$ magnetic constants for improved ion-clock accuracy." *Physical Review A* 100.1, p. 013409 (cit. on pp. 150, 154, 158).

Brewer, S. M., J.-S. Chen, A. M. Hankin, E. R. Clements, C. W. Chou, D. J. Wineland, D. B. Hume, and D. R. Leibrandt (2019b). "$^{27}\mathrm{Al}^{+}$ Quantum-Logic Clock with a Systematic Uncertainty below 10^{-18}." *Phys. Rev. Lett.* 123 (3), p. 033201 (cit. on pp. ix, xi, 12, 14, 22, 111, 137, 144, 148–151, 166, 171, 175).

CCTF (2016). *CCTF (Consultative Committee for Time and Frequency) Strategy Document*. `https://www.bipm.org/documents/20126/35554894/CCTF+Strategy/7cf0f648-2afe-d15c-0909-1f03406bbb8f`. Accessed: 2022-05-06 (cit. on p. 12).

Calmet, Xavier and Matthias Keller (2015). "Cosmological evolution of fundamental constants: From theory to experiment." *Modern Physics Letters A* 30.22, p. 1540028 (cit. on pp. ix, xi, 13, 14).

Campbell, C. J., A. G. Radnaev, A. Kuzmich, V. A. Dzuba, V. V. Flambaum, and A. Derevianko (2012). "Single-Ion Nuclear Clock for Metrology at the 19th Decimal Place." *Phys. Rev. Lett.* 108 (12), p. 120802 (cit. on p. 15).

Caves, Carlton M., Kip S. Thorne, Ronald W. P. Drever, Vernon D. Sandberg, and Mark Zimmermann (1980). "On the measurement of a weak classical force coupled to a quantum-mechanical oscillator. I. Issues of principle." *Rev. Mod. Phys.* 52 (2), pp. 341–392 (cit. on p. 130).

Chen, J.-S., S. M. Brewer, C. W. Chou, D. J. Wineland, D. R. Leibrandt, and D. B. Hume (2017). “Sympathetic Ground State Cooling and Time-Dilation Shifts in an $^{27}Al^+$ Optical Clock.” *Physical Review Letters* 118.5, p. 053002 (cit. on pp. 38, 146).

Chen, Jwo-Sy (2017). “Ticking near the Zero-Point Energy: Towards 1x10^{-18} Accuracy in Al^+ Optical Clocks.” PhD thesis. Boulder, USA: University of Colorado (cit. on p. 183).

Chepurov, S. V., N. A. Pavlov, A. A. Lugovoy, S. N. Bagayev, and A. V. Taichenachev (2021). “Optical frequency standard with a single $^{171}Yb^+$ ion.” *Quantum Electronics* 51.6. Publisher: IOP Publishing, p. 473 (cit. on p. 14).

Chou, C. W., D. B. Hume, J. C. J. Koelemeij, D. J. Wineland, and T. Rosenband (2010). “Frequency Comparison of Two High-Accuracy Al^+ Optical Clocks.” *Physical Review Letters* 104.7, p. 070802 (cit. on pp. 12, 45, 149, 150, 163, 166).

Chwalla, M., J. Benhelm, K. Kim, G. Kirchmair, T. Monz, M. Riebe, P. Schindler, A. Villar, W. Hänsel, C. Roos, R. Blatt, M. Abgrall, G. Santarelli, G. Rovera, and Ph. Laurent (2009). “Absolute Frequency Measurement of the $^{40}Ca^+$ $4s^2$ $S_{1/2}$-$3d^2$ $D_{5/2}$ Clock Transition.” *Physical Review Letters* 102.2, p. 023002 (cit. on pp. 22, 98).

Clements, Ethan R., May E. Kim, Kaifeng Cui, Aaron M. Hankin, Samuel M. Brewer, Jose Valencia, Jwo-Sy Chen, Chin-Wen Chou, David R. Leibrandt, and David B. Hume (2020). “Lifetime-Limited Interrogation of Two Independent $^{27}Al^+$ Clocks Using Correlation Spectroscopy.” *Phys. Rev. Lett.* 125 (24), p. 243602 (cit. on p. 16).

Cui, Kaifeng, Sijia Chao, Chenglong Sun, Shaomao Wang, Ping Zhang, Yuanfei Wei, Jinbo Yuan, Jian Cao, Hualin Shu, and Xueren Huang (2022). “Evaluation of the systematic shifts of a $^{40}Ca^+ - {}^{27}Al^+$ optical clock.” en. *The European Physical Journal D* 76.8, p. 140 (cit. on p. 14).

Cundiff, Steven T. and Jun Ye (2003). “Colloquium: Femtosecond optical frequency combs.” *Rev. Mod. Phys.* 75 (1), pp. 325–342 (cit. on pp. 6, 7).

Davis, Jack, Pierre Dubé, and Amar C. Vutha (2019). “Improved estimate of the collisional frequency shift in Al^+ optical clocks.” *Phys. Rev. Research* 1 (3), p. 033137 (cit. on pp. ix, xi, 149, 150, 165).

Degenhardt, C., T. Nazarova, Ch. Lisdat, H. Stoehr, U. Sterr, and F. Riehle (2005). “Influence of Chirped Excitation Pulses in an Optical Clock With Ultracold Calcium Atoms.” *IEEE Transactions on Instrumentation and Measurement* 54.2, pp. 771–775 (cit. on p. 163).

Dehmelt, H.G. (1968). “Radiofrequency Spectroscopy of Stored Ions I: Storage**Part II: Spectroscopy is now scheduled to appear in Volume V of this series.” Ed. by D.R. Bates and Immanuel Estermann. Vol. 3. Advances in Atomic and Molecular Physics. Academic Press, pp. 53–72 (cit. on p. 22).

Dehmelt, Hans (1990). “Experiments with an Isolated Subatomic Particle at Rest (Nobel Lecture).” *Angewandte Chemie International Edition in English* 29.7, pp. 734–738. eprint: `https://onlinelibrary.wiley.com/doi/pdf/10.1002/anie.199007341` (cit. on p. 23).

Delehaye, Marion and Clément Lacroûte (2018). “Single-ion, transportable optical atomic clocks.” *Journal of Modern Optics* 65.5-6, pp. 622–639. eprint: `https://doi.org/10.1080/09500340.2018.1441917` (cit. on p. 11).

Delva, P., N. Puchades, E. Schönemann, F. Dilssner, C. Courde, S. Bertone, F. Gonzalez, A. Hees, Ch. Le Poncin-Lafitte, F. Meynadier, R. Prieto-Cerdeira, B. Sohet, J. Ventura-Traveset, and P. Wolf (2018). “Gravitational Redshift Test Using Eccentric Galileo Satellites.” *Physical Review Letters* 121.23, p. 231101 (cit. on p. 164).

Delva, Pacôme and Jérôme Lodewyck (2013). “Atomic clocks: new prospects in metrology and geodesy.” *Acta Futura* 7, pp. 67–78 (cit. on p. 4).

Denker, H., N. Lindenthal, L. Timmen, and S. Weyers (2014). “Report on leveling and GNSS results for stations on the PTB campus.” *Internal PTB report* (cit. on p. 164).

Dick, G. J (1987). “Local Oscillator Induced Instabilities in Trapped Ion Frequency Standards.” *Proc. 19th Annual Precise Time and Time Interval (PTTI) Application and Planning Meeting*, pp. 133–147 (cit. on p. 10).

Dick, G. John, John D. Prestage, Charles A. Greenhall, and Lute Maleki (1990). “Local oscillator induced degradation of medium-term stability in passive atomic frequency standards.” *Proceedings of the 22nd Annual Precise Time and Time Interval (PTTI) Applications and Planning Meeting*. The 22nd Annual Precise Time and Time Interval (PTTI) Applications and Planning Meeting. Vienna (cit. on p. 10).

Diedrich, F., J. C. Bergquist, W. M Itano, and D. J. Wineland (1989). “Laser cooling to the zero-point energy of motion.” *Physical Review Letters* 62.4, pp. 403–406 (cit. on p. 38).

Doerscher, S, N Huntemann, R Schwarz, R Lange, E Benkler, B Lipphardt, U Sterr, E Peik, and C Lisdat (2021). “Optical frequency ratio of a $^{171}\mathrm{Yb}^{+}$ single-ion clock and a $^{87}\mathrm{Sr}$ lattice clock.” *Metrologia* 58.1, p. 015005 (cit. on pp. 12, 14, 15).

Doležal, Miroslav (n.d.). *HFSS simulations raw data provided by private communication* (cit. on pp. 54, 153).

Doležal, Miroslav, P Balling, P B R Nisbet-Jones, S A King, J M Jones, H A Klein, P Gill, T Lindvall, A E Wallin, M Merimaa, and et al. (2015). “Analysis of thermal radiation in ion traps for optical frequency standards.” *Metrologia* 52.6, pp. 842–56. eprint: `1510.05556` (physics.atom-ph) (cit. on pp. 50, 148, 200).

Donley, E. A., T. P. Heavner, F. Levi, M. O. Tataw, and S. R. Jefferts (2019). “Erratum: “Double-pass acousto-optic modulator system” [Rev. Sci. Instrum. 76, 063112 (2005)].” *Review of Scientific Instruments* 90.4, p. 049901. eprint: `https://doi.org/10.1063/1.5097130` (cit. on p. 70).

Drakoudis, A., M. Söllner, and G. Werth (2006). “Instabilities of ion motion in a linear Paul trap.” *International Journal of Mass Spectrometry* 252.1, pp. 61–68 (cit. on p. 26).

Drever, R. W. P., J. L Hall, F. V. Kowalski, J. Hough, G. M. Ford, A. J. Munley, and H. Ward (1983). “Laser phase and frequency stabilization using an optical resonator.” *Applied Physics B: Lasers and Optics* 31.2, pp. 97–105 (cit. on p. 70).

Droste, S., F. Ozimek, Th. Udem, K. Predehl, T. W. Hänsch, H. Schnatz, G. Grosche, and R. Holzwarth (2013). “Optical-Frequency Transfer over a Single-Span 1840 km Fiber Link.” *Physical Review Letters* 111.11, p. 110801 (cit. on pp. x, xii).

Dubé, Pierre, John E Bernard, and Marina Gertsvolf (2017). “Absolute frequency measurement of the $^{88}\mathrm{Sr}^{+}$clock transition using a GPS link to the SI second.” *Metrologia* 54.3, pp. 290–298 (cit. on p. 14).

Dubé, P., A. Madej, J. Bernard, L. Marmet, J.-S. Boulanger, and S. Cundy (2005). “Electric Quadrupole Shift Cancellation in Single-Ion Optical Frequency Standards.” *Physical Review Letters* 95.3, p. 033001 (cit. on p. 163).

Dörscher, Sören, Ali Al-Masoudi, Marcin Bober, Roman Schwarz, Richard Hobson, Uwe Sterr, and Christian Lisdat (2020). “Dynamical decoupling of laser phase noise in compound atomic clocks.” *Communications Physics* 3.1. Number: 1 Publisher: Nature Publishing Group, pp. 1–9 (cit. on pp. 11, 16, 175).

Einstein, Albert (1911). “Über den Einfluß der Schwerkraft auf die Ausbreitung des Lichtes.” *Annalen der Physik* 340.10, pp. 898–908 (cit. on pp. 4, 164).

Eschner, J., G. Morigi, C. Keitel, C. Roos, D. Leibfried, A. Mundt, F. Schmidt-Kaler, and R. Blatt (2001). “Ground state laser cooling of trapped atoms using electromagnetically induced transparency.” *Proceedings of the 15th International Conference on LASER Spectroscopy*. Ed. by S. Chu, V. Vuletić, A.J. Kerman, and C. Chin. Proceedings of the 15th International Conference on LASER Spectroscopy, 10-15 June 2001, Snowbird, UT, USA. Singapore, Singapore: World Scientific, pp. 325–8 (cit. on p. 39).

Eschner, J., G. Morigi, F. Schmidt-Kaler, and R. Blatt (2003). “Laser cooling of trapped ions.” *JOSA B* 20.5, pp. 1003–1015 (cit. on p. 39).

Evers, J. and C. H. Keitel (2004). “Double-EIT ground-state laser cooling without blue-sideband heating.” *EPL (Europhysics Letters)* 68.3, p. 370 (cit. on p. 40).

Fenske, Julia-Aileen (2015). “Implementierung eines digitalen PID-Reglers mit dem Entwicklungsboard „Red Pitaya“.” Bachelor Thesis. Wolfenbüttel: Ostfalia Hochschule für angewandte Wissenschaften (cit. on p. 80).

Flambaum, V. V and V. A Dzuba (2009). “Search for variation of the fundamental constants in atomic, molecular, and nuclear spectra.” *Canadian Journal of Physics* 87.1, pp. 25–33 (cit. on p. 14).

Flühmann, C., T. L. Nguyen, M. Marinelli, V. Negnevitsky, K. Mehta, and J. P. Home (2019). “Encoding a qubit in a trapped-ion mechanical oscillator.” *Nature* 566.7745, p. 513 (cit. on p. 174).

Franken, P. A., A. E. Hill, C. W. Peters, and G. Weinreich (1961). “Generation of Optical Harmonics.” *Phys. Rev. Lett.* 7 (4), pp. 118–119 (cit. on p. 6).

Franzen, Alexander (n.d.). *Component Library*. `http://www.gwoptics.org/ComponentLibrary/` (cit. on p. 68).

Gan, H. C. J., G. Maslennikov, K.-W. Tseng, T. R. Tan, R. Kaewuam, K. J. Arnold, D. Matsukevich, and M. D. Barrett (2018). “Oscillating-magnetic-field effects in high-precision metrology.” *Phys. Rev. A* 98 (3), p. 032514 (cit. on pp. ix, xi, 150, 153–155, 158, 167, 171, 197).

Gebert, Florian, Yong Wan, Fabian Wolf, Christopher N. Angstmann, Julian C. Berengut, and Piet O. Schmidt (2015). “Precision Isotope Shift Measurements in Calcium Ions Using Quantum Logic Detection Schemes.” *Physical Review Letters* 115.5, p. 053003 (cit. on p. 22).

Godun, R. M., P. B. R. Nisbet-Jones, J. M. Jones, S. A. King, L. A. M. Johnson, H. S. Margolis, K. Szymaniec, S. N. Lea, K. Bongs, and P. Gill (2014). “Frequency Ratio of Two Optical Clock Transitions in ^{171}Yb^{+} and Constraints on the Time Variation of Fundamental Constants.” *Phys. Rev. Lett.* 113 (21), p. 210801 (cit. on pp. 13, 14, 175).

Goldenberg, H. M., D. Kleppner, and N. F. Ramsey (1960). “Atomic Hydrogen Maser.” *Phys. Rev. Lett.* 5 (8), pp. 361–362 (cit. on p. 16).

Grangier, P. (2012). “Preserving quantum nondemolition.” *Physics Today* 65 (4), p. 11 (cit. on p. 130).

Gray, H. R., R. M. Whitley, and C. R. Stroud (1978). “Coherent trapping of atomic populations.” *Opt. Lett.* 3.6, pp. 218–220 (cit. on p. 40).

Grosche, Gesine (2014). “Eavesdropping time and frequency: phase noise cancellation along a time-varying path, such as an optical fiber.” *Opt. Lett.* 39.9, pp. 2545–2548 (cit. on pp. 71, 74).

Guggemos, M, M Guevara-Bertsch, D Heinrich, O A Herrera-Sancho, Y Colombe, R Blatt, and C F Roos (2019). “Frequency measurement of the ^{1}S$_0$, F=5/2 – ^{3}P$_1$, F=7/2 transition of $^{27}Al^+$ via quantum logic spectroscopy with $^{40}Ca^+$." *New Journal of Physics* 21.10, p. 103003 (cit. on pp. 19, 20, 110, 119).

Guggemos, M., D. Heinrich, O. A. Herrera-Sancho, R. Blatt, and C. F. Roos (2015). "Sympathetic cooling and detection of a hot trapped ion by a cold one." *New Journal of Physics* 17.10, p. 103001 (cit. on pp. 44, 61).

Gulde, Stephan Timo (2003). "Experimental Realization of Quantum Gates and the Deutsch-Josza Algorithm with Trapped ^{4}0Ca$^+$ Ions." PhD thesis. Institut fuer Experimentalphysik der Universität Innsbruck, Otto Hittmair-Platz 1, 6020 Innsbruck, Austria: Leopold-Franzens-Universitaet Innsbruck (cit. on p. 49).

Hall, John L. (2006). "Nobel Lecture: Defining and measuring optical frequencies." *Rev. Mod. Phys.* 78 (4), pp. 1279–1295 (cit. on pp. 5–7).

Hankin, A. M., E. R. Clements, Y. Huang, S. M. Brewer, J.-S. Chen, C. W. Chou, D. B. Hume, and D. R. Leibrandt (2019). "Systematic uncertainty due to background-gas collisions in trapped-ion optical clocks." *Phys. Rev. A* 100 (3), p. 033419 (cit. on pp. ix, xi, 93–96, 110, 125, 146, 148–150, 165).

Hannig, S., J. Mielke, J. A. Fenske, M. Misera, N. Beev, C. Ospelkaus, and P. O. Schmidt (2018). "A highly stable monolithic enhancement cavity for second harmonic generation in the ultraviolet." *Review of Scientific Instruments* 89.1, p. 013106 (cit. on pp. 69, 70, 82).

Hannig, S., L. Pelzer, N. Scharnhorst, J. Kramer, M. Stepanova, Z. T. Xu, N. Spethmann, I. D. Leroux, T. E. Mehlstäubler, and P. O. Schmidt (2019). "Towards a transportable aluminium ion quantum logic optical clock." *Review of Scientific Instruments* 90.5, p. 053204 (cit. on pp. 11, 57).

Hannig, Stephan (2018). "Development and characterization of a transportable aluminum ion quantum logic optical clock setup." PhD thesis. Leibniz Universität Hannover (cit. on pp. 57, 69, 70, 82, 111).

Hänsch, Theodor W. (2006). "Nobel Lecture: Passion for precision." *Rev. Mod. Phys.* 78 (4), pp. 1297–1309 (cit. on pp. 5–7).

Harcken, Hans (n.d.). *The Earth's magnetic field at PTB*. `https://www.ptb.de/cms/nc/en/ptb/fachabteilungen/abt2/fb-25/ag-251/live-data-earths-magnetic-field.html` (cit. on p. 64).

Hemmerling, Boerge, Florian Gebert, Yong Wan, Daniel Nigg, Ivan V Sherstov, and Piet O Schmidt (2011). "A Single Laser System for Ground State Cooling of $^{25}Mg^+$." *Applied Physics B: Lasers and Optics* 104.3, pp. 583–590 (cit. on pp. 38, 45).

Herbers, Sofia, Sören Dörscher, Erik Benkler, and Christian Lisdat (2019). "Phase noise of frequency doublers in optical clock lasers." *Optics Express* 27.16, p. 23262 (cit. on p. 87).

Herrmann, Sven, Felix Finke, Martin Lülf, Olga Kichakova, Dirk Puetzfeld, Daniela Knickmann, Meike List, Benny Rievers, Gabriele Giorgi, Christoph Günther, Hansjörg Dittus, Roberto Prieto-Cerdeira, Florian Dilssner, Francisco Gonzalez, Erik Schönemann, Javier Ventura-Traveset, and Claus Lämmerzahl (2018). "Test of the Gravitational Redshift with Galileo Satellites in an Eccentric Orbit." *Physical Review Letters* 121.23, p. 231102 (cit. on p. 164).

Herschbach, N., K. Pyka, J. Keller, and T. E. Mehlstäubler (2012). "Linear Paul trap design for an optical clock with Coulomb crystals." *Applied Physics B* 107.4, pp. 891–906 (cit. on p. 16).

Hoang, Thai M., Sang K. Chung, Thanh Le, John D. Prestage, Lin Yi, Robert L. Tjoelker, Sehyun Park, Sung-Jin Park, J. Gary Eden, Christopher Holland, and Nan Yu (2021). “Integrated physics package of micromercury trapped ion clock with 10^{-14}-level frequency stability.” *Applied Physics Letters* 119.4. Publisher: AIP Publishing LLCAIP Publishing, p. 044001 (cit. on p. 11).

Hobson, R., W. Bowden, S. A. King, P. E. G. Baird, I. R. Hill, and P. Gill (2016). “Modified hyper-Ramsey methods for the elimination of probe shifts in optical clocks.” *Physical Review A* 93.1, p. 010501 (cit. on p. 31).

Holliman, C. A., M. Fan, A. Contractor, S. M. Brewer, and A. M. Jayich (2022). “Radium Ion Optical Clock.” *Phys. Rev. Lett.* 128 (3), p. 033202 (cit. on p. 14).

Home, J. P., M. J. McDonnell, D. J. Szwer, B. C. Keitch, D. M. Lucas, D. N. Stacey, and A. M. Steane (2009). “Memory coherence of a sympathetically cooled trapped-ion qubit.” *Phys. Rev. A* 79 (5), p. 050305 (cit. on p. 44).

Huang, Yao, Baolin Zhang, Mengyan Zeng, Huaqing Zhang, Yanmei Hao, Zheng Chen, Miao Wang, Hua Guan, and Kelin Gao (2021). “Nearly continuous Ca^+ optical clocks with stability at the 10^{-18} level” (cit. on p. 14).

Huelga, S. F, C. Macchiavello, T. Pellizzari, A. K Ekert, M. B. Plenio, and J. I. Cirac (1997). “Improvement of frequency standards with quantum entanglement.” *Physical Review Letters* 79.20, pp. 3865–3868 (cit. on p. 11).

Hume, D., T. Rosenband, and D. Wineland (2007). “High-Fidelity Adaptive Qubit Detection through Repetitive Quantum Nondemolition Measurements.” *Physical Review Letters* 99.12, p. 120502 (cit. on pp. 45, 130, 135, 136, 171).

Hume, David B. (2010). “Two-Species Ion Arrays for Quantum Logic Spectroscopy and Entanglement Generation.” PhD thesis. Boulder, USA: University of Colorado. 129 pp. (cit. on pp. 124, 130).

Hume, David B. and David R. Leibrandt (2016). “Probing beyond the laser coherence time in optical clock comparisons.” *Physical Review A* 93.3, p. 032138 (cit. on p. 16).

Huntemann, N., B. Lipphardt, M. Okhapkin, Chr. Tamm, E. Peik, A. V. Taichenachev, and V. I. Yudin (2012a). “Generalized Ramsey Excitation Scheme with Suppressed Light Shift.” *Physical Review Letters* 109.21, p. 213002 (cit. on p. 31).

Huntemann, N., B. Lipphardt, Chr. Tamm, V. Gerginov, S. Weyers, and E. Peik (2014). “Improved Limit on a Temporal Variation of m_p/m_e from Comparisons of Yb^+ and Cs Atomic Clocks.” *Physical Review Letters* 113.21, p. 210802 (cit. on p. 175).

Huntemann, N., M. Okhapkin, B. Lipphardt, S. Weyers, Chr. Tamm, and E. Peik (2012b). “High-Accuracy Optical Clock Based on the Octupole Transition in $^{171}Yb^+$.” *Physical Review Letters* 108.9, p. 090801 (cit. on p. 14).

Huntemann, N., C. Sanner, B. Lipphardt, Chr. Tamm, and E. Peik (2016). “Single-Ion Atomic Clock with 3×10^{-18} Systematic Uncertainty.” *Phys. Rev. Lett.* 116 (6), p. 063001 (cit. on pp. 12, 14).

Häfner, Sebastian, Stephan Falke, Christian Grebing, Stefan Vogt, Thomas Legero, Mikko Merimaa, Christian Lisdat, and Uwe Sterr (2015). “8×10^{-17}fractional laser frequency instability with a long room-temperature cavity.” *Optics Letters* 40.9, p. 2112 (cit. on p. 83).

Hänsch, T. W. and B. Couillaud (1980). “Laser frequency stabilization by polarization spectroscopy of a reflecting reference cavity.” *Optics Communications* 35.3, pp. 441–444 (cit. on p. 70).

Imajo, Hidetsuka, Kazuhiro Hayasaka, Ryuzo Ohmukai, Utako Tanaka, Masayoshi Watanabe, and Shinji Urabe (1996). "High-resolution ultraviolet spectra of sympathetically-laser-cooled Cd^+ ions." *Phys. Rev. A* 53 (1), pp. 122–125 (cit. on p. 44).

Itano, W. M (2000). "External-field shifts of the $^{199}Hg^+$ optical frequency standard." *Journal of Research of NIST* 105.6, pp. 829–837 (cit. on p. 163).

Itano, W. M., J. C. Bergquist, J. J. Bollinger, J. M. Gilligan, D. J. Heinzen, F. L. Moore, M. G. Raizen, and D. J. Wineland (1993). "Quantum projection noise: Population fluctuations in two-level systems." *Phys. Rev. A* 47 (5), pp. 3554–3570 (cit. on pp. 123, 124).

Ivory, M., W. J. Setzer, N. Karl, H. McGuinness, C. DeRose, M. Blain, D. Stick, M. Gehl, and L. P. Parazzoli (2021). "Integrated Optical Addressing of a Trapped Ytterbium Ion." *Phys. Rev. X* 11 (4), p. 041033 (cit. on p. 11).

James, D. F. V. (1998). "Quantum dynamics of cold trapped ions with application to quantum computation." *Applied Physics B: Lasers and Optics* 66, pp. 181–190 (cit. on p. 22).

Javanainen, J. (1980). "Light-pressure cooling of trapped ions in three dimensions." *Applied Physics* 23.2, pp. 175–182 (cit. on p. 35).

Jiang, Y. Y., A. D. Ludlow, N. D. Lemke, R. W. Fox, J. A. Sherman, L.-S. Ma, and C. W. Oates (2011). "Making optical atomic clocks more stable with 10-16-level laser stabilization." *Nat Photon* 5.3, pp. 158–161 (cit. on p. 83).

Johansson, J.R., P.D. Nation, and Franco Nori (2012). "QuTiP: An open-source Python framework for the dynamics of open quantum systems." *Computer Physics Communications* 183.8, pp. 1760–1772 (cit. on p. 124).

– (2013). "QuTiP 2: A Python framework for the dynamics of open quantum systems." *Computer Physics Communications* 184.4, pp. 1234–1240 (cit. on p. 124).

Johnson, K. G., J. D. Wong-Campos, A. Restelli, K. A. Landsman, B. Neyenhuis, J. Mizrahi, and C. Monroe (2016). "Active stabilization of ion trap radiofrequency potentials." *Review of Scientific Instruments* 87.5, p. 053110 (cit. on p. 55).

Kalincev, D., L. S. Dreissen, A. P. Kulosa, C.-H. Yeh, H. A. Fürst, and T. E. Mehlstäubler (2021). "Motional heating of spatially extended ion crystals." *Quantum Science and Technology* 6.3. Publisher: IOP Publishing, p. 034003 (cit. on p. 111).

Karshenboim, Savely G. (2006). "Search for a possible variation of the fine structure constant." *General Relativity and Gravitation* 38.1, pp. 159–182 (cit. on pp. 13, 14).

Katori, Hidetoshi, Masao Takamoto, V. Pal'chikov, and V. Ovsiannikov (2003). "Ultrastable Optical Clock with Neutral Atoms in an Engineered Light Shift Trap." *Physical Review Letters* 91.17, p. 173005 (cit. on p. 15).

Keller, J., T. Burgermeister, D. Kalincev, A. Didier, A. P. Kulosa, T. Nordmann, J. Kiethe, and T. E. Mehlstäubler (2019). "Controlling systematic frequency uncertainties at the 10^{-19} level in linear Coulomb crystals." *Physical Review A* 99.1, p. 013405 (cit. on pp. 14, 16).

Keller, J., H. L. Partner, T. Burgermeister, and T. E. Mehlstäubler (2015). "Precise determination of micromotion for trapped-ion optical clocks." *Journal of Applied Physics* 118.10, p. 104501. eprint: `https://doi.org/10.1063/1.4930037` (cit. on pp. 111, 138, 139, 143, 144).

Kielpinski, D., B. E. King, C. J. Myatt, C. A. Sackett, Q. A. Turchette, W. M. Itano, C. Monroe, D. J. Wineland, and W. H. Zurek (2000). "Sympathetic cooling of trapped ions for quantum logic." *Physical Review A* 61.3, p. 032310 (cit. on p. 42).

King, Steven A., Lukas J. Spieß, Peter Micke, Alexander Wilzewski, Tobias Leopold, José R. Crespo López-Urrutia, and Piet O. Schmidt (2021). "Algorithmic Ground-State Cooling of Weakly Coupled Oscillators Using Quantum Logic." *Physical Review X* 11.4. Publisher: American Physical Society, p. 041049 (cit. on pp. 15, 43).

Kobayashi, T., D. Akamatsu, Y. Hisai, T. Tanabe, H. Inaba, T. Suzuyama, F. Hong, K. Hosaka, and M. Yasuda (2018). "Uncertainty Evaluation of an ^{171}Yb Optical Lattice Clock at NMIJ." *IEEE Transactions on Ultrasonics, Ferroelectrics, and Frequency Control* 65.12, pp. 2449–2458 (cit. on p. 15).

Koller, S.B., J. Grotti, St. Vogt, A. Al-Masoudi, S. Dörscher, S. Häfner, U. Sterr, and Ch. Lisdat (2017). "Transportable Optical Lattice Clock with 7×10^{-17} Uncertainty." *Physical Review Letters* 118.7, p. 073601 (cit. on p. 15).

Kreuter, A., C. Becher, G. P. T. Lancaster, A. B. Mundt, C. Russo, H. Häffner, C. Roos, W. Hänsel, F. Schmidt-Kaler, R. Blatt, and M. S. Safronova (2005). "Experimental and theoretical study of the $3d\,^2$D -level lifetimes of ^{40}Ca$^+$." *Physical Review A* 71.3, p. 032504 (cit. on p. 22).

Kumar, Ravi, S. Chattopadhyay, D. Angom, and B. K. Mani (2021). "Fock-space relativistic coupled-cluster calculation of a hyperfine-induced $^1S_0 \rightarrow {}^3P_0^o$ clock transition in Al$^+$." *Phys. Rev. A* 103 (2), p. 022801 (cit. on p. 20).

Lange, R., N. Huntemann, J.M. Rahm, C. Sanner, H. Shao, B. Lipphardt, Chr. Tamm, S. Weyers, and E. Peik (2021). "Improved Limits for Violations of Local Position Invariance from Atomic Clock Comparisons." *Physical Review Letters* 126.1. Publisher: American Physical Society, p. 011102 (cit. on p. 13).

Lange, Richard (2021). "High-Precision Frequency Comparisons and Searches for New Physics with Yb$^+$ Optical Clocks." PhD thesis. Hannover: Leibniz Universität Hannover (cit. on pp. 14, 175).

Laske, Torben, Hannes Winter, and Andreas Hemmerich (2019). "Pulse Delay Time Statistics in a Superradiant Laser with Calcium Atoms." *Phys. Rev. Lett.* 123 (10), p. 103601 (cit. on p. 17).

Le Kien, F., P. Schneeweiss, and A. Rauschenbeutel (2013). "Dynamical polarizability of atoms in arbitrary light fields: general theory and application to cesium." *The European Physical Journal D* 67.92 (5) (cit. on p. 153).

Leibfried, D., R. Blatt, C. Monroe, and D. Wineland (2003). "Quantum dynamics of single trapped ions." *Rev. Mod. Phys.* 75 (1), pp. 281–324 (cit. on pp. 23, 27, 31, 32, 35).

Leopardi, Holly, Kyle Beloy, Tobias Bothwell, Samuel M. Brewer, Sarah L. Bromley, Jwo-Sy Chen, Scott A. Diddams, Robert J. Fasano, Youssef S. Hassan, David B. Hume, Dhruv Kedar, Colin J. Kennedy, David R. Leibrandt, Andrew D. Ludlow, William F. McGrew, et al. (2021). "Measurement of the ^{27}Al$^+$and ^{87}Sr absolute optical frequencies." *Metrologia* 58.1. Publisher: IOP Publishing, p. 015017 (cit. on p. 21).

Leopold, T., S. A. King, P. Micke, A. Bautista-Salvador, J. C. Heip, C. Ospelkaus, J. R. Crespo López-Urrutia, and P. O. Schmidt (2019). "A cryogenic radio-frequency ion trap for quantum logic spectroscopy of highly charged ions." *Review of Scientific Instruments* 90.7, p. 073201. eprint: `https://doi.org/10.1063/1.5100594` (cit. on pp. 104, 106).

Leroux, Ian D., Nils Scharnhorst, Stephan Hannig, Johannes Kramer, Lennart Pelzer, Mariia Stepanova, and Piet O. Schmidt (2017). "On-line estimation of local oscillator noise and optimisation of servo parameters in atomic clocks." *Metrologia* 54.3, p. 307 (cit. on pp. 11, 16, 176).

Li, Jia-Jia, Feng-Feng Zhang, Zhi-Min Wang, Yi-Chen Xu, Xu-Chao Liu, Nan Zong, Shen-Jin Zhang, Feng-Liang Xu, Feng Yang, Lei Yuan, Yang Kou, Yong Bo, Da-Fu Cui, Qin-Jun Peng, Xiao-Yang Wang, Li-Juan Liu, Chuang-Tian Chen, and Zu-Yan Xu (2018). "High-energy single-frequency 167 nm deep-ultraviolet laser." *Optics Letters* 43.11, p. 2563 (cit. on p. 21).

Lisdat, C., G. Grosche, N. Quintin, C. Shi, S. M. F. Raupach, C. Grebing, D. Nicolodi, F. Stefani, A. Al-Masoudi, S. Dörscher, S. Häfner, J.-L. Robyr, N. Chiodo, S. Bilicki, E. Bookjans, et al. (2016). "A clock network for geodesy and fundamental science." *Nature Communications* 7, p. 12443 (cit. on p. 4).

Lisdat, Ch., S. Dörscher, I. Nosske, and U. Sterr (2021). "Blackbody radiation shift in strontium lattice clocks revisited." *Physical Review Research* 3.4. Publisher: American Physical Society, p. L042036 (cit. on p. 175).

Liu, Hongli, Wenhao Yuan, Feihu Cheng, Zhiyuan Wang, Zetian Xu, Ke Deng, and Zehuang Lu (2018). "Ultraviolet laser spectroscopy of aluminum atoms in hollow-cathode lamp." *Journal of Physics B: Atomic, Molecular and Optical Physics* 51.22, p. 225002 (cit. on p. 61).

Lodewyck, Jérôme (2019). "On a definition of the SI second with a set of optical clock transitions." *Metrologia* 56.5, p. 055009 (cit. on p. 12).

Lodewyck, Jérôme, S{\textbackslash}lawomir Bilicki, Eva Bookjans, Jean-Luc Robyr, Chunyan Shi, Grégoire Vallet, Rodolphe Le Targat, Daniele Nicolodi, Yann Le Coq, Jocelyne Guéna, Michel Abgrall, Peter Rosenbusch, and Sébastien Bize (2016). "Optical to microwave clock frequency ratios with a nearly continuous strontium optical lattice clock." *Metrologia* 53.4. Publisher: IOP Publishing, pp. 1123–1130 (cit. on p. 15).

Ludlow, A. D., X. Huang, M. Notcutt, T. Zanon-Willette, S. M. Foreman, M. M. Boyd, S. Blatt, and J. Ye (2007). "Compact, thermal-noise-limited optical cavity for diode laser stabilization at 1×10−15." *Opt. Lett.* 32.6, pp. 641–643 (cit. on p. 16).

Ludlow, Andrew D., Martin M. Boyd, Jun Ye, E. Peik, and P.O. Schmidt (2015). "Optical atomic clocks." *Reviews of Modern Physics* 87.2, pp. 637–701 (cit. on pp. 14, 16, 28, 34, 124, 137).

Mai, Enrico (2013). *Time, Atomic Clocks, and Relativistic Geodesy*. 124. München: Deutsche Geodätische Kommission bei der Bayerischen Akademie der Wissenschaften (cit. on p. 4).

Martin, W. C. and Romuald Zalubas (1979). "Energy levels of aluminum, Al I through Al XIII." *Journal of Physical and Chemical Reference Data* 8.3, pp. 817–864. eprint: `https://doi.org/10.1063/1.555608` (cit. on p. 20).

Matei, D.G., T. Legero, S. Häfner, C. Grebing, R. Weyrich, W. Zhang, L. Sonderhouse, J.M. Robinson, J. Ye, F. Riehle, and U. Sterr (2017). "1.5 μm Lasers with Sub-10 mHz Linewidth." *Physical Review Letters* 118.26, p. 263202 (cit. on pp. 5, 16, 72, 173).

McGrew, W. F., X. Zhang, R. J. Fasano, S. A. Schäffer, K. Beloy, D. Nicolodi, R. C. Brown, N. Hinkley, G. Milani, M. Schioppo, T. H. Yoon, and A. D. Ludlow (2018). "Atomic clock performance enabling geodesy below the centimetre level." *Nature* 564.7734, p. 87 (cit. on pp. 12, 15).

Mehlstäubler, Tanja E., Gesine Grosche, Christian Lisdat, Piet O. Schmidt, and Heiner Denker (2018). "Atomic clocks for geodesy." *Reports on Progress in Physics* 81.6, p. 064401 (cit. on pp. ix, xi, 4, 12, 13, 16, 164).

Meir, Ziv, Tomas Sikorsky, Ruti Ben-shlomi, Nitzan Akerman, Meirav Pinkas, Yehonatan Dallal, and Roee Ozeri (2018). "Experimental apparatus for overlapping a ground-state cooled ion with ultracold atoms." *Journal of Modern Optics* 65.5, pp. 501–519 (cit. on p. 167).

Meiser, D., Jun Ye, D. Carlson, and M. Holland (2009). "Prospects for a Millihertz-Linewidth Laser." *Physical Review Letters* 102.16, p. 163601 (cit. on p. 16).

Metrology (JCGM/WG 1), Working Group 1 of the Joint Committee for Guides in (2008). *Evaluation of measurement data - Guide to the expression of uncertainty in measurement (GUM)* (cit. on pp. 9, 108, 161).

Micke, P., T. Leopold, S. A. King, E. Benkler, L. J. Spieß, L. Schmöger, M. Schwarz, J. R. Crespo López-Urrutia, and P. O. Schmidt (2020). "Coherent laser spectroscopy of highly charged ions using quantum logic." *Nature* 578.7793, pp. 60–65 (cit. on p. 15).

Mølhave, K. and M. Drewsen (2000). "Formation of translationally cold MgH^+ and MgD^+ molecules in an ion trap." *Phys. Rev. A* 62 (1), p. 011401 (cit. on p. 44).

Monroe, C., D. M. Meekhof, B. E. King, S. R. Jefferts, W. M. Itano, D. J. Wineland, and P. Gould (1995). "Resolved-sideband Raman cooling of a bound atom to the 3D zero-point energy." *Physical Review Letters* 75.22, pp. 4011–4014 (cit. on p. 38).

Monroe, Ch. (2011). "Demolishing quantum nondemolition." *Physics Today* 64 (1), p. 8 (cit. on p. 130).

Monz, Thomas (2011). "Quantum information processing beyond ten ion-qubits." PhD thesis. Institut fuer Experimentalphysik der Universitaet Innsbruck, Otto Hittmair-Platz 1, 6020 Innsbruck, Austria: Leopold-Franzens-Universitaet Innsbruck (cit. on pp. 100, 104, 105, 174).

Morigi, G., J. Eschner, and C. H Keitel (2000). "Ground state laser cooling using electromagnetically induced transparency." *Physical Review Letters* 85.21, pp. 4458–4461 (cit. on p. 39).

Morigi, Giovanna (2003). "Cooling atomic motion with quantum interference." *Physical Review A* 67.3, p. 033402 (cit. on p. 39).

Müller, B. and Ch. Ottinger (1986). "Chemiluminescent reactions of second-row atomic ions. I. $Al^+ + H_2 \rightarrow AlH^+$ ($A\,^2\Pi$, $B\,^2\Sigma^+$)+H." *The Journal of Chemical Physics* 85.1, p. 232 (cit. on p. 93).

Nemitz, Nils, Takuya Ohkubo, Masao Takamoto, Ichiro Ushijima, Manoj Das, Noriaki Ohmae, and Hidetoshi Katori (2016). "Frequency ratio of Yb and Sr clocks with 5×10^{-17} uncertainty at 150 seconds averaging time." *Nature Photonics* 10.4, pp. 258–261 (cit. on p. 15).

Network, Boulder Atomic Clock Optical, Collaboration, Kyle Beloy, Martha I. Bodine, Tobias Bothwell, Samuel M. Brewer, Sarah L. Bromley, Jwo-Sy Chen, Jean-Daniel Deschenes, Scott A. Diddams, Robert J. Fasano, Tara M. Fortier, Youssef S. Hassan, David B. Hume, Dhruv Kedar, et al. (2021). "Frequency Ratio Measurements with 18-digit Accuracy Using a Network of Optical Clocks." *Nature* 591, pp. 564–569 (cit. on p. 12).

Newville, Matt, Renee Otten, Andrew Nelson, Antonino Ingargiola, Till Stensitzki, Dan Allan, Austin Fox, Faustin Carter, Michał, Ray Osborn, Dima Pustakhod, lneuhaus, Sebastian Weigand, Glenn, Christoph Deil, et al. (2021). *lmfit/lmfit-py: 1.0.3*. Version 1.0.3 (cit. on p. 161).

Norcia, Matthew A., Matthew N. Winchester, Julia R. K. Cline, and James K. Thompson (2016). "Superradiance on the millihertz linewidth strontium clock transition." *Science Advances* 2.10, e1601231 (cit. on p. 17).

Oates, Christopher W. and Andrew D. Ludlow (2015). “Optical Lattice Clocks.” *Optics and Photonics News* 26.1, pp. 36–43 (cit. on p. 15).

Oelker, E., R. B. Hutson, C. J. Kennedy, L. Sonderhouse, T. Bothwell, A. Goban, D. Kedar, C. Sanner, J. M. Robinson, G. E. Marti, D. G. Matei, T. Legero, M. Giunta, R. Holzwarth, F. Riehle, U. Sterr, and J. Ye (2019). “Demonstration of 4.8×10^{-17} stability at 1 s for two independent optical clocks.” *Nature Photonics*, pp. 1–6 (cit. on pp. 10, 16).

Ohmae, Noriaki, Masao Takamoto, Yosuke Takahashi, Motohide Kokubun, Kuniya Araki, Andrew Hinton, Ichiro Ushijima, Takashi Muramatsu, Tetsuo Furumiya, Yuya Sakai, Naoji Moriya, Naohiro Kamiya, Kazuaki Fujii, Ryuya Muramatsu, Toshihiro Shiimado, and Hidetoshi Katori (2021). “Transportable Strontium Optical Lattice Clocks Operated Outside Laboratory at the Level of 10^{-18} Uncertainty.” *Advanced Quantum Technologies* 2021 (n/a). _eprint: https://onlinelibrary.wiley.com/doi/pdf/10.1002/qute.202100015, p. 2100015 (cit. on p. 15).

Ohtsubo, Nozomi, Ying Li, Nils Nemitz, Hidekazu Hachisu, Kensuke Matsubara, Tetsuya Ido, and Kazuhiro Hayasaka (2020). “Frequency ratio of an $^{115}\mathrm{In}^{+}$ ion clock and a $^{87}\mathrm{Sr}$ optical lattice clock.” *Optics Letters* 45.21. Publisher: Optical Society of America, pp. 5950–5953 (cit. on p. 14).

Paul, Wolfgang (1990). “Electromagnetic traps for charged and neutral particles.” *Rev. Mod. Phys.* 62 (3), pp. 531–540 (cit. on p. 23).

Paul, Wolfgang and Helmut Steinwedel (1953). “Ein Neues Massenspektrometer Ohne Magnetfeld.” *Zeitschrift Naturforschung Teil A* 8, p. 448 (cit. on p. 22).

Pedrozo-Peñafiel, Edwin, Simone Colombo, Chi Shu, Albert F. Adiyatullin, Zeyang Li, Enrique Mendez, Boris Braverman, Akio Kawasaki, Daisuke Akamatsu, Yanhong Xiao, and Vladan Vuletić (2020). “Entanglement on an optical atomic-clock transition.” *Nature* 588.7838. Number: 7838 Publisher: Nature Publishing Group, pp. 414–418 (cit. on pp. 11, 16).

Peik, E., T. Schumm, M. S. Safronova, A. Pálffy, J. Weitenberg, and P. G. Thirolf (2021). “Nuclear clocks for testing fundamental physics.” *Quantum Science and Technology* 6.3. Publisher: IOP Publishing, p. 034002 (cit. on p. 15).

Peik, E and Chr Tamm (2003). “Nuclear laser spectroscopy of the 3.5 eV transition in Th-229.” *Europhysics Letters (EPL)* 61.2, pp. 181–186 (cit. on p. 15).

Peik, Ekkehard, Tobias Schneider, and Christian Tamm (2006). “Laser frequency stabilization to a single ion.” *Journal of Physics B: Atomic, Molecular and Optical Physics* 39.1, pp. 145–158 (cit. on pp. 176, 181, 182).

Pelucchi, Emanuele, Giorgos Fagas, Igor Aharonovich, Dirk Englund, Eden Figueroa, Qihuang Gong, Hübel Hannes, Jin Liu, Chao-Yang Lu, Nobuyuki Matsuda, Jian-Wei Pan, Florian Schreck, Fabio Sciarrino, Christine Silberhorn, Jianwei Wang, and Klaus D. Jöns (2021). “The potential and global outlook of integrated photonics for quantum technologies.” *Nature Reviews Physics*. Publisher: Nature Publishing Group, pp. 1–15 (cit. on p. 11).

Pelzer, L., K. Dietze, J. Kramer, F. Dawel, L. Krinner, N. Spethmann, V. Martinez, N. Aharon, A. Retzker, K. Hammerer, and P. O. Schmidt (2021). “Tailored optical clock transition in $^{40}\mathrm{Ca}^{+}$.” *Measurement: Sensors* 18, p. 100326 (cit. on pp. 16, 175).

Pham, Paul Tan The (2005). “A general-purpose pulse sequencer for quantum computing.” PhD thesis. Cambridge, Massachusetts, USA: Massachusetts Institute of Technology (cit. on p. 65).

Poli, N., C. W. Oates, P. Gill, and G. M. Tino (2013). “Optical atomic clocks.” *Riv. Nuovo Cimento* 36.12, pp. 555–624 (cit. on p. 34).

Poli, N., M. Schioppo, S. Vogt, St Falke, U. Sterr, Ch Lisdat, and G. M. Tino (2014). “A transportable strontium optical lattice clock.” *Applied Physics B*, pp. 1–10 (cit. on p. 15).

Porsev, S. G., V. V. Flambaum, E. Peik, and Chr. Tamm (2010). “Excitation of the Isomeric $^{229\mathrm{m}}$Th Nuclear State via an Electronic Bridge Process in ^{229}Th^{+}.” *Physical Review Letters* 105.18, p. 182501 (cit. on p. 16).

Pound, R. V. and G. A. Rebka Jr (1959). “Gravitational red-shift in nuclear resonance.” *Physical Review Letters* 3.9, pp. 439–441 (cit. on p. 4).

Predehl, K., G. Grosche, S. M. F Raupach, S. Droste, O. Terra, J. Alnis, Th Legero, T. W Hänsch, Th Udem, R. Holzwarth, and H. Schnatz (2012). “A 920-Kilometer Optical Fiber Link for Frequency Metrology at the 19th Decimal Place.” *Science* 336.6080, pp. 441–444 (cit. on pp. x, xii).

Pyka, Karsten, Norbert Herschbach, Jonas Keller, and Tanja E. Mehlstäubler (2014). “A high-precision segmented Paul trap with minimized micromotion for an optical multiple-ion clock.” *Applied Physics B* 114.1, pp. 231–241 (cit. on p. 24).

Quessada, Audrey, Richard P Kovacich, Ir ne Courtillot, Andr Clairon, Giorgio Santarelli, and Pierre Lemonde (2003). “The Dick effect for an optical frequency standard.” *Journal of Optics B: Quantum and Semiclassical Optics* 5.2, S150–S154 (cit. on p. 34).

Ralph, T. C., S. D. Bartlett, J. L. O’Brien, G. J. Pryde, and H. M. Wiseman (2006). “Quantum nondemolition measurements for quantum information.” *Phys. Rev. A* 73 (1), p. 012113 (cit. on p. 131).

Ramsey, Norman F. (1990). “Experiments with separated oscillatory fields and hydrogen masers.” *Reviews of Modern Physics* 62.3, pp. 541–552 (cit. on p. 30).

Rasmusson, A. J., Marissa D’Onofrio, Yuanheng Xie, Jiafeng Cui, and Philip Richerme (2021). “Optimized pulsed sideband cooling and enhanced thermometry of trapped ions.” *Phys. Rev. A* 104 (4), p. 043108 (cit. on pp. 36, 38, 109, 110, 125, 146, 173).

Rath, Robert (1960). “Kompensatoren.” *Abhandlungen der Braunschweigischen Wissenschatlichen Gesellschaft* 12, pp. 116–123 (cit. on p. 112).

Raupach, S. M. F., A. Koczwara, and G. Grosche (2014). “Optical frequency transfer via a 660 km underground fiber link using a remote Brillouin amplifier.” *Optics Express* 22.22, pp. 26537–26547 (cit. on pp. x, xii).

Rellergert, Wade G., D. DeMille, R. R. Greco, M. P. Hehlen, J. R. Torgerson, and Eric R. Hudson (2010). “Constraining the Evolution of the Fundamental Constants with a Solid-State Optical Frequency Reference Based on the ^{229}Th Nucleus.” *Phys. Rev. Lett.* 104 (20), p. 200802 (cit. on p. 15).

Riebe, M. (2005). “Preparation of entangled states and quantum teleportation with atomic qubits.” PhD thesis. University of Innsbruck (cit. on p. 104).

Riehle, Fritz (2004). *Frequency Standards: Basics and Applications*. 1st ed. Weinheim, Germany: WILEY-VCH Veralg GmbH & Co. KGaA (cit. on pp. 4, 5, 9, 10, 30, 99, 181, 182).

– (2015). “Towards a redefinition of the second based on optical atomic clocks.” *Comptes Rendus Physique*. The measurement of time / La mesure du temps 16.5, pp. 506–515 (cit. on pp. ix, xi, 11, 12).

Riehle, Fritz, Patrick Gill, Felicitas Arias, and Lennart Robertsson (2018). “The CIPM list of recommended frequency standard values: guidelines and procedures.” *Metrologia* 55.2, pp. 188–200 (cit. on p. 12).

Robinson, John M., Eric Oelker, William R. Milner, Wei Zhang, Thomas Legero, Dan G. Matei, Fritz Riehle, Uwe Sterr, and Jun Ye (2019). “Crystalline optical cavity at 4 K with thermal-noise-limited instability and ultralow drift.” *Optica* 6.2, pp. 240–243 (cit. on p. 30).

Roos, C. F., M. Chwalla, K. Kim, M. Riebe, and R. Blatt (2006). “‘Designer atoms’ for quantum metrology.” *Nature* 443.7109, pp. 316–319 (cit. on p. 16).

Roos, C. F., D. Leibfried, A. Mundt, F. Schmidt-Kaler, J. Eschner, and R. Blatt (2000). “Experimental demonstration of ground state laser cooling with electromagnetically induced transparency.” *Physical Review Letters* 85.26, pp. 5547–5550 (cit. on p. 39).

Roos, Ch., Th. Zeiger, H. Rohde, H. C. Nägerl, J. Eschner, D. Leibfried, F. Schmidt-Kaler, and R. Blatt (1999). “Quantum State Engineering on an Optical Transition and Decoherence in a Paul Trap.” *Physical Review Letters* 83.23, pp. 4713–4716 (cit. on p. 38).

Rosenband, T., D. B. Hume, P. O. Schmidt, C. W. Chou, A. Brusch, L. Lorini, W. H. Oskay, R. E. Drullinger, T. M. Fortier, J. E. Stalnaker, S. A. Diddams, W. C. Swann, N. R. Newbury, W. M. Itano, D. J. Wineland, and J. C. Bergquist (2008). “Frequency Ratio of Al^+ and Hg^+ Single-Ion Optical Clocks; Metrology at the 17th Decimal Place.” *Science* 319.5871, pp. 1808–1812. eprint: `https://science.sciencemag.org/content/319/5871/1808.full.pdf` (cit. on pp. 13, 14, 94, 149, 175).

Rosenband, T., W. M Itano, P. O Schmidt, D. B Hume, J. C. J Koelemeij, J. C Bergquist, and D. J Wineland (2006). “Blackbody radiation shift of the $^{27}Al^+$ $^1S_0$ - $^3P_0$ transition.” *Proceedings of the 20th European Frequency and Time Forum*. EFTF. Braunschweig, Germany, pp. 289–291 (cit. on p. 148).

Rosenband, T., P. O. Schmidt, D. B. Hume, W. M. Itano, T. M. Fortier, J. E. Stalnaker, K. Kim, S. A. Diddams, J. C. J. Koelemeij, J. C. Bergquist, and D. J. Wineland (2007). “Observation of the $^1S_0$ –> $^3P_0$ Clock Transition in $^{27}Al^+$.” *Physical Review Letters* 98.22, p. 220801 (cit. on pp. 20–22, 44, 119, 151).

Rubiola, E. (2005). “On the measurement of frequency and of its sample variance with high-resolution counters.” *Review of scientific instruments* 76.5, pp. 054703–054703 (cit. on p. 88).

Rugango, R., J. E. Goeders, T. H. Dixon, J. M. Gray, N. B. Khanyile, G. Shu, R. J. Clark, and K. R. Brown (2015). “Sympathetic cooling of molecular ion motion to the ground state.” *New Journal of Physics* 17.3, p. 035009 (cit. on p. 44).

Ruster, T., C. T. Schmiegelow, H. Kaufmann, C. Warschburger, F. Schmidt-Kaler, and U. G. Poschinger (2016). “A long-lived Zeeman trapped-ion qubit.” *Applied Physics B* 122.10 (cit. on pp. 99, 100, 104, 106, 174, 175).

Rutman, J. (1978). “Characterization of phase and frequency instabilities in precision frequency sources: Fifteen years of progress.” *Proceedings of the IEEE* 66.9, pp. 1048–1075 (cit. on p. 10).

Safronova, M. S., M. G. Kozlov, and Charles W. Clark (2011). “Precision Calculation of Blackbody Radiation Shifts for Optical Frequency Metrology.” *Phys. Rev. Lett.* 107 (14), p. 143006 (cit. on pp. 21, 148).

Safronova, M.S., D. Budker, D. DeMille, Derek F. Jackson Kimball, A. Derevianko, and Charles W. Clark (2018). “Search for new physics with atoms and molecules.” *Reviews of Modern Physics* 90.2, p. 025008 (cit. on p. 14).

Sandberg, John Carl (1993). “Research toward laser spectroscopy of trapped atomic hydrogen.” PhD Thesis. Cambridge: Massachusetts Institute of Technology, Department of Physics (cit. on p. 70).

Sanner, Christian, Nils Huntemann, Richard Lange, Christian Tamm, and Ekkehard Peik (2018). “Autobalanced Ramsey Spectroscopy.” *Physical Review Letters* 120.5, p. 053602 (cit. on p. 31).

Sanner, Christian, Nils Huntemann, Richard Lange, Christian Tamm, Ekkehard Peik, Marianna S. Safronova, and Sergey G. Porsev (2019). “Optical clock comparison for Lorentz symmetry testing.” *Nature* 567.7747, pp. 204–208 (cit. on p. 13).

Santarelli, G., C. Audoin, A. Makdissi, P. Laurent, G.J. Dick, and A. Clairon (1998). “Frequency stability degradation of an oscillator slaved to a periodically interrogated atomic resonator.” *IEEE Transactions on Ultrasonics, Ferroelectrics and Frequency Control* 45.4, pp. 887–894 (cit. on p. 10).

Savage, Albert and Robert C. Miller (1962). “Measurements of Second Harmonic Generation of the Ruby Laser Line in Piezoelectric Crystals.” *Appl. Opt.* 1.5, pp. 661–664 (cit. on p. 6).

Schäffer, Stefan A., Mikkel Tang, Martin R. Henriksen, Asbjørn A. Jørgensen, Bjarke T. R. Christensen, and Jan W. Thomsen (2020). “Lasing on a narrow transition in a cold thermal strontium ensemble.” *Phys. Rev. A* 101 (1), p. 013819 (cit. on p. 17).

Scharnhorst, Nils (2018). “Multi-mode ground state cooling of trapped ions.” PhD thesis. Leibniz Universität Hannover (cit. on pp. ix, xii, 38, 40, 143, 145, 165).

Scharnhorst, Nils, Javier Cerrillo, Johannes Kramer, Ian D. Leroux, Jannes B. Wübbena, Alex Retzker, and Piet O. Schmidt (2018). “Experimental and theoretical investigation of a multimode cooling scheme using multiple electromagnetically-induced-transparency resonances.” *Physical Review A* 98.2, p. 023424 (cit. on pp. 38–40, 77).

Scharnhorst, Nils, Jannes B. Wübbena, Stephan Hannig, Kornelius Jakobsen, Johannes Kramer, Ian D. Leroux, and Piet O. Schmidt (2015). “High-bandwidth transfer of phase stability through a fiber frequency comb.” *Optics Express* 23.15, pp. 19771–19776 (cit. on pp. 40, 72, 74, 171).

Schindler, Philipp (2008). “Frequency synthesis and pulse shaping for quantum information processing with trapped ions.” Diploma Thesis. Innsbruck, Austria: University of Innsbruck (cit. on p. 65).

Schioppo, M., R. C. Brown, W. F. McGrew, N. Hinkley, R. J. Fasano, K. Beloy, T. H. Yoon, G. Milani, D. Nicolodi, J. A. Sherman, N. B. Phillips, C. W. Oates, and A. D. Ludlow (2017). “Ultrastable optical clock with two cold-atom ensembles.” *Nature Photonics* 11.1, pp. 48–52 (cit. on pp. 11, 16).

Schioppo, M., J. Kronjäger, A. Silva, R. Ilieva, J. W. Paterson, C. F. A. Baynham, W. Bowden, I. R. Hill, R. Hobson, A. Vianello, M. Dovale-Álvarez, R. A. Williams, G. Marra, H. S. Margolis, A. Amy-Klein, et al. (2022). “Comparing ultrastable lasers at 7×10^{-17} fractional frequency instability through a 2220 km optical fibre network.” *Nature Communications* 13.1. Number: 1 Publisher: Nature Publishing Group, p. 212 (cit. on p. 14).

Schmidt, P. O., T. Rosenband, C. Langer, W. M. Itano, J. C. Bergquist, and D. J. Wineland (2005). “Spectroscopy Using Quantum Logic.” *Science* 309.5735, pp. 749–752 (cit. on pp. 22, 31, 34, 37, 117).

Schnatz, H., B. Lipphardt, J. Helmcke, F. Riehle, and G. Zinner (1996). "First Phase-Coherent Frequency Measurement of Visible Radiation." *Phys. Rev. Lett.* 76 (1), pp. 18–21 (cit. on p. 6).

Scholz, Matthias, Dmitrijs Opalevs, Patrick Leisching, Wilhelm Kaenders, Guiling Wang, Xiaoyang Wang, Rukang Li, and Chuangtian Chen (2012). "1.3-mW tunable and narrow-band continuous-wave light source at 191 nm." *Opt. Express* 20.17, pp. 18659–18664 (cit. on p. 21).

Schulte, Marius, Christian Lisdat, Piet O. Schmidt, Uwe Sterr, and Klemens Hammerer (2020). "Prospects and challenges for squeezing-enhanced optical atomic clocks." *Nature Communications* 11.1. Number: 1 Publisher: Nature Publishing Group, p. 5955 (cit. on pp. 11, 16).

Schwabl, F. and W.D. Brewer (2006). *Statistical Mechanics*. Advanced Texts in Physics. Springer Berlin Heidelberg (cit. on p. 126).

Schwarz, R., S. Dörscher, A. Al-Masoudi, E. Benkler, T. Legero, U. Sterr, S. Weyers, J. Rahm, B. Lipphardt, and C. Lisdat (2020). "Long term measurement of the ^{87}Sr clock frequency at the limit of primary Cs clocks." *Physical Review Research* 2.3. Publisher: American Physical Society, p. 033242 (cit. on p. 175).

Schwarz, Roman, Sören Dörscher, Ali Al-Masoudi, Stefan Vogt, Ye Li, and Christian Lisdat (2019). "A compact and robust cooling laser system for an optical strontium lattice clock." *Review of Scientific Instruments* 90.2, p. 023109 (cit. on p. 11).

Seck, Christopher M., Edward G. Hohenstein, Chien-Yu Lien, Patrick R. Stollenwerk, and Brian C. Odom (2014). "Rotational state analysis of AlH$^+$ by two-photon dissociation." *Journal of Molecular Spectroscopy*. Spectroscopic Tests of Fundamental Physics 300, pp. 108–111 (cit. on p. 93).

Seiferle, Benedict, Lars von der Wense, Pavlo V. Bilous, Ines Amersdorffer, Christoph Lemell, Florian Libisch, Simon Stellmer, Thorsten Schumm, Christoph E. Düllmann, Adriana Pálffy, and Peter G. Thirolf (2019). "Energy of the ^{229}Th nuclear clock transition." *Nature* 573.7773, pp. 243–246 (cit. on p. 15).

Shaniv, R., N. Akerman, and R. Ozeri (2016). "Atomic Quadrupole Moment Measurement Using Dynamic Decoupling." *Physical Review Letters* 116.14, p. 140801 (cit. on p. 16).

Sheridan, K. (2009). "Photoionization of Calcium." Master Thesis. University of Sussex (cit. on p. 61).

Shi, C., F. Gebert, C. Gorges, S. Kaufmann, W. Nörtershäuser, B. K. Sahoo, A. Surzhykov, V. A. Yerokhin, J. C. Berengut, F. Wolf, J. C. Heip, and P. O. Schmidt (2017). "Unexpectedly large difference of the electron density at the nucleus in the $4p^2P_{1/2,3/2}$ fine-structure doublet of Ca$^+$." *Applied Physics B* 123.1, p. 2 (cit. on p. 22).

Siverns, J. D., L. R. Simkins, S. Weidt, and W. K. Hensinger (2012). "On the application of radio frequency voltages to ion traps via helical resonators." *Applied Physics B* 107.4, pp. 921–934 (cit. on p. 52).

Splatt, Felicity Erin (2009). "Development and Operation of Miniaturised Ion Traps for Scalable Quantum Computation." PhD thesis. Institut fuer Experimentalphysik der Universitaet Innsbruck, Otto Hittmair-Platz 1, 6020 Innsbruck, Austria: Leopold-Franzens-Universitaet Innsbruck (cit. on p. 206).

Stadnik, Yevgeny V. (2017). *Manifestations of Dark Matter and Variations of the Fundamental Constants in Atoms and Astrophysical Phenomena*. Springer Theses. Cham: Springer International Publishing (cit. on pp. ix, xi, 13).

Steck, Daniel. A. (2022). *Quantum and Atom Optics*. [Online; revision 0.13.11, 7 April 2022] (cit. on pp. 39, 40).

Stenger, Jörn, Harald Schnatz, Christian Tamm, and Harald Telle (2002). "Ultraprecise Measurement of Optical Frequency Ratios." *Physical Review Letters* 88.7, p. 073601 (cit. on pp. 72, 73).

Stuhler, J., M. Abdel Hafiz, B. Arar, A. Bawamia, K. Bergner, M. Biethahn, S. Brakhane, A. Didier, J. Fortágh, M. Halder, R. Holzwarth, N. Huntemann, M. Johanning, R. Jördens, W. Kaenders, et al. (2021). "Opticlock: Transportable and easy-to-operate optical single-ion clock." *Measurement: Sensors* 18, p. 100264 (cit. on p. 11).

Takamoto, M. and H. Katori (2003). "Spectroscopy of the ${}^1S_0$-${}^3P_0$ Clock Transition of ^{87}Sr in an Optical Lattice." *Physical review letters* 91.22, p. 223001 (cit. on p. 15).

Takamoto, Masao, Tetsushi Takano, and Hidetoshi Katori (2011). "Frequency comparison of optical lattice clocks beyond the Dick limit." *Nat Photon* 5.5, pp. 288–292 (cit. on p. 16).

Takamoto, Masao, Ichiro Ushijima, Noriaki Ohmae, Toshihiro Yahagi, Kensuke Kokado, Hisaaki Shinkai, and Hidetoshi Katori (2020). "Test of general relativity by a pair of transportable optical lattice clocks." *Nature Photonics* 14. Publisher: Nature Publishing Group, pp. 411–415 (cit. on p. 164).

Terra, O., G. Grosche, and H. Schnatz (2010). "Brillouin amplification in phase coherent transfer of optical frequencies over 480 km fiber." *Opt. Express* 18.15, pp. 16102–16111 (cit. on p. 74).

Tommaseo, G., T. Pfeil, G. Revalde, G. Werth, P. Indelicato, and J. P. Desclaux (2003). "The g_J-factor in the ground state of Ca^+." *The European Physical Journal D - Atomic, Molecular, Optical and Plasma Physics* 25.2, pp. 113–121 (cit. on pp. 22, 157).

Träbert, E, A Wolf, J Linkemann, and X Tordoir (1999). "Measurement of the $B^+$and Al^+intercombination and Sc^{12+}forbidden transition rates at a heavy-ion storage ring." *Journal of Physics B: Atomic, Molecular and Optical Physics* 32.2, pp. 537–552 (cit. on p. 20).

Versolato, O. O., L. W. Wansbeek, K. Jungmann, R. G. E. Timmermans, L. Willmann, and H. W. Wilschut (2011). "Potential of electric quadrupole transitions in radium isotopes for single-ion optical frequency standards." *Phys. Rev. A* 83 (4), p. 043829 (cit. on p. 14).

Wan, Yong, Florian Gebert, Fabian Wolf, and Piet O. Schmidt (2015). "Efficient sympathetic motional-ground-state cooling of a molecular ion." *Physical Review A* 91.4, p. 043425 (cit. on pp. 38, 44).

Wan, Yong, Florian Gebert, Jannes B. Wübbena, Nils Scharnhorst, Sana Amairi, Ian D. Leroux, Börge Hemmerling, Niels Lörch, Klemens Hammerer, and Piet O. Schmidt (2014). "Precision spectroscopy by photon-recoil signal amplification." *Nature Communications* 5, p. 4096 (cit. on p. 22).

Wcisło, P., P. Ablewski, K. Beloy, S. Bilicki, M. Bober, R. Brown, R. Fasano, R. Ciuryło, H. Hachisu, T. Ido, J. Lodewyck, A. Ludlow, W. McGrew, P. Morzyński, D. Nicolodi, et al. (2018). "New bounds on dark matter coupling from a global network of optical atomic clocks." *Science Advances* 4.12, eaau4869 (cit. on p. 13).

Wineland, D. J., J. J. Bollinger, W. M. Itano, F. L. Moore, and D. J. Heinzen (1992). "Spin squeezing and reduced quantum noise in spectroscopy." *Physical Review A* 46.11, R6797–6800 (cit. on pp. 11, 16).

Wineland, D. J., W. M Itano, J. C. Bergquist, and R. G Hulet (1987). "Laser-cooling limits and single-ion spectroscopy." *Physical Review A* 36.5, pp. 2220–2232 (cit. on p. 38).

Wineland, D. J. and Wayne M. Itano (1979). “Laser cooling of atoms.” *Physical Review A* 20.4, p. 1521 (cit. on p. 38).

Wineland, D. J., C. Monroe, W. M. Itano, D. Leibfried, B. E. King, and D. M. Meekhof (1998). “Experimental issues in coherent quantum-state manipulation of trapped atomic ions.” *Journal of Research of the National Institute of Standards and Technology* 103.3, pp. 259–328 (cit. on pp. 27, 31–33, 99, 107).

Wübbena, Jannes B. (2011). “Photoionisation von Calcium.” Diploma Thesis. Leibniz University Hannover (cit. on pp. 61, 69, 77).

Wübbena, Jannes B., Sana Amairi, Olaf Mandel, and Piet O. Schmidt (2012). “Sympathetic cooling of mixed-species two-ion crystals for precision spectroscopy.” *Physical Review A* 85.4, p. 043412 (cit. on pp. 22, 35, 42–45, 93, 145, 146, 207).

Wübbena, Jannes (2014). “Controlling Motion in Quantum Logic Clocks.” PhD thesis. Institut fuer Quantenoptik der Leibniz Universität Hannover, Welfengarten 1, 30167 Hannover, Germany: Leibniz Universität Hannover (cit. on pp. 49, 51, 53, 56, 57, 66, 69).

Yamanaka, Kazuhiro, Noriaki Ohmae, Ichiro Ushijima, Masao Takamoto, and Hidetoshi Katori (2015). “Frequency Ratio of ^{1}99Hg and ^{87}Sr Optical Lattice Clocks beyond the SI Limit.” *Physical Review Letters* 114.23, p. 230801 (cit. on p. 15).

Yudin, V. I., A. V. Taichenachev, C. W. Oates, Z. W. Barber, N. D. Lemke, A. D. Ludlow, U. Sterr, Ch. Lisdat, and F. Riehle (2010). “Hyper-Ramsey spectroscopy of optical clock transitions.” *Physical Review A* 82.1, p. 011804 (cit. on p. 31).

Zimmermann, K., M. V. Okhapkin, O. A. Herrera-Sancho, and E. Peik (2012). “Laser ablation loading of a radiofrequency ion trap.” *Applied Physics B* 107.4, pp. 883–889 (cit. on p. 59).

I will take love wherever I find it and offer it to everyone who will take it...,
seek knowledge from those wiser than me and try to teach those who wish to learn from me.
— Duane Allman

Acknowledgments/Danksagung

Während meiner Zeit als Doktorand habe ich viele Menschen kennen gelernt, die mir den Weg erleichtert und oftmals erst in die richtige Richtung gewiesen haben.

Vielen Dank zuerst an Prof. Piet Schmidt, der zu jeder Frage eine Antwort und mit ganzem Herzen am Fortschritt des Experiments und meiner selbst gewirkt hat. Vielen Dank an die Mitglieder der Prüfungskomission PD Dr. Ekkehard Peik und Dr. Christian Roos, die einen Teil ihrer wertvollen Zeit darauf verwendet haben, meine Arbeit zu lesen und zu begutachten.

Vielen Dank an die gesamte Abteilung 4, insbesondere Erik Benkler, der sich um die Pflege und Bereitstellung des MNPQ Lasers kümmerte und an Thomas Legero, der beim Aufbau der Logikcavity eine große Hilfe war.

Vielen Dank an Miroslav Doležal, der unermüdlich mit mir die Resultate der Simulationen diskutierte, die er für uns anfertigte.

Vielen Dank an Sandra Ludwig, Birgit Ohlendorf und Sina Bußmann, die mir bei so mancher verwaltungstechnischer Spitzfindigkeit zur Hand gingen.

Aus meiner Anfangszeit möchte ich vor allem Nils Scharnhorst, Ian Leroux und Kornelius Jakobsen erwähnen, die mich in ihrem Team aufnahmen und mir das Experiment erklärten. Cornelius, Ruhe in Frieden da oben. Stephan Hannig war mir ein guter Mentor. Ebenfalls vielen Dank an Nicolai Beev, der die erste Version unserer Magnetfeldstabilisierung designte, und die, vielen Dank, Tjeerd Pinkert vollendete. Vielen Dank Nicolas Spethmann, während deiner Zeit und durch deinen frischen Pragmatismus im Labor haben wir viel erreicht. Vielen Dank Lennart Pelzer, niemand hat einen größeren auf Mainz basierenden Erfahrungsschatz mit nützlichen Informationen allenthalben. Vielen Dank Fabian Wolf für die vielen Diskussionen. Vielen Dank Kai Dietze, du hast mir viel Wissen über Helical Resonatoren und Nordseekrabben vermittelt.

Vielen Dank an meinen guten Freund Tobias Leopold, die Jahre mit dir am Institut waren durchdrungen von Freude und Witz, und an meine Freunde Steven King und Peter Micke. Ohne Stevens gelegentliche Auftritte im Labor und mit wenigen Handgriffen gelösten Problemen würde ich noch immer im Labor sitzen. Peter, Dankeschön für deine Hilfe, insbesondere bei den heiklen Vakuumarbeiten. Dein penibles Auge war Gold wert.

Vielen Dank an die Mitglieder des mittwöchlichem Stargateabends Julia Buschermöhle, Ludwig Krinner, Marek Hild, Maximilian Zawierucha und Fabian - Guf - Dawel. Es war, *in der Tat*, ein Höhepunkt in jeder Woche. Besonders danken möchte ich Guf, der neben Lennart, Tobias, Steven, Stephan und Max, mein größter Korrekturleser war und zum Schluss viele Messungen vorgenommen hat. So manche Stunden haben wir gemeinsam im Labor verbracht, gemessen, diskutiert und erzählt. Vor allem durch deine Fragen habe ich sehr viel gelernt. Ganz besonders danken möchte ich m. l. Julia, es war nicht immer einfach mit mir, danke dass du für mich da bist und mir Freude bereitest.

Meinen Magdeburger Freunden, Rob, Basti, Markus, Sven, Chris und Linn möchte ich danken. Die wunderbare Studienzeit mit euch bereitete mir den Weg nach Braunschweig.

Zu guter Letzt möchte ich meiner Familie danken: Meinen Eltern, Albrecht und Sibylle Kramer, meinen Großeltern, Brigitte und Hans Storch und Isolde und Karl Kramer, und meinen Brüdern, Georg und Bernhard mit Frau Anja und Kindern Benjamin, Jonathan und Annelie. Da wo die Familie ist, da bin ich zuhause.